THÈSE

En vue de l'obtention du

DOCTORAT DE L'UNIVERSITÉ DE TOULOUSE

Délivré par **l'Institut Supérieur de l'Aéronautique et de l'Espace**
Spécialité : Énergétique et transferts

Présentée et soutenue par **Chao HUO**
le 26 mars 2012

Analyse numérique et expérimentale d'un doublet de rotors contrarotatifs caréné au point fixe

---

JURY

M. Smaïne Kouidri, président, rapporteur
M. Jérémie Gressier, co-directeur de thèse
M. J. Gordon Leishman, rapporteur
M. Jean-Marc Moschetta, directeur de thèse

École doctorale : **Mécanique, énergétique, génie civil et procédés**

Unité de recherche : **Équipe d'accueil ISAE-ONERA EDyF**

Directeur de thèse : **M. Jean-Marc Moschetta**
Co-directeur de thèse : **M. Jérémie Gressier**

ACKNOWLEDGEMENTS

I would like to thank the China Scholarship Council who provides me the financial support, and to Northwestern Polytechnical University for the procedure guidance and the opportunity that help me to study abroad. I am eternally grateful to Institut Supérieur de l'Aéronautique et de l'Espace for the facilities, technics and education, and to the Lab of Propulsion and Aerodynamic for the wonderful work environment which let me feel in a family.

I owe my gratitude to my advisor Dr. Jean-Marc Moschetta for the chance given to me as a grad student. The beginning introduction from the papers sent by him greatly inspired me. He allowed me much freedom in the study and his abundant experiences benefit my work a lot. Especially thanks for his support on the defense procedures. Thanks him to the committee organization.

I am grateful to my advisor Dr. Jérémie Gressier for his guidance on my simulation work. His technical insight motivates me to look at the work in multiple ways and aspects. His enrich knowledge on the CFD gave me a good guidance on the exploration of physics. He let me know that the fluid dynamics should be an amazing word to be explored.

I would like to acknowledge the invaluable help of M. Roger Barènes, without whom this research would never have occurred. Three years ago, when I sent a letter to him to seek for an opportunity as a PH.D student, it was him who introduced me to my advisors Dr. Jean-Marc Mochetta and Dr. Jérémie Gressier and provided me the chance working in the Lab of Propulsion. He taught me the fundamental skills for the experimental work and helped me to understand the France education. His humor and passion as a father-figure encouraged me to conquer every difficulty during all the course of this research.

I feel so proudly to be their student and so honored with their guidance on the research.

I would like to acknowledge the staff members: thanks to M. Gilles Grondin for his patient explanations on the mesh built method; thanks to M. Patrick Cazenave, M. Philippe Mouligné and M. Serge Gérard for the preparation and fabrication on the test bench; thanks to Mme. Christiane Boyer, she always companied with me to deal with all the difficulties in the daily life, especially thanks to her for the help in the hospital when I got an operation; thanks to M. Nicolas Garcia-Rosa for his enthusiasm and advices on the complicate procedures of the thesis.

I would like to thanks some of the students who were incredibly patient to helpful solve the questions I had. David Ferrer Desclaux, Hubert Fabre, Vincent Périer, Kochems Filip, Valverde Salazar Alfredo and Jolan Ropton etc., thanks for all your help.

Finally and most important, I owe my deep gratitude to my father, my mother and my sister who always provides me with the emotional support and inspire me

to work hard. I would like to thank my boyfreind An bang. He calmly dealt with the stress of his work and my Ph.D. His constant love and support accompany with me to get through the periods of immense bleakness and exhaustion even though we were always separated far away. Without him I would never have made it to the finish line.

ABSTRACT

This study aims to analyze the behavior of shrouded, contrarotating coaxial rotor in the reduced MAVs'scale in order to exploit its potential to improve the free rotor steady performance. The high hover ability under low operational Reynolds number is therefore, a scientific challenge. Generally, comparing with free rotor, the addition of the shroud decreases the flow contraction and gives the potential to generate an extra thrust. A suitable nozzle can control the mass flow for a given power. The increased mass flow, comparing with free rotor, amplifies the thrust offered by the low pressure formed at the air entrance.

To understand the principals of shrouded propulsion system, a simplified theory model was first proposed through the extension of Froude theory for free rotors: the double rotor is initially treated as an actuator disk, generating the flow at varied sections through the shroud passage.

A 2D simulation which accounts for an axial flow of viscous effects within the actual shroud profile, confirmed effects of all defined geometrical parameters. It further demonstrated that within the non-stalling region of the different cross-sections, shroud shape and inlet shape do not have a significant impact on performance.

The experimental study, carried out with coaxial rotor, contributed to the confirmation of the overall performance and the approximation of the flow field through the shroud. Innovative diagrams adapted for dual rotor allow to analysis the optimized performance along with its respective speed regime. The shroud presence was revealed to substantially decrease the slipstream contraction and the tip vortex loss when compared to free rotors, which is beneficial for the entire system.

By introducing the actual flow, the 3D simulation, developed to better model the actual coaxial rotor in counter rotation, was validated to well solve the steady performance. It was applied to complement the analysis of the flow around the coaxial rotor and to prepare the comparison with the unstationary experiments in the future.

Keywords: Coaxial rotor, contrarotating rotor, shrouded rotor, Froude theory, actuator disk, shroud, performance optimization, MAVs.

RÉSUMÉ

Cette étude se propose d'analyser le comportement du double rotor contra-rotatif caréné dans le cadre des échelles réduites des microdrones, pour exploiter le potentiel d'amélioration des performances stationnaires des rotors libres. La demande d'une performance propulsive de haut niveau, alors que les échelles sont très réduites constitue un véritable défi scientifique. De façon générale, par rapport au rotor libre, l'ajout de la carène permet de piloter la contraction de l'écoulement et offre un potentiel de poussée de carène. La tuyère par sa condition d'adaptation pilote le débit entrant à puissance donnée. L'augmentation du débit massique, par comparaison au système de rotor libre, amplifie la poussée à travers la dépression distribuée sur toute la surface de captation.

Pour comprendre les lois de fonctionnement d'un système propulsif caréné, il a d'abord été proposé un modèle théorique simplifié basé sur une extension de la théorie de Froude pour les rotors libres: le système rotor est assimilé à un disque actuateur, générateur de débit dans une conduite à section variable.

Une simulation Navier Stokes 2D axisymétrique a permis d'optimiser les paramètres de forme du carénage. Les simulations ont confirmé l'influence déterminante des sections d'entrée et de sortie, et relativisé l'impact des formes possibles, pourvu que les variations de sections limitent le décollement de la couche limite.

Après conception d'un banc d'essai utilisant un doublet de rotor coaxial placé dans cette carène optimisée, l'étude expérimentale complète et confirme les performances globales du système et qualifie l'écoulement méridien. Quelques nouveaux modèles de diagrammes concernant plus spécifiquement le double rotor permettent d'analyser les performances optimisées, fonction des régimes de vitesse et des positions de rotors. Les comparaisons croisées, simples et double rotors d'un côté, carénés ou non de l'autre, ont mis en relief l'intérêt du système birotor caréné.

Enfin, une simulation 3D instationnaire a été entreprise pour compléter l'analyse de l'écoulement autour des rotors, pour valider le comportement moyen déjà observé, et préparer les comparaisons expérimentales instationnaires futures.

Mots clés: Rotor coaxial, rotor contra-rotatif, rotor caréné, théorie de Froude, disque actuateur, carène, optimisation de performance, microdrone.

RÉSUMÉ DE LA THÈSE

Chapitre 1: Introduction

Depuis que la science a permis le développement d'aéronefs de tous types pour les usages les plus divers, deux catégories de vecteurs ont été mis au point: l'avion à voilure classique, nécessitant un déplacement rapide pour générer des capacités de portance, et les hélicoptères et leurs dérivés, regroupés sous le nom d'aéronefs à voilures tournantes, pour des usages autorisant des vols stationnaires ou quasi stationnaires dans les conditions souvent difficiles, à proximité du sol ou des parois. Depuis quelques années, on a vu se développer une miniaturisation de ces différents vecteurs, d'abord basés sur le monde du modélisme, répétant la même distinction entre micro-drone d'avancement et micro-drone à vol stationnaire, mini hélicoptères, tri-rotors ou quadri-rotors [2, 3, 4, 5, 6, 7]. De façon générale, parmi tous les choix de conception possibles, les aéronefs à voilure tournante semblent particulièrement intéressants pour leur maniabilité en vol stationnaire.

Une contrainte nouvelle apparait dès lors que le micro-aéronef se propose d'explorer des domaines de vol très limités par des parois proches, des murs, des falaises, dans un milieu urbain, ou même à l'intérieur des habitations, pouvant aller jusqu'à proposer d'explorer des grottes ou des milieux particulièrement exigus. L'enjeu est alors non seulement de réduire le volume global tout en conservant une possibilité d'emport de charge utile, mais aussi de protéger la voilure tournante tout en augmentant la durée du vol possible. Il est alors nécessaire d'améliorer la génération de portance par unité d'énergie disponible, quantité qui reste limitée par le poids des batteries embarquées.

Il faut alors faire face aux contraintes de taille des MAVs (micro aircrafts vehicles). Les exigences de faible vitesse de déplacement, ou de capacité à rester en vol stationnaire forcent ces ensembles à fonctionner à de nombres très bas de Reynolds, 10,000 à 50,000 [3] lorsqu'on les référence aux carènes et aux diamètres, même si les régimes de rotation sont très élevés, pour compenser leurs très faibles diamètres. Par conséquent, les effets de viscosité sur l'échelle du microdrone seront prépondérants par rapport aux effets d'inertie, nécessitant des études particulières à ce domaine des petites échelles.

Un indice de performance important, qualifiant particulièrement le système du rotor est le chiffre de mérite (Figure de Merit, FoM) qui évalue la capacité de transférer de la puissance mécanique venant de l'arbre rotor au fluide dans lequel tourne ce rotor; cette valeur ne pouvait atteindre qu'un maximum de 0.35 pour les premiers micro-rotors [4, 5] et a atteint 0.65 lors des recherches actuelles [6]. Cela reste tout de même une très faible valeur quand on sait que les hélicoptères de taille grandeur réelle de plusieurs mètres d'envergure, peuvent atteindre un FoM de 0.8 [7]. Un autre indice de performance, évaluant le système tout entier, est le Power Load-

ing (PL) qui caractérise la capacité du système énergétique à générer une poussée globale pour une puissance initiale donnée. Cet indice propulsif, qui n'est pas un rendement, est lui aussi pénalisé par la réduction d'échelle: dans le cas des micro systèmes, sa valeur maximum ne peut pas dépasser la moitié de celle obtenue pour les hélicoptères.

Avec ces données d'échelles, des configurations alternatives à l'hélicoptère classique doivent être étudiées pour tenter d'améliorer ces performances basiques. Une de ces dernières configurations est le "rotor contra-rotatif caréné". Elle sera basée sur un doublet de deux rotors tournant dans le sens opposé sur le même axe, ainsi qu'une partie fixe spécifique, un carénage entourant les rotors, mais de forme spéciale optimisée pour la performance propulsive, appelée pour cette raison une carène. Voir figure suivante.

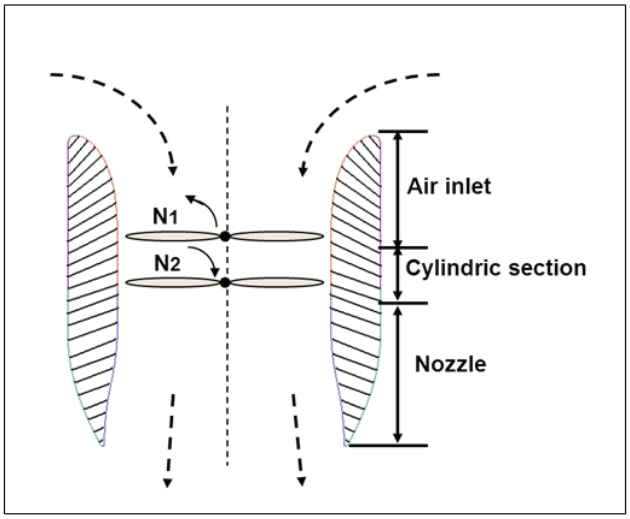

Figure 1: Schéma de la section méridienne du rotor contra-rotatif caréné en fonctionnement stationnaire

Un tel assemblage combine simultanément les avantages des deux composants: le rotor coaxial peut permettre de réduire la dimension du système grâce à l'augmentation du saut de pression de chaque rotor pour une surface frontale donnée, et permet de plus la compensation du couple résiduel de chaque rotor, augmentant par là même le rendement propulsif [8, 9]. H. Glauert avait en effet montré que ce rendement pouvait aussi être réduit par la rotation résiduelle du fluide en mouvement. De son côté, le carénage limite les pertes générées par le contournement de tête de pale, sans négliger sa forme spécifique qui peut présenter des gains significatifs en terme d'amélioration de la poussée, ou en terme de réduction de consommation de puissance [10, 11, 13, 14]. En tant que composant indépendant, la carène accélère le flux en direction des rotors, ce qui crée une dépression sur le profil interne, générant ce qui est connu comme la poussée additive de captation, force qui dans les configurations des micro-rotors peut devenir dominante [15, 16, 19, 20, 21, 22].

L'extrémité du carénage de propulsion, appelée tuyère, peut limiter la contrac-

tion naturelle du flux à la sortie des rotors, et obtenir ainsi un gain de débit par la diminution de la charge rotor et l'effet d'aspiration complémentaire obtenu en amont du système rotor [20]. Au vu de tels avantages, plusieurs études se sont focalisées sur les problèmes de forme et de modélisation du carénage mais également sur l'interaction entre les deux rotors. L'application immédiate des recherches préexistantes à notre problème de rotor contra-rotatif canalisé à échelle réduite se heurte à plusieurs obstacles:

- Les quelques études publiées concernent des systèmes canalisés au rotor unique [20, 27, 36, 38, 40];
- La plupart des investigations concernent des hélices opérant à des nombres de Reynolds de l'ordre de 10^5 à 10^6. Cette valeur est beaucoup plus élevée que celle que l'on va trouver pour les MAVs, qui ont des nombres de Reynolds de l'ordre de 8×10^4, pour les parties statiques et de 4.5×10^4 pour les profils caractéristiques de pales [27, 24];
- Il n'existe pas de programme disponible permettant de fournir des critères d'optimisation du profil de carénage: il faudra donc adapter le CFD 2D à cet usage [50, 51, 52, 53, 54].

A l'évidence, il reste encore beaucoup de zones d'ombre à propos de la conception de la forme du carénage, de la modélisation du système et de l'optimisation qui s'ensuit, dès lors que nous devons traiter le problème du fonctionnement sous influence réciproque de la carène et du doublet de rotor contra-rotatif. Pour résoudre progressivement les problèmes de conception de forme sur de tels systèmes -et particulièrement sur la carène- l'étude va donc proposer une démarche séparant les deux problématiques: le carénage et le double rotor. La décomposition du problème est proposée figure suivante:

Les deux rotors étant entrainés aux vitesses de rotation N_1 et N_2, la différence de pression ΔP apparaissant des deux côtés du double rotor va transmettre de la puissance au fluide. Ce débit massique $\dot{m}$ crée un gradient de pression multidirectionnel sur la carène, et lui permet de générer une poussée supplémentaire pour le système, en plus de la poussée du rotor elle-même. La conception de la forme du carénage peut donc être approchée dès lors que nous aurons déterminé un écoulement, à travers la donnée d'un ΔP ou d'un débit. Ce problème peut être résolu par approches successives, nécessitant des modélisations à plusieurs niveaux, de la simple conservation de la quantité de mouvement sur le carénage, à la modélisation complète du phénomène physique et l'optimisation des configurations de l'ensemble, étudiant même les influences spécifiques du double rotor à travers des résultats expérimentaux ou utilisant des résultats de mécanique des fluides numériques CFD 3D basées sur un modèle physique du rotor et contra rotor caréné.

Les différentes phases de cette étude seront donc les suivants:

- Adaptation de la théorie des quantités de mouvement des rotors libres au rotor contra-rotatif caréné afin d'obtenir une proposition de modélisation de la portance globale comparée au coût énergétique;

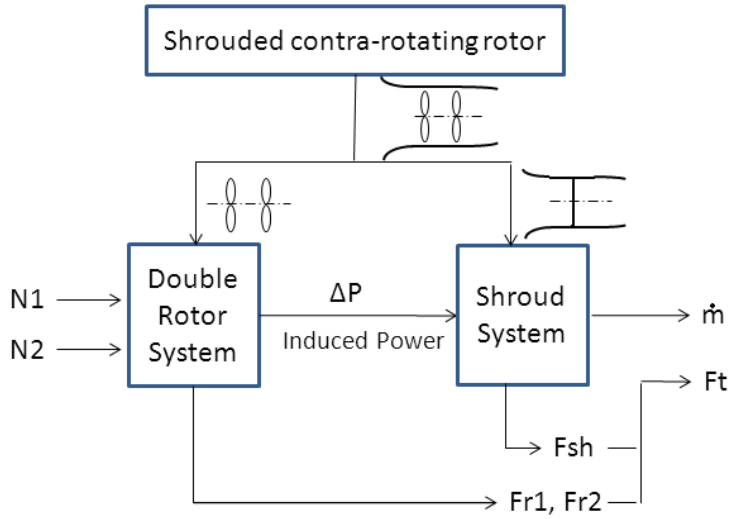

Figure 2: Système propulsif et schéma de décomposition de l'étude

- Utilisation d'un modèle numérique CFD à deux dimensions permettant l'analyse des effets de fluide réel sur les performances de carène, fonction des paramètres géométriques du carénage, en conservant l'hypothèse du disque actuateur. Définition d'une carène optimisée pour le cas proposé;
- Développement et utilisation d'un banc d'essai instrumenté pour caractériser un système réel avec un modèle optimal de carénage et un doublet de rotors contrarotatifs donné, optimisé en utilisant le logiciel Xrotor de M Drela, pour entreprendre des optimisations supplémentaires portant sur des paramètres tels que l'emplacement des rotors et la répartition optimale de leur charge vitesses de rotation respectives;
- Développement et utilisation d'un modèle numérique à trois dimensions permettant l'exploration numérique du fonctionnement de l'ensemble et la caractérisation de différents flux en plusieurs plans caractéristiques;
- Validation des modèles analytiques et numériques en 2D et 3D par les campagnes d'essais expérimentales. Perspective d'utilisation des méthodes pour la conception supplémentaire de profils et d'éventuelles optimisations complémentaires.

Partie I: Prédiction théorique et simulation numérique de l'écoulement méridien sur le profil du carénage

Chapitre 2: Extension de la théorie de Froude pour les systèmes carénés

Dans le but d'étudier, expliquer et prédire les performances d'un rotor, on choisit d'utiliser un modèle de disque actuateur utilisé initialement dans la théorie de Froude pour les systèmes à rotors libres, basée sur les lois de conservation de la dynamique des fluides. Cela réduit le rotor à un disque plat et infiniment fin qui génère un saut de pression uniforme à la traversée du disque, qui n'a donc pour effet que d'impulser une accélération axiale à l'écoulement, répartie continument de l'infini amont à l'infini aval. Le flux est alors considéré comme un tube d'air de section évolutive calée sur la surface du disque actuateur. Lorsque les rotors sont libres, la forme d'un tel tube d'écoulement est naturellement déterminée par son équilibre de pression avec l'air ambiant, donnant un rapport de contraction de "surface infinie aval/surface rotor" de 1/2. Si le même disque actuateur est inséré dans une carène, les équilibres de pression seront modifiés et susceptibles de générer une force complémentaire.

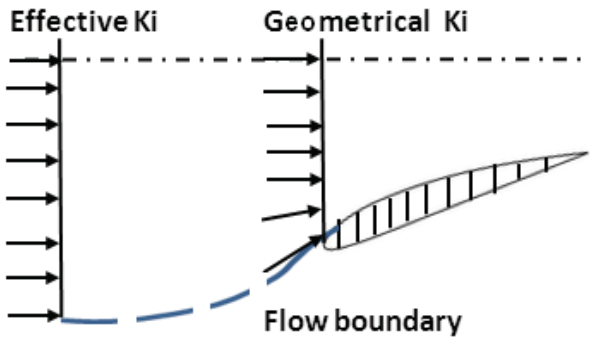

Figure 3: Définition de la prise d'air pour les systèmes carénés

Dans la première hypothèse, l'écoulement est supposé être axial dans toutes les sections du passage du fluide, ce qui inclut la prise d'air et la tuyère de sortie. La définition de la section de sortie est en général la section de sortie planaire réelle du carénage, qui présente des caractéristiques d'écoulement approximativement uniforme. Par contre, l'entrée d'air, en forme de pavillon de débit caractéristique des turbomachines utilisées au point fixe, présente un bord d'attaque très incurvé. Cela produit à proximité de la captation une importante déviation radiale du vecteur vitesse de l'écoulement par rapport à la direction de l'axe. On mettra en évidence cette limite du modèle ultra simplifié, et pour recaler ce modèle par rapport aux résultats numériques, on s'appuiera sur le fait que, dès que le fluide entourant le bord d'attaque commence à être aspiré, sa vitesse étant encore faible, sa pression ne présente pas de différence notable avec celle du fluide situé à l'infini amont, et l'hypothèse d'écoulement axial peut être retenu en ce plan. La véritable section de

prise d'air utile au modèle simplifié pourra être ainsi considérée comme différente de la section géométrique, et retenue comme section caractéristique applicable à la théorie de Froude. Voir la figure ci-dessus.

Par conséquent, par l'introduction des deux paramètres géométriques – K_i et K_e, qui correspondent aux rapports respectifs des aires d'entrée et de sortie sur la surface du disque actuateur, les performances de poussée du système entier, des rotors, de la prise d'air, et de la tuyère en vol stationnaire peuvent être obtenus comme des fonctions du débit massique, en se basant sur la conservation des quantités de vitesse et sur l'équation de Bernoulli. D'après les calculs des performances de poussée, la puissance induite P_i qui représente la puissance transmise au fluide, peut être déterminée à partir de la poussée du rotor F_R comme l'indique l'équation suivante obtenue comme résultat du modèle:

$$P_i = \frac{\Delta P \cdot \dot{m}}{\rho} = \frac{\dot{m} \cdot F_R}{\rho\, A_R} = \frac{1}{2}\frac{1}{K_e^2}\left(\frac{F_T}{\rho\, A_R}(\frac{1}{K_e} - \frac{1}{2\, K_i})^{-1}\right)^{\frac{3}{2}} \cdot \rho A_R \qquad (1)$$

D'après l'extension de la théorie de Froude, les caractéristiques globales du système caréné peuvent être évaluées grâce aux diagrammes de caractéristiques présentés sur les figures suivantes.

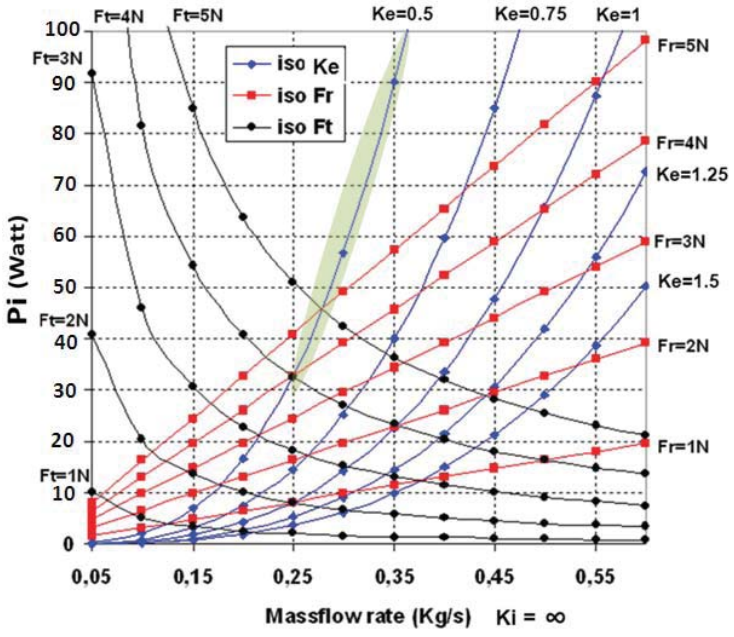

Figure 4: Performance globale du système avec $K_i = \infty$

Ils offrent un guide utile à la compréhension du phénomène et à la conception de la carène, présentant la puissance induite P_i nécessaire fonction du débit de masse d'air aspiré. L'équation proposée ci-dessus montre que la P_i minimum est obtenue sous la condition que K_e est égale à la moitié de K_i, quelque-soit la valeur recherchée pour la poussée totale F_T du système.

La première représentation, supposant une entrée d'air infinie, permet de retrouver la ligne de contraction K_e=0.5, où la poussée de carène s'annule, correspondant exactement au fonctionnement du rotor libre.

En se basant sur ces fonctions, les effets du carénage sur les performances du système peuvent être prédits.

- En ce qui concerne les performances de poussée, de façon générale, une prise d'air de section large combinée à une grande section de sortie de tuyère peut créer une amélioration sur la poussée de la carène. La valeur K_e=0.5, qui correspond exactement à la contraction du rotor libre, est la véritable limite entre les effets positifs et négatifs sur la poussée du carénage. Une tuyère simplement cylindrique K_e=1 distribuerait uniformément la poussée sur le rotor et la carène pour un système ayant une prise d'air infinie. Ces cas ne se retrouvent pas avec une entrée de section finie. En comparaison avec le système qui a une entrée infinie, un tel diagramme présenté ci-dessous offre une meilleure orientation de conception pour le système avec une entrée finie. Pour une prise d'air infinie, une telle amélioration ne trouve pas de limite théorique, puisque quelque-soit la poussée totale proposée, la puissance induite nécessaire tend vers zéro lorsque le débit devient infini lui aussi.

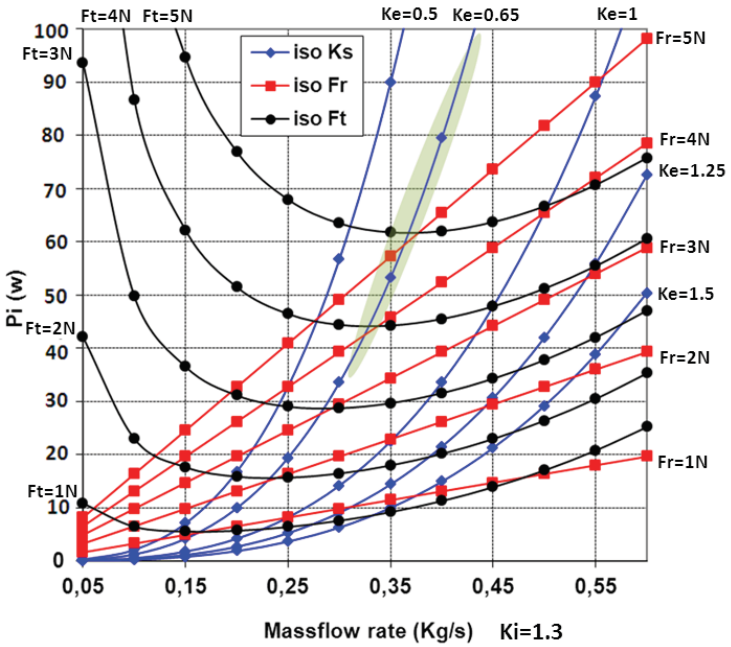

Figure 5: Performance globale du système avec $K_i = 1.3$

On peut tirer quelques conclusions de l'examen de ce diagramme:

- Génération de poussée par chaque partie composant le carénage: une fois le profil de carène fixé, la contribution de l'entrée d'air et de la tuyère sur la

poussée totale sont constants, quel que soit le débit. L'entrée d'air contribue toujours à toute ou plus de la poussée totale. La tuyère a toujours un effet négatif, sauf dans le cas de la géométrie cylindrique où cet effet s'annule. Toutes ces contributions sont liées à l'évolution des pressions statique de sortie de carène, qui facile l'éjection, alors que le rotor libre est pénalisé par l'équilibre de pression en sortie.

- Rôle particulier de la tuyère sur les performances du système: même si elle apparait comme un élément de sillage aérodynamique, elle permet d'augmenter le débit. Quelque soit la géométrie de l'entrée d'air, une large surface d'éjection peut obtenir un débit bien supérieur à celui des rotors libres, et ce pour une puissance induite donnée. Mais, de façon plus réaliste, pour une prise d'air finie, la performance optimisée qui correspond à la consommation minimale de puissance induite pour une poussée totale donnée, se retrouve pour une grande surface d'éjection. La théorie montrerait que la surface de sortie optimisée, est égale à la moitié de la surface d'entrée effective.

L'extension de la théorie de Froude offre donc une prédiction sur les performances du système caréné, et permet d'évaluer théoriquement les effets de la prise d'air et de la sortie sur les performances globales de la carène. Cependant, comme expliqué dans l'extension de la théorie, la surface effective de prise d'air nécessite d'être mieux définie, pour respecter une contrainte de flux axial. De plus, en regard des faibles nombres de Reynolds de l'écoulement en carène, les effets de la viscosité ne peuvent être davantage négligés et seront pris en compte dans la suite de l'étude.

Chapitre 3: Simulation numérique 2D et étude paramétrique de la carène

Les analyses théoriques révèlent que le carénage peut améliorer le comportement propulsif du système et que cette amélioration peut être maximisée quand le profil de la carène est correctement conçu de manière à ce que les deux plus importants paramètres, K_e et K_i, soient, comme le prévoit la théorie, dimensionnés l'un par rapport à l'autre. Cependant, le dessin d'une telle géométrie, basé sur une analyse théorique, est évidemment limité par les contraintes de dimensions possibles et les effets réels de la couche limite sur le carénage. Dans le même temps, dans le plan de sortie des rotors, le flux n'est pas réparti de façon uniforme, un peu à cause de l'équilibre radial. Ce chapitre a donc pour objectif de développer une étude numérique en deux dimensions utilisant un logiciel CFD commercial (Fluent 6.3), en explorant davantage la conception du profil du carénage pour optimiser les performances du système, afin de fournir l'essentiel des résultats sur chaque paramètre géométrique pour une conception optimale de la forme du carénage.

Pour débuter cette étude numérique en deux dimensions, le modèle analytique paramétrable concernant les deux rotors et le carénage doit être déterminé en premier. L'influence principale du doublet de rotor contra-rotatif sera ramené au saut de pression, et sera donc modélisée par un disque, hypothèse acceptable dès lors

que la première partie du projet se focalise sur la conception des paramètres de la carène. Dans un carénage fermé, la fonction du double rotor peut être résumée comme créant une différence de pression ΔP puisque dans le cylindre, par continuité des débits, il ne peut y avoir de saut de vitesse. Cette hypothèse permet de regarder plus simplement le reste du fonctionnement du système dans des conditions de vol stationnaire. Le carénage au droit des pales est un simple cylindre neutre, puisque le but est de générer le débit, et que l'on n'attend pas de véritable gain de poussée de carène à ce niveau. Cela nous conduit à distinguer la méthode de conception du profil du carénage de celle du profil des pales. En se basant sur les fonctions des différentes parties du carénage, le carénage pourra donc être divisé en trois zones: la prise d'air qui génère une forte poussée avec la très basse pression statique générée à sa surface, la section cylindrique du milieu utilisée pour l'installation des deux rotors, et enfin la tuyère de sortie du carénage, qui laisse l'écoulement retrouver la pression ambiante après le dernier rotor. Pour chaque partie, tous les paramètres géométriques envisageables sont identifiés comme reporté sur la figure suivante.

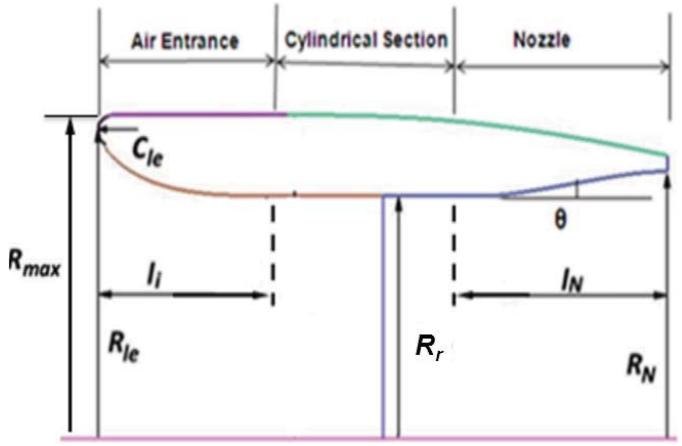

Figure 6: Modèle de Froude pour le système caréné

- Pour la prise d'air – largeur l_i, forme intérieure, courbure du bord d'attaque C_{le} et rayon du bord d'attaque R_{le};
- Pour la section cylindrique – rayon maximum R_{max} et rayon cylindrique (ou rayon du rotor) R_r;
- Pour la tuyère – rayon de sortie R_e, largeur l_N, forme intérieure pour la tuyère et l'angle divergent θ.

Comme il est exigé dans les méthodes numériques d'analyse des écoulements, nous devons définir le domaine d'étude, des conditions aux limites aérothermodynamiques aux frontières du domaine, et la qualité du maillage. Pour éviter d'avoir à définir les conditions aux limites uniformes en entrée et en sortie de carénage à cause du gradient de pression radiale, le champ modélisé n'inclut pas seulement le canal de

flux interne au carénage, mais contient aussi une large zone englobant le carénage. À l'entrée du champ modélisé, qui est éloignée de l'entrée du carénage, l'écoulement est supposé lent, et le calcul est initialisé de manière à éviter un écoulement contraire à la limite de sortie. La condition sur la pression est utilisée au niveau de l'échappement du fluide, ce qui se rapproche vraiment de la réalité. Avec ANSYS ICEM 11.0, un maillage structuré a été réalisé à partir d'une topologie en "O-grid" générée tout autour du carénage pour une meilleure résolution de la couche limite. Après avoir bien établi ce cadre, les évaluations des conditions limites sur la vitesse V_∞, du modèle de turbulence et de la comparaison avec la théorie ont été effectuées en utilisant la variable de performance, "power loading", évaluée par le rapport de la poussée totale à la consommation de puissance, identique à celui utilisé dans l'analyse théorique.

Les premiers résultats de la simulation ont montré que la vitesse incidente V_0 ne peut pas être nulle sous peine d'amorcer une recirculation interne au domaine, mais qu'une valeur finie peut introduire une erreur sur l'évaluation de la performance du système. Elle doit donc être aussi petite que possible, et la valeur de 0.3 m/s a été retenue comme le minimum qui puisse éviter le flux inverse et en même temps limiter l'erreur d'éloignement du cas de point fixe. Tous les modèles de turbulence que l'on applique dans la simulation en deux dimensions - S-A, RNG k-ε ou SST k-w, se comportent vraiment de façon similaire pour les performances. En considérant des critères basés sur les coûts informatiques et l'efficacité, le modèle de turbulence Spalart-Allmaras semble donc le meilleur; la comparaison de la dépendance des ΔP révèle que les résultats de la simulation en deux dimensions sont en accord avec l'analyse théorique du disque actuateur caréné. Une bonne cohérence est obtenue sur les lois associées à ΔP. Cette concordance implique la faisabilité des simulations en deux dimensions avec pour vitesse limite 0.3 m/s et en employant le modèle de turbulence Spalart-Allmaras.

D'après ces méthodologies, la simulation CFD 2D a tout d'abord été effectuée pour permettre des recoupements expérimentaux. On a d'abord retenu une différence de pression de 100 Pascals, puis en second lieu, on a imposé le δP nécessaire pour obtenir la poussée désirée de 5 Newtons, en se basant sur rapport entre la poussée totale obtenue et le saut de pression provenant de la dernière simulation. En suivant cette démarche, avec un diamètre de rotor constant, valant 90 mm, les différents modèles numérisés du carénage seront proposés avec un paramètre géométrique variable, tandis que les autres resteront constants, afin d'explorer indépendamment leurs effets.

Les simulations ont révélé les effets de chaque paramètre sur les performances du système, et ont permis de déterminer celui qui serait le plus pertinent pour l'optimisation de la variable de charge portante "power loading". Les conclusions principales sont les suivantes:

- Pour la tuyère du carénage, le "power loading" est fortement amélioré avec un rayon d'extrémité de tuyère plus large. Cependant cette amélioration est limitée par l'apparition du décollement de la couche limite, qui réduit le rayon

effectif du passage du fluide en extrémité et produit une perte de pression. Sa dimension optimale est située autour de 1.15 fois le diamètre du rotor. La forme interne pourrait être un facteur important, mais en réalité son effet est drastiquement réduit par la viscosité. élargir l'embout pourrait aussi améliorer le système, mais ce paramètre est contraint par l'angle de divergence de l'extrémité de tuyère. L'angle optimal de divergence pour différentes largeurs d'embout reste calé à environ 10.5^o.

- De son côté, l'entrée d'air devant être conçue pour adapter au mieux la structure du flux, on constate que l'amélioration obtenue par la variation des paramètres d'entrée reste très limitée. Le rayon maximum du carénage et le rayon du bord d'attaque sont des variables pertinentes. La variation du rayon maximum limite la modification du rayon de bord d'attaque pour tenir compte de l'intégralité de la géométrie. L'augmentation simultanée des deux paramètres implique une augmentation de la surface interne de la prise d'air. Cela pourrait élargir la zone de dépression et finalement améliorer le système vis-à-vis de ses performances de poussée. Mais cela est limité par le rayon maximum. Les valeurs optimisées des rayons de bord d'attaque et de rayon maximum sont respectivement de 1.3 fois et 1.44 fois le rayon du rotor.

- Les autres paramètres ont une faible influence, la variation de "power loading" n'étant jamais supérieure à 1%. Cependant ils jouent un rôle important dans la distribution de pression le long du carénage. Le critère basique de conception des profils est de réduire le risque de faire décoller la couche limite à la fois sur la prise d'air et sur l'embout de tuyère.

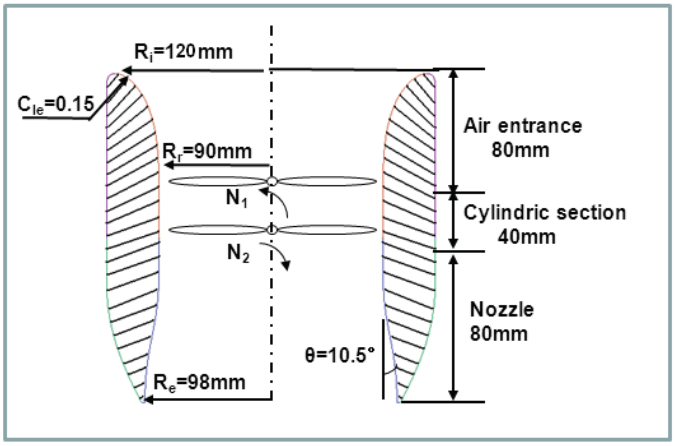

Figure 7: Nouveau modèle de carénage avec profil optimal

En se basant sur les formes optimales de la carène ainsi que sur les valeurs de différents paramètres issus des simulations, un nouveau modèle de carénage présentant un profil optimal a été proposé. Le détail des paramètres géométriques et du profil du carénage peut être observé sur la figure ci-dessus. À l'issue de cette étude

préliminaire, une nouvelle carène a pu être réalisée, testée et ensuite étudiée en simulation par des moyens expérimentaux et numériques pour déterminer les performances du système, l'écoulement de l'air lors de son passage dans le carénage et à la traversée du rotor, et voir ainsi les optimisations supplémentaires résultant de toutes les configurations du système.

Partie II: Étude expérimentale sur le rotor contra-rotatif caréné avec le nouveau modèle de carène

Chapitre 4: Introduction expérimental

Ce travail expérimental vient donc après une étude ciblant la connaissance des effets induits par la conception du profil de carène utilisant une analyse théorique et des simulations méridiennes 2D en première partie. Il a pour but d'explorer profondément les comportements du système en se basant sur les effets de la carène incluant ses performances globales, ainsi que les caractéristiques de l'écoulement obtenu, en sachant que pour ce cas, pour les mesures expérimentales, le profil de carénage est optimal et le doublet de rotors contrarotatif est fixé [73, 74, 75]. Dans ce chapitre, on présente les nouveaux dispositifs expérimentaux, conçus et réalisés par le département Aérodynamique, Énergétique et Propulsion de l'ISAE (Institut Supérieur de l'Aéronautique et de l'Espace). Ce banc d'essai est spécialement dédié d'abord à une validation des performances, puis à une meilleure compréhension des écoulements, notamment sous l'influence des interactions entre les différents composants du rotor contra-rotatif canalisé. Sur ces bases, un programme d'essai a été conçu pour analyser les performances globales, ainsi que le champ des écoulements traversant l'ensemble du système réel caréné.

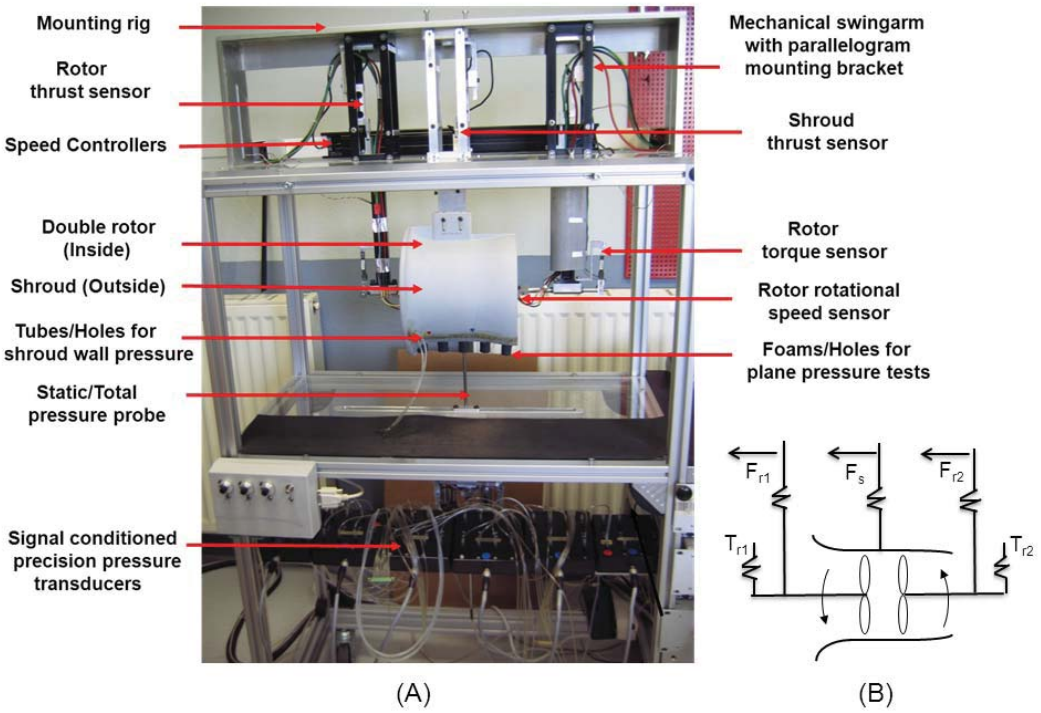

Figure 8: Configuration du banc d'essai (A) et plan de travail simplifié (B)

Si on observe le dispositif expérimental, le banc d'essai statique est constitué d'un cadre rectangulaire de métal, comme on peut le voir sur la figure ci-dessus. Le système générateur de débit pression à rotors contrarotatifs caréné est installé au centre avec chaque composant, à savoir le carénage et les deux rotors, chacun séparément suspendus à trois bras mécaniques mobiles. Ainsi, les capteurs de poussée et de couple peuvent les tester indépendamment. À la surface de la carène et tout au long de l'axe, une série de perçages ponctuels a été réalisée pour mesurer l'évolution de la pression statique pariétale, tous ces perçages étant reliés à des capteurs de pression de très faible gamme. Parallèlement, cinq autres emplacements ont été créés au bas du carénage, chacun permettant le passage étanche de la sonde de pression totale à trois trous à tête cylindrique, ou bien de la sonde de pression statique ayant une géométrie de col de cygne. Les champs de pression totale et de pression statique sur ces plans perpendiculaires à l'axe ont pu ainsi être mesurés. En se basant sur ce dispositif de mesure, le champ de vitesse stationnaire, et par conséquent de débit massique ont aussi pu être calculés. Prenant soin de mesurer toujours aussi les performances globales – poussée, couple, puissance et vitesse, la pression surfacique le long de l'axe, les pressions statique et totales sur les plans perpendiculaires à l'axe ont d'abord été calibrées et validées.

Pour les programmes d'essais, basés d'abord sur les performances globales telles que la poussée, le couple et la puissance, quatre configurations – simple rotor libre (free simple rotor FSR), double rotor libre (free double rotor FDR), rotor simple caréné (shrouded simple rotor SSR) et double rotor caréné (shrouded double rotor SDR), ont été retenues. Il s'agissait de réaliser des campagnes d'essais pour explorer en performance certains domaines de vitesse et d'emplacement des rotors. Pour toutes les configurations sauf la SDR, la vitesse de rotation est comprise dans un intervalle allant de 3000 tr/mn à 9000 tr/mn avec un pas de 500 tr/mn. Quant au SDR, le seuil minimum de vitesse de rotation est à 4000 tr/mn en considérant que la carène entraine un fonctionnement de windmilling dès lors que l'un des rotors génère à lui seul un débit supérieur à la limite de décharge de l'autre. Concernant l'emplacement des rotors, deux valeurs sont introduites: la distance absolue entre le premier rotor et la prise d'air Dabs, et la distance relative entre les deux rotors Drel. Celles-ci sont déterminées d'après différentes configurations possible, d'après les degrés de liberté du banc d'essai pour faire varier les emplacements. Pour le système SDR, se basant sur les résultats d'essais de performances globales, un doublet de régime de rotation, ainsi que quelques positionnements des rotors ont été choisis pour les expériences sur l'effet local du carénage et sur le champ d'écoulement du système.

Toutes les données expérimentales ont besoin d'être standardisées en raison des perturbations de l'environnement et des conditions météorologiques. Sur les performances standardisées, deux variables qualitatives ont été définies pour les évaluations expérimentales. L'une d'elles est le chiffre de mérite (Figure of Merit, FoM) qui évalue la capacité des rotors à transférer l'énergie mécanique au fluide, l'autre – un indice propulsif, le Power Loading, est le même que pour les simulations 2D. Cependant, il faut noter que le calcul du PL lors des expériences utilise la puissance

mécanique consommée par les deux rotors, alors que le PL obtenu en analyse basé sur disque actuateur se base sur la puissance induite proposée. Ayant établi cela, la comparaison des performances globales telles que la poussée des deux rotors simple isolés, la pression testée par différents instruments et le débit massique mesuré sur plusieurs plans de section axiale a permis de calibrer et valider la qualité du banc d'essais.

Chapitre 5: Évaluation des caractéristiques des systèmes carénés

Utilisant ces équipements, et en particulier les programmes de pilotage et d'acquisition des mesures du banc d'essais, les campagnes expérimentales ont été menées pour étudier les performances globales et les champs de caractéristiques aérothermodynamiques de l'écoulement. Par rapport aux modèles initiaux de carènes de conception empiriques, les résultats d'essais ont d'abord montré les améliorations du système contra-rotatif caréné qui utilisait le dernier modèle de carénage, obtenu après conception optimisée. Pour présenter les résultats, il a fallu ensuite proposer de nouveaux diagrammes, nécessaires puisque le double rotor ne permet plus d'exploiter les diagrammes classiques de type diagramme de l'hélicier ou champ compresseur. Ces nouveaux diagrammes présentent les performances obtenues en faisant varier chacun des régimes séparément, et ainsi permettent de présenter les comportements globaux du système; on trouvera ainsi un diagramme en double N et un diagramme en $ln(N_1/N_2)$, proposés pour faciliter l'analyse; Enfin, sans doute le plus important, les campagnes d'essais devaient analyser les avantages du carénage à travers l'analyse du champ d'écoulement développé le long de l'axe de la carène, et en faisant des comparaisons sur les performances globales. En accord avec toutes ces recherches, le système caréné avec le nouveau modèle de carénage est censé être finalement validé.

Indépendamment des régimes, différentes configurations peuvent aussi se présenter en fonction de l'emplacement des rotors. Les essais sur différentes combinaisons possibles ont révélé que le déplacement des deux rotors le long de l'axe du carénage ne produit pas réellement de grosse différence sur la variable PL. Une des meilleures positions relatives des rotors est la suivante: le premier rotor est installé à 80 mm, soit environ un diamètre rotor, du plan d'entrée de l'entrée d'air, le second rotor étant situé immédiatement après, au quart de diamètre, environ 20 mm en arrière du plan de rotation du premier. Comparé au modèle de carénage précédent, avec la même localisation des rotors, le nouveau modèle de carène permet d'augmenter la poussée du carénage d'environ 20% ainsi que sa contribution à la poussée totale, pour une puissance d'entrée donnée.

De plus, lorsqu'on la compare avec les trois autres configurations possibles - simple rotor libre (FSR), double rotor libre (FDR), rotor simple canalisé (SSR), la configuration complète SDR présente les meilleures performances. Et la présence du carénage fournit l'amélioration la plus déterminante. Un tel avantage a été ensuite mis en évidence par les essais qui ont suivi sur le champ d'écoulement par la comparaison en particulier avec la configuration FDR.

Lorsqu'on observe le comportement général de la configuration complète SDR, la performance optimale exprimée en PL est obtenue lorsque la première vitesse de rotation est inférieure à la seconde, et dans ces conditions, le couple total résiduel est différent de zéro, ce qui entrainera des difficultés ultérieures de pilotage si on voulait conserver cet optimum.

Même si les deux hélices étaient strictement symétriques d'un point de vue géométrique, deux vitesses de rotation identiques ne génèreraient pas des couples égaux et opposés pour annuler le couple résultant. En effet, elles sont sous l'influence mutuelle l'une de l'autre, dans des positions amont aval. La conception optimisée des deux rotors a proposé deux rotors presque symétriques, et on cherche donc à déterminer le doublet de régime optimum avec cette hypothèse. A l'examen de la performance réelle obtenue dans le diagramme double régime, on constate:

- que la performance optimale est obtenue quand la vitesse de rotation du rotor amont est supérieure à la vitesse de rotation du rotor aval.
- que le couple résultant des deux rotors s'annule quand la vitesse de rotation du rotor amont est un peu inférieure à la vitesse de rotation du rotor aval.

Ces deux constats font donc apparaître une contradiction, et un choix sera nécessaire, montrant qu'il faudra orienter la conception de chacun des deux rotors pour tenir compte de ce comportement dissymétrique.

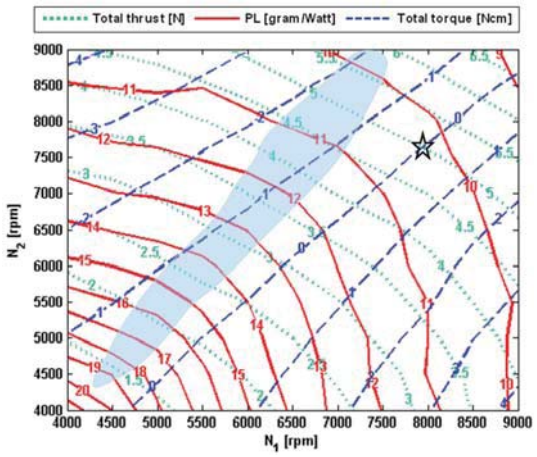

Figure 9: Configuration SDR80-20: Iso performances en fonction de N_1 & N_2

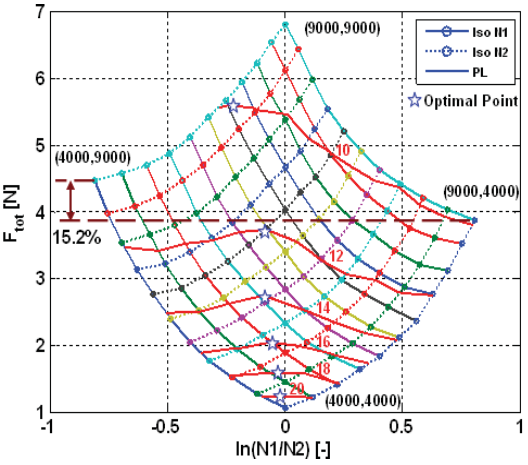

Figure 10: Configuration SDR80-20: Poussée totale en fonction de $ln(N_1/N_2)$

Pour mettre encore en relief cette performance décalée, le diagramme $ln(N_1/N_2)$ affiche le détail du "comportement miroir" lorsque les vitesses de rotation sont interverties. Là aussi, en cas de symétrie parfaite d'écoulement et de charge, échanger la vitesse des deux rotors produirait une performance similaire. On constate qu'une telle similarité est imparfaite. Le fait qu'une vitesse de rotation du premier rotor plus faible permette d'obtenir une meilleure performance peut être observé à travers

différentes présentations. Ces phénomènes seront explorés plus complètement dans le chapitre suivant.

Le même diagramme de comparaison peut être utilisé entre les configurations FDR et SDR. L'amélioration due à la présence du carénage apparait immédiatement. Cependant, pour mieux comprendre les raisons de cette différence, les essais des caractéristiques de l'écoulement ainsi qu'une comparaison en profondeur ont été réalisés. En ce qui concerne les performances du système complet, la présence de la carène entraine à même puissance induite une augmentation du débit massique d'environ 65%. Cela améliore directement la poussée totale qui pourrait être augmenté d'environ 80%.

Bien que la poussée du rotor elle-même diminue en valeur absolue, la capacité de transférer l'énergie mécanique au fluide est augmentée par la carène, avec un FoM de 0.65 qui se compare à un FoM valant 0.45 pour le doublet libre. Bien-sûr, nous avons vu que pour l'effet local du carénage, la contribution de poussée est issue d'une pression statique pariétale inférieure avec le débit augmenté. Les résultats montrent que, quelle que soit la vitesse de rotation, un pic de forte dépression est formé en début de carène, là où la concavité importante génère des accélérations locales alors que parallèlement, la pression statique dans la tuyère de sortie atteint facilement la pression ambiante. Tout cela montre une première fois que la forme du nouveau carénage adapte très bien l'écoulement, sans effets de viscosité ni même décollement importants.

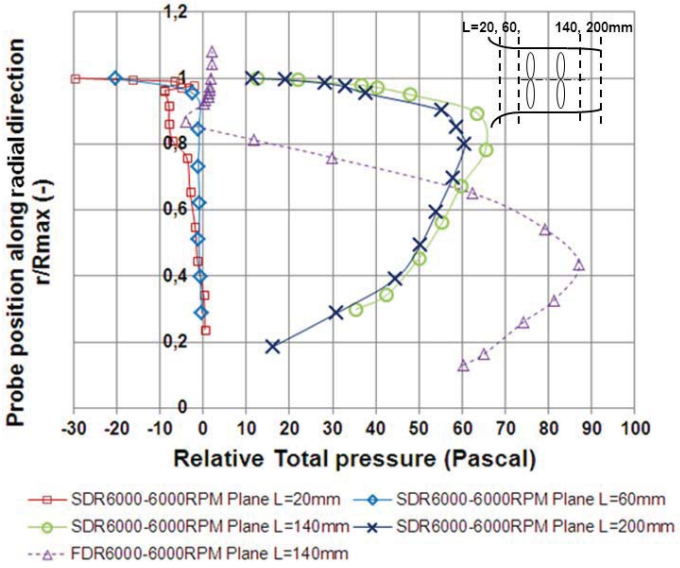

Figure 11: La pression totale sur les différents plans axiaux de SDR et le FDR

Lorsqu'on observe le champ d'écoulement formé sur la distribution de pression statique sur plusieurs plans perpendiculaires à l'axe, à travers toute la carène, le système caréné souffre à plusieurs niveaux de pertes de pression totale: la viscosité dans la couche limite, les tourbillons de contournement de tête de pale, dues au

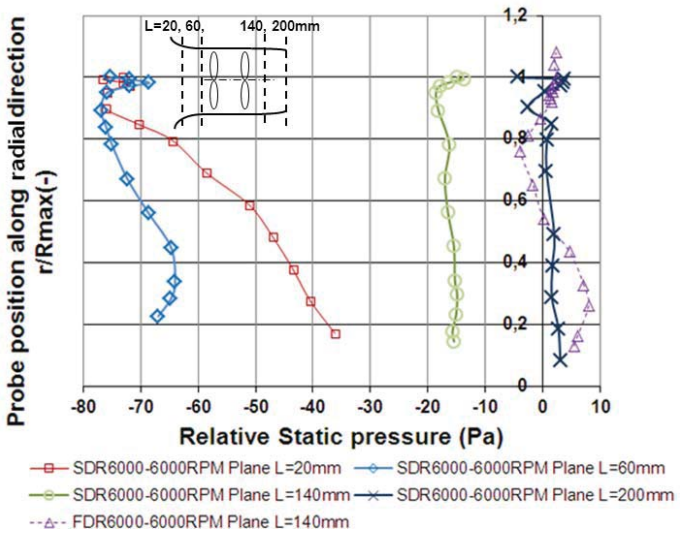

Figure 12: La pression statique sur les différents plans axiaux de SDR et le FDR

jeu résiduel, et enfin le sillage de contournement de moyeu qui avec les moteurs et les ensembles filaires disposés au mieux, restent un facteur de perte de charge non négligeable. Lorsqu'on compare les profils radiaux SDR à ceux obtenus en configuration FDR, on montre que le carénage réduit très efficacement la contraction du flux sortant, et l'adapte assez bien au profil de la carène, sans éviter bien sur le développement d'une couche limite. Même si le jeu de tête de pale n'est pas annulé, les pertes de pression totale dues aux tourbillons de bout de pales sont bien plus faibles que celles de la configuration rotor libre. Notons cependant que nous comparons alors deux fonctionnements utilisant les mêmes rotors, l'idéal ayant été de comparer avec des rotos optimisés pour un fonctionnement sans carène. On peut ensuite observer la figure suivante concernant la pression statique: la manière dont le gradient radial de pression statique évolue en passant dans tous les plans caractéristiques correspond bien aux lois de l'équilibre radial. Un gradient négatif généré dans le plan très amont par des effets de courbure de carène, un premier redressement de cet effet dans le plan amont du premier rotor, un gain important de valeur moyenne au passage du premier rotor accentué au passage du second rotor, et un gradient de pression statique moyenne bien recalée sur la pression ambiante dans le plan de sortie, qui indique un profil de carénage adéquat qui adapte l'écoulement.

Chapitre 6: Effets de divers paramètres de forme sur le système caréné

Pour les systèmes à double rotor carénés, la présence d'une carène et l'ajout d'un second rotor en rotation dans le sens opposé, introduit les variables supplémentaires de conception correspondant aux positions absolues et relatives des deux rotors le long de l'axe du carénage (D_{abs}, D_{rel}), et aussi à la combinaison des régimes de rotations respectifs.

Comme il a été montré dans le chapitre précédent, la différence de PL causée par l'emplacement des rotors semble vraiment petite, en particulier lorsque les puissances de rotation deviennent importantes. Cependant, pour davantage optimiser les performances du système, il reste à étudier les caractéristiques de l'écoulement sous influence des variations de paramètres de position. Concernant les vitesses de rotation des deux rotors, comme il a été indiqué, même si le comportement du système est presque un fonctionnement "miroir" quand les deux vitesses sont échangées entre les rotors, nous avons vu qu'une vitesse de rotation plus importante sur le premier rotor peut tout de même produire une amélioration. Ce chapitre a donc pour objectif d'explorer les effets spécifiques des deux variables au-delà des performances globales du système, pour explorer les caractéristiques de l'écoulement. Pour faciliter les explorations de l'effet des deux variables, d'autres emplacements de rotor D_{abs}=80 mm et D_{rel}=40 mm (SDR80-40) ont été proposés.

En ce qui concerne l'effet de l'emplacement du rotor sur les performances globales, le simple rotor caréné (SSR) et le double rotor libre (FDR) ont été testés pour divers emplacements des rotors: on a retenu la distance absolue à partir du bord de la prise d'air (D_{abs}) pour le simple rotor caréné SSR et la distance relative entre les deux rotors (D_{rel}) pour le doublet de rotors libres FDR. On constate à l'examen des résultats que même si l'effet sur le PL reste faible, il y a un effet relativement important pour une basse vitesse de rotation ou une basse puissance d'entrée. Cela est similaire au système SDR. Avec les essais de plusieurs combinaisons différentes d'emplacements de rotor, on montre que toutes les possibilités de positions induisent une poussée de carénage à plus de 50% de la poussée totale, et qu'aucune tendance évidente n'apparait lorsque l'on fait varier les emplacements. Par contre, concernant la poussée du rotor, il est clair que le déplacement des deux rotors en arrière rend plus évident le rôle du rotor arrière sur la génération de la poussée.

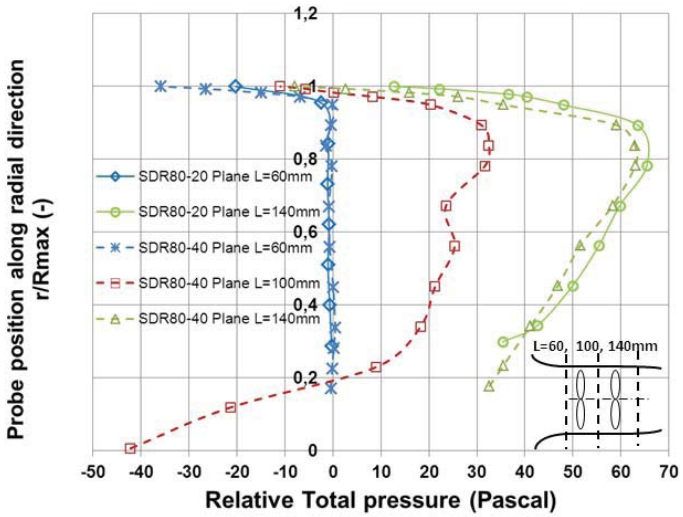

Figure 13: Les comparaisons sur la pression totale entre D_{abs}=80, D_{rel}=20 mm et D_{abs}=80, D_{rel}=40 mm

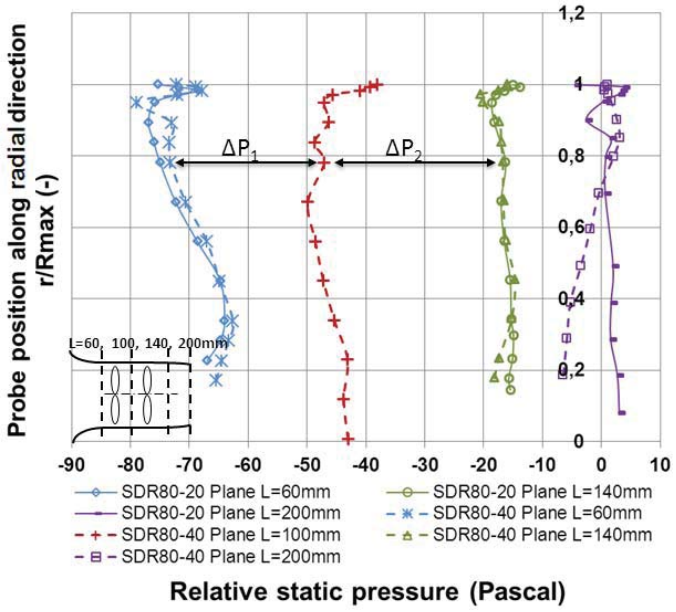

Figure 14: Les comparaisons sur la pression statique entre D_{abs}=80, D_{rel}=20 mm et D_{abs}=80, D_{rel}=40 mm

Deux combinaisons de positionnement des rotors 80-20 et 80-40 ont été comparées. Comme pour les performances globales, l'effet sur le champ d'écoulement est là aussi peu sensible. On peut cependant observer qu'une distance entre les rotors (IRD) réduite 20 mm, favorise la capacité du doublet à transférer de l'énergie mécanique à l'écoulement. Et la pression totale relevée juste après le second rotor est plus élevée que celle du cas SDR80-40. Sur la pression statique, on pourrait remarquer la distribution en sortie de carène. Comparé au SDR80-20, déplacer le second rotor vers l'arrière rend l'écoulement après les rotors sous détendus et perturbé par l'effet de l'équilibre radial. Tous ces éléments peuvent être vus dans les deux figures suivantes. Concernant l'effet local de la carène, puisque les deux rotors peuvent aspirer un débit massique similaire, la pression statique à la surface du carénage a presque la même distribution, sauf aux niveaux des chacun des deux rotors. En conclusion, comparée aux autres effets, la différence causée par l'emplacement des rotors peut être considérée comme négligeable, sous réserve que le jeu entre l'extrémité des pales de rotors et la carène, fortement contraint par le profil intérieur du carénage, ne soit pas trop important.

Concernant l'effet de la permutation des vitesses des deux rotors, le doublet N_1=6000 tr/mn, N_2= 9000 tr/mn ainsi que le doublet complémentaire ont été sélectionnés pour être testés sur le système SDR80-40. En effet, cette configuration laisse ouverte la possibilité de tester le plan situé au milieu de la distance inter-rotors. Cependant, l'interprétation des mesures effectuées sur la distribution des pressions totale et statique sur des plans perpendiculaires à l'axe reste difficile: leurs distributions en amont et en aval des rotors ne présentent pas de différence évidente.

Cependant, la vitesse induite distribuée sur le plan médian est un peu plus grande lorsque le régime de rotation du rotor amont est inférieur à la vitesse de rotation du rotor aval. Ces deux fonctionnements ne sont pas identiques en puissances consommées. Cet effet correspond à une hausse du débit et par conséquent à un plus fort pic de dépression sur la surface concave de l'entrée d'air de la carène.

En comparaison avec les performances du rotor, on pourrait penser que le second rotor ayant un régime de rotation plus rapide pourrait jouer un rôle dominant dans la génération de la poussée par rapport au premier rotor si ce dernier avait eu la vitesse la plus rapide. Au total, le doublet de régime montrant un rotor amont plus lent que le rotor aval produit une amélioration sur les comportements du système. Voir le tableau suivant.

Table 1: Comparaison des performances

SDR 80-40 N_1&N_2	**6000**& **9000**	**9000** & **6000**
F_{r_1} (N)	0.26	1.76
F_{r_2} (N)	2.04	0.31
F_{sh} (N)	2.79	2.62
PL (gram/watt)	10.03	9.80
$\dot{m}$ (Kg/s)	0.431	0.422
FoM (-)	0.63	0.59

Partie III: Simulations numériques 3D et comparaisons entre les expériences et les calculs

Chapitre 7: Méthodologie des simulations 3D

L'extension de la théorie des quantités de mouvement et la simulation numérique paramétrique en deux dimensions utilisent toutes les deux un disque actuateur, imposant une différence de pression amont aval disque pour remplacer le rotor réel. Cela néglige les effets induits par le mouvement de rotation et on ne peut donc pas simuler le sillage produite derrière les rotors, même si elle peut être réduite par la compensation du second rotor tournant dans le sens opposé. De plus, pour le rotor contra-rotatif caréné, l'entrainement en rotation est plus compliqué que celui d'un ou plusieurs rotors libres, à cause de l'interaction entre le carénage de propulsion et les rotors. Le carénage rétrécit le flux entrant et le sillage. Pour le double rotor, le vortex d'extrémité de pale du rotor supérieur se répercute sur le rotor inférieur. Pour le rotor lui-même, il existe des interactions instationnaires des écoulements. Par conséquent, pour approfondir la compréhension des caractéristiques des écoulements au sein du système caréné, une méthodologie de simulation numérique en trois dimensions a été explorée: les méthodes comparées et choisies pour simuler le mouvement de rotation concernaient la définition de la zone à modéliser, les conditions initiales, les conditions aux limites, et le maillage construit grâce à ANSYS ICEMCFD 10.0. Les méthodologies appropriées ont été choisies en se basant sur le logiciel Fluent 6.3.

Depuis que l'objet de l'étude implique des pales de rotor, le résoudre dans un référentiel tournant présente des avantages. Mais pour une configuration complexe, avec deux rotors en rotation contraire, plusieurs repères peuvent être utilisés en séparant le problème en plusieurs zones. Le système a été divisé en quatre parties: la zone du flux dans la partie amont du carénage, jouant le rôle d'entrée d'air, une zone tournante pour chaque rotor ayant une longueur de 30 mm, et le domaine du flux aval du carénage, jouant le rôle de tuyère d'éjection. Dans les plans de séparation des différentes zones, un traitement particulier devra être réalisé sur les interfaces pour la transformation des quantités vectorielles. Nous avons deux manières de traiter de telles interfaces: les plans mélangés (mixing plane), et le maillage glissant (sliding mesh). Ces deux méthodes ont été comparées une première fois dans Fluent dès que la zone modélisée et la grille ont été construites.

Pour définir la zone à modéliser, nous devons prendre en compte les conditions aux limites, particulièrement à l'entrée et à la sortie du flux où elles sont supposées imposer les conditions de pression entrante et sortante qui correspondent le mieux à la réalité. La condition de pression exige une pression uniforme sur la zone limite, ce qui rend difficile la définition de la surface et de sa position. Donc, pour la prise d'air, afin d'être sûrs que le flux entrant a des caractéristiques uniformes, une sorte de demi-sphère ayant un rayon valant 2.5 fois celui du rotor a été introduite en haut de la prise d'air du carénage. Pour la zone d'échappement de l'écoulement, une limite de sortie semble difficile à définir à cause des turbulences provoquées lors de

l'éjection du flux. Deux définitions de la limite ont alors été données: la première est la surface de sortie directement située au bout du carénage, la seconde est un cône tronqué, élargi, mais conservant tout de même une économie de ressources informatiques. Finalement, deux modèles de zones de sortie d'expulsion ont été construits et appliqués dans la simulation, comme on peut le voir dans la figure suivante.

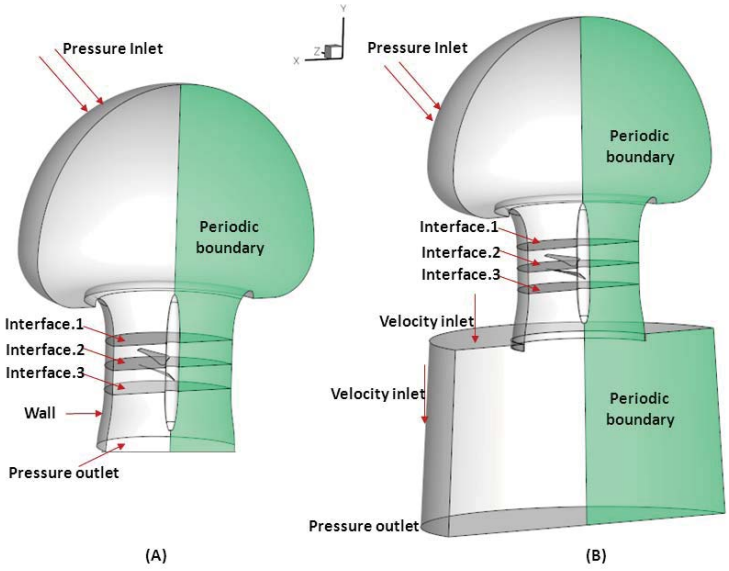

Figure 15: Conditions aux limites et champ informatisé sans (A) et avec (B) cône d' écoulement

D'après les deux définitions du champ modélisé, le maillage pour chaque partie a été construit ainsi: pour les zones de rotation, une grille structurée a été retenue, le maillage structuré permettant le raffinement de la grille autour des pales; pour les zones d'entrée et de sortie, un maillage non structuré a été réalisé comme un ensemble global après avoir au préalable vérifié la faisabilité des deux méthodes de traitement des interfaces.

Les études numériques ont été menées avec le solver "pressure based" et le modèle de turbulence "Spalart-Allmaras" parce que le nombre de Mach est inférieur à 0.3 et que le nombre de Reynolds reste supérieur à 3000. Les résultats ont révélé que la méthode du plan de mélange ne donnait pas de solution satisfaisante à propos de la conservation du débit. Lorsqu'on compare le modèle avec et sans zone aval d'éjection, on constate que la zone d'éjection permet de mieux retrouver le débit expérimental. La différence constatée sur la pression statique à proximité de la surface de sortie carène pourrait avoir été causée par le profil courbé de l'embout de tuyère et l'effet conique du sillage. La modélisation a été testé en maillage structuré et non structurée. Les résultats ont montré qu'il était préférable d'investir dans les maillages multiblocs structurés.

On a donc retenu pour les études suivantes le maillage structuré construit pour

les parties prise d'air et de tuyère, cette dernière zone étant modélisée par le cône tronqué, et la méthodologie de maillage glissant à toutes les interfaces.

Chapitre 8: Validation et exploration de la simulation en 3D

En se basant sur les méthodologies choisies dans le chapitre précédent, qui incluent la " sliding mesh method ", sur la définition du champ de modélisation par une demi sphère pour l'entrée d'air, et par la forme d'un cône tronqué, la condition limite et le maillage structuré, ce travail vise premièrement à valider les résultats de la simulation 3D grâce aux expériences effectuées sur les caractéristiques stationnaires incluant la performance globale et le champ d'écoulement. En comparaison avec l'extension de la théorie des quantités de mouvement et les simulations à symétrie axiale en 2D, les simulations 3D ont introduit les rotors réels pour explorer d'une manière plus efficace les caractéristiques instantanées. Les caractéristiques instationnaires ont alors été analysées par les simulations 3D, en utilisant particulièrement le modèle de l'écoulement à travers le carénage, l'envergure des pales et le bout. En raison de la contrainte des expériences, les effets de la commutation des vitesses et des emplacements des rotors sur l'écoulement ont été complémentés en 3D de manière numérique.

Avant de débuter la validation, une référence adéquate devrait tout d'abord être déterminée. Usuellement, la même vitesse de rotation pourrait être choisie pour toute la validation des calculs qui mettent en jeu une rotation periodique. Cependant, concernant le système contra-rotatif caréné dans ces travaux, la même vitesse de rotation pourrait générer des débits différents. Cela affecte sans aucun doute la validation depuis que le débit est la plus importante cause de différence de performances à la fois pour la carène et les rotors. Donc, les mêmes flux de masse et vitesse de rotation sont tout deux considérés comme les références pour faciliter la validation des simulations 3D.

Table 2: Comparaison sur la performance globale entre CFD et Exp

Performance	**Ref.N 3D CFD**	**Ref.$\dot{m}$ 3D CFD**	**Exp Exp**	**Ref.N Var (%)**	**Ref.$\dot{m}$ Var (%)**
N_{r_1} (rpm)	6000	5790	6000	0	3.3
N_{r_2} (rpm)	6000	5790	6000	0	3.3
$\dot{m}$ (Kg/s)	0.3360	0.329	0.326	3.1	0.9
F_{r_1} (N)	0.641	0.558	0.535	15.5	4.3
F_{r_2} (N)	0.793	0.723	0.760	4.4	-4.8
F_s (N)	1.790	1.600	1.530	16.9	4.5
F_t (N)	3.224	2.881	2.825	14.1	2.0
Q_{r_1} (N.m)	0.0168	0.0152	0.0148	13.4	2.7
Q_{r_2} (N.m)	0.0194	0.0179	0.0184	5.6	-2.7
P_t (watt)	22.730	20.140	21.215	7.2	-5.1
PL (g/watt)	14.6	14.5	13.6	7.5	6.6

Concernant la validation des performances stationnaires, il a été trouvé que, en comparant la validation basée sur les mêmes vitesses de rotation, les résultats de la simulation pour le même flux de masse d'entrée, fournit une meilleure cohérence avec les expériences sur les performances globales, vu le tableau ci-dessus, telles que la poussée, la distribution de pression sur la surface du carénage, vu la figure suivante, les pressions totale et statique sur les plans perpendiculaires à l'axe. Parallèlement, plusieurs phénomènes ont été observés: un sillage a été généré par le tranchant du bord de la tuyère qui sépare l'écoulement interne du flux ambiant. Une telle structure de sillage n'existe pas dans le modèle réel à cause du coin arrondi par le procédé de fabrication. Cela fait la différence sur la validation de la pression surfacique près de la sortie. également, les différentes configurations expérimentales du moyeu génèrent un sillage ayant une taille relativement grande dans l'écoulement post-rotors. Cela modifie le profil de la vitesse et génère une différence sur la pression statique à la sortie avec l'expérience. Puisque il est difficile pour les simulations de représenter exactement la même géométrie que celle du modèle réel, de telles différences ne peuvent pas être évitées. La comparaison à la fois des pressions totales et statiques révèle que la précision des données testées par les sondes diminue quand elles sont proches de la surface du carénage car les sondes peuvent facilement séparer l'écoulement local de la surface. En général, la distribution des quantités stables comme la pression et la vitesse axiale montre des caractéristiques uniformes dans la direction radiale.

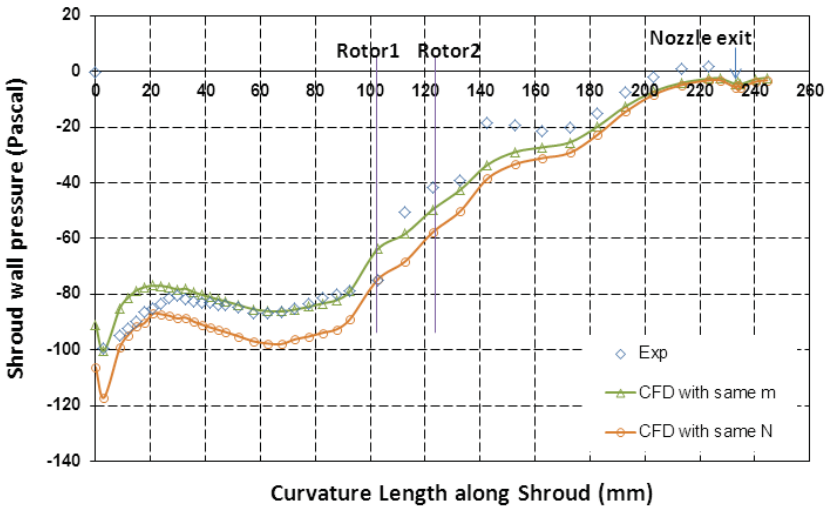

Figure 16: Comparaison sur pression statiques pariétales du carénage entre CFD et expériences

Concernant les caractéristiques instationnaires, l'envergure de la pale, les distributions de la norme des vorticités sur les surfaces radiales au niveau de l'envergure des pales $0.2R_r$, $0.75R_r$ et $0.96R_r$ montre qu'à proximité de la base et du bout des pales du rotor, le sillage du bord de fuite des pales du rotor amont affectent forte-

ment celle du rotor aval. Cela crée des pertes pour le système. Spécifiquement pour l'écoulement en tête de pale, les lignes de courant issues de l'extrémité montrent la structure des vortex de tête de pale, comme on peut le voir sur la figure suivante, ce qui se produit quand un vortex secondaire est généré à la surface de dépression en même temps. Ces deux vortex sont finalement mélangés et forment le vortex principal ayant une taille relativement grande.

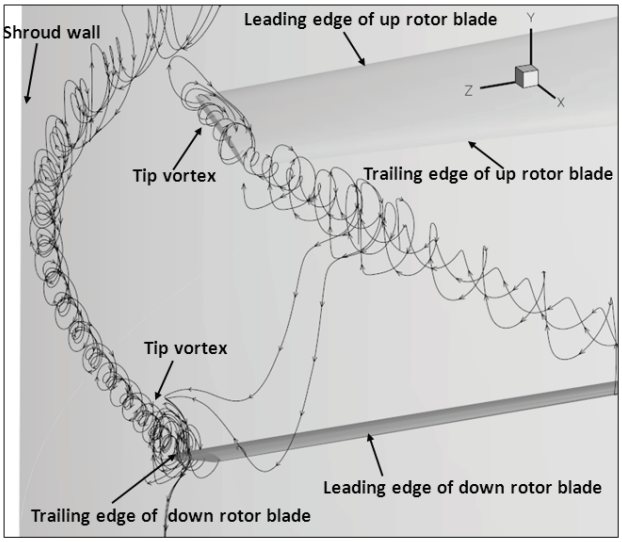

Figure 17: Lignes d'écoulement en bout de pale des rotors supérieur et inférieur

Concernant l'effet de l'emplacement des rotors, une interaction plus forte se produit entre les deux rotors plus proches. Et les lignes de courant dans l'écoulement d'éjecté du carénage indiquent que le sillage développée après les rotors a une échelle relativement petite lorsque le second rotor est positionné plus en arrière. Cela implique que l'intensité de la sillage est relativement forte pour de telles positions du rotor. Et finalement, cela diminue les performances du système quand le second rotor est installé en arrière.

Concernant l'effet de la commutation des vitesses de rotation rotors, à cause de la réalité, la simulation numérique semble moins fiable sur des cas fortement désadaptés tels que des écarts de vitesse de rotation importants. Il n'est donc pas possible de comparer les études expérimentales et numériques lors de la commutation des vitesses de rotation des rotors.

Chapitre 9: Comparaison des calculs 1D, 2D et 3D avec expériences

Dans ce chapitre, on s'intéressera à la comparaison des mesures de performances globales avec les simulations numéques 2D et 3D. L'ensemble de ces données permettront de comfirmer les lois de comportement obtenues par l'extension de la théorie de Froude aux systèmes carénés, et de calibrer les effets d'entrée d'air par la définition d'un paramètre K_i de surface effective. En gardant à l'esprit le fait que l'on ait

utilisé un disque actuateur pour les calculs théoriques et en 2D, il est nécessaire de préciser que les comparaisons et validations ont respectivement été effectuées pour les mêmes puissances induites et pour les mêmes flux de masse.

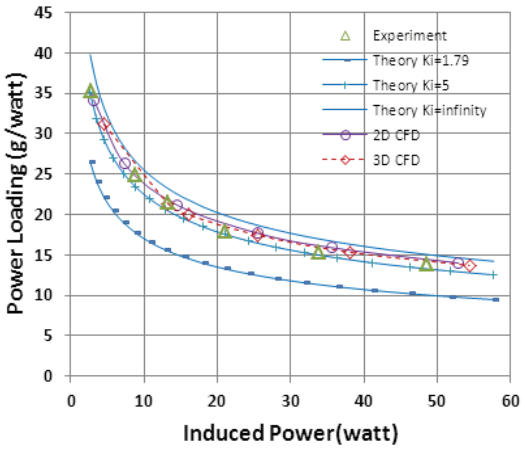

Figure 18: Comparaisons de "Power loading" en fonction de la puissance induite

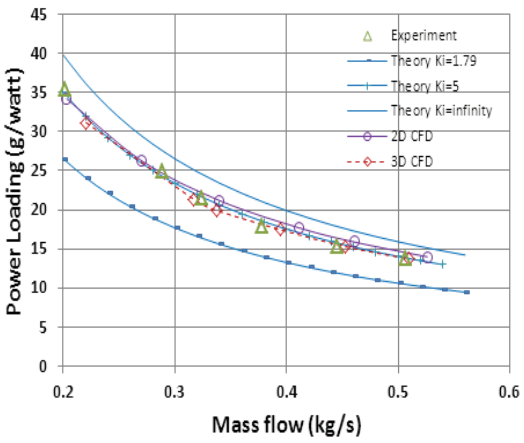

Figure 19: Comparaisons de "Power loading" en fonction du débit

Les comparaisons pour une puissance induite et un flux de masse fixés ont apporté les conclusions suivantes: premièrement, l'application de la théorie de Froude avec le coefficient d'entrée d'air K_i défini directement par la surface géométrique d'entrée d'air, n'est pas capable de prédire les performances globales du système, telles que la poussée et le Power Loading (PL), voir les figures ci-dessus. Concernant la poussée du carénage et du système tout entier, un K_i de valeur infinie semble être plus efficace que pour la valeur réelle, ou bien peut constituer une limite supérieure parfaite. Cependant, une autre valeur de ce paramètre: K_i=5, a été trouvée comme fournissant un meilleur calcul du PL comparé à l'entrée infinie; cette valeur, grâce à l'extension de la théorie de Froude, est pratique pour concevoir la tuyère de la carène. Les simulations 2D appliquées au profile du carénage en évaluant les comportements du système tels que le PL, correspond aux performances réelles du système. Pour les simulations 3D, calculer les performances globales se fait de manière similaire à la simulation 2D, même si on remplace le disque actuateur utilisé en 2D par le profil du rotor réel. Cela implique probablement, que les sillages après le double rotor n'affecte pas considérablement les performances globales du système puisque son intensité est réduite par le second rotor en contra rotation, et modifiée par la présence de la carène, comme il a été expliqué pour les expériences et simulations 3D.

Chapitre 10: Conclusions et perspectives

Conclusions:

L'étude proposée a montré que la carène peut représenter un composant essentiel pour les véhicules conventionnels à voilure tournante. La première partie à consisté à prédire l'effet du carénage en utilisant l'équation basique de conservation des quantités de mouvement. La problématique du générateur de débit, constitué dans la réalité par un double rotor, a d'abord été simplifiée en utilisant le concept de saut de pression, appelé disque actuateur, qui à l'origine avait été proposé pour les rotors libres par Froude. La théorie initiale a donc été étendue à l'analyse d'un système caréné, par l'introduction de deux paramètres géométriques qui représentent les rapports des surfaces de prise d'air et d'éjection à la surface du disque actuateur lui même.

Comparé au rotor libre, dont le tube de courant se contracte naturellement jusqu'à la moitié de l'aire du disque, il a été montré que la tuyère a une influence dominante sur le contrôle du débit entrant pour une puissance donnée. Le débit massique, augmenté par la tuyère ayant une large sortie d'éjection, amplifie la poussée du carénage qui est générée entièrement au niveau de la prise d'air en raison d'une forte dépression statique du débit entrant, avant le disque rotor. La limite de la contribution de la carène à la poussée totale- positive ou négative – correspond à ce rapport de contraction de 0.5 en sortie. Le diagramme résultant pourrait être utilisé pour concevoir facilement un profil optimisé du système ayant une prise d'air finie, en supposant connue la surface effective de l'entrée d'air. Le développement théorique suppose l'admission de l'air axial, il est donc difficile pour un tel modèle théorique de prendre en compte une forme réelle de prise d'air et les effets induits par la viscosité.

Une simulation axisymétrique 2D a donc été conduite avec un disque actuateur pour résoudre le passage du flux axial à travers le système qui a le véritable profil du carénage. Tous les paramètres géométriques possibles qui décrivent le profil de la carène ont été extraits et classés en fonction de chaque composant du carénage - prise d'air, section cylindrique du milieu et tuyère. Leurs effets ont été explorés en les faisant varier indépendamment.

Les résultats de la simulation 2D concernant les effets sur la tuyère ont prouvé que l'extension de la théorie de Froude prédit raisonnablement les influences de la surface d'éjection en tuyère, sauf l'apparition du décollement. La valeur optimisée du rayon de sortie a pu être proposée à 1.15 fois le rayon du rotor. Et quelque soit la largeur de la tuyère, l'angle divergent optimal reste autour de 10.5 degrés.

Concernant la définition de la prise d'air, le rayon de bord d'attaque est le seul ayant des effets significatifs sur les performances. Son influence la plus importante provient de la zone de basse pression à la surface interne de la prise d'air, qui est contrainte par le rayon maximal du carénage défini dans la section cylindrique. Sa valeur optimale est 1.3 fois le rayon du rotor. Parallèlement, un rayon maximum - qui équivaut au rayon de l'extérieur de la carène - semble devoir être dimensionné

à approximativement 1.44 fois le rayon du disque rotor.

Pour les autres paramètres, à l'intérieur de la zone de non-séparation des différentes sections-transversales du carénage ayant des aires équivalentes, la forme de la tuyère d'éjection et de la prise d'air n'ont pas d'impact significatif sur les performances.

Utilisant ces critères de conception concernant les détails du profil de la carène, un nouveau carénage de forme optimisée a été proposé et fabriqué pour ensuite déterminer des principes sous-jacents et les limites du domaine opérationnel. Une optimisation supplémentaire a été conduite à travers une approche expérimentale et des simulations.

En introduisant le véritable rotor contre-rotatif coaxial, l'étude expérimentale complète a d'abord été conduite pour confirmer les performances globales, puis pour analyser le champ moyen et enfin optimiser la configuration du rotor. En se basant sur le banc d'essai dédié à cette étude, de précision dument validée par étalonnage à des références, les grandeurs suivantes ont été mesurées: poussée, moment, vitesse de rotation, distribution de pression sur la surface de la carène, et les champs de pression incluant la pression totale et statique sur les sections situées tout au long de l'axe du système.

Plusieurs diagrammes innovants tels que les diagrammes double N et $ln(N_1/N_2)$, adaptés au fonctionnement d'un double rotor, ont permis d'analyser les performances optimisées pour chaque régime de vitesse.

Comparé au précédent, le nouveau modèle de carénage a montré un gain de poussée de la carène de 20% pour une puissance d'entrée donnée, en contribuant à plus de 50% à la poussée totale. La comparaison avec les trois autres configurations possibles, le simple rotor libre (FSR), le double rotor libre (FDR) et le simple rotor caréné, a montré que la configuration du double rotor caréné (SDR) améliore la performance évaluée en "power loading" (PL), représentant la capacité à générer une poussée par unité de puissance allant jusqu'à 86% dans le cas SDR/FSR.

Pour explorer plus en profondeur les avantages du carénage aussi bien que les caractéristiques du système, les systèmes à double rotor caréné et libre ont été comparés sur d'autres paramètres. On a ainsi pu montrer une augmentation du débit massique d'environ 65% dû à la présence de la carène, ce qui augmente directement la poussée totale de 80%. Le chiffre de mérite (FoM) lui-même, évaluant la capacité à convertir l'énergie mécanique en énergie cinétique par les rotors, a augmenté de 35%. Lorsqu'on analyse le comportement du doublet de rotor plus en détail, on montre que le rôle prépondérant du premier rotor sur la génération de poussée pour les FDR devient secondaire quand le système est caréné.

Concernant le champ d'écoulement, quelque soit la vitesse de rotation, la plus forte dépression se forme en amont de la prise d'air, dans une zone où la courbure est la plus importante, et crée le potentiel de contribution à la poussée. En sortie de carène, lorsque le débit est éjecté à la fin de la tuyère, les mesures de pression pariétales et les tests de pression statique interne ont montré une pression ambiante équivalente à la sortie. Le nouveau carénage permet donc à l'écoulement de s'adapter correctement à la pression ambiante.

L'étude de l'écoulement interne en présence de la carène a montré que cette dernière réduit efficacement les pertes par contournement de bout de pale et a permis d'observer le changement radical concernant la contraction du flux à la sortie, en comparaison avec le FDR.

Afin d'optimiser la configuration du rotor, les effets des emplacements des rotors et de la vitesse de rotation ont été explorés. Les nouveaux diagrammes double N et $ln(N_1/N_2)$, les tests sur les champs d'écoulement permettent d'affirmer que les emplacements des rotors n'entraînent pas de différence remarquable sur les performances globales, le recul du second rotor limitant une surcompression à la sortie; L'optimum de performance semble se produire lorsque la première vitesse de rotation est plus faible que celle du rotor aval, ce qui présente une capacité plus importante à aspirer le débit massique.

Enfin, en raison des interactions qui se produisent entre la carène et les rotors, ou bien entre les deux rotors, on doit observer que le champ d'écoulement est complexe, surtout lorsqu'on s'intéresse à la partie concernant le rotor coaxial contre-rotatif caréné. Par conséquent, dans une dernière partie de l'étude, pour explorer et mieux comprendre les caractéristiques de l'écoulement du système caréné, une simulation numérique en 3D qui modélise le véritable rotor coaxial à contre-rotation a été développé en tant qu'outil supplémentaire pour obtenir une première base de données d'expérimentation numérique, particulièrement en ce qui concerne les caractéristiques non-stationnaires.

En gardant à l'esprit la difficulté de construire exactement la géométrie des dispositifs expérimentaux dans la simulation, on a pu expliquer la petite différence sur l'écoulement à la sortie relevée lors de la validation avec l'expérience basée sur le même débit massique: Elle provient vraisemblablement de la géométrie du moyeu, dont la modélisation est différente de la réalité, aboutissant dans l'écoulement de sortie de carène, ce qui engendre un sillage et affecte la représentativité de la solution numérique.

L'observation des résultats stationnaires, moyennés azimutalement, a montré qu'une distribution radiale uniforme apparaît pour toutes les mesures le long du passage à travers le carénage sauf pour la position axiale située entre les deux rotors, ce qui est dû à la rotation du premier rotor. Les caractéristiques uniformes apparaissant sur la position située juste après le second rotor implique que le rotor arrière tournant dans la direction opposée compense le sillage.

Pour les performances non-stationnaires, une forte interaction de sillage induite entre les rotors amont et aval est présente sur la pale à proximité de la base et de l'extrémité. Le sillage induit par le rotor amont rentre en interaction avec le sillage aval. Des appariements tourbillonnaires complexes se forment à l'extrémité des pales. Un sillage de relativement grande taille apparaît dans la zone d'écoulement de sortie avant la sortie. Toutes ces caractéristiques montrent le caractère instationnaire de l'écoulement.

Pour finir, la simulation a révélé que positionner le second rotor en arrière diminue la taille du sillage mais augmente son intensité dans la zone aval d'écoulement de sortie, ce qui pourrait confirmer la conclusion expérimentale. Concernant l'effet

de la permutation des vitesses, les simulations n'arrivent pas à modéliser exactement le phénomène réel.

Finalement, tous les calculs de l'extension de la théorie, les simulations 2D et 3D ont été comparées avec les résultats expérimentaux. La cohérence entre toutes les simulations et les expériences ont validé le profil optimal du carénage et quelques caractéristiques d'instabilité.

A l'issue de ces travaux de thèse, plusieurs éléments sont donc venus confirmer l'utilité de l'extension de la théorie du disque actuateur dans les systèmes carénés. Mais la définition de la prise d'air du carénage devra être adaptée à une définition dynamique au lieu de coller à une vision géométrique de la définition. Cette définition d'une entrée d'air étendue permettra de capturer des caractéristiques de flux uniforme, en amont de la géométrie réelle. Le rapport 5, qui se comporte déjà de manière très similaire à une prise d'air infinie, offre une cohérence acceptable avec les essais expérimentaux. Il semblera donc de bonne pratique d'utiliser ce rapport pour estimer la performance avec une bonne approximation, et ainsi de définir la meilleure surface de la tuyère d'éjection.

Perspectives:

A l'issue des premières conclusions proposées tant pour le modèle analytique du disque actuateur caréné que pour les analyses expérimentale et numérique, plusieurs recommandations sont envisageables pour la suite de l'étude: Pour la conception du système global, le point le plus important concernait la conception optimisée de la carène pour mettre en relief ses avantages potentiels, alors qu'en ce qui concerne les pales du rotor, une forme optimisée par un code simplifié de ligne portante a été retenue à priori et utilisée tout au long de l'étude. Une des conclusions de l'étude expérimentale a été que les conditions de fonctionnement optimales, en terme de power loading, ne se situaient pas dans la plage d'annulation du couple total, et qu'il reste donc un domaine d'amélioration du design des pales pour faire correspondre ces deux conditions, au moins en agissant sur l'angle de calage. Puisque que dans ce domaine des Micro Aéronefs (appelés MAV), un système équilibré autour du couple résultant, avec une possibilité de contrôle complet de la position, sont deux paramètres tout à fait essentiels, une meilleure optimisation de la forme des rotors sera sans doute la tâche suivante à prendre en compte. On pourrait ainsi envisager d'améliorer le chiffre de mérite du doublet de rotor en agissant non seulement sur la forme des profils de pale retenus, mais aussi sur le nombre de pales, et se donner les moyens de faire varier la charge par rotor en fonction du point de fonctionnement local demandé par chaque cas de vol.

Si on regarde le développement du modèle du disque actuateur caréné lui même, nous avons vu que l'extension proposée dans cette étude pouvait prédire convenablement les performances du système global moyennant une donnée d'entrée d'air infinie et la tuyère de sortie réelle. Des progrès dans cette prévision de performance du système pourraient cependant être réalisés par une meilleure modélisation des phénomènes en cause dans l'entrée d'air.

En ce qui concerne l'exploration expérimentale, les performances globales sur la poussée, le couple, la puissance et les régimes pouvaient être obtenus indépendamment avec grande précision, et l'étalonnage réalisé en amont de chaque campagne d'essai était la garantie de qualité de mesure sur les capteurs de pression pariétale. D'autre part, pour l'essentiel du domaine d'exploration interne, les sondes utilisées pour mesurer les pressions statiques et totales sur les plans caractéristiques donnent des résultats satisfaisants. Cependant, la précision attendue est nettement moins bonne lorsque les sondes sont proches de la paroi de carène, à cause de leur influence sur l'écoulement local. Même si le problème vient de la façon de mesurer l'écoulement mais pas de la sonde elle-même, il reste à proposer une autre type de sonde qui aurait une influence minime sur l'écoulement en zone limite de paroi. De même, dans ce domaine de l'écoulement, l'hypothèse de bi-dimensionnalité retenu jusqu'alors devient caduque, puisque les effets de bout de pale, comme de moyeu sur les extrémités de la pale, génèrent localement des composantes radiales. Il serait intéressant d'utiliser des sondes 5 trous, permettant de mieux évaluer ce coté tridimensionnel de l'écoulement, source de perte locale à évaluer.

Cette mesure par sonde pourrait être aussi basée sur l'anémométrie film chaud, qui aurait l'avantage de prendre en compte la composante instationnaire. Une étude au film chaud pourrait donc être la suite logique de l'étude expérimentale. Elle ouvre un domaine d'étude complexe puisqu'il ne sera pas possible de faire une représentation de moyenne de phase dès lors que nous avons deux rotors en rotation. Il faut imaginer une représentation par déphasage des rotors eux même, existant dès lors que les deux rotors ne tournent pas à la même vitesse de rotation, pour étudier la pulsation générée par ce phénomène.

Enfin, pour les simulations réalisées au cours de l'étude, la méthode développée dans le cadre de l'étude 3D montre un bon accord avec les résultats expérimentaux. Cependant, pour résoudre l'écoulement en domaine de couche limite proche paroi de carène en amont des rotors, les simulations montrent encore une différence notable. Cela est dû au fait d'avoir imposé la turbulence dans tout le système. Alors que l'on sait qu'autour des rotors, l'écoulement est probablement laminaire, sur la première partie de la corde puis transitionne vers l'état turbulent. Par conséquent, rechercher un moyen d'utiliser des modèles de turbulences différents et des modèles de transition pour chacune des parties du système caréné pourrait être intéressant pour l'amélioration globale de la solution proposée par les simulations CFD de ce problème complexe.

Proposition ultérieure: la qualité globale d'un ensemble doublet de rotor contrarotatif caréné utilisé dans le monde du microdrone se mesure non seulement dans les deux indices de qualité proposé tout au long de l'étude, mais aussi sur la capacité à obtenir ce résultat dans un volume global le plus limité possible. D'autres études pourront donc être menées en modifiant les formes de carène, en diminuant les bords d'attaque qui donnent des carènes trop larges, en prenant des précautions d'études sur les capacités d'absorption de débit par ces nouvelles formes. L'autre paramètre très important est la pilotabilité du système, ou capacité à générer des efforts transversaux sans détériorer les performances globales. Un champ d'étude

très large s'ouvre si on envisage de modifier les plans de rotations de l'un des rotors pour générer ces nouveaux degrés de liberté.

L'étude, jusqu'alors limitée au point fixe ou quasi fixe, devra ensuite être étendu aux points de fonctionnement voisins pour évaluer la sensibilité aux déplacements transversaux sur l'absorption du débit et les effets générés par la distorsion attendue.

Contents

Chapter 1

Introduction

1.1 Background and Motivations

With the increased requirement in miniaturization, in 1992, the concept of Micro Air Vehicles (MAVs) was firstly introduced in a DARPA workshop titled "Future Technology - Driven Revolutions in Military Operations" [1]. Lots of feasibility studies were performed in the following years at MIT Lincon laboratory and at the U.S Naval Research Laboratory, seen in Fig.1.1. It gave the definition of MAVs with the restriction in size to a dimension of about 15 cm, in weight to approximately 100 g including a payload of 20 g and an endurance of one hour [2]. All such kind of micro vehicles possess few similar characteristics: portable, autonomous and low-cost. In view of these advantages, a series of prototypes with different configurations suitable for different military or civilian missions were developed by the participants. However, whatever the mission is, the ability to operate in highly-congested and cluttered environments, like "urban canyons", becomes more and more important with the development of the technics and requirements, specially for indoors. This requires a high ability of maneuvering at low speeds or even hovering. Due to the simpler mechanics and relative higher efficiency in hover compared to fixed and flapping wings, along with the advantages in terms of noise, rotary wing vehicles are especially attractive for MAV applications.

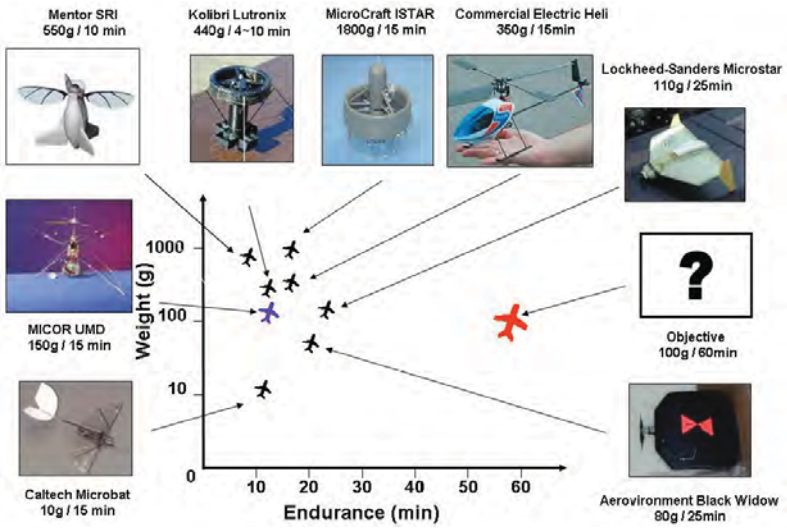

Figure 1.1: Typical Re vs. Mass for animals and vehicles [1]

However, the size constraints of MAVs and the requirement of low speed or hover-capable, force rotors to work at Reynolds numbers much closer to the ones faced by small birds and insects in a regime of approximately 10,000 to 50,000, seen in Fig.1.2 [3]. In such regime, the flow is more strongly affected by the effects of viscosity rather than inertial ones. A decreased ability of the fluid to maintain adverse pressure gradients is following happened probably along with the flow separation, transition, and reattachment within a short chordwise distance. In the current investigation, initial hover rotor testing show that small-scale rotors with airfoils and blade geometries similar to those found in full-scale vehicles had maximum Figures of Merit (FoM), which is the hover efficiency dimensionless parameter and it is equal to the ratio of the ideal and actual amounts of power, of the order of 0.35 for the early micro-rotor [4, 5] and 0.65 for the current research [6]. Even if there is an improvement, for a certain disk loading (DL) that is still a low value considering that full-scale helicopters can reach maximum FoM of 0.8 [7]. And the power requirements remain high. This decreases the global performance like power loading which is the ratio of the thrust to the power. Certain airfoil shapes, similar to those found in bird and insect wings, are optimized for low-Re flight, and these do fare better in this flight regime than conventional airfoils that have been designed for larger, manned aircraft. However, the performance as the highest L/D ratios achieved by even these optimized low-Re airfoils are still substantially lower than those achieved by the conventional airfoils at higher Reynolds numbers [3].

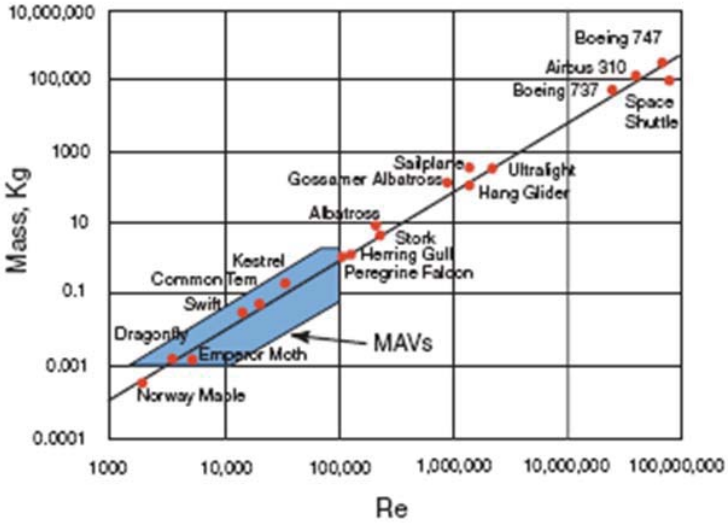

Figure 1.2: Typical Re vs. Mass for animals and vehicles [3]

For the current study, even though there exist plenty optimization methods in the design of airfoils or rotors to increase the efficiency of hover-capable MAVs, the improvements still can not reach the requirement. So alternative propulsion configurations that have the potential to improve the performance should be investigated. One of such configurations is the "Shrouded contra-rotating coaxial rotor".

It involves two axially aligned rotors spinning in opposite directions and a special component–shroud surrounding them, seen in Fig.1.3.

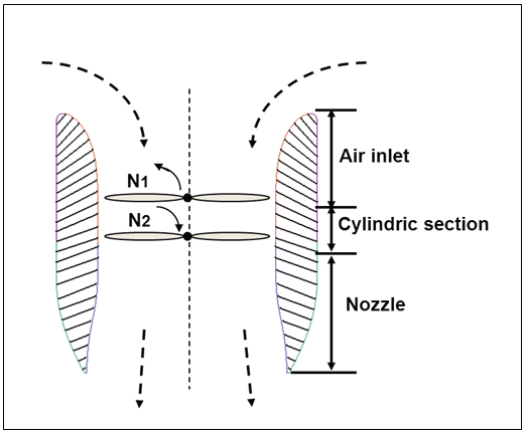

Figure 1.3: Cross section scheme of shrouded contra-rotating system in hovering

Such combination combines the advantages from both components: on one hand, contra-rotation minimizes net torque without the need for a tail rotor, as found in conventional rotorcraft systems. The rear rotor rotating in opposite direction refines the wake direction closer to the axial flow, and then provides the improvement [8]. This concept is beneficial for MAV applications in terms of decreasing dimensions [9]; on the other hand, the distinguished component – shroud with a common form resembling an annular airfoil, with varying camber and thickness throughout its length, a leading edge and a trailing edge respectively forming the inlet and outlet for shroud, could have significant gains in aerodynamic performance as increment of thrust and reduction of power consumption when compared to the unshrouded rotors [10, 11, 13]. In addition, such shrouded contra-rotor configuration could greatly reduce the noise by both the presence of the second rotor and the shroud. Furthermore, the shroud also serves as a safety feature to protect both the rotating blade from damage as well as the operators from injury. All of these, specially shroud presence, make the application of such configuration extremely attractive. It has been utilized in various forms, ranging from ducted propellers and ducted fans on powered-lift V/STOL aircrafts to Fenestron tail rotors on helicopters and ducted-rotor UAVs.

As a distinguished component with the free rotors, the shroud plays a critical role on the system performance. It was found to bring a thrust increment and power consumption decrement. For the shroud with an inward camber, seen in Fig.1.3, the convergent inlet accelerates the flow towards the rotors, which forms a suction pressure on its inner profile and then produces an extra thrust for the system [12]. Such performance benefit derives principally from the ability of the shroud nozzle to restrain the natural contraction of the flow after passing through the rotors, which is greatly dependent on the nozzle shape, whether convergent, cylindric or divergent. These is well known amongst users of such configurations [11, 13, 14].

However, for the dependence of performance parameters such as power loading, thrust, power and others, specifically to the exact quantity, here is still a need to find a way to evaluate them. Meanwhile, since the shroud shape change could happen together with some physical phenomenons as flow separation, friction loss, extremely adverse pressure gradient and so on, which might cause a dramatical decrease of performance, careful design of the shroud thus becomes one of the most important issues. Also, the combination of the contra-rotating rotor brings the interactions between the shroud and the rotor or between the two rotors which might cause a complicated flow structure certainly influencing system behaviors. Consequently for obtaining an adaptive flow, the arrangements of rotor positions and their rotational speeds etc., are needed to be resolved as well. Therefore, for such special configuration, more sophisticated theoretical models as well as experimental and computational fluid dynamic (CFD) are essentially developed for the successful design of shrouded contra-rotating MAVs.

1.2 Research on Experiments and Calculations

Shrouded rotors or propellers configuration has been extensively investigated for over half a century on the design issues, including the experiments and numerical methods.

Experimental research

First, for the research history, it mainly focused on the experiments. In 1931, Stipa did static and wind-tunnel tests on two conventional airplane propellers. It was found the "intubed" propellers exhibited higher thrust, power loading and propulsive efficiencies, than the open propellers for a certain inflow velocity. The shroud model with the thinner profile exhibited lower drag, higher propulsive efficiency and higher static shroud thrust [15]. Shortly it was followed by Kruger in the early 1940s for further systematic testing of different shroud profile shapes [16]. it was revealed, in static and near-static conditions, the sharper lip caused the flow to separate which reduced the total thrust, although same rotor thrust could be achieved. Flow visualization using smoke and equipping the shroud stator guide vanes showed that the cross-sectional area of the slipstream did not change with varying loading. This indicated the expansion ratio depends only on the shroud shape. The tested largest expansion ratio, 1.7, showed the greatest power loss and lowest efficiencies. In 1948, a pair of contra-rotating propellers which were 48 inches in diameters with three different shrouds was tested by Platt [17]. The longer shroud nozzle was proven to perform better based on the same expansion exit ratio. The smaller expansion resulted in low coefficient ratio of thrust and power (C_T/C_P) with same nozzle length. Increasing expansion ratio caused a reduction in power consumption for all propeller blade. As same as shrouded single propeller, it was improved that the shrouded contra-rotating propeller produced (C_T/C_P) more than twice higher comparing to the free propeller. United Aircraft Corporation Research Labs provided

a good overview of ducted propeller research [18]. It showed the most powerful shrouded propeller variable was exit area ratio. Taylor and Robert in Langley Aeronautical Lab indicated decreasing shroud length resulted in relatively minor losses in static thrust efficiency in 1958 [19]. Mississippi State University did a comprehensive investigation on shrouded propeller for the Marvelette aircraft in 1960s [20]. The measurements on static and dynamic thrust, propeller inflow, flight and so on, was respected toward the design refinement and the redefinition of low-speed aerodynamic research. Mort reported for Bell X-22A in 1966 that increasing tip gap made a great reduction on the static thrust coefficient caused by the reduction of shroud thrust [21]. Around the same time, a comprehensive, three-year investigation of the effects of various shroud parameters in axial flow flight was conducted at Hamilton Standard by Black, Wainauski and Rohrbach [22].

Figure 1.4: Model of GIANT [36]

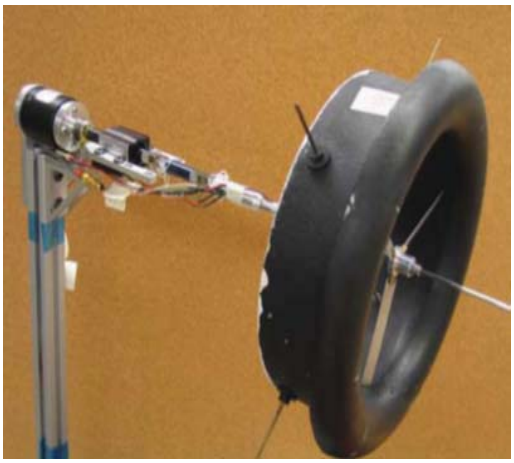

Figure 1.5: Shrouded rotor model [38]

The early researches almost were about the great scale systems as aircraft, helicopter and turbomachinery [23, 24, 25, 26]. Specifically for the unmanned vehicles, besides the VTOL vehicles using the shrouded single rotor as Sandia AROD, Honeywell Kestrel, Microcraft/Allied Aerospace iSTAR and so on [27], several typical ones with shrouded contra-rotating rotor give an important references for the following studies. The first is the Cypher even though it was still in great scale with the shroud diameter around 50 inch. It was developed by Sikorsky in 1990s [28, 29, 30, 31, 32]. some experimental work performed in designing the shroud indicated that decreasing the inlet lip radius caused FoM to either decrease or to remain constant, and then sharply decrease to 0.50 at a lip radius of zero. Another one is the Perching UAV which has a 10 inch diameter. It was developed at MIT's Charles Stark Draper Laboratory during 2000-2002 [33, 34, 35]. Dyer made an investigation of various shroud parameters [34]. Several models with three different lip radii, nozzle expansion angles and two blade tip clearances were tested. As expected, increasing the lip radius caused thrust and power loading to increase. Not as showed as in the one used in helicopter or other large scale systems, the reduction in tip gap had no significant

improvement even if it still decreased the power consumption. Measurements with probes on the wake indicated flow separation from the rotor centerbody resulted in a large reversed flow region there. A vehicle named "GIANT" was developed in University of Maryland [36]. Sirohi and Tischenko designed and implemented a ducted fan. The experimental data of the ducted and isolated rotor performance was given. Pereia also studying in University of Maryland found the optimal values of shroud nozzle angle and length are 10° and 50% of the shroud throat diameter respectively [37]. The surface pressure measurements was done as well both in hovering and translational flight [38]. Meanwhile specifically in shrouded coaxial rotor, seen in Fig.1.6, Lee and Leishman made a comprehensive experiments on the aerodynamical effects of some important varaiables [39]. They indicated that the aerodynamic forces on the duct itself recovered the net system thrust close to the isolated coaxial performance and also recovered efficiency. In addition, Martin in Ames Research Center conducted measurements on flowfield of a 10-inch Ducted Rotor VTOL UAV [40]. It aimed to determine the performance penalty in hover and axial flight.

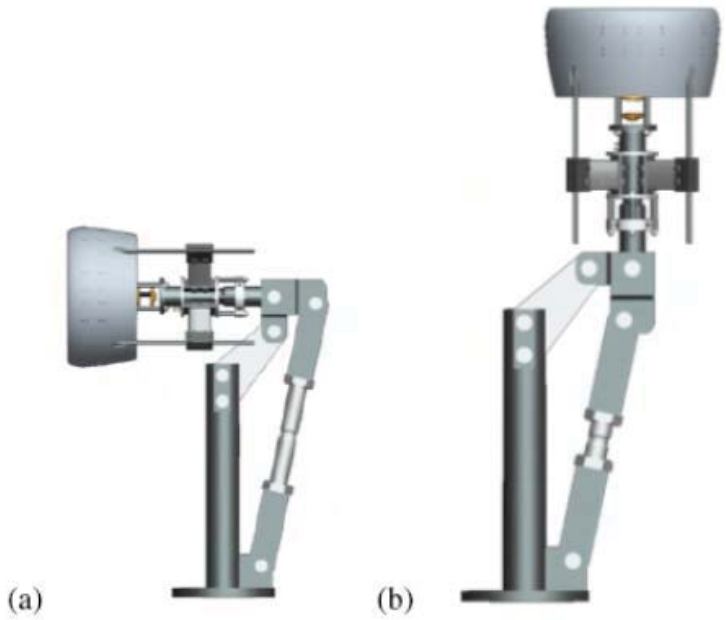

Figure 1.6: Test bench with different stand pitch angle: (a) axial mode, (b) hover mode [39]

Theory and simulation research

For analytical methods, it generally includes the momentum theory, blade element momentum theory (BEMT), blade element vortex theory (BEVT) and more complicate potential flow models. Almost all of the theory studies on shrouded rotors have been developed from the free single or coaxial ones. A NASA report gave a

broad perspective of the aerodynamic issues and state of the art of coaxial rotor or propeller [41]. Later, Leishman in University of Maryland made intensive research on the theory development, including defining a suitable formula for FoM and optimizing design on coaxial proprotor [42]. As for shrouded rotors, Kucheman and Weber are considered to be the ones initially doing such work in the 1950s. They developed potential flow solutions for ring shaped cowlings in a uniform flow using vortex rings [43, 44, 45]. Then, Wright et al. developed a model based on momentum approach. However, the algorithm required an empirical correction factor and did not account the prediction on duct thrust [46]. Hua and Spyro modeled the contra-rotating and ducted propellers for marine application via coupling a Vortex-Lattice for each blade row with a finite volume method for the global flow-field to account for the interactions between the two blade rows [47]. In 2003, Guerrero made a program or code on the design and analysis of ducted fan VTOL UAVs. Same as Wright, for the interaction between shroud and rotor, it was still not clear [48]. The code made by Quackenbush through the use of free wake, a potential flow model was obtained coincident with the experiment results. However that was only in the pre-stall region [49].

Since the experiments require expensive infrastructure and a thorough methodology, the numerical tools for aerodynamics becomes extremely useful. Computational fluid dynamics showed an important role in the design and analysis of the shrouded contra-rotating rotor. In 1970s, Micheal and Selden at Ames Research Center did a computational and theoretical study for predicting the performance of a ducted fan in uniform axial flow at very low advance ratios [50]. It had good agreement on blade loading, fan inflow profiles, forces, duct pressure distribution and so on except the pitch momentum. Joan and Francesc did a numerical analysis on the flow between a Pair of corotating enclosed disks by a pair of counter-rotating cross-stream vortices near the outer cylindrical wall [51]. Ahn and Lee developed a computational model applying actuator disk for an axisymmetric ducted fan system to identify its design parameters and their influence on the system performance [52]. The results showed increasing diffuser angle of the duct improved the propulsion efficiency of the ducted fan system, while the inlet geometry had less of an effect on it. Rajneesh and Matthew in US Army Research Laboratory investigated ducted rotor thrust using CFD, and proposed momentum theory calculation for thrust on the inlet [53]. Comparisons of the inlet thrust prediction between these two suggested a better correlation once the maximum inflow velocity was given to the momentum theory calculation. Currently Rajneesh, in cooperation with Surya from Lockheed Martin Company, carried out a parametric study to optimize the design of a ducted rotor system through CFD [54]. It showed the surrogate model approach was able to predict the performance within 3% of the computed data. Kazutoyo, et al. investigated the tip leakage flow field in a transonic axial compressor rotor, NASA Rotor 37, by large-scale numerical simulations [55]. It was found the tip leakage vortex interacting with the shock wave and forming upstream of the leading edge of rotor blade resulted in a great loss.

Apart from studies on the shroud design and flow explorations in shrouded rotors,

the research about the modeling tools, acoustic features, stability and control etc. has been carried out by NASA, aerospace companies and universities [56, 57, 58, 59, 60, 61, 62].

Our current research:

Particularly in Toulouse, France, the aerodynamic, propulsion and energy department of "Institut Supérieur de l'Aéronautique et de l'Espace" have conducted a series of studies on both experiments and CFD for shrouded contra-rotating MAVs during the current years. Amongst these, Satoorn can be highlighted. New platform of short shrouded coaxial rotor has been designed, seen in Fig.1.7 since 2003 by Thipyopas, Barènes and Mochetta [63, 64]. Hovering performance and horizontal forward flight characteristics of the short-shrouded coaxial concept were tested respectively. It indicated that the optimization was happened when both rotors produced approximately identical thrust, almost same pitch angle and lower rotor rotating relative higher than the upper one. In CFD, numerical simulations were used to calculate the flow field around the shrouds by Grondin [65]. The results agree well on total lift induced by the mass flow rate through the rotor. Poor agreement on power comparisons is due to disregard for swirl flow and rotor losses. Satoorn could be applied for the missions both indoors and outdoors. However, due to the length, the system can not benefit much from the shroud.

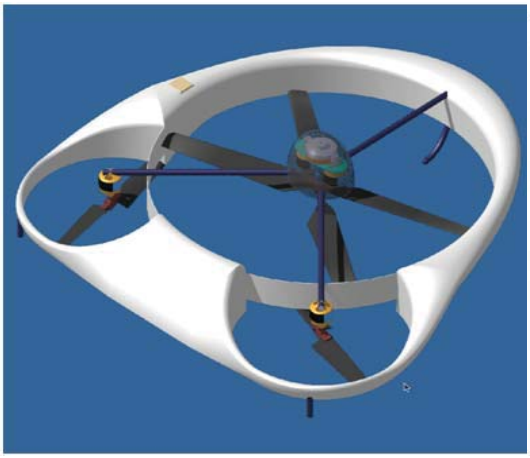

Figure 1.7: Configuration of Satoorn

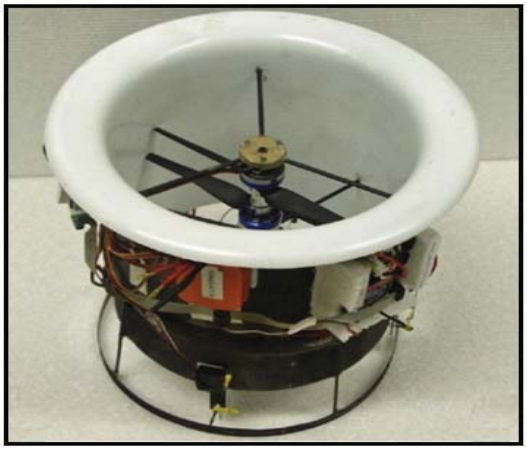

Figure 1.8: Configuration of BR2C

Therefore, as a parallel research, another special concept for indoors mission with longer endurance was proposed by ISAE as well. That is BR2C (French name: Bi-Rotor Contrarotatif Caréné), seen in Fig.1.8. Such MAV has been expected to have a endurance reaching one hour. A longer shroud was thus applied to it. Lots of works had been made for designing such system including the shroud and contra rotor. The issues on researching suitable blade airfoils and basic geometry parameters of shroud have been researched by Rowland, Sayers, Quixada and Henrion with the support of

Barènes [66, 67, 68, 69]. It was found XROTOR and experiments showed agreement in terms of the general trend. The tests on different designed propellers showed that increasing blade number decreased their performance, due to profile drag in lower Reynolds number. A computational investigation with actuator disk was done by Ritter under the guidance of Gressier for studying the ground aerodynamic effects including an inclination of the longitudinal axis of the MAV towards the ground [70].

1.3 Objective and Arrangement of the Work

The attractive performance of relative long shroud have been addressed over years by much experimental, theoretical and computational work, as the research introduced above. A considerable amount has focused on the design and modeling issues of the shroud. However, there are several constraints to apply the existing prior research to the micro-scale shrouded contra-rotating rotor:

Firstly, they were mostly constrained on the shrouded single rotor systems. In addition, some of the fundamental aerodynamic designs based on the shroud effects are only starting to be identified through the basic overall performance. That might not be suitable for the application in the shrouded double rotor which surely has different flow conditions, and impossible for the extra design issues as the arrangements of rotor positions, the two rotational speeds and so on;

Secondly, even if there has some on the similar configurations, those investigations are for the propellers operating at blade tip Reynolds numbers on the order of 10^5 to 10^6 or even higher. It is not practical to use them in the MAVs with tip Reynolds number on the order of 10^4, where viscous effects become more significant and the flow separates much more readily in the face of adverse pressure gradients;

Third, the research on shroud parametric effects have been conducted in a great number of tests and simulations. Unfortunately, they are lack of a systematic definition on the shroud geometry and have no complete design understanding on each shroud parameter as well as their relationships on the performance.

Obviously, there still has much unknown on the shroud design and system modeling which demands the understanding of the flow physics for micro-scale propulsion system combining the shroud together with the contra-rotating rotor.

Considering BR2C as the application background, in order to progressively solve the design problems on such system particularly on shroud model, it could be divided into two: the shroud and the double rotor, seen in Fig.1.9. Once the two rotors are given rotational speeds N_1 and N_2, a pressure jump ΔP will be produced on both sides of the double rotor, and thus inducing power into the fluid. This mass flow $\dot{m}$ makes a pressure gradient to form on the shroud and allow it to generate an extra thrust for the system except the rotor thrust itself. Therefore the shroud design problem could be independently made under either a given ΔP or $\dot{m}$. And this could be solved by the momentum conservation through the shroud and also a computation through simplifying the rotor as an actuator disk. For the further

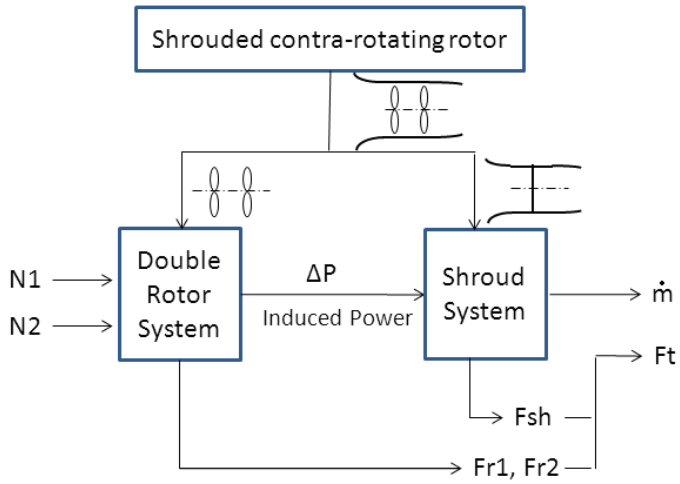

Figure 1.9: System and its working scheme

modeling and optimization of whole configurations, the specific influences from the double rotor could be introduced through the experiments or the computations with physical rotor models.

Objectives:

The present work aims to systematically design the shroud, model the whole shrouded contra-rotating rotor configuration, and further optimize its performance in hovering. It will involve the issues of theoretical prediction, computational design and modeling and experimental testing along with the optimization targets. The specific objectives in this dissertation are as following:

Since the propulsion system applies a special component– shroud, when compared to the free rotor system, the first objective is to adapt the momentum theory of free rotor to shrouded contra-rotating rotor for the preliminary prediction of system overall performance in hover;

Due to the highly experimental costs, the second objective is to build a suitable two dimensional CFD computation for systematic analyses on the effects of shroud geometry parameters based on a complete definition of its configuration feathers. The design criteria or guidelines of shroud parameters and a shroud model with optimal design will be targeted to propose;

The third objective is to develop a test bench for identifying and characterizing the system with a optimal shroud model and a given pair of rotors. The system behavior, its benefits from the shroud, and a further optimization for the parameters mattering both shroud and rotors like rotor locations and speeds, are attempted to be obtained though the experiments on both global performance and flow field;

Considering the constraints on the exploration of flow pattern from experiments and the further improvement of such system in a more efficient method, this objective is to develop a three dimensional CFD numerical model and computations with

a validation through experiments. More information on the flow passing through the rotors and more depth influence from rotor locations and speeds is tried to observe in 3D CFD computation;

The final objective is to compare and validate analytical and numerical models of 2D and 3D with the experiments. This is to confirm the theoretical prediction, the shroud design by 2D simulations and the deep exploration by 3D computations, which can be efficiently applied to further design and eventual optimization of shrouded contra-rotating rotor.

Organization of dissertation:

The objectives above certainly correspond to the work organizations. The dissertation is separated into three parts: theory prediction and 2D simulation for shroud design; experimental identification and exploration; 3D computation for modeling and analysis. Fig.1.10 shows the structure of the dissertation.

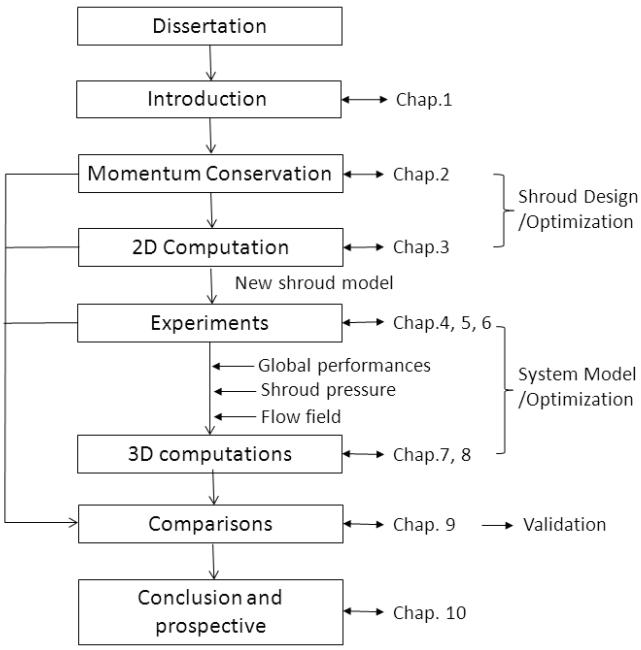

Figure 1.10: Dissertation organization

Under each chapter the specific work are:

Chapter 1: Introduction. The background, motivation and researches on experiments, theory and computations on the shrouded system design issues are introduced. The problem and objectives are addressed.

Chapter 2: 1D Froude theory extension. The Froude or momentum theory are extended for the shrouded rotors through the introduction of two geometry parameters. The preliminary prediction on shroud effects and system overall performance are made.

Chapter 3: 2D axisymmetric simulation on shroud parametrical study. By modeling the real shroud geometry, all the parameter influences from nozzle, inlet, cylindrical section are conducted through a well developed methodology. The design criteria and a new shroud model with optimal design are proposed.

Chapter 4: Experimental introduction. A test bench with multiple testing possibilities are developed. The procedures of different experiments as global performance, shroud pressure and flow field are made.

Chapter 5: Characteristic assessment of shrouded system. The shrouded contra-rotating rotor is compared to the other three configurations. And its corresponding global performance is explored with two new diagram propositions. The benefit from the shroud is specifically quantified with the comparison with free systems.

Chapter 6: Effects of varied design parameters for shrouded system. Through experiments, the effects of two rotors' locations and speeds are explored on both global performance, shroud contribution and flow field.

Chapter 7: Methodology of 3D simulation. The definition of computational field, hybrid mesh, boundary conditions and so on are discussed based on two multiple reference frames: mixing plane and sliding mesh approaches simulating the interfaces between stationary zones and rotating zones.

Chapter 8: Validation and exploration of 3D simulation. Compared with experimental results on global performance and steady flow field, the 3D simulation is validated and applied to explore the unsteady characteristics and depth influence accomplishing the experimental analysis on rotor locations and speeds.

Chapter 9: Comparisons of 1D, 2D and 3D calculations and experiments. The theoretical prediction, 2D simulations for shroud profile design, 3D simulation for flow explorations are validated by the comparison with experiments based on the same induced power to fluid and same mass flow induced.

Chapter 10: Conclusion and prospective. A summary for the conclusions and a prospective for the further work are made.

Part I

Theoretical Prediction and 2D Axisymmetric Simulation on the Shroud Design

Plan of Part

Chapter 2

Froude Theory Extension for Shrouded System

To preliminarily explain and predict the performance of a rotor, the typical model is the actuator disk for free rotor system based on the conservation laws of fluid dynamics. It simplifies the rotor as a flat and infinitely thin disk which produces a uniform pressure jump between both sides of the disk. The rotor is assumed to impact only axial momentum to the flow as explained in App.A. According to this theory, the flow could be considered as a streamtube around the rotor system. For free rotors, such streamtube shape is naturally developed by its pressure equilibrium with a final contracted area ratio of $\frac{1}{2}$. Once the streamtube is shrouded, it would be developed according to the shroud tube itself, which can have further effects. Generally, after the rotating rotor, a wake is generated with a concentrated vortex formed at the blade tip. Its intensity could be decreased by the compensation of the second rotor rotating in the opposition and also by the shroud presence. That is more close to Froude theory which considers the rotors as a disk to generate thrust, through the disk, only the flow and the velocity are induced, and pressure conditions of upstream and downstream are changed.

This chapter aims to extend this theory developed by the momentum conservation to adapt the shrouded system by introducing the effect of the shroud profile in place of the free flow boundary. Two important geometry parameters which greatly constraint and affect the flow field were studied first. The evaluations on global characteristics of the shrouded system differing the free rotor system were then approached in initially by the analysis of this extended theory.

2.1 Froude Theory Extension

2.1.1 Assumptions

For Froude model used in both free and shrouded rotor, considering a one dimensional approach to rotor modeling, the rotor system is modeled as an actuator disk that produces pressure discontinuity but continuious velocities. The static pressure infinitely far from the rotor is considered as P_∞. It is far enough to permit the fluid to return to the static state. And the swirl of the influences flow is omitted. This hypothesis could be properly used for the coaxial rotor system, that should contribute to reduce the fluid swirl. It also gives the possibility to use the theoretical equations which take the rotational speed transmitted to the fluid into account.

Therefore a number of simplification are assumed.

1. Quantity evaluations from the integration form based on conservation laws.
2. Axial flow, if not, swirl velocity will contribute as additional losses, which are not considered in such theory.
2. Perfect fluid, no viscosity effects are considered.
3. Steady state flow, $\frac{\partial}{\partial t} = 0$, and incompressible($\nabla \cdot u = 0$).

Even though some of assumptions are inconsistent with the real case, this simplified theory allows to conduct successfully the preliminary study and identify the parameters influencing the performance of shrouded contrarotative systems.

2.1.2 Theory extension

Fig.2.1 shows the flow fields of both free and shrouded rotor system in the hovering-flight condition. Since the theory imposes the uniform flow features only on the inlet, actuator disk and outlet, and it simplfies the rotor function as a pressure jump, it could be considered as single or multiple rotors. For the shroud, it should be noted that the air comes from all around the shroud at the inlet, being tangential to the shroud inlet curve at its beginning, hence there is no stagnation point. This is assumed surely for a stationary flight. If the axial velocity at the infinity upstream is not null as the system is in movement, the flow velocity field would change and a stagnation point would appear. The theory extended by the actuator disk should then be adapted. At the inlet, where should have uniform features of the inflow such as velocity. However, for the preliminary analysis, it is defined as the actual shroud inlet. For the exit, in the case of a shrouded system, the flow is assumed to have expanded back to ambient atmospheric pressure at the nozzle exit plane.

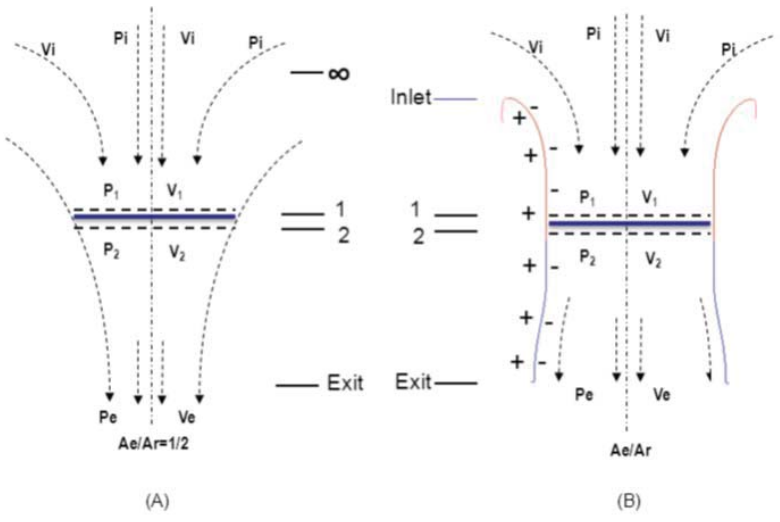

Figure 2.1: Froude model for free (A) and shrouded system (B)

Compared to the flow configuration in free system in Fig.2.1, the behavior of the air flow for the shrouded system is cowled by the shroud which is featured in

particular with two most important parameters:

$$K_i = \frac{A_i}{A_R}, \quad K_e = \frac{A_e}{A_R} \tag{2.1}$$

Where A_i, A_R and A_e denote the area of the inlet, rotor disk and outlet area respectively. $K_e = \frac{1}{2}$ is exactly correspondent to the natural "area expansion" that Froude theory predicts for a free rotor.

Specifically for shrouded system, the flow is assumed axial at any section during the course of flow development which surely includes the inlet and outlet. The definition of outlet is usually considered as the actual exit due to mainly uniform flow feature. For the inlet, as shown in Fig.2.2 (A), Froude theory expects to have axial flow at its inlet as presented at the infinite inlet of the free rotor. Actually the shroud has a curvature at its leading edge. It makes the flow have a velocity deviated from axial direction near its inlet leading edge, seen in Fig.2.2 (B). This fact conflicts the assumption given by Froude theory.

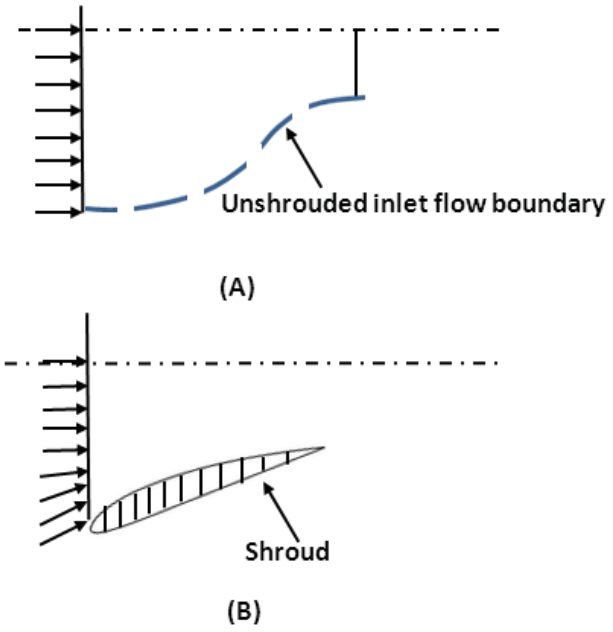

Figure 2.2: Flow at inlet of free (A) and shrouded system (B)

Since the flow passing surround the leading edge just starts to be aspirated and its velocity is small, the pressure does not present obvious difference with the far away upstream flow. Moreover, the position of the flow attachment on the shroud inlet is difficult to be identified because of the aerodynamic unsteady factors. The actual geometrical inlet can be thus considered as the primary applied in Froude theory extension, as shown in Fig.2.3. However, in reality, there surely exists an aerodynamic inlet in upstream which has a uniform velocity distribution, it should keep in mind that such definition of the inlet by Froude theory extension should be

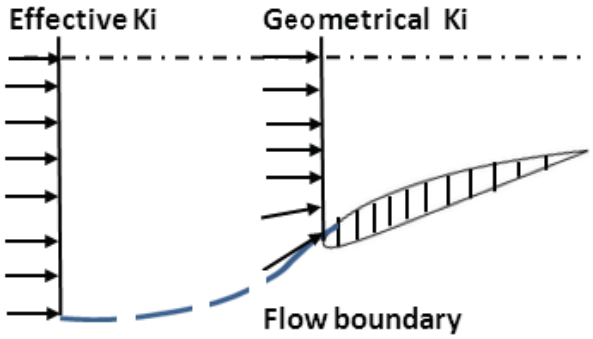

Figure 2.3: Definition of inlet for shrouded system

further identified.

Through introducing these two geometry parameters, the thrust performance of each shroud composition could be obtained according to dynalpy theorem, which reveals for any stationary closed volume, the addition of fluid dynalpy and the pressure experiencing the solid wall could be equal to zero. According to this principle, by applying the conservation laws to a control volume like nozzle, this control volume is therefore bounded by the nozzle walls, the rotor disk plane and the nozzle exit. Applying the momentum equation and summing the forces in the axial direction, it has:

$$F_{noz} + P_2 A_2 - P_e A_e = -v_2 \rho A_2 v_2 + v_e \rho A_e v_e \tag{2.2}$$

Where F_{noz} is the force exerted by the nozzle on the control volume. Combined to the mass conservation law, Eq.2.2 can be obtained as:

$$\begin{aligned} F_{noz} + P_2 A_R - P_{atm} K_e A_R &= -\rho A_R V_R^2 + \rho K_e A_R \frac{V_R^2}{K_e^2} \\ F_{noz} &= \rho A_R V_R^2 \left(\frac{1}{K_e} - 1 \right) + A_R \left(K_e P_{atm} - P_2 \right) \end{aligned} \tag{2.3}$$

Applying the Bernoulli equation:

$$\begin{aligned} P_2 + \frac{1}{2}\rho v_2^2 &= P_e + \frac{1}{2}\rho v_e^2 \\ P_2 &= P_{atm} + \frac{1}{2}\rho V_R^2 (\frac{1}{V_R^2} - 1) \end{aligned} \tag{2.4}$$

Introducing Eq.2.4 into Eq.2.3:

$$F_{noz} = -\frac{\rho A_R V_R^2 (K_e - 1)^2}{2K_e^2} + A_R (K_e - 1) P_{atm} \tag{2.5}$$

It should be noted that $-F_{noz}$ is the force exerted by the volume on the nozzle in the axial direction which is opposite to the propulsion. Therefore the thrust which

is in the positive axial direction on the nozzle due to the control volume is equal to $-(-F_{noz})$. However, the net thrust on the nozzle is the sum of thrusts due to both the internal control volume and the external atmosphere. The latter quantity is:

$$-P_{atm}(A_e - A_2) = -P_{atm}A_R(K_e - 1) \tag{2.6}$$

Combining the Eq.2.6 and 2.5, the net thrust produced by the nozzle or the thrust generated at the downstream rotor is:

$$F_{noz} = -\frac{\rho A_R V_R^2 (K_e - 1)^2}{2K_e^2} \tag{2.7}$$

As the equation above, the nozzle theoretically always contributes negative thrust. Using the same way, the contributions of other components can be deviated as well. And the total thrust can be then summed. Introducing the mass passing through the rotor $\dot{m} = \rho A_R v_R$, their expressions are as following:

Total thrust:

$$\frac{F_T}{\rho A_R} = \left(\frac{1}{K_e}(1 - \frac{K_e}{2K_i})\right)\left(\frac{\dot{m}}{\rho A_R}\right)^2 \tag{2.8}$$

Where, K_e should be lower than $2K_i$ for allowing an positive total thrust. And that is usually satisfied.

Rotor thrust:

$$\frac{F_R}{\rho A_R} = \frac{1}{2}\frac{1}{K_e^2}\left(\frac{\dot{m}}{\rho A_R}\right)^2 \tag{2.9}$$

The thrust from the air entrance:

$$\frac{F_{ent}}{\rho A_R} = \frac{1}{2}\left(\frac{K_i - 1}{K_i}\right)\left(\frac{\dot{m}}{\rho A_R}\right)^2 \tag{2.10}$$

The thrust from the nozzle:

$$\frac{F_{noz}}{\rho A_R} = \frac{1}{2}\left(-\frac{(K_e - 1)^2}{K_e^2}\right)\left(\frac{\dot{m}}{\rho A_R}\right)^2 \tag{2.11}$$

Here, V_R is the induced axial velocity of air through rotors:

$$V_R = \frac{\dot{m}}{\rho\, A_R} \tag{2.12}$$

2.2 Shroud Effect

The distinguishing characteristic of shrouded rotors compared to the free rotors is from the shroud presence. Based on the preliminary evaluation of the two geometrical parameters K_i and K_e on the thrust performance, this section aimed to specify the shroud effect on pressure variation and propulsive performance of each component through the theoretical tools. Here, for all the performance analysis, the air density ρ was considered as 1.225 Kg/m^3, and the actuator disk was kept a constant radius value of 90 mm.

2.2.1 The effect of K_i and K_e on thrust performance

As the theory extension above, it was known that for shroud the inlet area ratio K_i and exit expansion ratio K_e are the most critical parameters.

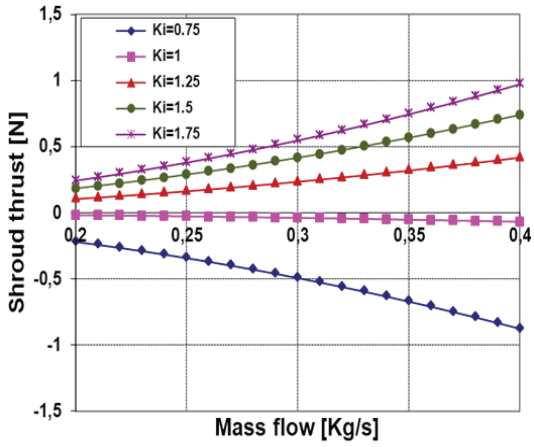

Figure 2.4: Shroud thrust for $K_e = 1.2$

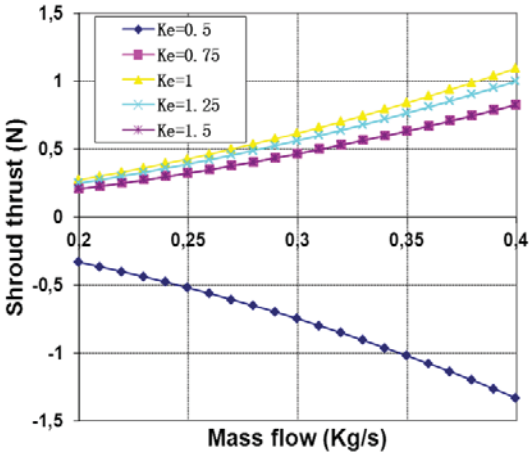

Figure 2.5: Shroud thrust for $K_i = 1.8$

For the parameter K_i, Fig.2.4 indicates that the larger inlet can improve the propulsive performance. However, this improvement on the total thrust is limited and becomes less with the increased K_i. The great difference caused by different value of K_i implies that the inlet could play an important role on the shroud thrust generation. For the parameter K_e, Fig.2.5 shows its influences on the shroud thrust performance with a constant inlet parameter $K_i = 1.8$. It is found that the cylindrical nozzle which means K_e equal to 1 could provide a maximum thrust compared to others. This implies that whether the nozzle is divergent or convergent, is not obviously relevant with the shroud thrust. It should be noticed that, K_e equal to 0.5 which is rightly correspondent to the expansion ratio of free system generates a great negative thrust.

2.2.2 Thrust contributions of shroud components

As the composition of the shroud, the system propulsive behavior could be supported by the shroud air entrance and nozzle which could be also called upstream and downstream rotors in theoretical analysis as well as the rotor itself. For the cylindrical section, as the general configuration has no curvature, there is surely no thrust generation. According to Froude theory extension in Chap.2.1, based on the equations from Eq.2.8 to Eq.2.11, the contribution of each component on the total thrust are given:

$$\frac{F_{ent}}{F_T} = \frac{K_i K_e - K_e}{2K_i - 1} \tag{2.13}$$

$$\frac{F_{noz}}{F_T} = \frac{K_i(K_e-1)^2}{K_e^2 - 2K_iK_e} \tag{2.14}$$

$$\frac{F_R}{F_T} = \frac{K_i}{2K_eK_i - K_e^2} \tag{2.15}$$

The relationships between the components and whole system on thrust performance above indicates that the contributions from different components to the total thrust are stable once the system configuration is decided. And they are only affected by two main geometrical parameters which are K_i and K_e. Fig.2.6 and 2.7 show the contributions from different parts of the shrouded systems with different inlets (K_i) and exits (K_e).

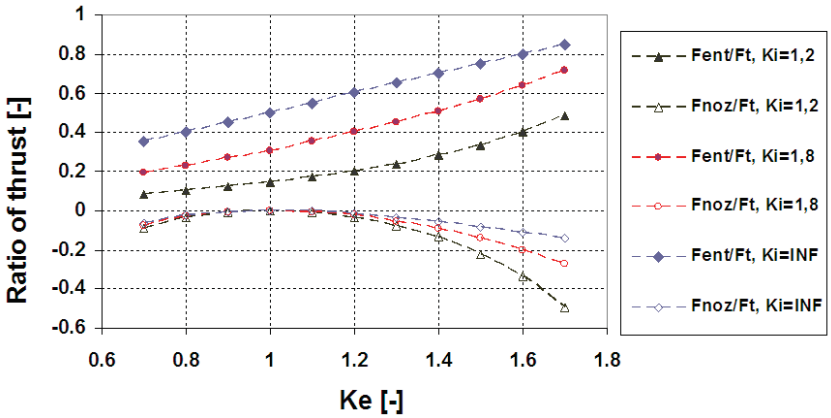

Figure 2.6: Thrust ratio of each component with different $K_i = 1.2, 1.8, \infty$

In Fig.2.6, it is evident that the air entrance always performs a positive role on the generation of thrust. The larger inlet which corresponds to the increased K_i makes greater thrust contribution. However, this improvement is limited when the K_i reaches infinite. The abilities to generate the thrust for all the air entrance of different K_i have almost "linear" increment relationships with the increased exit expansion ratio K_e. Meanwhile, for the nozzle part, whatever nozzle is used, convergent or divergent, it always generates the negative thrust, except cylindrical nozzle, even if the shroud has a large inlet. And the parameter K_e has no significant effect on the nozzle contribution when it is lower than 1.2. Its contribution decreases with the increasing K_e and becomes evident as K_e is greater than 1.2. The analysis shows that, for the shroud, it is the air entrance that provides almost all of the thrust. The design of the inlet would be a critical part for the whole system. In order to get better performance, it is necessary to broaden the area of the entrance plane, however the constraints of mass and size should be considered at the same time.

Fig.2.7 independently shows the rotor contribution on the total thrust. On the other hand this could reveal the information for the whole shroud as well. For the $K_i = 1.2$, the system thrust is completely provided by the rotor when $K_e = 0.7$ or 1.7. This does not imply the shroud does not work, but the air entrance part compensates the negative contribution of the nozzle part under these two design

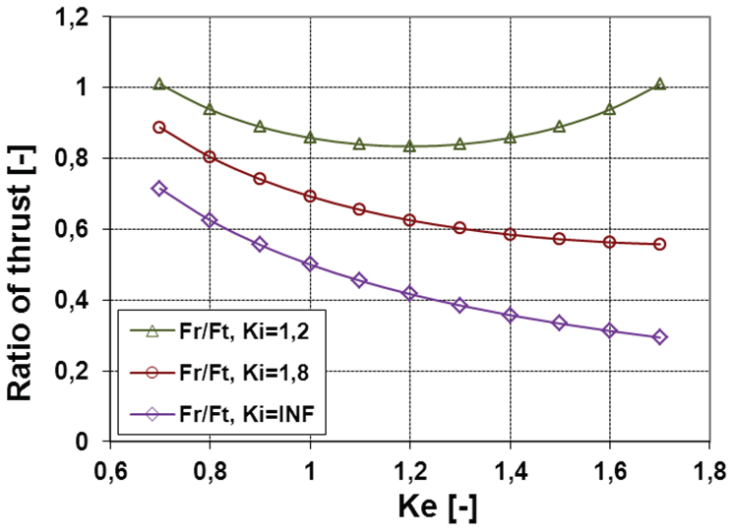

Figure 2.7: Rotor thrust with different $K_i = 1.2, 1.8, \infty$

points. And globally, the increased K_i and K_e make the rotor contribution decrease. This means the shroud takes a more important role on thrust generation. Thus as a complementary analysis, for the purpose of generating thrust of the entire shroud, it is necessary to have relative larger inlet and outlet exit as well. However, this should be decided according to the whole flow conditions.

2.2.3 Pressure distribution in the shroud

As a result of Froude model extension for shrouded system, the variations in air pressure through the flow-field along the shroud can be predicted. This is a quite important quantity to directly explain the thrust generation of the shroud.

Compared to the free rotors which have correspondent $K_e = 0.5$, the pressure variation is estimated by the Landgrebe wake model in the downstream rotor and the assumption of the 'linear' variation of the cross sectional area in the upstream flow. For a shrouded system, the inflow geometry at the inlet can be defined using the "sphere-cap" model proposed by Dyer[34] as explained in Chap.2.1. The geometry of the downstream wake is defined by the shape of the diffuser, here taking K_e equal to 1.2 as a example. Meanwhile for the shrouded system with the double in-line rotor, the pressure distribution between two rotors could be considered as a pressure jump averagely separated on each rotor. The pressure variations of both free rotor and the corresponding shrouded system of this work can be seen in Fig.2.8.

Compared to the pressure variation of free system, the relative pressure value on the shroud along the system axis for shrouded rotors is all lower than ambient, even in the downstream wake caused by the shroud nozzle. Since the flow is accelerated before the rotors due to the rotation which aspirates the air coming inside the shroud passage, the pressure is reduced greatly and a lowest pressure is formed before the

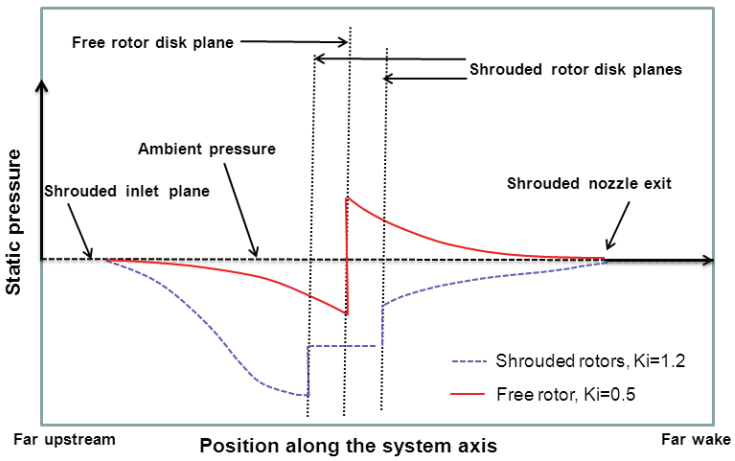

Figure 2.8: Pressure distribution for free and shrouded systems

rotor system. However, according to mass conservation and Bernoulli equation, this greatly depends on the shroud inner shape. All of this indicates that the shroud profile greatly refines the flow field inside the system and also the physics of induced flow on its surface.

2.3 Prediction on Global Characteristics of Shrouded System

On the basis of Eq.2.8 and 2.9, the induced power P_i which is the power power induced into the flow, can be calculated from the pressure jump ΔP generated across the rotors or directly from the rotor thrust F_R as in the following equation:

$$P_i = \frac{\Delta P \cdot \dot{m}}{\rho} = \frac{\dot{m} \cdot F_R}{\rho A_R} = \frac{1}{2}\frac{1}{K_e^2}\left(\frac{F_T}{\rho A_R} \cdot K_e(1 - \frac{K_e}{2K_i})^{-1}\right)^{\frac{3}{2}} \cdot \rho A_R \tag{2.16}$$

According to the Froude theory extension, the global characteristics of shrouded system can be evaluated from the characteristics diagram proposition. It offers a design guidance, which is the massflow rate versus the induced power P_i. It can be proved from above equation that the minimun P_i is obtained under the condition that K_e is equal to $K_i/2$, whatever the system desired total thrust F_T is.

2.3.1 Characteristic analysis of the system with $K_i = \infty$

Fig.2.9 shows the performance of shrouded system with $K_i = \infty$. For the outlet parameter $K_e = 0.5$, this is exactly equivalent to the free system. Under it, certainly the "shroud" has no contribution on the thrust at all. The same iso values of total and rotor thrust could always be under the condition of $K_e = 0.5$. And it could

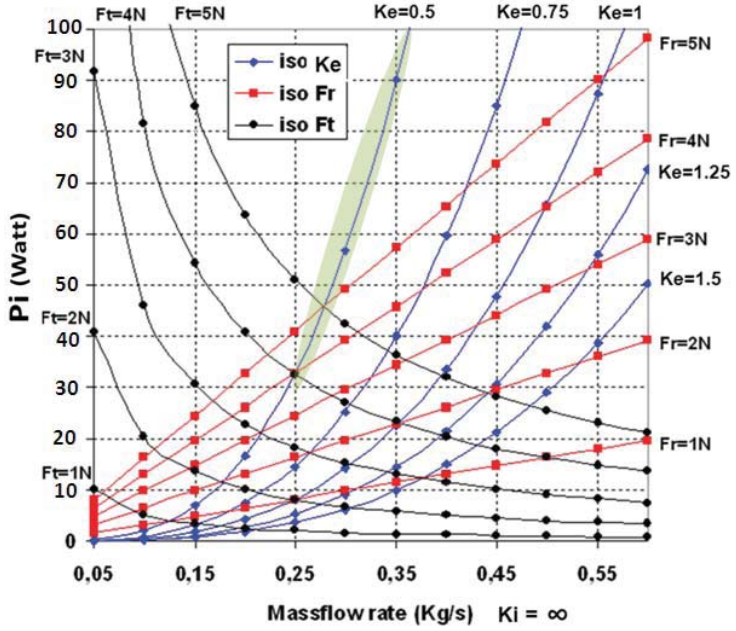

Figure 2.9: Overall performance of the system with $K_i = \infty$

be also considered as a separation for the shroud thrust contribution – negative for K_e less than 0.5 or positive for K_e greater than 0.5. For $K_e = 1$, which means a cylindric nozzle shape, it can be proved that the rotor always produces half of the total thrust. It implies that the cylindric shroud nozzle averagely distributes the thrust for the shroud and rotors. Comparing the free system $K_i = 0.5$ and the shrouded system, based on the same induced power, a greater K_e generates far more mass flow. Given certain amount of mass flow, the increment of K_e consumes less induced power. For system optimization, since the induced power tends to decrease smoothly, for the shrouded system with infinite K_i, it is difficult to find the best operational state.

As explained, to obtain a given total thrust, is is known that increasing the ratio K_e will lead to an increase of a mass flow (+1% for example). A direct consequence is the increase of the shroud thrust (+2%) because it directly benefits from the dynamic pressure effect. Since the aim is to keep the total thrust constant desired by the BR2C application, less rotor thrust is needed (-2%). As a result, it can be shown that the needed induced power which is a product of the rotor thrust and the mass flow will decrease (-1%). This is a way to explain why, for a perfect shroud inlet, the thrust per unit power will always benefit from a greater nozzle.

2.3.2 Characteristic analysis of the system with different K_i

In reality, it is impossible to reach the design above for a system with ideal infinite large inlet. Fig.2.10 thus gives the general trends of the global performance for a normal shrouded system with $K_i = 1.3$. Comparing these two shrouded systems in

Fig.2.9 and 2.10, it could be observed that the change of inlet area ratio does not change at all the performance distribution with iso K_e and rotor thrust. This means the performances of mass flow, induced power and rotor thrust are theoretically not affected by the inlet. On the other hand, for the shroud system with $K_i = 1.3$, the induced power does not tend to be a smooth change but increase dramatically again after a great decrease. This provides the possibility to find an optimized design state of minimum consumption of induced power but maximum thrust generation for any desired constant thrust, which is under the value of K_e equal to 0.65, as shown in the highlighted region Fig.2.10.

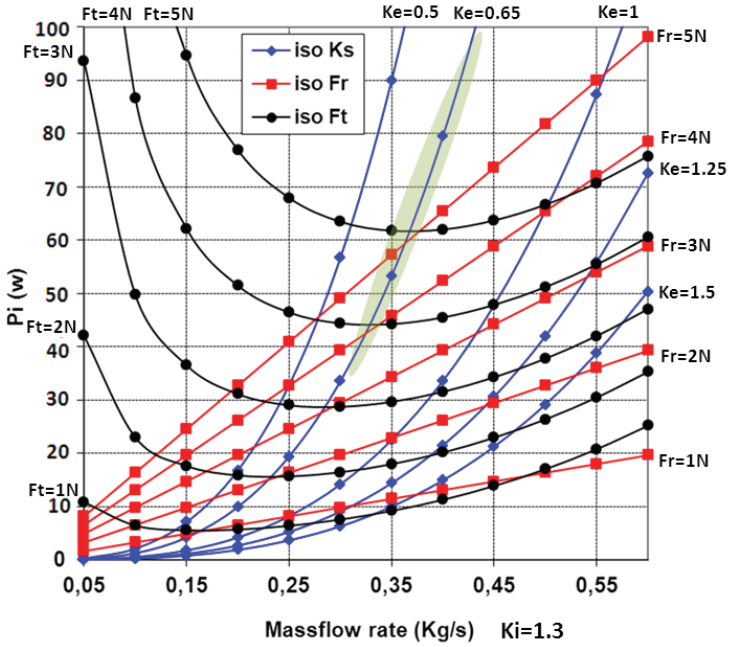

Figure 2.10: Overall performance of the system with $K_i = 1.3$

Comparing to the finite inlet of K_i equal to 1.3, the larger inlet of $K_i = 3$ allows the larger nozzle or K_e to make greater improvement on the mass flow by given the same induced power, as shown in Fig.2.11. For the finite inlet of $K_i = 3$, the optimized performance turns to the nozzle design of qpproximately $K_e = 1.5$. Relative to infinite inlet in Fig.2.9, which allows an infinite increased mass flow caused by extreme large outlet, this is not possible to achieve in a finite inlet.

The reason why the induced power will finally increase when increasing Ke with a finite Ki can be introduced. From Eq.2.11 and 2.10, comparing with a same increase of mass flow (as in the infinite or perfect inlet), the increase of shroud thrust will be smaller. At the same time, the decrease of rotor thrust will be smaller too. This effect is all more effective as K_e is increasing to K_i. Again, the induced power which is a product of the rotor thrust and the mass flow will decrease less, compared to the perfect inlet, or even increase. It can be shown that the induced power still decreases for $K_e < K_i/2$ and increases for $K_e > K_i/2$.

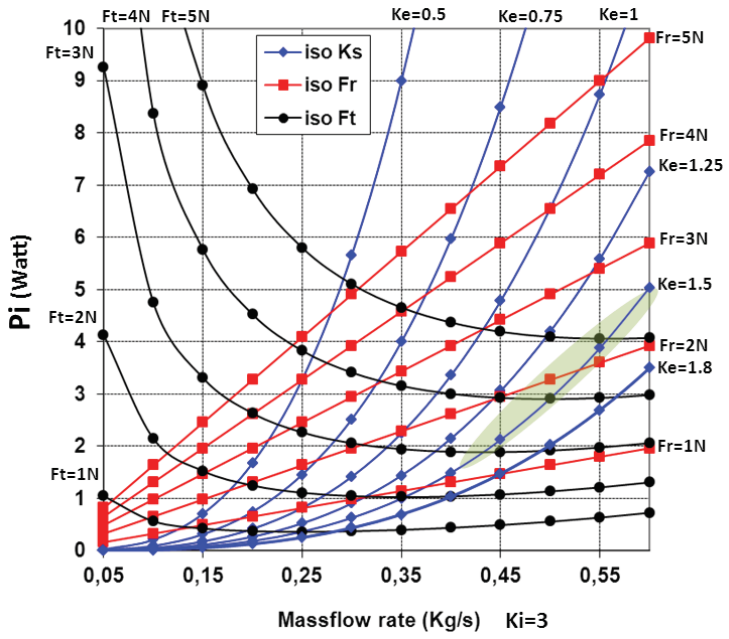

Figure 2.11: Overall performance of the system with $K_i = 3$

2.4 Conclusions

By extending Froude theory for free rotor to shrouded system with two geometrical parameters K_i and K_e defining the inlet and the outlet, the shroud effect on its thrust performance, and the system overall characteristics were analyzed. The main following points are:

- For thrust performance, both large inlet and outlet can usually make an improvement on the shroud thrust. The value of $K_e = 0.5$, which rightly corresponds to the contraction of free rotor, is a limit between positive and negative effect on the shroud thrust. The cylindrical nozzle averagely distributes the thrust on the rotor and shroud for a system with infinite inlet. This is not presented in the finite inlet;

- For the thrust generation by each shroud composition, once the shroud profile is fixed, the contribution on total thrust from the air entrance and nozzle are constant too. The air entrance always contributes all or more than the shroud thrust. Except the cylindrical geometry, the nozzle usually has negative production. All such contributions are related with the lower pressure distribution on shroud wall when compared to the free rotor which suffers from pressure equilibrium;

- For nozzle's role on system performance, more importance is on the mass flow. Whatever the inlet is, a great outlet can increase the mass flow far more than the free rotors by a given induced power. For a infinite inlet, such improvement

caused by a large outlet can be theoretically infinite as well. For a finite inlet, the optimized performance which is the minimum induced power consumption for any certain total thrust generation, is provided under the nozzle with a great outlet. Theoritically the area of such outlet for optimized performance is increased propotionally to half of the increased inlet area.

Based on the actuator disk model, the Froude theory extension offers a preliminary prediction on the performance which considers that the ideal power is the one induced into the flow, and mainly evaluates the effects of the inlet and outlet on both thrust and overall performance. However, as explained in the theory extension, the inlet definition needs to be identified further due to the confliction with axial flow. Also the effects from the viscosity should be more explored in following work because of the low operational Reynolds number.

Chapter 3

2D Simulation on Shroud Parametrical Design

From the extension of one dimensional Froude theory, the theoretical analysis on the overall performance reveals, for the shroud that it certainly exists an optimal design regime for the two most important parameters K_e and K_i. These two parameters are theoretically desired to be large. Compared to free system, which has nozzle expansion rate of 0.5, the shroud greatly influences the flow field through the shroud and rotor passages. Stronger negative pressure distribution relative to the ambient is formed along the shroud inner profile. The air entrance plays a critical role to generate the thrust, and the nozzle seems always to behave negatively in terms of the thrust production. In conclusion, the shroud could improve the system propulsive behavior and this improvement could be maximized when the shroud profile is properly designed. However, such theoretical analysis on the geometry design is obviously limited due to the dimension, the analysis is constrained on the cross sections and it can not involve the air entrance shape for well modeling the inflow at the inlet. Moreover, the viscosity effects is not considered.

Therefore in order to explore more on the shroud profile design for optimizing the system performance, this chapter aimed to develop a two dimensional axisymmetrical numerical methodology through the application of one commercial CFD software Fluent6.3, which accounts for a viscous flow within tha actual shroud profile. The effects of shroud geometrical parameters under each composition – air entrance, cylindric section and nozzle, their optimal design regimes and basic criteria were explored independently. A new shroud model with optimized design was finally proposed for following experimental and numerical study.

3.1 Analytical Model

As the introduction in Chap.1, the shrouded contra-rotating rotor is composed of two parts: the double rotor and the shroud. The two rotors rotate in the opposite direction and are installed inside the shroud on the same axis. The overall configuration is axisymmetric. To begin the 2D numerical study, both rotor and shroud model will be firstly decided.

3.1.1 Contra-rotating rotor model

As a resource to transform the mechanical power to kinetic energy, the double rotor is obviously a key part for the rotary vehicles. Since the first part of the project emphasizes on the shroud parameters design, the main effect of rotor system could be replaced by an actuator disk for the shrouded rotating propulsion systems. It simplifies the rotors as a flat and infinitely thin disk which produces an uniform pressure jump between both sides of the disk as Froude theory extended in Chap.2. Herewith the function of double rotor could be simulated as a pressure jump ΔP which launches the system works under hovering conditions. The general configuration of the model modified is as shown in Fig.2.1 of Chap.2. The contrarotative rotor in this model is expected to provide the least swirl as possible.

Therefore for both theory and 2D simulation which all apply the same rotor model, on the rotor function part there is no difference between these two methods. The thrust generated by the rotor can be also calculated using ΔP:

$$F_R = \Delta P \cdot A_R = (P_2 - P_1) \cdot A_R \tag{3.1}$$

Through the pressure jump imposed on the rotor, the corresponding mass flow, the thrust of different components could be obtained from the simulation. Although it is known that the specific rotor profile is not to be specifically considered on the system, this quite simplifies the simulation and reduces its computational cost.

3.1.2 Shroud model

Basically, the main idea of shroud cross-section profile comes from the geometry of airfoil because of the aerodynamic principles to produce the lift. For the shrouded system, the purpose for applying the shroud is to generate the thrust but the lift. This drives the shroud design method distinguished with the airfoil. According to the functions of different shroud parts, the shroud could be separated into three parts as introduced in the last chapters: inlet, middle cylindrical section and nozzle.

For the shroud inlet, its importance is that the incoming air forms a low pressure region on the inlet lip, which is the main reason why the shroud generates thrust itself. In the hovering situation, the rotating rotor with the shroud aspirates the air from all around the propulsion system, a suction peak is therefore formed on the inlet; For the cylindrical section in the middle, it offers a space to the double rotor system to minimize the gap between the shroud and rotor tip to reduce the tip vortex loss; The nozzle function is to expand the slipstream after the rotor. This could decrease the final wake velocity and increase the mass flow through the rotor.

For each part, as the way to constrain the shroud profile, all of the possible geometrical parameters are extracted as Fig.3.1. In the figure, the parameters considered include:

- For inlet – length l_i, internal shape, leading edge curvature C_{le} and leading edge radius R_{le};

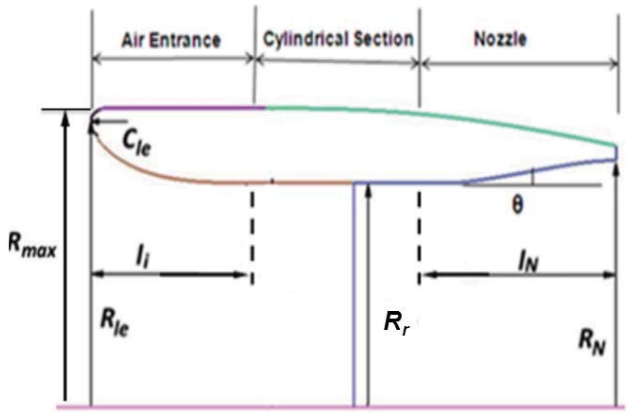

Figure 3.1: Froude model for shrouded system

- For cylindrical section – maximum radius R_{max} and cylindrical radius;
- For nozzle – exit radius R_e , length l_N internal shape for the nozzle and divergent angle θ.

Here the cylindrical radius is the rotor radius R_r once the Froude theory or actuator disk is applied in the simulation.

3.2 Numerical Methodology

During 2D axisymmetric simulation, the Finite Volume Method (FVM) was used to discrete the basic governing equations from the conservation laws of fluid mechanics. For this propulsion system at the normal operational condition, because its Mach number is generally far smaller than 0.3, the aerodynamic flow can be considered incompressible. And according to empirical data of such system which has Reynolds number on the order of 4 at least, the flow is then thought to be turbulent. In order to solve the turbulent flow, the Reynolds Average Navier-Stokes equations and Spalart-Allmaras model were firstly chosen to validate the simulation in this work. The detail on other parameter settings in Fluent could be seen in App.B.

3.2.1 Computational field and boundary condition

As the explanation for the geometry, the shrouded system was simplified as a 2D axisymmetric configuration, hence the necessary computed field was half of the structure. Meanwhile in order to avoid the definition of the boundary condition at the shroud inlet and outlet because of the uniform radial pressure gradient, and also to obtain as much flow information as possible, the computational field did not only include the shroud internal flow filed but also contained a large zone around the shroud. The axisymmetric computational field is shown in Fig.3.2. The computed field is composed by the air inlet and outlet, the shrouded system with an actuator disk, and the symmetric axis.

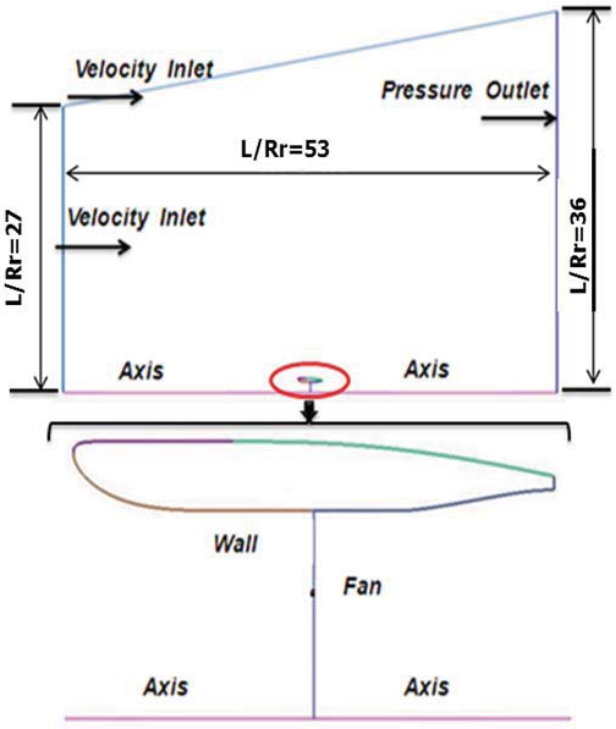

Figure 3.2: Computational field and boundary conditions in 2D simulation

The boundary definition corresponding to the geometry could be seen in Fig.3.2. For the shrouded system, the rotor was modeled as an actuator disk which was imposed a fan boundary producing the pressure discontinuity in the flow properties. Flow was imposed slowly on the inlet and outlet when the calculation is initialized in order to keep the flow from reversing at the outlet boundary, which could induce a nonphysical solution and also the divergence problem. The pressure condition that was used at the outlet is close to reality.

3.2.2 Axisymmetric mesh generation

The structural mesh was made with ANSYS ICEM 11.0. It consists of a 2D structured mesh containing exclusively "quad" shells. It was created with the blocking method available in ANSYS ICEM. An O-grid was generated around the shroud in order to be able to refine the mesh and have a better turbulent boundary layer solution. It contains about 10000 elements, as seen in Fig.3.3.

Since the flow is considered turbulent and solved with a Spalart-Allmaras turbulence model – a low-Reynolds number model in its complete implementation. This means the model is used with the meshes properly resolving the viscous-affected region, and damping functions have been built into the model in order to properly attenuate the turbulent viscosity in its sublayer. Therefore, compared to the coarse mesh with $Y^+ > 30$ for a standard wall function, the full benefit of the Spalart-

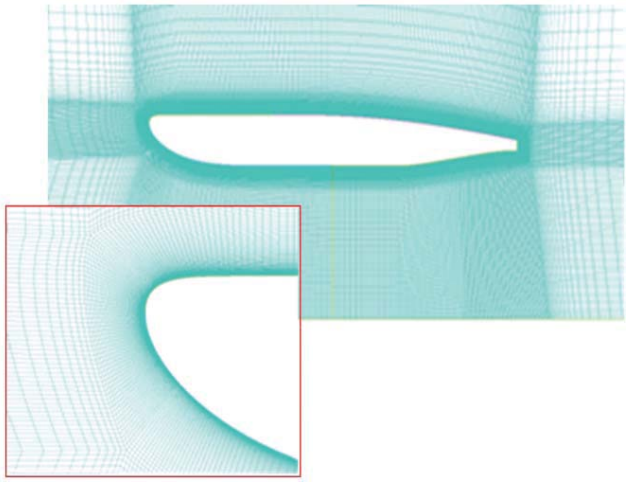

Figure 3.3: 2D Mesh around the shroud and on the boundary layer

Allmaras model is obtained with the mesh height at shroud wall lower than 1 for enhanced wall treatment.

3.2.3 Evaluated parameters

Generally, in order to evaluate the propulsion system, the propulsive efficiency η shown in the following equation is adopted.

$$\eta = \frac{(F_{R_1} + F_{R_2} + F_{sh}).V_0}{Q_1.\omega_1 + Q_2.\omega_2} \tag{3.2}$$

In Eq.3.2, F_{R_1}, F_{R_2} and F_{sh} are the thrusts of the first rotor, second rotor, and shroud respectively, while V_0 is the velocity of vehicle. Q_i and ω_i represent the torque and angular velocity of each rotor.

Equation.3.2 implies the system with a sufficiently high efficiency could transform the available mechanical power into the kinetic energy necessary for supporting the flight of whole propulsion system. However, the work in this paper focused on the hovering performance of the shrouded system. The system velocity stays zero ($V_0 = 0$) when the vehicle hovers in the space. Therefore propulsive efficiency given above cannot be used for the shrouded system in hover. Another metric usually applied is the Figure of Merit (FoM). It is used to qualify the ability of rotor to transform the mechanical power into the kinetic energy of the flow. As for the rotor in Froude theory and 2D simulation, it was modeled as actuator disk and it was assumed that the rotor perfectly converts the mechanical power into the kinetic energy of the flow. These assumptions imply that these two metrics which generally evaluate the rotorcraft propulsion system are not suitable for this 2D axisymmetric simulation.

Therefore a third quantity – power loading, is proposed to evaluate the system.

It is presented in Eq.3.3. However it should be noticed that the power used here is not the mechanical power but the induced power.

$$PL_i = \frac{F_T}{P_i} \tag{3.3}$$

Clearly, the optimal design should produce a maximum total thrust F_T while consuming a minimum power P_i. In 2D simulation, as mentioned above, the actuator disk is capable of energy conversion and it does not involve the mechanical power, therefore the induced power consumed by the air flow is applied into the calculation of PL. Such induced power is calculated with the pressure jump which is imposed on the actuator disk as a "fan boundary condition" as same as Eq.2.16 in Chap.2.

3.3 2D Axisymmetric Simulation Evaluation

As in the introduction on 2D axisymmetrical simulation, before applying the methodologies of the shroud parametrical study, it is necessary to first check the condition imposed on the boundary which is not completely correspondent to the reality, and the consistency of the 2D simulation and Froude theory. Once the consistency is validated, the application of Froude theory will obtain a certain amount of total thrust as 5 N for BR2C application without executing an iterating 2D simulation.

3.3.1 Influence of V_∞

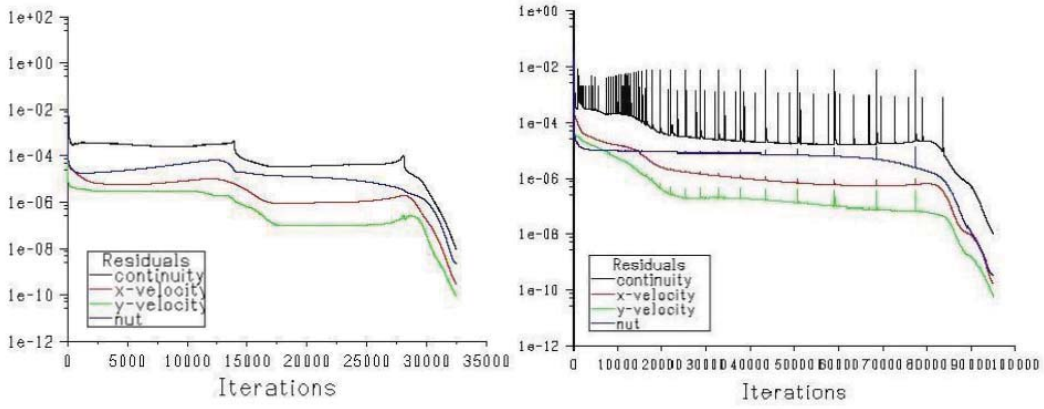

Figure 3.4: Residuals for normal and reversed flow at the outlet

This work focuses on the hovering state of shrouded contrarotating rotor. This means MAV would keep static in space and the velocity far away is naturally null. However, for 2D axisymmetrical simulation, an incident velocity at the inlet boundary must be imposed in order to avoid the reversed flow at the outlet boundary.

This reversed flow happens because the mass flow exiting the outlet due to the micro drone's jet is higher than the one entering the inlet, so to compensate, an amount of flow must enter through the outlet. This fact gives a non-physical solution and, moreover, the solution experiences convergence problems, seen in Fig.3.4.

Fig.3.4 shows the residuals convergence for both a reversed flow situation on the right and a normal situation on the left. A strong fluctuation occurred on the calculation which has reversed flow on outlet. Therefore it is unavoidable to impose an incident velocity for obtaining a zero velocity at the outlet, except at the zone affected by the microdrone jet. However, this is not consistent with reality. In order to evaluate the influence of imposing an incident velocity, it is necessary to see how this incident velocity affects the real solution. By taking certain shroud geometry with $K_i = 1.63$ and $K_e = 1.21$ and solving the problem for different incident velocities but constant pressure jump ΔP of 100 Pascal set on the fan boundary, the effect was determined as shown in Fig.3.6

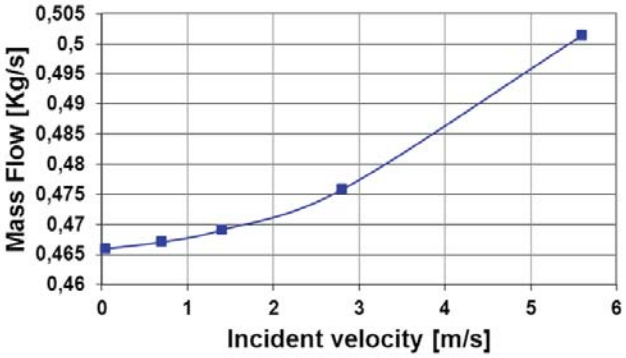

Figure 3.5: Mass flow with different incident velocity

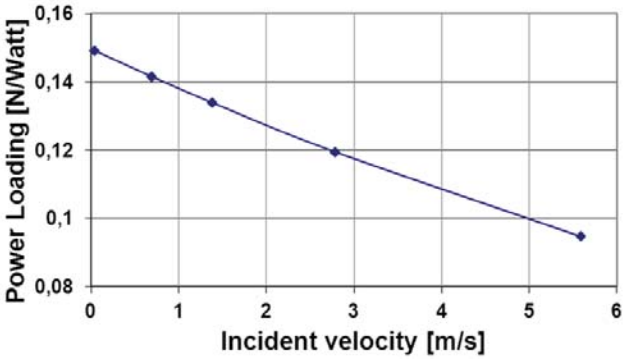

Figure 3.6: PL_i with different incident velocity

Reasonably imposing an incident velocity makes an increment of mass flow as an additional driving resource. Fig.3.5 indicates the mass flow gently increases with the increased incident velocity V_∞. The variation of mass flow is quite small between the first two V_∞. Then it is increased dramatically. The system behavior depends on the

mass flow aspirated. The great variation of mass flow caused by the incident velocity would definitely affect the power loading performance, seen in Fig.3.6. Fig.3.6 shows PL_i has an almost linearly reduction with increased V_∞. This is greatly related to the increased mass flow shown in Fig.3.5. Both figures imply that imposing an incident velocity which is far from the situation under hovering at the inlet can introduce an error on the evaluation of the system performance. However, in order to avoid a non-physical solution caused by the reverse flow, a velocity imposed on the inlet must be as small as possible. That should be controlled to be lower than 0.7 m/s, the second value of incident velocity on the figure, which could make the error from incident velocity acceptable. Therefore the incident velocity 0.3 m/s, avoiding the reverse flow and at same time limiting the error, was chosen for the following 2D simulation.

3.3.2 Turbulent model chosen

The turbulent flow is characterized by small random velocity fluctuations in certain regions of the flow field. One possibility for the simulation of turbulence is to use turbulent models for the numerical simulation. One frequently used approach for their applications is Reynolds-Averaged-Navier-Stokes (RANS) equations, where the velocity field is composed of "normal" velocity and small velocity fluctuation arising in turbulent flows due to their chaotic behavior. The turbulent viscosity coefficient must be calculated in the Boussinesq hypothesis. This can be done with zero, one or two additional equations depending on the turbulence model used. The detail on some of the more commonly used turbulence models such as Spalart-Allmaras, Standard $k-\varepsilon$ and Shear Stress Transport $k-\omega$ etc. could be found in App.B.2.

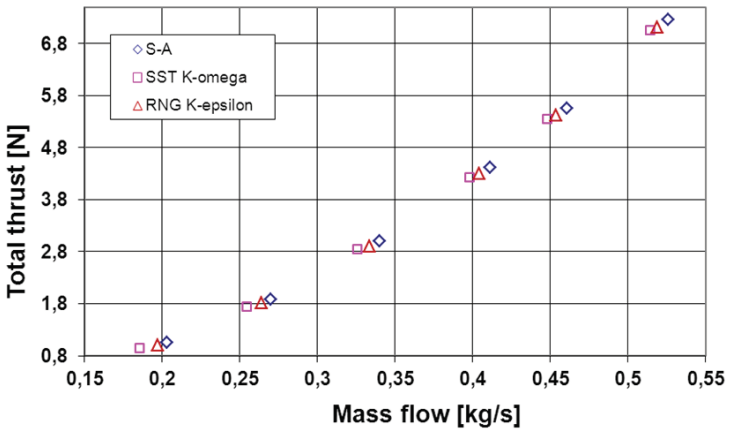

Figure 3.7: F_T versus $\dot{m}$ for different turbulent models

In order to compare and choose one model which must be suitable for solve the specific case in this work, the turbulent models S-A, RNG $k-\varepsilon$ and SST $k-\omega$ are applied respectively on the same cases based on the analysis of the incident velocity. For a certain shroud and refined mesh which has around 14000 cells,

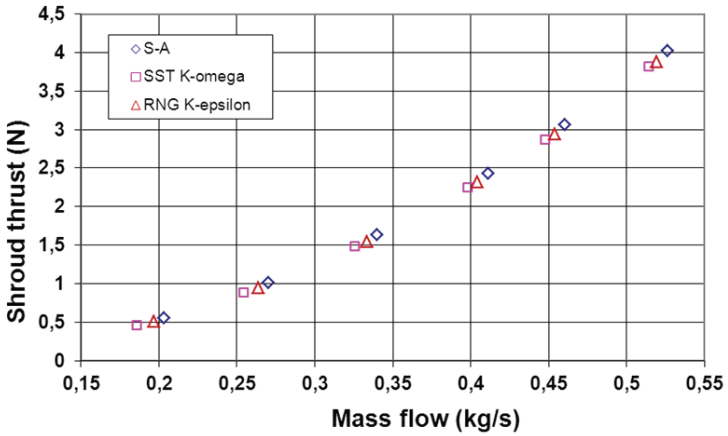

Figure 3.8: F_{sh} versus $\dot{m}$ for different turbulent models

through imposing an pressure jump ΔP on the rotor with different values as 20, 35, 55, 80, 100 and 130 Pascal, the variation of total thrust and shroud thrust are calculated by 2D simulations as shown in Fig.3.7 and 3.8. Both thrusts have almost the same relations with the changed mass flow. They all appear with a quadratic variation which is correspondent to the Froude theory as shown in Eq.2.8 to Eq.2.11. Whichever turbulent model was applied in 2D simulation, Fig.3.7 and 3.8 reveal that they evidently behave similarly. Therefore, considering the computational costs and the efficiency, Spalart-Allmaras turbulent model was applied through the whole 2D axisymmetrical simulation study.

3.3.3 Validation on ΔP dependency by 1D Froude theory

Based on the extension of Froude theory in Chap.2, it is easy to obtain the dependency of the mass flow, the thrust, the power and the power loading on the pressure jump introduced by the rotors.

Equalizing Eq.2.9 and 3.1, the mass flow $\dot{m}$ depends on ΔP:

$$\frac{\dot{m}}{\rho A_R} = \left(\frac{2\,K_e^2}{\rho}\right)^{0.5} \Delta P^{0.5} \tag{3.4}$$

By introducing the equation above in Eq.2.8, the total thrust dependency on ΔP could be obtained:

$$\frac{F_T}{\rho\, A_R} = \left(\frac{1}{K_e} - \frac{1}{2\,K_i}\right) \frac{2\,K_e^2}{\rho} \Delta P \tag{3.5}$$

Taking the definition of induced power and introducing Eq.3.4, the induced power P_i has the relation with δP:

$$P_i = \frac{\Delta P\, \dot{m}}{\rho} = \left(\frac{2\,K_e^2}{\rho}\right)^{0.5} A_R \Delta P^{1.5} \tag{3.6}$$

The power loading in Eq.3.3 could be finally calculated through the two equations above.

$$PL_i = \frac{F_T}{P} = \frac{(\frac{1}{K_e} - \frac{1}{2\,K_i})2K_s^2}{(\frac{2\,K_e^2}{\rho})^{0.5}} \Delta P^{-0.5} \tag{3.7}$$

The shroud geometry with the parameters $K_i = 1.6$ and $K_e = 1.2$ was used to validate 2D simulation on the dependency of ΔP. Six different ΔP from 20 Pascal to 120 Pascal with the step of 20 Pascal on the rotor were made in the calculations. Fig.3.9 shows the results of the relations between different variables and pressure jump. Based on the 2D axisymmetric simulations, through presenting the different variables as the function of pressure jump ΔP, the exponential trends were obtained. Comparing the index of pressure jump for each variable to the ones introduced in the equations from Eq.3.4 to Eq.3.7, a correct consistency of the 2D simulation results with Froude theoretical analysis can be observed. Even though the consistency is not exactly the same, this difference could be negligible in the first approximation.

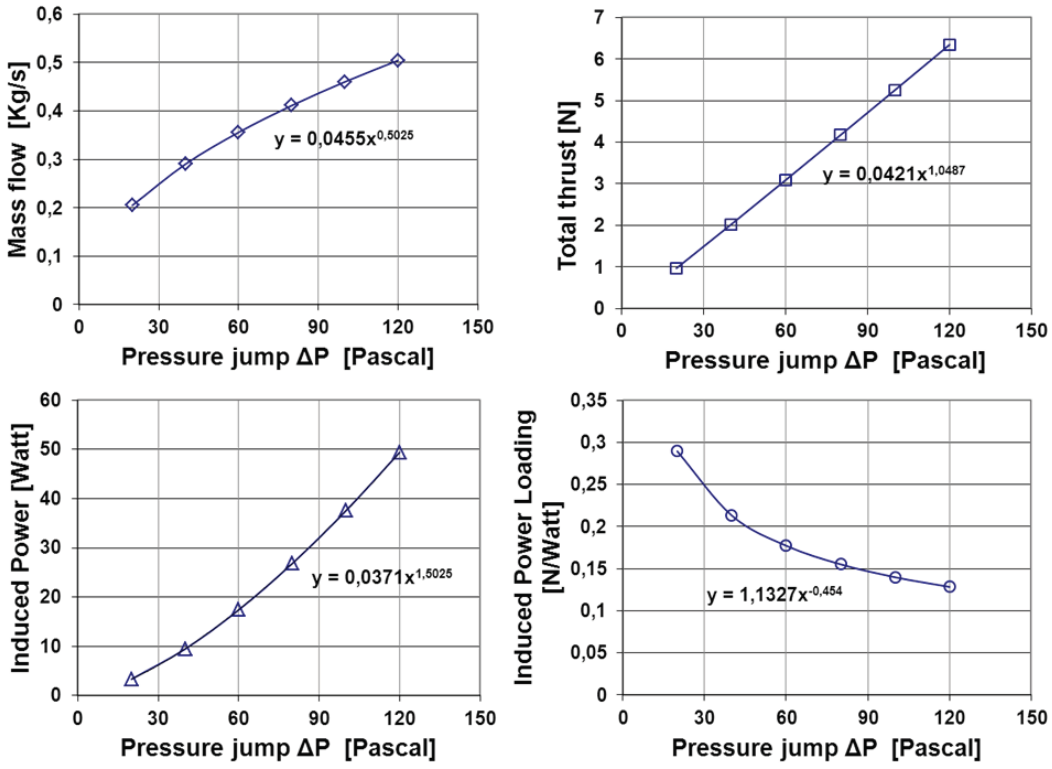

Figure 3.9: Mass flow, total thrust, power and power loading versus ΔP

The agreement between 2D simulation and Froude theory proves in one sense that the numerical methodologies used in simulations are effective, and the imposing of velocity on the inlet boundary is reasonable and acceptable. In addition, this consistency offers an efficient way to do the calculations, which desire a constant thrust

without doing an iterative process. It allows the simulation to use the pressure jump equal to 100 Pascal for all cases to get the coefficients for the necessary variables in function of ΔP. Based on the coefficient corresponding to the variable total thrust, the ΔP needed to have a constant total thrust would be obtained. Then other variables can be solved as well. According to this method, with constant rotor diameter 90 mm, the computation of different shroud models will be given with independently changeable geometry parameters to explore their individual effects.

3.4 Influences of Nozzle Design Parameters

Nozzle is an important component for the shroud, it is used to expand the flow after rotor and affect the absorbed mass flow. For the profile of nozzle shown in the Fig.3.1, it is defined by nozzle exit radius, length and the internal shape.

3.4.1 Nozzle exit radius

The nozzle exit radius was changed from $R_e = 80$ mm to $R_e = 115$ mm with the step of 5 mm which corresponds to the ratio from 0.89 to 1.28 of nozzle exit radius divided by rotor radius. Fig.3.10 shows the configurations of both extreme cases.

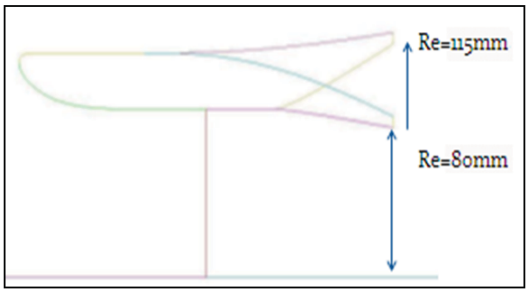

Figure 3.10: Extreme cases of varied nozzle radius

With changing nozzle exit radius R_e , the contributions of different components from shroud are changed as shown in Fig.3.11. For the demand to produce a certain total thrust, the mass flow $\dot{m}$ is increased with the increment of R_e. This implies the relative greater nozzle radius can expand the flow better so that more air is absorbed inside the shrouded system. The shroud consequently produces more thrust (F_{sh}) and its contribution becomes more important until R_e is equal to 1.15 times the rotor radius. At this value, the shroud generates greater than 50% of total thrust. For such contribution, it mainly comes from the air entrance part (F_{ent}). And the nozzle always generates a negative thrust (F_{noz}). However the nozzle is still critical for system performance because of its pilot role on the increment of mass flow. While the basic reason of thrust production for shroud inlet and nozzle is the pressure distribution on their surfaces due to the mass flow $\dot{m}$. Meanwhile, since the shroud produces more and more thrust, it naturally makes the importance of the rotor (F_R) becomes less for a total thrust demand.

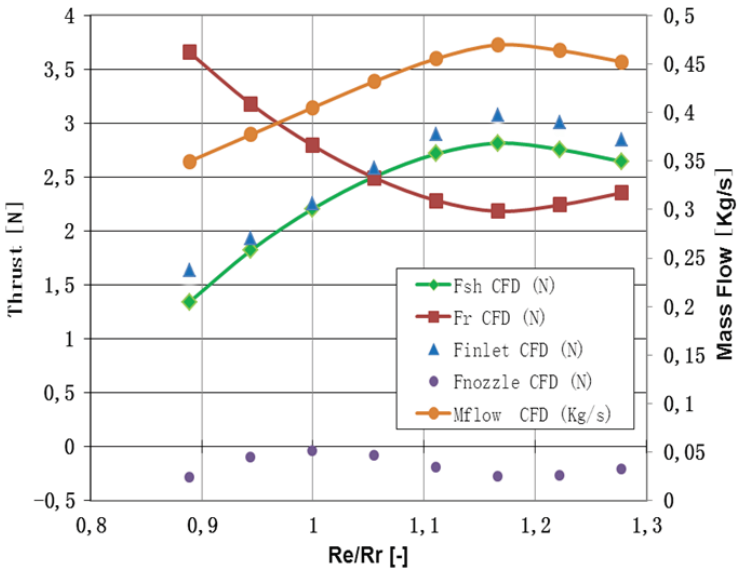

Figure 3.11: Thrust of shroud and its components for given Ft of 5N

However, after $R_e > 1.18R_r$, Fig.3.10 shows a condition on the contrary, the increased R_e leads to a decreased thrust performance with the decreased mass flow. The limited improvement is due to the flow separation seen in Fig.3.12. Fig.3.12 shows the velocity magnitude distribution around the shroud. The flow separation appears on the boundary layer of the nozzle with radius ratio greater than $R_e/R_r = 1.22$.

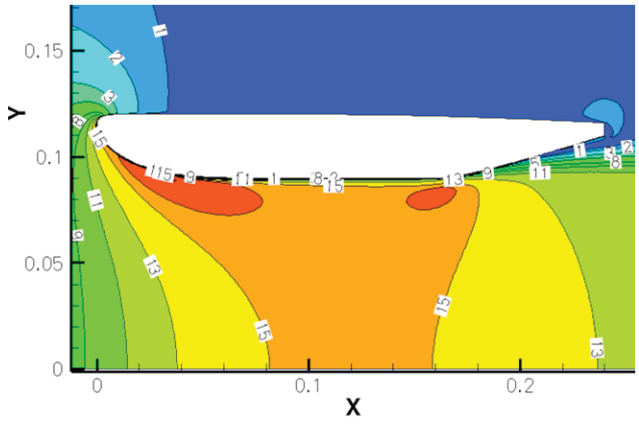

Figure 3.12: Velocity magnitude distribution for $R_e/R_r = 1.22$

One effect of the flow separation is a loss of total pressure, and another is the thickening of the boundary layer on the nozzle. This effect is to reduce the effective nozzle radius. Another physical phenomenon is the vortex on the up corner of shroud trailing edge. This might be more severe when exit nozzle radius R_e is increased greater than the radius of shroud cylindrical section.

Besides the realization on the performance with increased R_e from the simulation, according to the introduction on the Froude theory, a comparison to the simulation on the shroud thrust was made in order to clarify the behavior of the system. Fig.3.13 shows the shroud thrust from the Froude theory based on the Eq.2.9-2.11 with $K_i = \infty$ (infinite) and 1.63 respectively and the 2D axisymmetric simulation result as well.

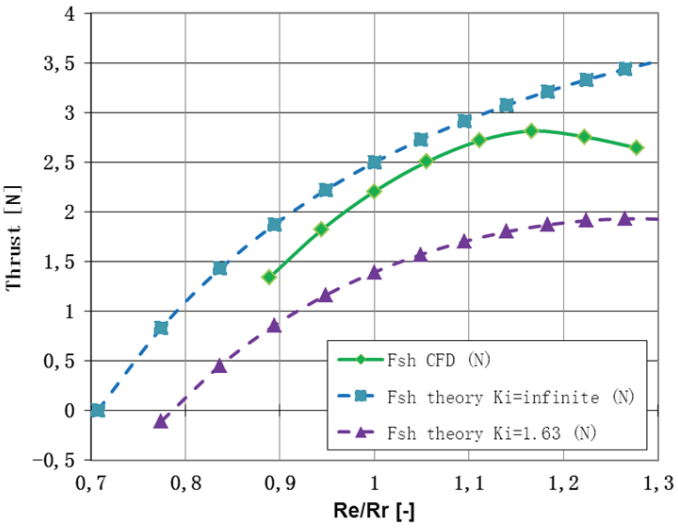

Figure 3.13: Comparison on F_{sh} between 2D simulation and Froude theory

In Fig.3.13, globally the tendencies of the shroud thrust with the increased nozzle radius are similar in both simulation and Froude theory. And the simulation result is closer to the theoretical one of K_i equal infinite but 1.63 which is used in the simulation. This is because of the definition of the parameters K_i in Froude theory, which is the area ratio of air inlet divided by the rotor disk. In Froude theory, it is actually difficult to obtain the real value of the air inlet because the attachment point of the air on the shroud inlet, which might be more outside of the leading edge defined in the simulation, is hard to be clear. It could be changed with the environment and any dynamic factors. Therefore according to the comparison with simulation, here the real air inlet area in the Froude theory should be greater. Also, the theory does not consider the flow separation that has happened on the nozzle with greater radius as shown in the Fig.3.12. That is the reason why the shroud thrust always increases and its difference between the theory for $K_i = \infty$ and the simulation becomes obviously after $R_e > 1.18R_r$.

More in depth, Fig.3.14 shows the power loading PL_i with varied radius R_e from the Froude theory especially for $K_i = \infty$ and the simulation.

Firstly, for the Froude theory combined the Eq.2.8, 2.9, 3.3 and 3.6, the function of PL_i can be expressed:

$$PL_i = \frac{K_e}{\dot{m}} \cdot (2 - \frac{K_e}{K_i}) \cdot (\rho \cdot A_R) \tag{3.8}$$

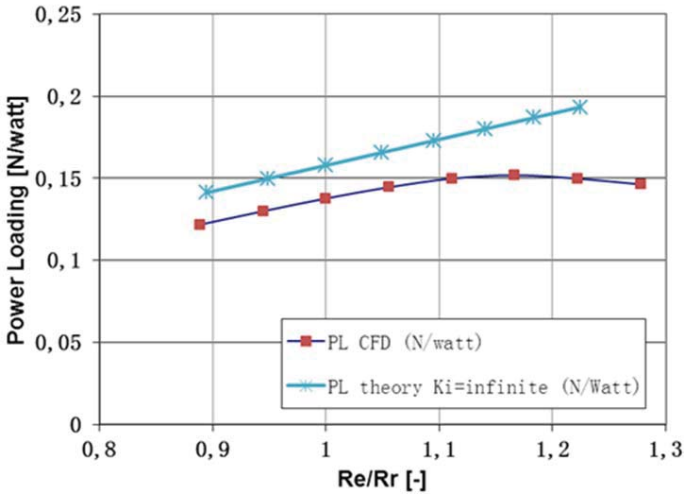

Figure 3.14: Comparison on PL_i between 2D simulation and Froude theory

For $K_i = \infty$, by inducing Eq.2.8 into the equation above, PL_i is:

$$PL_i = \frac{K_e \cdot (\rho \cdot A_R)}{F_T} = \frac{(\rho \cdot A_R)}{F_T} \cdot \frac{R_e}{R_r} \tag{3.9}$$

As shown in Eq.3.9, under the condition of infinite inlet area, constant rotor radius and a certain total thrust generation, PL_i from the Froude theory is the function only referring to the parameter K_e. Fig.3.14 shows a linear relation between PL_i and R_e/R_r. It has globally similar trends of PL_i performance with the 2D simulation results: Generally more divergent nozzle improves the PL_i performance and behaves better as the analysis on the thrust performance. Therefore the more divergent nozzle has greater ability to perfectly expand the injected flow and converse the kinetic energy of the fluid into the pressure effect.

3.4.2 Internal nozzle shape

While reality there are many possibilities for the nozzle internal shape, the basic design rule is to adapt the flow structure as much as possible and avoid the flow separation to decrease the total pressure loss and drag as well. In this paper the internal nozzle shape was induced by the degree of convexity or concavity of the nozzle internal profile related to the external nozzle profile, as shown in the subfigure of Fig.3.15. A set of eight cases were calculated. Case(a) means the internal shape is the most concave and case(h) is the one which is the most convex.

Fig.3.15 indicates that a very low influence of internal nozzle shape on the global performance of power loading PL_i. The improvement on PL_i is limited by boundary layer separation due to the viscosity of the fluid. Because of it, the variation of PL_i is reduced by about 1%.

The profile of the shroud in 2D simulation is actually composed of four curvature lines P.1-P.2, P.2-P.3, P.3-P.4 and P.4-P.1 as shown in the subfigure of Fig.3.15.

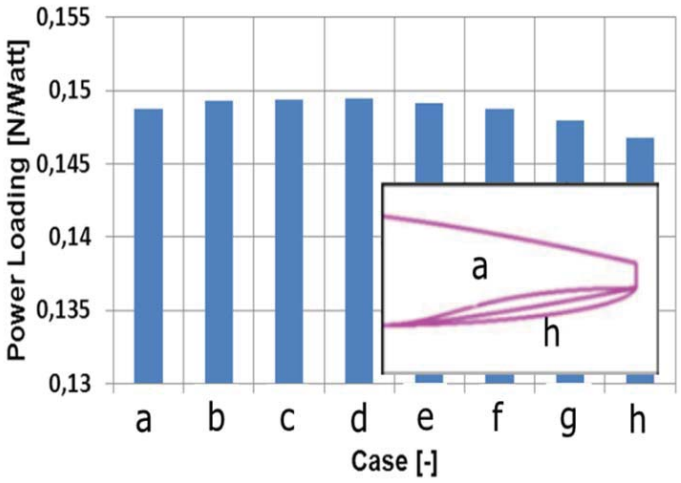

Figure 3.15: PL_i versus cases with different internal nozzle shapes

Another important influence is the static pressure distribution along these four curvature lines, as shown in Fig.3.16. Comparing the extremely concave case(a) and extremely convex case(h), it is indicated that for the demand of total thrust, the pressure jumps of both cases which could be seen on the point P.4 are almost the same, and they all result in a higher pressure gradient. It appears on the place where the nozzle profile (P.3 to P.4) has the greatest curvature. And the comparison of the case(a) and (h) on PL_i reveals that the performance is extremely limited by the higher adverse pressure gradient on the nozzle exit P.3 as case h. This might lead to a relatively lower mass flow and then affect the region P.4-P.1 of suction pressure which is weaker than the case (a).

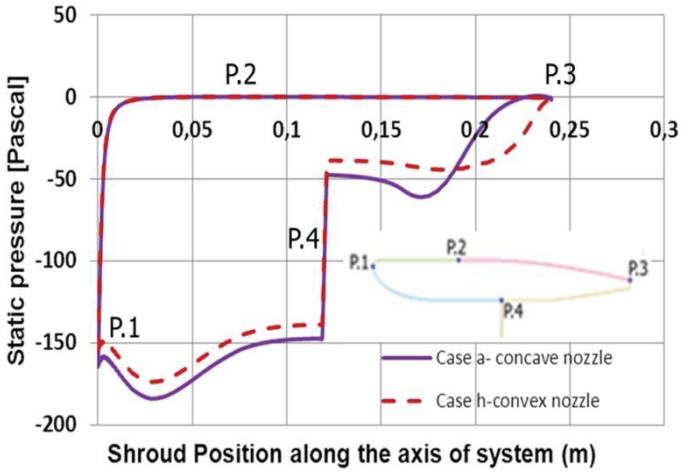

Figure 3.16: P_s on the shroud along system axis for case(a) and (h)

In conclusion, both extreme cases indicate that the curvature variation of nozzle internal shape should be smooth as much as possible, in order to avoid the higher

adverse pressure gradient and keep from an early boundary layer separation.

3.4.3 Nozzle length and divergent angle

In reality, it is not possible to change the nozzle length l_N independently. It is always related to the overall shape of the nozzle. Here in order to keep the overall shape constant, it is defined by the parameter divergent angle. It is obvious that the divergent angle θ is directly related to the nozzle length. Thus for each l_N, θ is varied from 7° to 17.5° with a step of 3.5°. Meanwhile, for each divergent angle, the nozzle length is changed from 70 mm to 90 mm with a step of 10 mm as shown in the subfigure of Fig.3.17, this variation also corresponds to the change of nozzle radius.

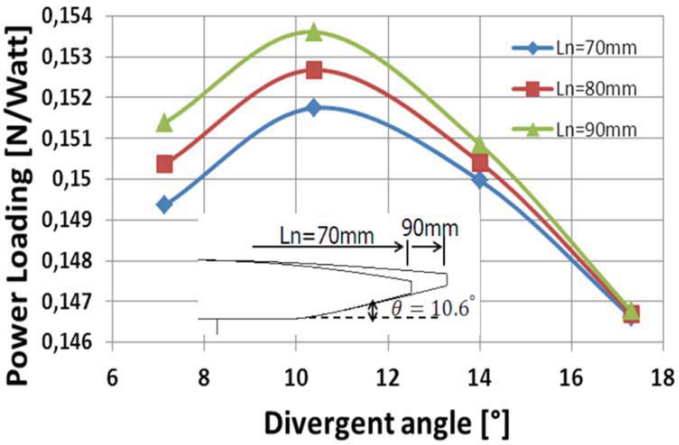

Figure 3.17: PL_i versus l_n/R_r

Fig.3.17 shows the performance PL_i of three series of nozzle lengths with varied divergent angles. For all the nozzle lengths, the power loading is increased with increased divergent angle until $\theta = 10.5°$, which is the optimal divergent angle to obtain the best PL_i performance, after that, PL_i sharply drops down. It means that at the divergent angle of 10.5°, the profile of nozzle adapts the flow structure best. However, it does not mean the nozzle could perfectly expand the mass flow, since this is more dependent on the nozzle length. Fig.3.17 indicates that the longer the nozzle is, the better the performance is. However, it is severely constrained by the greater nozzle radius along with the longer nozzle due to flow separation happened on the nozzle exit. This is also the reason why the greatest divergent angle $\theta = 17.5°$, drives the performance for all three series of nozzle lengths to the same value. For nozzles with a relatively greater divergent angle, the boundary layer flow separation has greater risk to appear. And this makes no sense to continue to increase the nozzle length because the effective nozzle radius will keep constant and the increased nozzle length will not work at all for expanding the flow after rotors and also for the improvement of the system behaviors.

3.5 Influence of Inlet Design Parameters

The inlet, is a considerably important part which enables shroud thrust to be optimized under the constant mass flow. Its configuration is constrained by the parameters such as leading edge curvature, internal shape and length.

3.5.1 Leading edge curvature and internal inlet shape

The curvature of a path at one point is a measurement of how sensitive its tangent line is to moving that specific point to its neighboring points. For the shrouded system studied in this work, the leading edge curvature C_{le} is referred to the one of point A in Fig.3.18. According to the definition of curvature and, by introducing the first and second order derivation of B-spline, Equation.3.10 was applied to calculate the leading edge curvature.

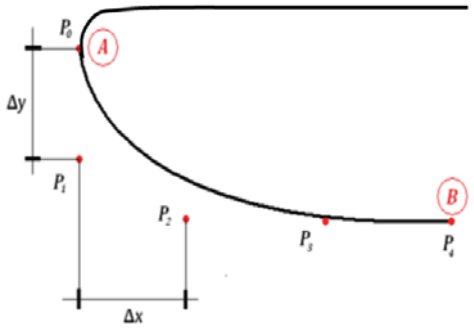

Figure 3.18: The B-spline of inlet lip

$$Curv = \frac{n-1}{n}\frac{\Delta x}{\Delta y^2} = \frac{3}{4}\frac{(x_2 - x_1)}{(y_0 - y_1)^2} \tag{3.10}$$

Obviously, C_{le} at position A is controlled by the points P_0, P_1 and P_2. In this paper C_{le} is arranged from 0.045 mm^{-1} to 0.27 mm−1, seen in the subfigure of Fig.3.19. Since the curvature is changed, the inlet internal shape might be changed along with it. In the reality, it is difficult to separate the geometry parameters which are originally related. Therefore particularly for internal shape, seven different ones with constant $C_{le} = 0.15$ mm^{-1} were explored.

In Fig.3.19, both C_{le} and inlet internal shape have a minor influence on the PL_i. Based on the same $C_{le} = 0.15$ mm^{-1}, the variation with changed internal shape seems smaller than the one from the parameter C_{le}. Based on the simulations of these cases, flow separation was not found, which should have happened somewhere on the inlet. This implies, once the inlet could be designed to adapt the flow pattern and no boundary flow separation occurred, the effects on global performance by variation of geometry parameters can be ignored. The more important effects are on the pressure distribution.

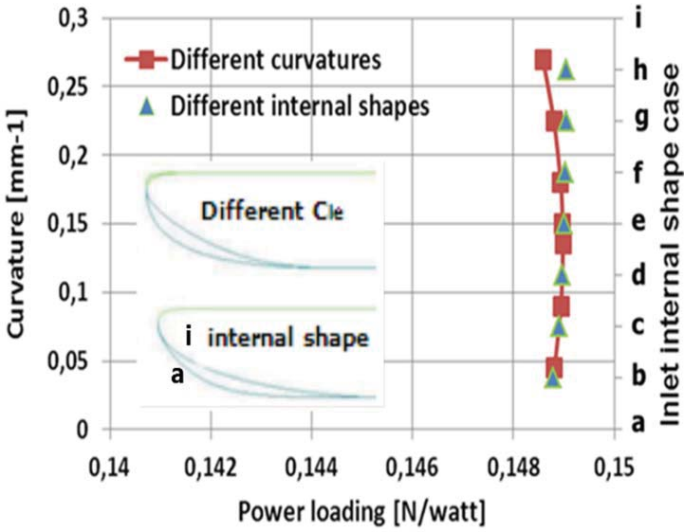

Figure 3.19: PL_i versus C_{le} and inlet internal shape cases

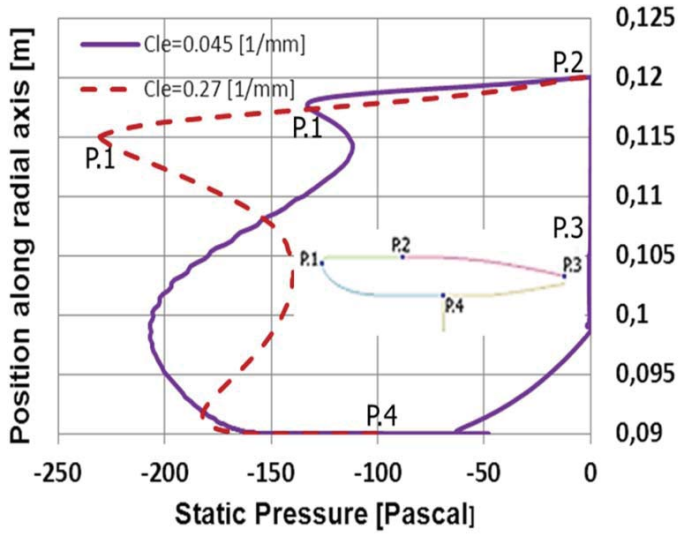

Figure 3.20: P_s on the shroud along radial axis for $C_{le} = 0.045$ and 0.27

Fig.3.20 shows a superposition of pressure distribution on shroud inlet along the radial axis for two different leading edge curvatures. For these two extreme cases of $C_{le} = 0.045$ and 0.27 mm^{-1}, they all could reach a suction peak at P.1, which is the reference position of leading edge curvature. A far lower pressure is formed at that position of $C_{le} = 0.27$ mm^{-1}. However it increases drastically until the second relative weaker suction peak appears on the place with lower curvature. For $C_{le} = 0.045$ mm^{-1}, globally the lower pressure keeps to be continued and even much lower after the first suction peak even though there is a slight recovery. It lets the shrouded system take full advantages of the curvatures along the inner inlet to

produce more thrust.

The physical phenomenon could be revealed more clearly in Fig.3.21 and 3.22. It shows that there is a continued lower pressure region formed on the inner inlet leading edge for $C_{le} = 0.045$. On the contrary, for $C_{le} = 0.27$ the suction peak is discontinued. It is separated into two regions at one position of the inlet. It reduces the effective surface to produce the positive thrust. This is the reason why the PL_i performance tends to decrease when the leading edge curvature is increased after a specific value as shown in Fig.3.19.

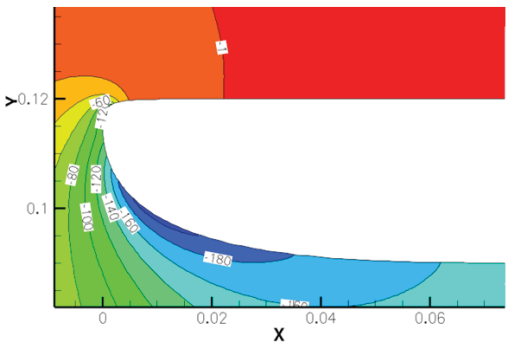

Figure 3.21: Static pressure, $C_{le} = 0.045$

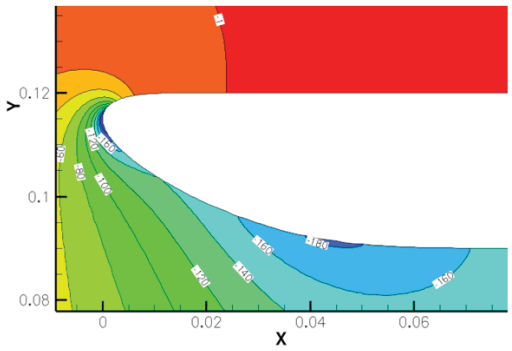

Figure 3.22: Static pressure, $C_{le} = 0.27$

As demonstrated in the exploration above, the system can benefit if the pressure gradient is changed more smoothly or continuously. This greatly depends on whether the inlet design is adapted with the flow. That is critical to reduce the adverse pressure gradient to decrease the boundary separation risk.

3.5.2 Inlet length

The inlet length l_i was varied from 100 mm to 70 mm with a step of 5 mm which corresponds to the ratio of l_i divided by the rotor radius, as seen in Fig.3.23. It shows that l_i viration slightly affects the global performance. As the study above on the inlet leading edge curvature and internal shape, comparing to the effect on the thrust, the more important is on the pressure distribution. Except the consideration on loading other instruments, it is not worth to lengthen the inlet in views of the weight and size increment as same as nozzle length.

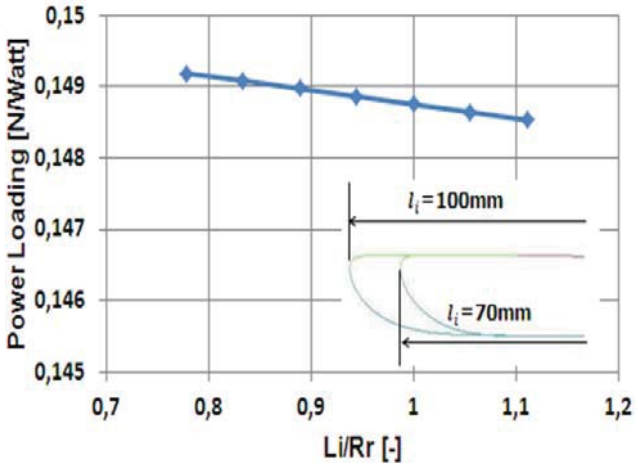

Figure 3.23: PL_i versus l_i/R_r

3.5.3 Influence of Leading Edge Radius and Shroud Maximum Radius

A combined study of two parameters: shroud maximum radius R_{max} and leading edge radius R_{le}, was made. R_{max} was changed from 110 mm to 170 mm with the main step of 5 mm which corresponds to the ratio of R_{max} divided by the rotor radius 90 mm from 1.22 to 1.89. The increment of R_{max} means an increment of shroud thickness. For each R_{max} , two or three different values of R_{le} from $R_{le} = (R_{max} - 15)$ mm to $R_{le} = (R_{max} - 5)$ mm were studied. One example of the geometry is shown in Fig.3.24.

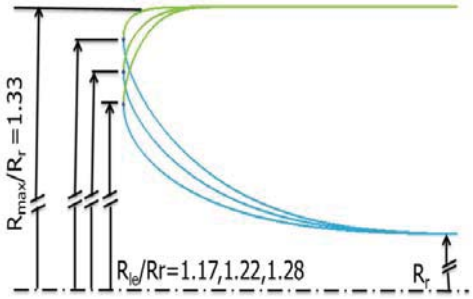

Figure 3.24: Geometry scheme for $R_{max}/R_r = 1.33$ and $R_{le}/R_r = 1.17, 1.22, 1.28$

Fig.3.25 shows the power loading performance of all systems with different leading edge radius and maximum radius. A significant improvement of the performance on PL_i could be found as the increment of both R_{max} and R_{le} until the stabilization occurs, that is $R_{max}/R_r > 1.44$ or $R_{max} > 130$ mm. Under these conditions, the overlapping points on PL_i of 0.1465 N/Watt with different values of $R_{max}/R_r = 1.22$, 1.28 and 1.33 can reveal the less importance of the parameter R_{max} on PL_i before the stabilization appearance. Compared to it, the parameter

R_{le} plays a critical role on improving the system behavior. PL_i is increased along with the increment of leading edge radius. The value of this radius around $1.3R_r$ provides the greatest improvement on the system performance.

Figures.3.26-3.28 reveal that the variation of R_{le}/R_r from 1.17 to 1.28 makes a backward movement of the suction peak formed on the inlet. This reduces the effective suction region to a certain extent. However, a greater leading edge radius gives more possibility to widen the lower pressure surface. Balancing these two factors, the latter plays a more important role in the improvement of the shroud thrust. Therefore for different leading edge radii 1.17, 1.22 and 1.28 times the rotor radius, under almost the same mass flow around 0.449 kg/s which is decided by the nozzle as analysis above, the relative largest leading edge radius $R_{le}/R_r = 1.28$ can produce the greatest thrust 2.812 N. This increased thrust from the inlet contributes

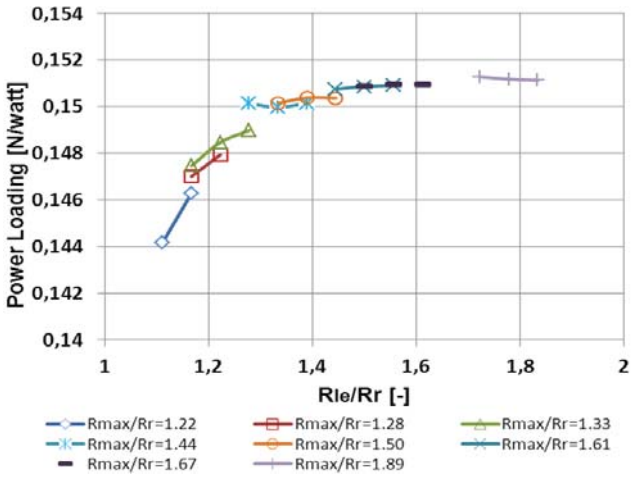

Figure 3.25: PL_i versus R_{le}/R_r for different R_{max}

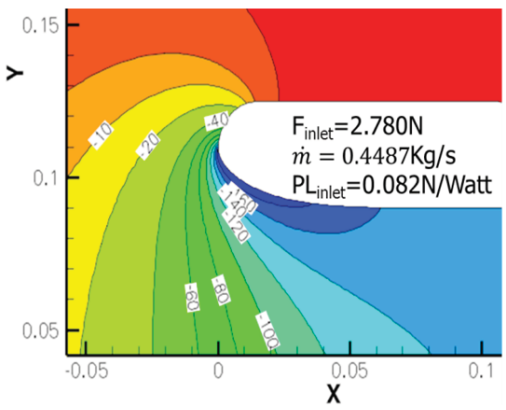

Figure 3.26: Static pressure, $\frac{R_{le}}{R_r} = 1.17$

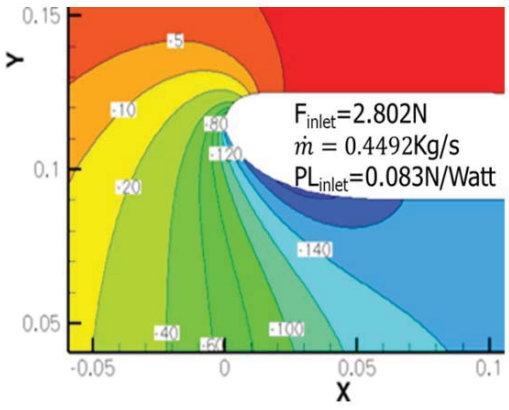

Figure 3.27: Static pressure, $\frac{R_{le}}{R_r} = 1.22$

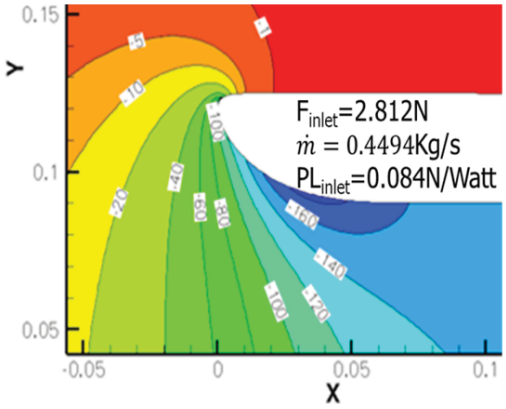

Figure 3.28: Static pressure, $\frac{R_{le}}{R_r} = 1.28$

mostly on the power loading improvement of the whole system such as PL_i of 0.084 N/Watt produced by the inlet with $R_{le}/R_r = 1.28$.

However, this effect becomes less evident when $R_{max}/R_r > 1.5$ in Fig.3.25. The performance PL_i is kept almost constant when both R_{le} and R_{max} are varied. Considering the additional size and weight along with increased R_{max}, the benefit of PL_i performance from it should be balanced with these disadvantages.

3.6 Conclusions

3.6.1 Conclusion for 2D parametrical study

Based on the definitions of the shroud geometry parameters, the work above revealed the effect of each parameter on the system performance, and explored which of the different considered parameters would be relevant for the optimization of the power loading. The main conclusions could be obtained as following:

For the nozzle, the power loading is improved greatly with a greater nozzle radius. However it is limited by the appearance of boundary layer separation, this actually decreases the effective nozzle radius and produces a pressure loss. The internal shape might be an important factor, but in reality its effect is drastically reduced due to viscosity. Lengthening the nozzle can improve the system, but it is constrained by the nozzle divergent angle. The optimal designed divergent angle for different nozzle length is kept to be around 10.5°;

For the inlet, once the inlet is designed to adapt to the flow structure, the improvement by changing any inlet parameters is limited. The shroud maximum radius and leading edge radius are relevant. The variation of maximum radius must change the leading edge radius to some degree due to geometry integration. The increment of both parameters means an increment of inlet internal surface. This could widen the low pressure region and finally improve the system on the thrust

performance. But it is limited by the greater maximum radius. The ideal design regimes for leading edge radius and maximum radius are around $1.3R_r$ and $1.44R_r$;

The other parameters have a low influence which will not make a difference on the power loading greater than 1%. However, they play an important role in pressure distribution along the shroud. The basic design criterion is to reduce the risk of boundary layer separation both on the inlet and nozzle.

3.6.2 Shroud proposition

According to the conclusion above, obtained from the shroud parametrical study, taking into account that the design should permit the pressure gradient on the air entrance and nozzle to vary smoothly, an optimally designed shroud was proposed. The detail on the geometry parameters and the shroud profile could be seen in Tab.3.1 and Fig.3.29. This new shroud will be fabricated, tested and simulated through experimental and numerical ways by introducing the coaxial rotor configuration, in order to further determine the system performance and flow development during the system passage.

Table 3.1: Parameters of new shroud

Component	Parameter	Value
Air entrance	Entrance length:	80 mm
	Leading edge radius:	120 mm
	Leading edge curvature:	0.15
Cylindric section	Cylindric length:	40 mm
	Maximum radius:	125 mm
	Rotor radius:	90 mm
Nozzle	Nozzle length:	80 mm
	Nozzle radius:	98 mm
	Nozzle Initial angle:	10.2°

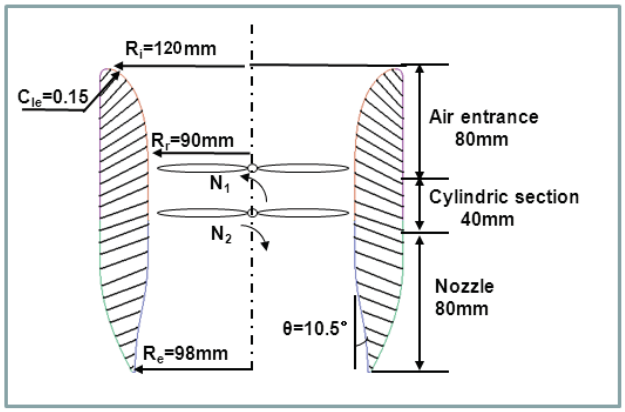

Figure 3.29: New shroud model with optimal design

Part II

Experimental Study on Long Shrouded Contra-rotating Rotor with New Shroud Model

Plan of Part

Chapter 4

Experimental Introduction

As a continuation of an ongoing investigation of the shroud design variables' effects through theory analysis and 2D simulations in the first part, by introducing the actual coaxial rotor, the experimental work aims to deeply underly the system principles including the overall behavior and flow physics based on the optimally designed shroud. Furthermore, the optimization of coaxial rotor configuration referring to the combination of the shroud is expected to be explored.

In this chapter, new experimental facilities were designed and fabricated by the ISAE (Institut Supérieur de l'Aéronautique et de l'Espace)-Aerodynamics, Energy and Propulsion Department in Toulouse, France. Based on the experimental settings with multiple testing possibilities, in order to explore in detail the characteristics of the shrouded contrarotating coaxial rotor, a suitable test program was made. Different tests on the global performances as thrust, the pressure field and the mass flow should be validated before starting the experimental exploration.

4.1 Test Facilities

Considering the stability, precision and flexibility, the test bench is specially oriented to understand the flow physics and the interaction between different components of the shrouded contra-rotating rotor as much as possible. Obviously the corresponding characteristic quantities determined by the test bench are not only constrained to the global performances as thrust, torque, rotational speed etc., but also the variables which characterize the flow along shroud locations as the pressure, velocity or the mass flow rate.

4.1.1 Test bench and measuring equipment

Fig.4.1 gives a good overview of the static test bench layout. The main framework consists of a rectangular metal frame. At least 10 times the rotor diameter in the upstream and downstream frame should have no obstruction. The propulsion model components including the shroud and double rotor are hanged by three mechanical swing-arms which are connected to three mechanical parallelogram constructions respectively at the top, upon which a rig had been constructed for these three constructions' installations. They are held in place using allan bolts through a channel which run along the length of the test bench. As a result, the position of each swingarm along the length of the test bench could be varied individually. This allows the absolute distance D_{abs} from shroud inlet to the first rotor and the

relative distance D_{rel} between two rotors, also called inter-rotor distance (IRD), to be adjusted. All the possible rotor locations inside the shroud will be tested to optimally design the shroud parameters.

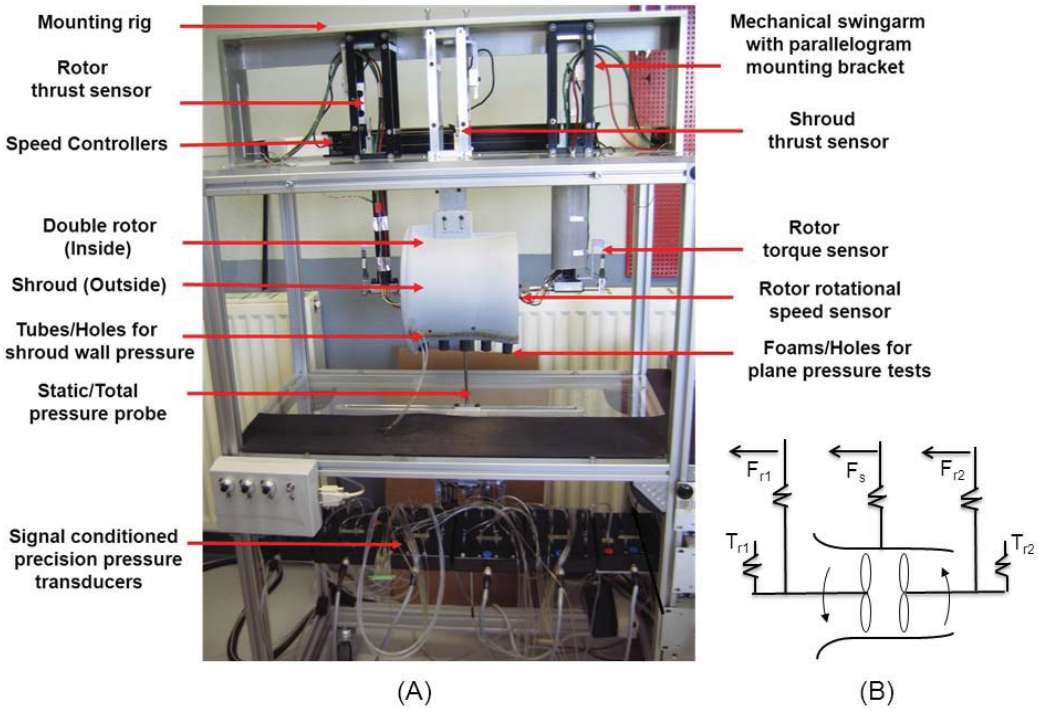

Figure 4.1: Test bench configuration (A) and simplified working scheme (B)

As for three swingrams to mount rotors and shroud, they are designed using four axles that could make a tiny movement under loading. The thrust sensor is installed within each parallelogram which, when displaced, is pressed against a metal mount attached to the fixed test bench frame. As a result, the sensor is able to measure the thrust produced by each rotor and shroud. The constructions for each sensor can be seen in App.C.1. Specifically for both rotors, additional axles are installed at the bottom of each swingarm. Aluminium mounting brackets seen in Fig4.2 are connected to each axle. These are used to attach the AXI 2208/20 Gold Line brushless motors with a maximum achievable efficiency of 82% to the mechanical swingarm, seen in App.C.2. There, a circular disk with a rectangular hole cut into its circumference is installed to the axle of each motor. This is used to measure the rotational velocity of each propeller. Due to identical alignment of the axles along the same axis, both propellers are in perfect alignment therefore permitting the analysis of coaxial propeller systems. A torque sensor is attached to the axle via a aluminium arm, which could be fixed to the movement of the axle via a grub screw. As the propeller rotates it exerts a torque on the mounting bracket which in turn forces the sensor against the swingarm.

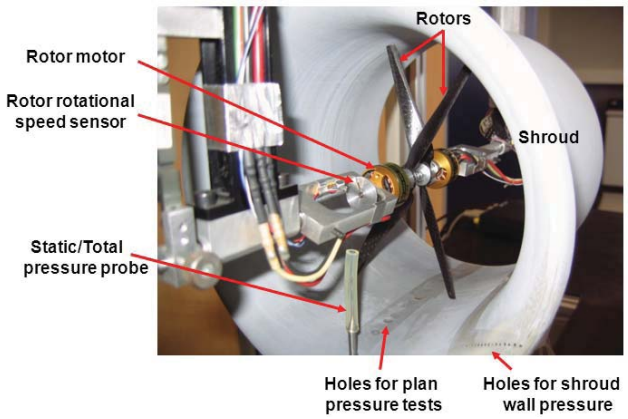

Figure 4.2: Configuration of shrouded contra-rotating propulsion system

The propulsion thrust is expected to support approximate 500 gram. Thus to measure the thrust, Phimesure load cells with a maximum capacity of 2 daN are selected. Using a Meiri load cell from the F1200 series, the maximum torque will be limited to 0.2 N.m. These 5 sensors are connected to a signal condition unit (Strain Gauge Transducer 690 22 3310) fabricated by Sensorex France. To measure the rotational velocity, an optic sensing technique is used on the disk in conjunction with an EE-SX 671 photoelectric sensor seen in Fig.4.2. Since the motor is run with an electromagnet generated by a speed controller, the rotational speed is detected by the measurement of the slight groove passing in a measuring wheel. So based on this test bench, the thrust of rotors/shroud and torque/rotational speed of rotors can be measured separately in order to quantify each component of the system.

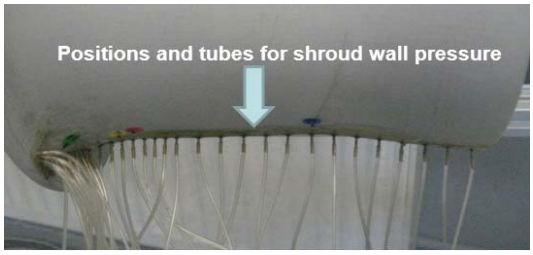

Figure 4.3: Instrumented positions on the shroud

The main missions of the test bench are not only the measurements of the global performance variables, but also the characteristics of the flow pressure/velocity field based on the shroud effect. Hence signal conditioned precision pressure transducers 110L/430L with a range of ± 1000 Pa is used for testing the pressure distribution of the shroud inner surface. They are connected via the tubes to 36 positions distributed on the shroud along the axis seen in Fig.4.3. The distribution of tested positions are different for different shroud parts. It is ten times more intensive at the air entrance than other shroud parts. It should be noted that the final position is not at the end of the nozzle because of the fabrication difficulty.

Figure 4.4: Different types of probes

In addition, to explore the characteristic of flow developed in the shrouded system, the measurements of static and total pressure in the flow on the axial stations are necessary. Three-hole total pressure probe with the cylindrical head, is frequently used for two-dimensional flow measurements in rotary machinery components. It yields the total pressure and the direction of the flow field. For the static pressure probe, it has goose head geometry. Both total and static pressure probe were fabricated seen in Fig.4.4. They are connected to pressure transducers which have a range of ±200 Pa. Both of them measure the pressure in two dimensions with the position adjusted along the radial direction seen in Fig.4.2. The flow direction must be measured first by the total pressure probe rotation and found when the pressure difference between the side holes is extremely small. This angle guides the measurements of the static pressure. For the pressure tests with these two probes, because the blade passing makes the pressure to be unsteady, measurements are difficult to stabilize when probes are closer to the blade. Therefore considering the probe accuracy and security, the distance from the rotor should be kept at 20 mm at least. Several specific axial stations positions could be seen in Fig.4.5. The detail on the pressure tested positions on and along system can be seen in App.C.3.

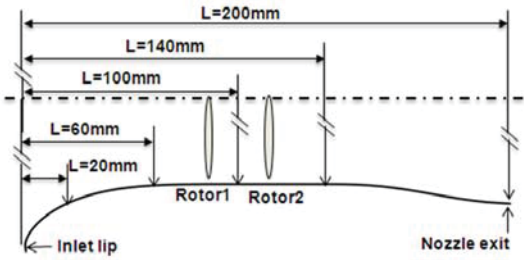

Figure 4.5: Positions of tested axial planes

For each variable during the tests, 100 samples of data are measured at a frequency of 1 KHz and then averaged. Output signals are transferred to the PC through an analog numerical card (CAN) inserted in it. The data is organized by a

Labview program as different parameters in the output file for further postprocessing.

4.1.2 Model: shrouded contra-rotating rotor

The model shown in Fig.4.1 and Fig.4.2 is mounted parallel to the ground to avoid ground effects on its performance. It consists of a 180 mm main inner diameter shroud, and contrarotative 2-bladed rotors installed in the same axis as the shroud. Based on the 2D axisymmetrical simulation in shroud design, the shroud is usually made up of three parts: the inlet, middle section and nozzle, seen in the Fig.3.29 of Chap.3.6.2. In the hovering case, the rotating rotor with the shroud aspirates and absorbs the air from all around the propulsion air entrance. The incoming air forms a low static pressure region on the inlet lip, that is the main reason why the shroud itself generates thrust. For the nozzle, its function is to expand the slipstream after the rotor until the flow reaches ambient pressure. This could decrease the final wake velocity and increase the mass flow through the rotor. Therefore, one optimally designed shroud is chosen and characterized by two area ratios, which are inlet and outlet area to cylindric middle section area ratios, $K_i = A_i/A_r = 1.63$ and $K_e = A_e/A_r = 1.2$. The cylindric section surface radius R_r for the area A_r, is referenced the same as the actuator disk, $R_r = 90$ mm. The length of each shroud part is 80 mm, 40 mm and 80 mm respectively. It is made out of a true industrial thermoplastic ABS and is fabricated as a whole. The detail of shroud model can be seen in App.C.3.

Figure 4.6: Profile of double rotor

Compared to the conventional helicopter rotor with the same scale, which typically has uniform chord and controls attitude and flight direction through collective and cyclic pitch control [71], the concept of contra-rotating in-line rotor has the advantages of compactness and high thrust. However, because of the small size and the effect of the shroud, conventional controls are not feasible. Rotor blades with twisted and non uniform chord are then particularly attractive for propulsion optimization. Thus, a pair of contra-rotating rotor special for shrouded systems has been designed using XROTOR code, which was developed by Mark Drela, Harold Youngren et al [73], seen in Fig.4.6. This program was based on classical vortex/blade-element methods of Betz [74] and Glauert [75], and a general 3-D vortex-lattice or panel

method. In order to introduce the effect of the shroud, the circulation at the blade tip is not equal to zero. Through a similar inflow velocity input, after several iterations, the upper and rear rotors'profiles were designed. The rotor blades are made out of carbon (Tissue G803/914) with a multi-layer composition: 0-90°, ±45°, 0-90°. The thickness is 0.4 mm. The blade parameters are summarized in Table.4.1. The blades of both rotors are not exactly same because of the small differences in their pitch angle designs and construction inaccuracies.

Table 4.1: Parameters of rotor

	Upper Rotor	**Lower Rotor**
Parameter	**Value**	**Value**
Root radius	9.6 mm	9.6 mm
Tip radius	88.9 mm	88.9 mm
Root chord	13.2 mm	13.2 mm
Tip chord	6.4 mm	6.4 mm
β_{root}	42.2°	41.3°
β_{tip}	18.6°	18.1°

4.1.3 Calibration and uncertainty of measurement

For the test bench, the uncertainties would be caused by different factors: non linearity, repeatability and hysteresis from the measuring equipments, fabrication precision, experiment operation, reading and so on. Therefore the test bench was initially calibrated by changing the values of gain and zero on the electronic capture hardware which linked each sensor and probe, via a National Instruments acquisition card to PC. Readings were processed using Labview software. While this improved the accuracy of the measurements, some error remained due to the sensors non-linear response in particular for the thrust and torque sensors. In order to correct the equipments, zero calibration was further improved by hanging weights of a known mass from each swingarm. For instance, torque forces were replicated by hanging weights from a torque arm at a distance of 10 cm from the central axis. Recorded forces were then multiplied by ten in order to have results in the format of Newton per centimeter (N.cm). Thrust was replicated by hanging weights via and string using a mounting brackets which simulated thrust forces. Thrust was measured in Newton (N). The detail on this calibration has been included in Fig.4.7. Calibration curves seen in App.C.4 were then constructed using Matlab programs and fourth order polynomial equations were calculated and applied to all experimental results. These calibration procedures were carried out several times during the experiments.

Zero calibration on the shroud wall pressure measures should be done every time before the tests, which is automatically modified by the Labview program. For the quantities of total pressure and static pressure on axial stations, as talked above, the nulling technique is applied as the most accurate method, even though it requires a very sophisticated traversing system and long data acquisition time. And it is the

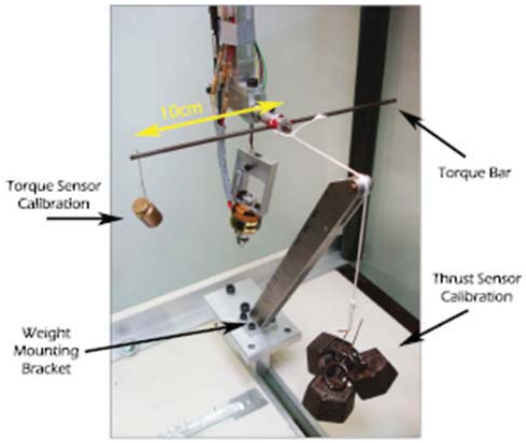

Figure 4.7: Calibration of torque

most simple in terms of data analysis as well.

The probe is mounted on a three degree of freedom traversing system and is oriented so that the center hole axis is parallel to the flow. The center pressure tap measures the stagnation pressure which is rightly the total pressure, and the pressures in the two outer tubes are equal ($P_1{}' = P_2{}'$) and proportional to the static pressure, seen in Fig.4.8. Finally, the probe position and flow direction α is noted taking the shroud axis as a reference line.

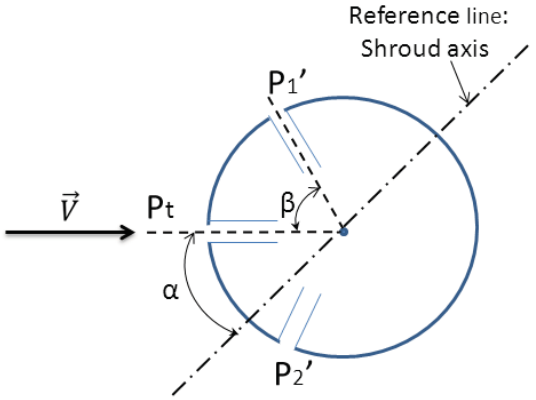

Figure 4.8: Scheme of total pressure probe

From Fig.4.8, the pressure on the two outer holes could be obtained:

$$\begin{aligned} P_1{}' &= P_{sta} + \frac{1}{2} \cdot \rho \cdot V^2 \cos^2(\alpha - \beta) \\ P_2{}' &= P_{sta} + \frac{1}{2} \cdot \rho \cdot V^2 \cos^2(\alpha + \beta) \end{aligned} \tag{4.1}$$

Therefore:

$$\Delta P' = P_2{}' - P_1{}' = \frac{1}{2} \cdot \rho \cdot V^2 (\cos^2(\alpha + \beta) - \cos^2(\alpha - \beta)) \tag{4.2}$$

The air density is calculated by the relationship: $\rho = nRT/V\text{kg.m}^{-3}$. Here, $\beta = 40°$. Thus for the rotational speed $N_1 = N_2 = 6000$ rpm, the velocity of main flow was supposed to be around 10 m/s from the following tests, the comparison between theoretical results and experiments on the relationship of $\Delta P'$ and flow direction can be obtained, seen in Fig.4.9. Even though for the experiment the pressure difference greatly fluctuates, the main trend of $\Delta P'$ as the function of α is quite similar and close to the one from theoretical analysis. Since the experiment data definitely is averaged and the difference surely exists between the reality and theory, this similar trend validates in some sense the test on total pressure.

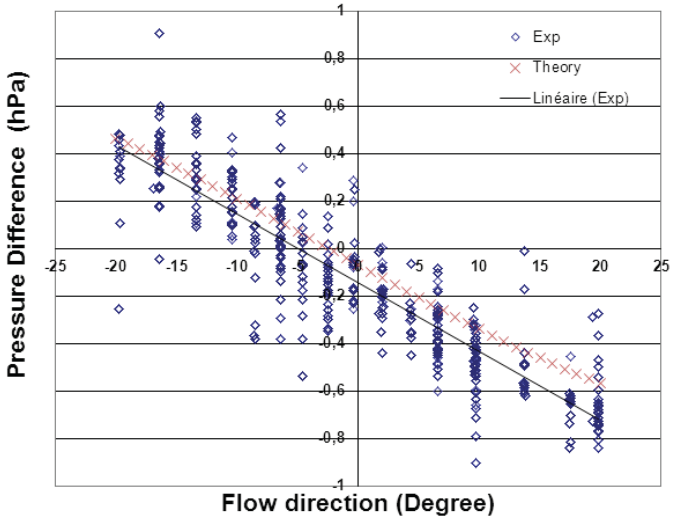

Figure 4.9: Pressure difference of the two outer holes from test and theory

The measurements on total pressure direct the static pressure tests through provided the flow direction. As the fluctuation of the value seen in Fig.4.9, both static and total pressure measurements should be done in a number of repetitive times as 100 samples under each case in order to get the averaged value and reduce the uncertainty.

Table 4.2: Accuracy of measurements

Parameter	**Mechanical Accuracy**	**Calibration /Reading error**	**Total Accuracy**
Thrust(N)	± 0.05	$\pm(0.6\%)$	$\pm(0.05 + 0.6\%T)$
Torque(N.cm)	± 0.02	$\pm(0.7\%)$	$\pm(0.02 + 0.7\%Q)$
Rotational velocity(rpm)	± 50	± 14	$\pm(30 + 14)$
Wall static pressure(Pa)	± 1	± 5	$\pm(1 + 5)$
Plan static pressure(Pa)	± 1	± 3	$\pm(1 + 3)$
Plan total pressure(Pa)	± 1	± 3	$\pm(1 + 3)$

The precision and resolution of sensors was finally evaluated by their character-

istics and by the acquisition system provided by manutacturers. For the mechanical accuracy, it was defined as the least amount of load, rotational speed or pressure which the respective sensor can measure. This was found by experimental means. Standard deviation of sampling data was used to determine the uncertainty of measurement according to the method of Kline and McClintock [72], seen in Table.C.4.

4.2 Working Principal and Designed Variables

The objective of this work is to improve the optimal designed shroud, in the first place. Then based on the best performed system, it targets to evaluate the global performance and flow characteristics developed in the propulsion system through the experimental ways. Furthermore, in order to optimize system behavior, it aims to resolve the problems caused by the combination of shroud and contra-rotating rotor such as the arrangements of two rotational speeds and rotor locations, amongst others.

4.2.1 Working principal

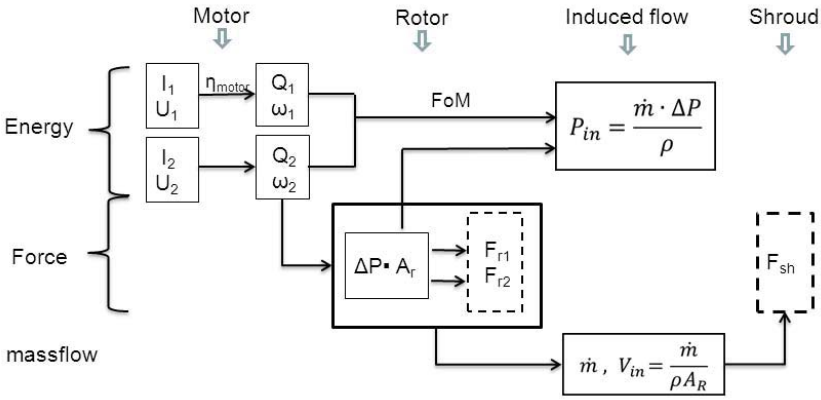

Figure 4.10: System working principal and relation among the variables

Based on the explanation of the actuator disk model for the flow field of the shrouded contra-rotating rotor and how it is affected by the shroud, the preliminary understanding of the shrouded system is obtained. Corresponding to the real mechanical shrouded contra-rotating propulsion system, the shroud thrust could be considered as a consequence of the flow momentum due to the energy output mechanically given by the system, seen in Fig.4.10. It clearly shows the energy transformation between different sub-systems like motor, rotor or shroud and the relationships between different variables under them. The input electric energy is transformed into mechanical shaft energy by the motor with an efficiency η_{motor}. This dual rotor is driven to rotate at rotational speeds N_1 and N_2, and introduces the air flow coming into the system. Except the rotor can therefore contribute to the propulsive function

in terms of thrust (F_{r_1} and F_{r_2}) due to the pressure jump ΔP formed upstream and downstream from rotors, the different pressure distribution outside and inside the shroud surface could produce that additional shroud thrust F_{sh}, as analyzed above. Meanwhile, the presence of the shroud can modify the rotor performance through the reduction of tip vortex loss, mass flow and so on.

4.2.2 Designed variables

In order to assess the shrouded contra-rotating double rotor system (SDR), different combinations of D_{abs} and D_{rel} were tested and one of the relative better performed combinations was chosen for following system explorations. For two rotor locations, there exist plenty of possibilities even though it is limited by the length of the test bench rig on the top. D_{abs} was chosen to be from 28% to 61% of the rotor disk diameter which corresponds the range from 50 mm to 110 mm with a step of 10 mm. D_{rel} was decided to be from 11% to 44% by the step of 11%. To specify the improvement of the optimally designed shroud, one or several rotor locations were used to compare the previous shroud models and another three kinds of propulsion systems as free single rotor (FSR), free double rotor (FDR) and shrouded single rotor (SSR). All these comparisons were made in a certain regime of rotational speed and rotor locations.

Table 4.3: *Ranges of design variables*

Design Var.	System	Value regime
$\overline{D}_{abs} = \frac{D_{abs}}{D_R} \& D_{abs}(\text{mm})$	SDR	$[28\% : 5.5\% : 61\%] \& [50 : 10 : 110]$
	SSR	$[28\% : 5.5\% : 66.5\%] \& [50 : 10 : 120]$
$\overline{D}_{rel} = \frac{D_{rel}}{D_R} \& D_{rel}(\text{mm})$	SDR	$[11\% : 11\% : 44\%] \& [20 : 20 : 80]$
	FDR	$[17\% : 5.5\% : 50\%] \& [30 : 10 : 90]$
$N_1 = N_2(\text{rpm})$	SDR	$[4000 : 500 : 9000]$
	FSR, FDR,SSR	$[3000 : 500 : 9000]$
$N_1 \neq N_2(\text{rpm})$	SDR	$(6000, 9000), (9000, 6000)$

Based on the best combination of D_{abs} and D_{rel}, for the evaluation of the SDR system itself, firstly on the system analysis, the measurements were conducted with the two rotors operating at the same rotational speed in the regime from 4000 rpm to 9000 rpm with a step of 500 rpm. Secondly, to explore the specific effect of rotor positions upon the flow field, according to the SDR location comparisons, two combinations of rotor positions were finally selected, $D_{abs} = 80$ mm and $D_{rel} = 20$ or 40 mm. To explore the effect of switching two rotors' different rotational speeds, for the system with two different rotational speeds, the slower one should be kept above

6000 rpm in order to make both rotors propulsive, the switched rotational speeds were selected to be 6000 rpm and 9000 rpm. Table.4.3 presents all the variables designed for the experiments.

For the evaluation on the performance of different configurations, as discussed in Part.I, two performance parameters Power Loading (PL) and Figure of Merit (FoM) are used. PL has the same definition as applied in the theory and 2D simulation. However, it is calculated with the mechanical power but induced one, since the experiments involves the actual rotor configuration. FoM defined in this work determines the system capability to convert the available mechanical power into thrust and qualifying the rotor ability to convert available mechanical power into induced power. According to the definitions and the feasibility to test the necessary variables by experiments, their calculations are given in Eq.4.3 and Eq.4.4 respectively:

$$PL = \frac{F_T}{W_{t_{\text{mech}}}} = \frac{F_{sh} + \sum_i F_{r_i}}{\sum_i |Q_{r_i}\,\omega_{r_i}|} \tag{4.3}$$

$$FoM = \frac{\dot{m}[(\frac{1}{2}V_e^2 - \frac{1}{2}V_\infty^2) + (\frac{P_e - P_{atm}}{\rho})]}{W_{t_{\text{mech}}}} \tag{4.4}$$

For the adapted nozzle, seen in Fig.2.1, the exit pressure (P_e) is equal to the ambient one (P_{atm}). Then, based on Bernoulli theorem, Eq.4.4 becomes:

$$FoM = \frac{\dot{m}[(\frac{1}{2}V_e^2 - \frac{1}{2}V_\infty^2)]}{W_{t_{\text{mech}}}} = \frac{\dot{m}\,[\frac{(P_2 - P_1)}{\rho}]}{W_{t_{\text{mech}}}} \tag{4.5}$$

The thrust generated by the rotors is due to the pressure jump $\triangle P = P_2 - P_1$ which appears on the two sides of the double rotor with its rotation. It could be calculated as $F_r = \triangle P \cdot A_R$, where A_R is the disk surface area of the rotor diameter. Combined the application of the mass flow rate expression $\dot{m} = \rho\, A_R\, V_{in}$, where V_{in} is the induced velocity from momentum theory, Eq.4.5 could be simplified in two ways.

$$FoM = \frac{\dot{m}\, F_R}{\rho\, A_R\, W_{t_{\text{mech}}}} \qquad \text{or} \qquad \frac{F_R\, V_{in}}{W_{t_{\text{mech}}}} \tag{4.6}$$

Here, according to Bernoulli theorem, V_{in} was calculated at different circumferences on each axial station through the measurements of the static pressure P_s and total pressure P_t, seen in Eq.4.7. The mass flow can be then obtained through integration of the air passing on each circumferential ring area, by inserting V_{in} in Eq.4.8.

$$V_{in} = \sqrt{\frac{2\,(P_t - P_{sta})}{\rho}} \tag{4.7}$$

$$\dot{m} = \sum_{j=1}^{n} \pi \left(r_{j+1} - r_j\right)^2 \rho \, V_{in_j} \tag{4.8}$$

All the calculation of the performance above are derived from the measurements on the basic quantities of two rotors and the shroud: the thrust, the torque, the rotational speed, and the flow field including the pressure, mass flow tests as presented in Fig.4.10. However some quantities like thrust, torque, power and the pressure tested might be varied with the external perturbations and weather condition which would change the environment pressure and temperature, all of them were thus corrected to a standard condition $T_s = 288.15$ K and $P_{stan} = 101325$ Pa.

$$N_s = \frac{N}{\sqrt{\frac{T}{T_s}}} \qquad F_s = \frac{F}{\frac{P_{atm}}{P_{stan}}} \qquad Q_s = \frac{Q}{\frac{P_{atm}}{p_{stan}}} \qquad P_s = \frac{Q}{\frac{P_{atm}}{p_{stan}}} \tag{4.9}$$

In order to generalize those quality indicators, these two main performances should be proposed in terms of reduced parameters. As it is common in engineering, two non-dimensional parameters are defined to facilitate the analysis of the problems. These are thrust coefficient, C_T, and power coefficient, C_P. For rotor analysis they are given with the following equations:

$$\begin{aligned} C_T &= \frac{T}{\rho \, A_R \, \omega^2 \, R_r^2} \\ C_P &= \frac{P}{\rho \, A_R \, \omega^3 \, R_r^3} \end{aligned} \tag{4.10}$$

However, for system with two different rotational speeds, the equations above on the calculations for C_T and C_P can not be so easily adapted. Therefore in this work, since the components of system model are not changed, the comparisons on the system with different rotational speed combinations will be made dimensionally. The detail for the performance calculation can be found in App.C.5.

4.3 Comparisons on Tested Quantities

4.3.1 Free rotor

Before studying shrouded rotors system, free rotor tests were first performed and evaluated. Then the same rotor has been used for all experiments. Each rotor was tested separately in order to identify their own characteristics. The performance of the rotor was obtained at a rotational speed between 2200 and 10100 rpm. In terms of power loading performance, Fig.4.11 shows a minor difference. The second rotor power loading is slightly higher than that of the first rotor because there is sleeve outside the second rotor's mounting bracket which can be seen in Fig.4.1. The sleeve has the same shape of an airfoil, it can decrease drag and skin friction of air flow and therefore slightly improve the performance.

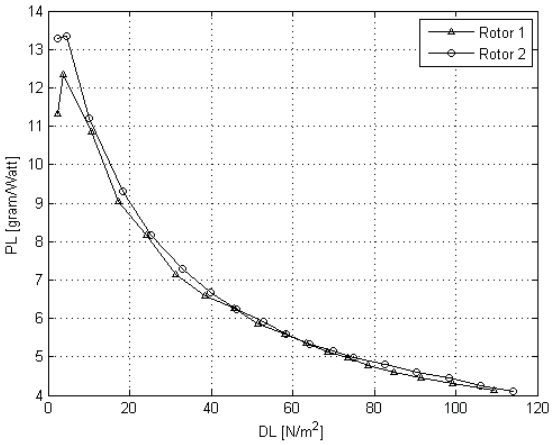

Figure 4.11: Power Loading vs Disk Loading for FSR

4.3.2 Pressure test

As introduced in Sec.4.1.1, for the test on shroud wall pressure it uses the signal conditioned precision pressure transducer via the tubes to 36 positions distributed on the shroud. Meanwhile for the total and static pressure test on each axial station inside the shroud, it uses the two types of probes with cylindric and goose head geometry respectively. According to the angle tested by the total pressure probe, the pressure value got by the static pressure probes at their corresponding positions on shroud wall, should be the same as the ones tested by the signal conditioned precision pressure transducers on their positions.

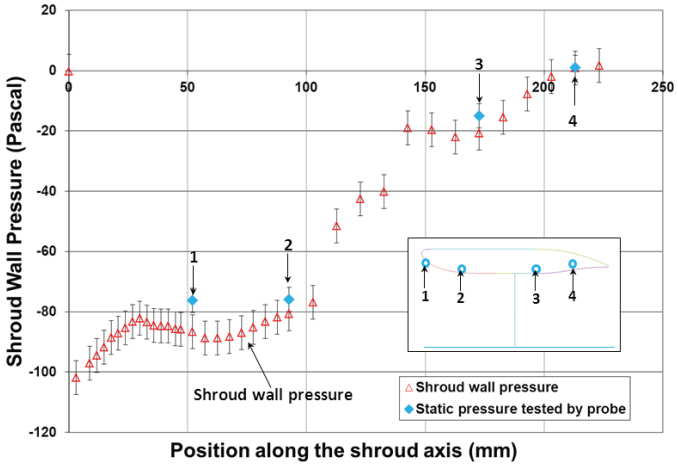

Figure 4.12: Shroud wall presssure tested by the transducers and probe

Fig.4.12 shows the shroud wall pressure tested by those two measuring equipments for SDR with rotor locations D_{abs} = 80 mm and D_{rel} = 20 mm at the rotational speed $N_1 = N_2$ = 6000 rpm. Pressure transducers tested 36 positions

along the shroud inner profile length, and static pressure probe tested 4 positions which could be seen in the subfigure. Comparing the results, it can be seen that both have good agreement on the shroud nozzle. There are differences on the shroud air entrance part. This can be explained by the great inlet profile curvature, where the air can be accelerated most. When the static probe is installed extremely close to the wall, it can easily modify the local flow. However, due to relative thin boundary layer comparing to the system scale, such influence becomes less significant when the probes' testing positions move to the system axis and ends in a short distance near the shroud wall. This does not affect the analysis of the global development of the flow along the shroud passages.

4.3.3 Mass flow

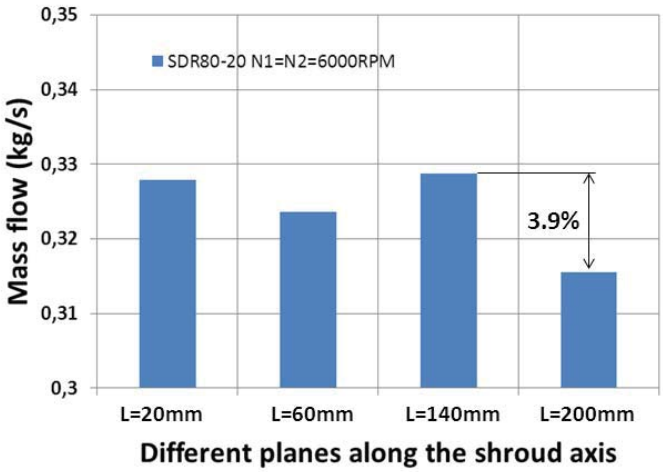

Figure 4.13: Mass flow comparison between different axial stations

Under a certain condition like the one discussed above, through the total and static pressure tested on four axial planes which are 20 mm, 60 mm, 140 mm from the inlet and the nozzle exit, the mass flow passing through the shroud and rotor passages could be calculated according to Eq.4.8. Since the study is on a similar pipeline flow, according to the mass conservation laws, the mass flow passing on each plane should be always kept the same. Fig.4.13 shows the mass flow calculated based on the measurements of pressure field on each axial station. There is a difference on the value of the mass flow among different stations. However, the greatest difference which exists between the plane $L = 140$ mm and $L = 200$ mm is limited to 3.9%. Considering that at the nozzle's exit there is a possibility for the mass flow in the mixing boundary between the shroud ejected flow and the environment one, escape easily, such difference is acceptable. The mass flow and flow field made by two probes can conduct the analysis on such shrouded system.

4.4 Conclusions

This chapter introduced the test facilities, the experimental programs and its validation. Based on this developed test bench, the measurements can be made on both global variables such as the thrust, and the flow field including the shroud wall pressure by pressure transducers and the pressure at axial stations by total and static pressure probes. Two main performances, power loading in which mechanical power was applied and figure of merit, were applied to evaluate the whole system and the two rotors under different conditions. According to the evaluation on the measurements made by the test bench, the following can be validated:

The hover platform that could independently measure the thrust, torque, rotational speed, power and pressure field for different configurations, free single rotor (FSR), free double rotor (FDR) and shrouded single rotor (SSR), the shrouded double rotor (SDR) was well developed with multiple testing parameters such as rotor locations. The evaluations on the system global variables, shroud wall pressure tested by different instruments and mass flow tested on different locations proved the test bench could work effectively.

Chapter 5

Characteristic Assessment of Shrouded System

The experiments on overall performance and flow field in this chapter aim to: prove the improvements of the shrouded contra-rotating system with optimal designed shroud model through comparisons; explore the system global behaviors based on the propositions of new diagrams; the most importantly, analyse the shroud benefits through the comparison on both global performance and flow field developed along the shroud axis. According to all these explorations, the shrouded system with the new shroud model can finally be assessed.

5.1 System Comparisons

5.1.1 Comparison among different rotor locations

According to the shape of shroud inlet and nozzle, the changes of rotor locations can result in the variation of the leakage between blade tip and shroud which might lead to a decreased performance. To decrease this effect, the rotor locations should be limited to a specific range. Thrust, power and torque measurements are therefore conducted with combinations of $\overline{D}_{abs}$ and $\overline{D}_{rel}$ which vary from 28% to 61% and 11% to 44% of the rotor diameter respectively, as shown in Table.4.3. In order to eliminate the structure vibration due to the interaction between rotors, the rotational speed is explored from 4000 rpm for all the experiments. Both rotors rotational regimes vary from 4000 to 9000 rpm with a step of 500 rpm.

The traditional graph Fig.5.1 presents the comparison of results among the shrouded systems with different arrangements of the two rotor locations. From Fig.5.1, where the same rotational speeds are input to the two rotors, it reveals that even if D_{abs} is moved from 50 mm to 110 mm far away from the shroud inlet, and D_{rel} is changed from the minimum distance of 20 mm up to the maximum of 60 mm, the difference on PL performance caused by them is small. However, it still could be seen that lower rotational speeds can surely bring higher performance. The SDR system with $D_{abs} = 80$ mm and $D_{rel} = 20$ mm (SDR80-20) has the best PL performance. The maximum difference between the best and worst systems in terms of PL is 19.9% increment (4.6 gram/watt) at the lowest speed 4000 rpm, and it is logically decreased with the increased thrust generated by the higher rotational speed, brought by which, the high overall performance like mass flow reduces the influences of rotor location.

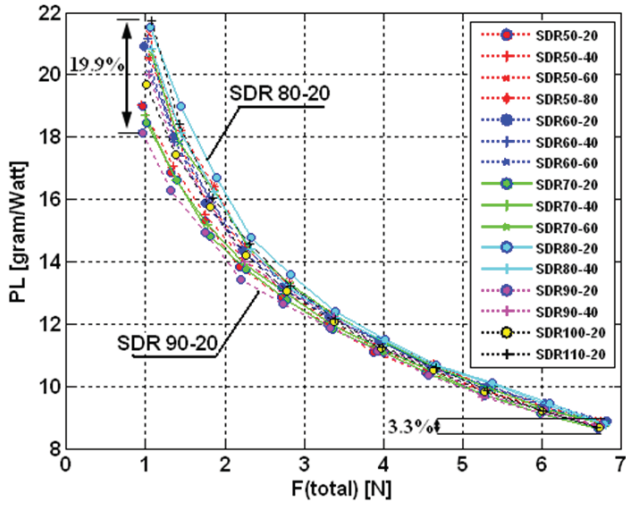

Figure 5.1: PL comparison among different locations

Actually, the information presented as the global performance on different rotor locations can offer a good comparison result for best chosen locations, but for the locations effect, this can only give a preliminary impression: the rotor location does not greatly affect the performance specially under higher rotational speed or mass flow. The result showed here is quite limited for the specific effect analysis, which will be discussed detailedly in following sections based on flow explorations.

5.1.2 Comparison with previous shroud model

In previous work [76], it focused on the two main geometrical parameters K_i and K_e. It fabricated separately several models of shroud air entrances: $K_i = 1.43, 1.7$, and nozzles: $K_e = 0.87, 1, 1.23, 1.47$, as shown in Fig.5.2. These different components could be combined into eight system models together with the fixed cylindric middle sections.

Figure 5.2: Previous models of nozzles and air entrances

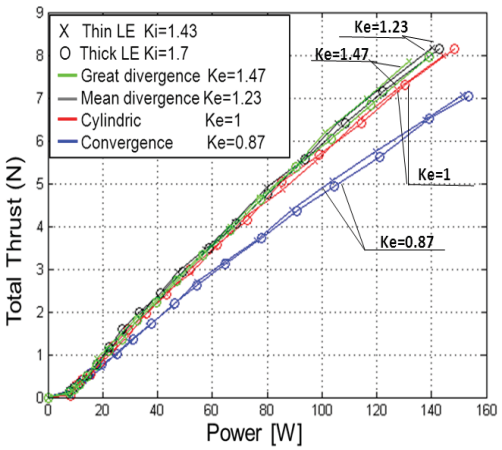

Figure 5.3: Shroud thrust of previous model

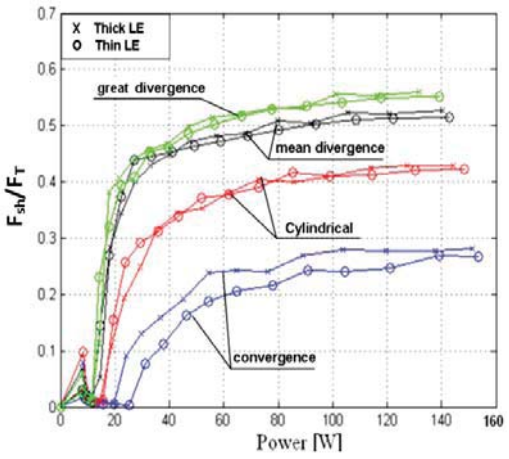

Figure 5.4: Shroud thrust ratio over total thrust of previous model

In Fig.5.3 and 5.4, the data was available for eight models, which can be divided into two groups, each group has the constant inlet but different nozzle areas. As for the effect of K_i and K_e, here the shroud with the relatively larger inlet radius generally has a better improvement on the thrust, but the difference on the two inlet seems small when the divergent nozzle is used. Meanwhile it is clear that as K_e increases, in this case the performance greatly improves. The thrust increment is limited by the overdivergent nozzle of $K_e = 1.47$. It implies that for any nozzle with an expansion ratio higher than this value, the flow is probably unable to counter the adverse pressure gradient in the nozzle and might separate from the shroud wall. All of these rightly correspond to the analysis from Froude theory and 2D axisymmetrical simulations.

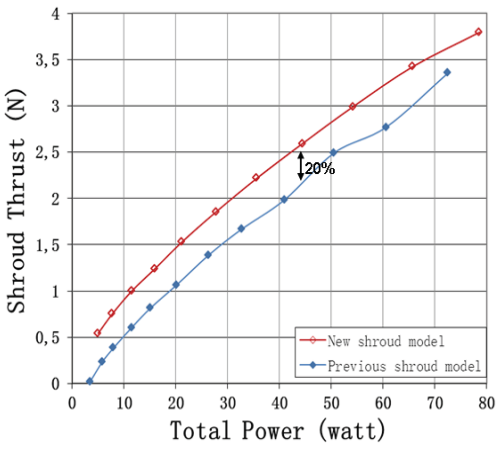

Figure 5.5: Comparison on shroud thrust

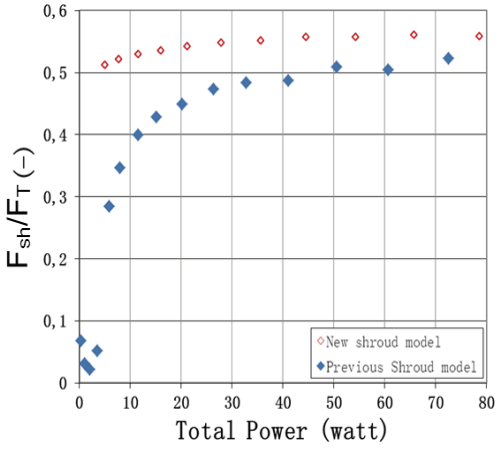

Figure 5.6: Comparison on F_{sh}/F_T

Meanwhile, compared to the performance produced by the system with new

shroud model in Fig.5.5, what should be noticed is: for shroud performance, based on the same input mechanical power, the new model could generate more thrust than the previous shroud model. Such increment is kept constant at around 0.5 N, which becomes quite evident in the lower power input. For the contribution on the total thrust, seen in Fig.5.6, the new designed shroud could generally produce more than 50% of the total thrust, or even higher. This could only be reached for previous designed models when the divergent nozzle is used and while the input power or mass flow satisfies a certain quantity. Therefore, a better performance could be proved to the same degree for the system with an optimally designed shroud.

5.1.3 Comparison with different propulsion configurations

As the test bench is capable of testing varied configurations with different combinations of shroud presence (Yes or No) and rotor number (1 or 2), four different propulsion configurations: FSR, FDR, SSR and SDR, were compared on this test bench.

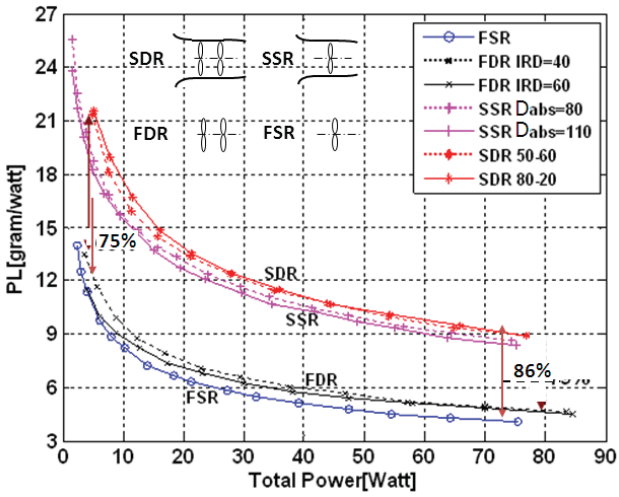

Figure 5.7: PL comparison among different locations of SDR

Fig.5.7 shows PL performance of each configuration with selected rotor locations. It indicates that increasing the rotor number actually does not give evident improvement on PL. This implies that, even though the increased rotor number could improve the propulsion system by transforming the electric power into mechanical power, they also suffer from wake interaction effects which might reduce the system's efficiency. However, the application of double rotor is mainly in views of its torque compensation and easier control. In terms of the shroud presence, the improvement caused by it is quite significant. The PL of SDR systems can be increased a maximum of 86% at high speed and a minimum of 75% at low speed, relative to the FSR systems. The possible reasons for this improvement, the tested pair of propellers were originally designed for shrouded system. In addition, the shroud could generate an extra thrust and has the potential to reduce the losses.

Combined with those advantages of different configurations, the shrouded coaxial double rotor can get the best PL performance based on the same given power. This is rightly in accordance with the purpose to choose this kind of propulsion systems.

5.2 Global Performance Based on New Diagram Propositions

Since known that the SDR80-20 performs best, the performance complete experiments was decided to be done on this system.

5.2.1 System behaviors with double N diagram

The basic overall performance metrics for the SDR system are total thrust (F_t), power (W_t), torque (Q_t) and power loading (PL). The generation of these performances are stemmed from the two rotational speeds (N_1 and N_2) as shown in Fig.4.10. To include and directly view the relation between both rotational speeds and the performance, a new double N diagram was developed to replace the traditional diagrams which is based on only one rotational speed as compressor map, seen in Fig.5.8. This diagram can present the main measured parameters thrust, power and torque, which are offered to measure global performance. Meanwhile, PL performance which emphasizes the system quality is available in this kind of diagram that is useful for designers looking for the optimal operational speeds N_1 and N_2.

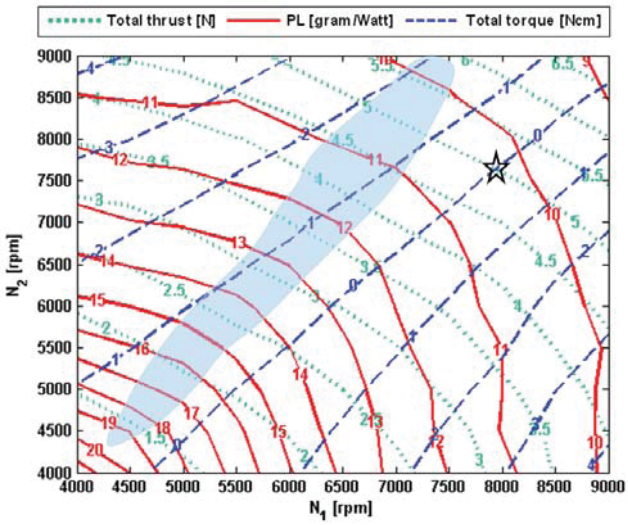

Figure 5.8: Iso performance versus N_1&N_2,SDR80-20

Double N diagram in Fig.5.8 is a more comprehensive representation of catching the system global performance which is determined by two different speeds. It shows that, for the whole SDR80-20 system, PL is improved with lower rotational speed.

The system could be optimized to an extreme level that it consumes minimum power but generates maximum thrust, this is coincident to the shadowed region in Fig.5.8 where the tangents to PL line and thrust lines are parallel to each other. It demands the rotational speed should satisfy the condition of N_2 greater than N_1. This is in conflict with the zero total torque require and consequently on the contrary to the design operational points which ask zero total torque for any specific quantity of total thrust. The speed region with optimum PL is not situated on the place where torque is balanced. The zero total torque happens at a configuration where N_1 is approximately equal to N_2 plus 17% of N_1 at lower speeds, and it moves closer to the condition of $N_1 = N_2$ as the speeds become higher. This unbalance behavior might came from the interaction between the two rotors. Since two rotors have quite symmetrical geometry and the only charge or pressure jump difference is from the rotational speed, a variable blade pitch can be considered as a way to balance such system behavior. However, that will be not specifically studied in this work.

5.2.2 "Mirrored behavior" with $ln(N_1/N_2)$ diagram

Due to the presence of shroud and the effect of the interaction between two rotors, the performance of SDR systems have been detected to not be strictly symmetric with respect to the line of $N_1 = N_2$, as seen in Fig.5.8. It implies that the different arrangement of two rotational speeds can bring different performances on thrust, torque, power and PL. Even if double N diagram include all the information, presenting results as a map in this combined format could not be as clear as directly highlighting each parameter individually.

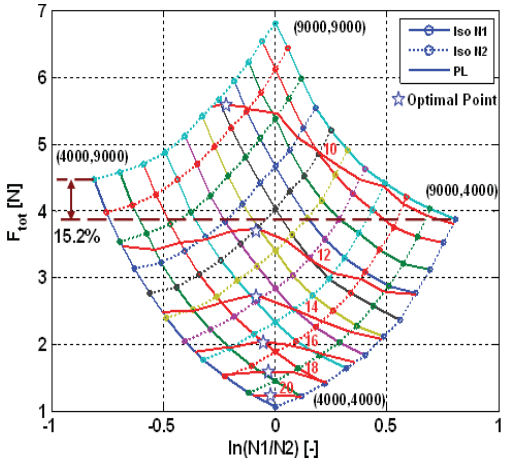

Figure 5.9: Total thrust vs. $ln(N_1/N_2)$, SDR 80-20

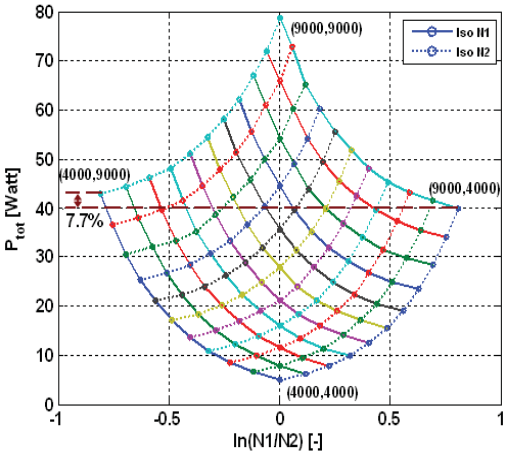

Figure 5.10: Total power vs. $ln(N_1/N_2)$, SDR 80-20

Therefore, the performances thrust, power, torque and PL have to be presented to emphasize the difference between current system and the mirrored one, where the rotational speed regimes are switched. The generally traditional way in which the performance is presented versus the ratio N_1/N_2, results in "unbalanced" and

"nonlinear" diagrams. This does not facilitate comparisons. Using the logarithm of N_1/N_2 is thus proposed. By plotting against the indices of this ratio, as shown in Fig.5.9-5.12, the resulting graph addresses the potential symmetry of the system.

Fig.5.9-5.12 presents that a "mirrored behavior" appears on SDR80-20 with the exchanged speeds. Comparing the measured variables with $N_1 < N_2$ to their mirrored condition $N_2 < N_1$, the individual performances: total thrust, power, torque, and PL are generally symmetric. However, the difference between the current speeds to the switched one could be still observed. Globally, the individual performances are improved under the condition $N_1 < N_2$ which is coincident with $\ln N_1/N_2 < 0$.

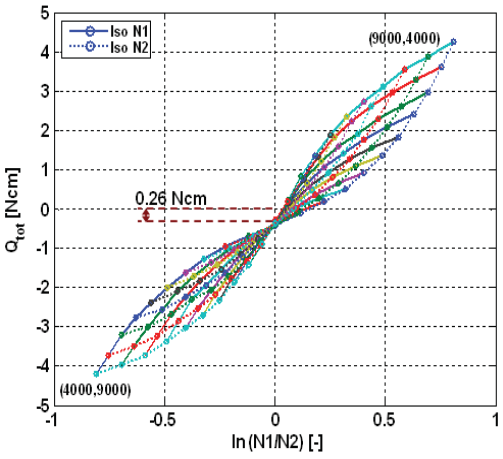

Figure 5.11: Total torque vs. $ln(N_1/N_2)$, SDR 80-20

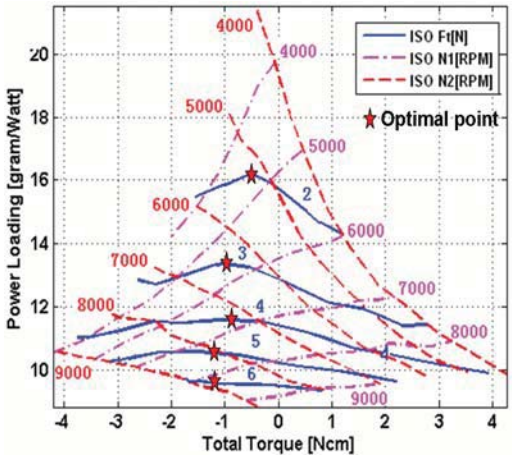

Figure 5.12: PL vs. Total power, SDR 80-20

From Fig.5.9, for the most severe switched speed $N_1 = 9000$ rpm and $N_2 = 4000$ rpm, the thrust is increased by 15.2% at the speed $N_1 = 4000$ rpm and $N_2 = 9000$ rpm. It should be noted that the values of $ln(N_1/N_2)$ for optimal thrust performance for each iso PL value, corresponding to the peak of the iso PL line, are deviated from the zero indices line and lower than zero. Regarding thrust, Fig.5.10 shows that the distribution of power is more symmetric, the greatest increment is 7.7%. As for total torque in Fig.5.11, it is observable that the total torque is not zero under the condition of $N_1 = N_2$. The minimum deviation is 0.26 N.cm. Considering the control and stability, this indicates that the rotational speeds can not be switched from one another under some situations.

Fig.5.12 shows another represention way. It pilots iso thrust and two rotational speeds in forms of PL versus torque. This could be easier to obtain the regime of rotational speed pair according to the iso thrust peak positions, which corresponds to the maximum PL performance with minimum power consumption for a specific demand of thrust. It reveals as well at optimal PL performance is always given in a speed field such that the first rotational speed is slower than the rear one.

Actually, due to the asymmetric flow direction and the fundamental differences between the two rotors flow interactions, perfect "mirror behaviors" with exchang-

ing speed shouldn't be expected. However the realization and exploration on this phenomenon would be useful for system optimization and also for the achievement of some spacial missions such as a turning stationary vehicle. The analysis on different presenting ways and different performances from Fig.5.9 to Fig.5.12 indicate: for the practical rotational speed regime on design, a slower rotating first rotor has a beneficial effect on PL and thrust performance.

5.2.3 Performance improvement with comparison diagram

As the comparison result with other three different propulsion configurations shown in Fig.5.7, the shroud presence together with the application of contrarotating rotor behaves best. In terms of rotor number effect, the shroud performs a critical role on propulsion system improvement. In order to make the improvement clear on individual performance, the FDR system of the same rotor configurations as for shrouded system is introduced.

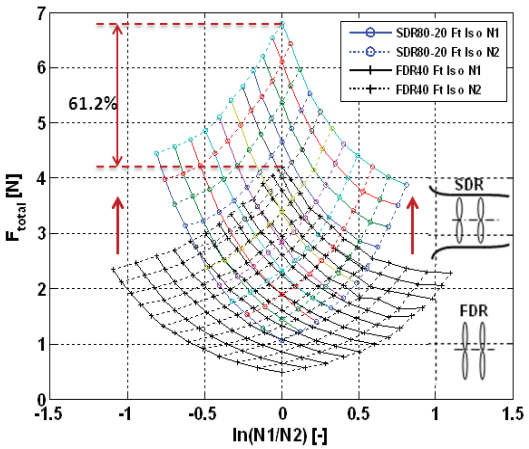

Figure 5.13: Comparison on F_t between shrouded and free system

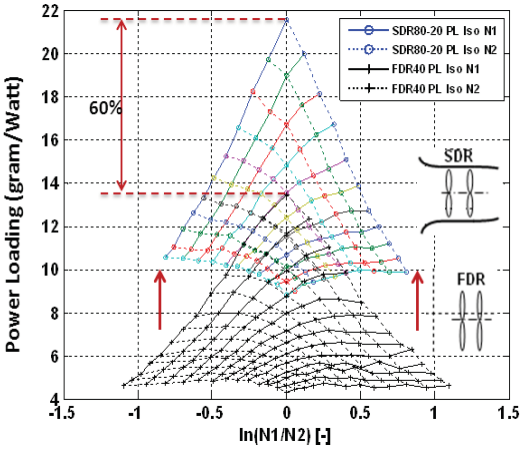

Figure 5.14: Comparison on PL between shrouded and free system

Based on the proposition of the two new diagrams introduced above, the individual performance can be compared in all possible combination of rotational velocities for double rotor systems. Fig.5.13 and 5.14 show the comparative results on total thrust and PL between SDR80-20 and FDR with relative or inner rotor distance of 40 mm (FDR40). Globally the shrouded system can generate more thrust than the free one in all the speed regime. The maximum improvement occurs at highest speed 9000 rpm, which is 61.2%. This directly promotes the improvement of PL in all the speed regime as well. The information obtained from these two diagrams gives a general impression. It should be noticed that, from such comparison diagram, the improvement from a slower rotational speed is amplified when the system is shrouded.

In order to explore the source which improves the system, it is necessary to specify the effect in more detail on the flow characteristics from the shroud comparing the free system.

5.3 Flow Characteristics Based on Shroud Benefits

In order to facilitate the exploration, the FDR system with the same pair of rotors as shrouded system was introduced, and an internal distance between two rotors of 40 mm was applied for all the analysis.

5.3.1 Shroud benefits: overall performance

Due to the presence of shroud, with two same rotational speeds, Fig.5.15 shows an increment of mass flow is generated by the shrouded system comparing to the free one. This improvement is kept constant at around 65% more than the one aspirated by the free system. Since the shroud inlet was designed to adapt the flow, it could be considered the same as the flow boundary of FDR. The strong ability to aspirate the mass flow is greatly affected by the nozzle with the appropriate nozzle exit area ratio 1.2. Compared to the 0.5 for FDR, this one better expands more sufficiently the slipstream after the rotor, decreases the final wake velocity and ultimately increases the mass flow passing through the shroud passage.

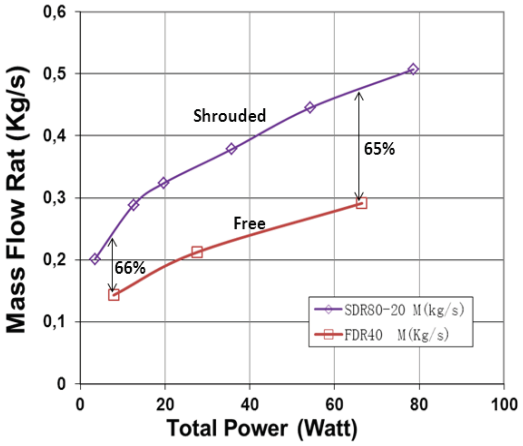

Figure 5.15: $\dot{m}$ for SDR and FDR

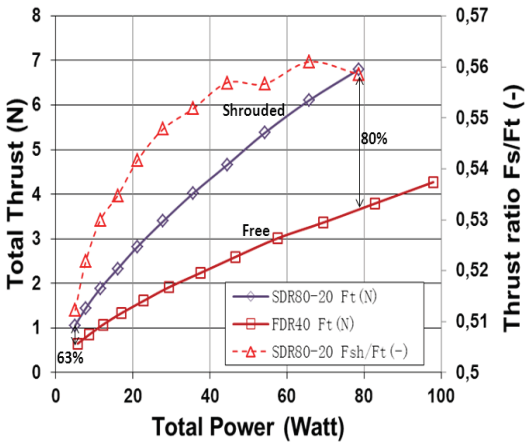

Figure 5.16: Thrust for SDR and FDR

The increased mass flow over the shroud directly reflects an improvement of system thrust performance, as seen in Fig.5.16. For a total thrust augmentation from 63% and up to 80% of the free system with increased power, the shroud could generally contribute more than half, which could reach to 56%. This means the thrust augmentation for shrouded system completely comes from the shroud. With increased power input, the shroud thrust ratio over the total thrust shows a negative

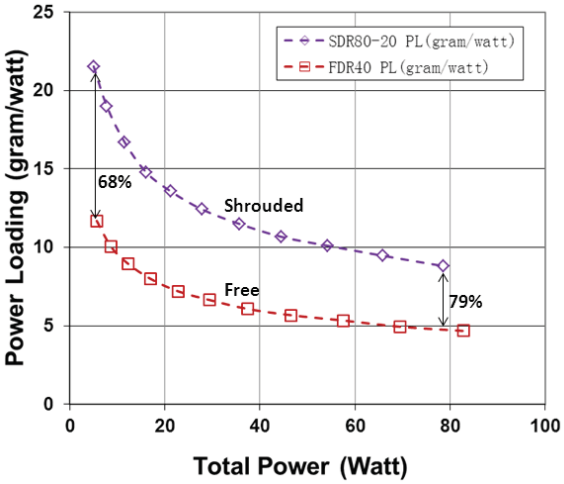

Figure 5.17: PL of shrouded and free system

second derivative augmentation. The maximum benefit might happen between 20 and 40 Watt input power. And this ratio tends then to be constant.

The substantial increments on the total thrust based on the same power input improve the global performance of the shrouded system as PL for whole system, seen in Fig.5.17. Better behavior corresponds to less power input. Corresponding to the thrust performance, its greatest improvement by up to 79% occurs at the highest power input.

As the shroud presence could cause an improvement, there might be a question about the rotor's behaviors. Fig.5.18 reveals that for both shrouded and free systems, the similar performances from two rotors can not be obtained even if they are designed to be symmetric. For FDR, the front rotor appears to have better propulsive performance than the rear one. This is logic because of the aerodynamic interference between two rotors [77]. The rear rotor works under the wake produced by the front rotor, and suffers more from its downwash flow. The flow on main area aspirated by the rear rotor already has an axial velocity given by the front one, this makes the flow continuously exert by less force. Consequently, the thrust given by the air to rear rotor becomes less. On the contrary, for SDR, the leading role on the thrust contribution is given to the second rotor. Compared to FDR, the thrust generated by the first rotor of SDR is decreased greatly, this is probably because the aspirated flow is more accelerated as it passes through the air entrance with bell profile which tends to be narrow, and less force is exerted from the first rotor to allow air continue to develop. Furthermore, regarding the thrust contribution from the second rotor, it seems to be similar to FDR thrust, since it balances out the effects from higher velocity and it reduces vortex loss reduction due to the presence of shroud.

Although the rotor thrust is lower than in the FDR at given power, the SDR system benefits more from the shroud presence, which is not only on an additional

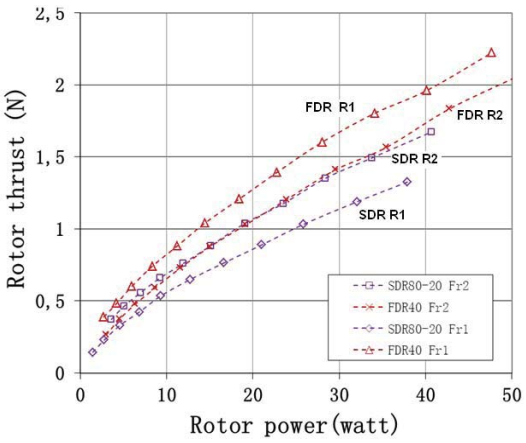

Figure 5.18: Two rotor thrusts comparison between SDR and FDR

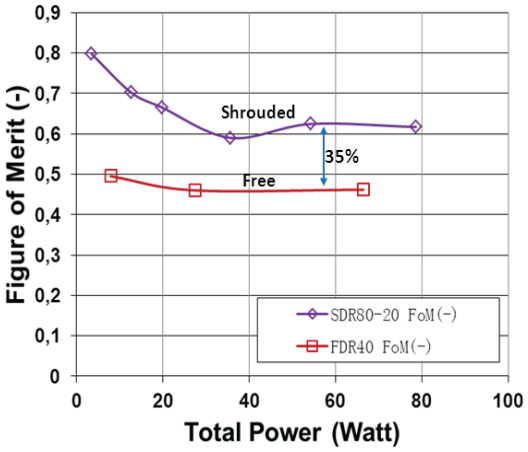

Figure 5.19: FoM performance of shroud and double rotor

thrust contribution far more than the decrement of rotor thrust, but also increased mass flow. The increased induced mass flow is directly reflected on a greater ability for rotors to transfer the mechanical power into flow. That is the figure of merit (FoM). Fig.5.19 shows different levels occurring on the shrouded and free systems. The shrouded system behaves far more efficiently at inducing the input mechanical shaft power to the flow. It could reach 0.8 at lower power input with more than 50% increment compared to FDR. This tends to be decreased and constant of 0.62. Compared to FDR whose FoM is 0.46, SDR has a constant increment of 35%. Such improvement would result by the reduction of blade tip loss which generally dominate the flow of free rotors. Another reason is that the rotor was originally designed for the shrouded system. A better performance might be obtained for the rotor design of free system.

Overall, compared to the free system, due to the shroud presence, the shrouded contra-rotating system increases the mass flow almost constantly by about 65%. As a higher power is consumed, this makes an augmentation in thrust by more than 80%, completely provided by shroud which could contribute a thrust of up to 56% for the whole system. Both significantly improve the system performance and rotor ability in terms of PL and FoM respectively.

5.3.2 Shroud benefits: shroud wall pressure

The basic reason for shroud contribution is because the mass flow produces a pressure distribution on the shroud surface, seen in Fig.5.20. It shows two ways to present the wall static pressure on the shroud relative to the ambient atmospheric at the two same rotational speeds from 4000 rpm to 8000 rpm with the step of 2000 rpm. One plots the pressure distribution with shroud inner profile length along the system axis in the main figure, another B is with the shroud profile itself

as the coordinate system for a better visualization.

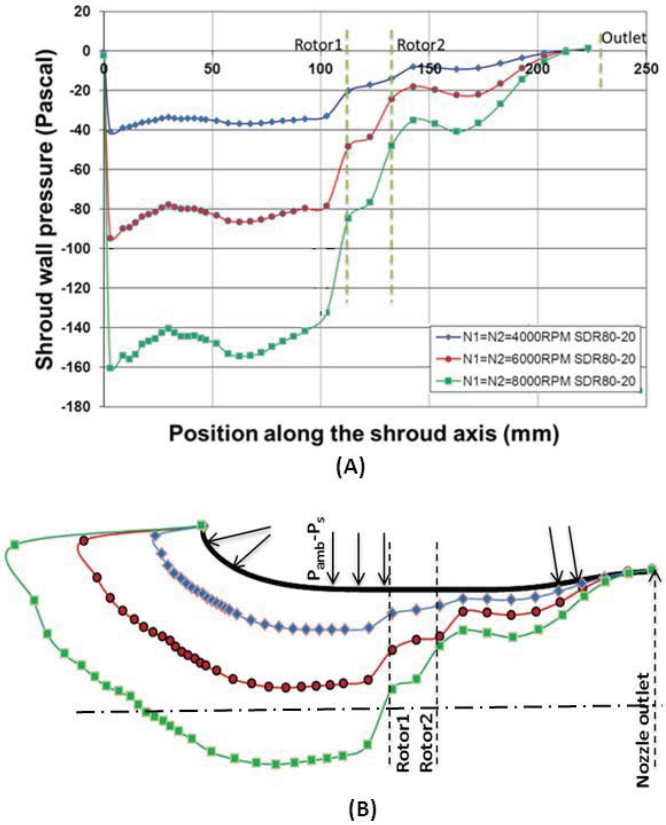

Figure 5.20: Wall pressure of SDR80-20 along shroud axis (A) and profile (B)

The negative pressure is formed over the entire inner surface of the shroud except the position 10 mm upstream far from the outlet, where the pressure almost equals the atmospheric value. In hovering, the flow is purely axial, the first test position which right at the lip starting point, has a negative pressure. Followed by it, due to the profile curvature and the internal flow acceleration, the first suction peak is formed at the beginning of the air entrance where the formation of a lower pressure region starts. Since the curvature smoothly becomes less around the lip, the pressure after the first suction tends to go up. A secondary suction peak is then formed 50 mm before the rotor where the inlet lip ends. This recompression becomes clearer at higher rotational speeds due to the radial equilibrium for the relative slower air flow passing in the center of the system compared to the flow accelerated in the lower pressure region near the wall. Under all the speed conditions, the pressure is followed by a dramatical increment through the two rotors. The flow gains energy in terms of the pressure increment after each rotor. The magnitude of the pressure jump formed in the upstream and downstream double rotor is positive and proportional to the rotational speeds. Finally the pressure approaches the ambient atmospheric value after rotors. This means the nozzle inner profile design is well adapted to the

flow streamlines which makes a smooth recovery until the atmospheric pressure at the end.

Therefore for the three components of the shroud, in views of the profile curvature and pressure distribution illustrated above, the air entrance surely contributes most of the axial thrust integration for the system due to the suction peak formed there; the cylindrical middle section contributes null for system hover as its axisymmetrical geometry compensates the thrust; the contribution on thrust from nozzle seems less or even negative because of the curvature and the substantially increased pressure.

5.3.3 Shroud benefits: flow field exploration

Since the flow characteristics inside the system directly effects its overall performance, several axial stations were thus selected to perform the tests with the static pressure probe and total pressure probe as discussed in Chap.4 and App.C. For SDR80-20, the distance between the two rotors is only 20 mm. Moreover the twist angle of 42.2° at the blade root makes the space within rotors smaller. It is impossible to do the test on the middle plane. The planes located at 20 mm, 60 mm, 140 mm and nozzle exit 200 mm far from the inlet were thus selected. Flow characteristics in the middle plane within rotors will be specifically discussed in the following chapter for SDR80-40.

Fig.5.21 and Fig.5.23 present the total and static pressure distribution for each chosen plane. This facilitates the comparison between different planes and visualization of the flow developed in the shroud passage. Both values of total and static pressure showed here are relative to the ambient atmospheric pressure versus the probe position ratio over the current axial station's radius.

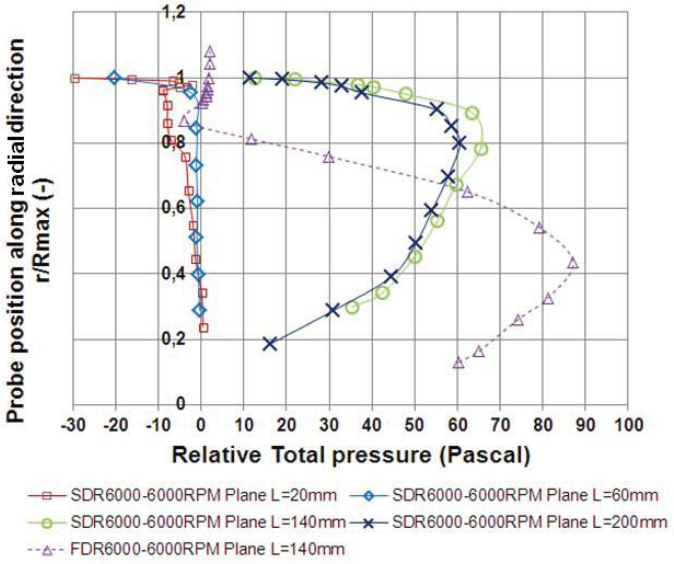

Figure 5.21: Total pressure distribution on different axial planes of SDR and FDR

Fig.5.21 shows the global development of total pressure from the air entrance to the nozzle exit for SDR80-20. First, the first plane which is located at the position with the greatest curvature, has general total pressure value close to zero. This is consistent with the theoretical analysis because there is no energy input to the flow. However, on this station and near the shroud wall, approximately 20% of the station region where the pressure value is several pascals lower than the environment zero one. As illustrated in Chap.4.3.2, this is probably caused by the greatest curvature appearance. The pressure suction formed with increased mass flow accelerates the most here. In addition, the relatively big gap between the installation hole and the probe makes the flow to fluctuate easily as seen in Fig.5.22. With the decreased shroud inner profile curvature, this influence is decreased as well and the total pressure measurement on corresponding positions of plane $L = 60$ mm turns to be more precise. The pressure is mainly close to zero because no great losses happen before the rotors. At the radial position closer to the blade tip, r/R_{max} near to 1, the total pressure drops almost to -20 Pascal, this is mainly due to the viscosity of shroud boundary layer which dominates the local velocity. Compared to this plane, loss occurring on the planes of $L = 140$ mm and at the exit, are more significant, since the flow is affected by the blade tip vortices as well. For both at their main radial regions close to the middle of the blade, total pressure gains most of the energy induced by the double rotor. It implies that the rotor design well charges most of the flow where it is not under the influence of strong viscous or shear effects. Meanwhile in the region closer to the root, total pressure suffers the second loss affected by the strong swirl provoked by the root of the rotating rotors. It is noted that this loss happens on a relatively larger part of the plane, when compared to the region having the tip vortices and viscosity. On the exit, the total pressure is slightly lower than the one on the plane $L = 140$ mm. This is because of the viscosity of air and friction from the shroud surface.

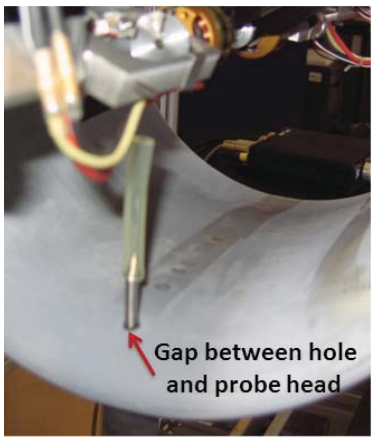

Figure 5.22: Gap between the probe cylindric head and its first installation hole

Comparing these two systems SDR and FDR at the same axial plane $L = 140$ mm, SDR has a more uniform flow after the rotors. And FDR has smaller ef-

fective pressure region due to contracted flow. The total pressure at $r/R_{max} > 0.85$ has already achieved a ambient pressure. Around that position, FDR is probably strongly influenced by a mixing flow boundary. Evidently the pressure loss caused by blade tip vortex is far greater than SDR.

All of these imply further that for SDR system, firstly, the shroud makes the pressure to distribute more uniformly; secondly, its presence substantially reduces the slipstream contraction when compared with the conventional free propellers; thirdly, it effectively reduces and minimizes the loss at the blade tip.

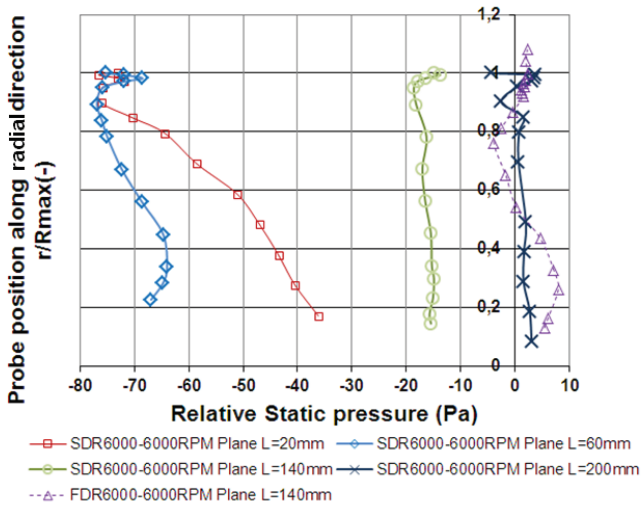

Figure 5.23: Static pressure distribution on different axial planes

Fig.5.23 shows that the static pressure distribution on each plane is generally constant except in the first plane $L = 20$ mm. The static pressure distribution on station $L = 20$ mm is coincident with the analysis on the shroud wall static pressure and total pressure. It indicates again that lower static pressure or strong suction formed around the shroud wall due to the curvature. This curvature influence consistently decrease as the tested positions are closer to the shroud center. After the complete acceleration of the flow, on the plane $L = 60$ mm, the zero constant total pressure lets the static pressure reach to a minimum value, comparing the other rear two planes which benefit from the induced power. Also it should be noted that on this plane the static pressure at the tip is a few pascals lower than the one at the root when compared to other planes with uniform static pressure. This can be explained by the radial equilibrium that the centrifugal effect is compensated by the difference of the static pressure. The most interesting is the pressure distribution on the exit plane. The static pressure is nearly equal to zero except the region near to the system center. This reflects again that the nozzle design of SDR with this rotor locations at least under such condition adapts the flow on all of the outlet. It fully expands the flow, reduces the wake velocity and makes the shrouded system take full advantages of the induced power.

Compared to the SDR on plane $L = 140$ mm, the static pressure distribution has globally reached ambient pressure. The radius for which the contracted slipstream is same as total pressure, which is around $r/R_{max} = 0.85$. However, it seems the mixing flow boundary with the environment and propeller ejection affect the static pressure distribution in a relatively great region from r/R_{max} equal to 0.85 to 0.55. Furthermore, using total and static pressures, the flow induced velocity caused by free rotors can be seen to be smaller than its corresponding shrouded one, due to the environment pressure equilibrium.

5.4 Conclusions

Based on the measurements made of thrust, torque, rotational speeds, wall pressure distribution on the shroud, and the pressure field including total and static pressure on system axial stations, the characteristics of the shroud system and the shroud benefits were explored. Double N, $\ln(N_1/N_2)$ and comparison diagrams were proposed to facilitate the analysis and the visualization. Based on all of these, the following observation and key discussed results were made from the measurements:

- For the new shroud design, the different rotor locations do not affect PL greatly. The best rotor location is the first rotor set 80 mm or $0.9R_r$ from the inlet and the second one just put 20 mm or $0.2R_r$ backward from it. With such rotor locations, an increase of about 20% on shroud thrust under the same input power was obtained, which could always contribute above 50% thrust for the system. Compared with the other three configurations – free single rotor (FSR), free double rotor (FDR) and shrouded single rotor (SSR), the shrouded double rotor (SDR) obtains an improvement on PL by up to 86% for a given power;

- For the overall behavior of such shrouded system, the analysis on two new diagrams – double N and $\ln(N_1/N_2)$, reveals that, for the current rotor profile, the zero total torque is deviated from the condition $N_1 = N_2$ and always happens as $N_1 > N_2$. This conflicts with the region situated by the optimized performance, which always happens with the first slower rotational speed. This makes the "mirrored behavior" or symmetry from switching speeds imperfect;

- For the shroud benefits, it was obtained by the comparison with FDR:

  - First on global performance, an increase on mass flow around 65%, kept by the shroud presence, directly augments the total thrust by up to 80%. This increment basically comes from the shroud thrust due to its high thrust contribution. All these make the improvements on PL by up to 80% and on FoM constantly by 35%, which evaluates the ability to convert the mechanical power into kinetic energy by rotors, even though the shrouded first rotor is great decreased comparing with the free first one.

Furthermore, the dominant role on rotor thrust for the first rotor of FDR turns to the second one of SDR;

- For shroud local effect, whatever the rotational speed is, the strongest suction peak (the lowest pressure) formed at the inlet where it has the greatest curvature makes the potential of thrust contribution. Both shroud wall pressure and the static pressure tests have an equivalent ambient pressure at the exit. All those imply that the new designed shroud well adapts the flow;
- For flow field of total and static pressure, two great total pressure losses appear near the root and the shroud wall for shrouded coaxial rotor. And the shroud presence effectively reduces the tip vortex loss and the contraction of the slipstream in the downstream wake, comparing to FDR which has contraction just after the second rotor of a radius about 0.85 times the local shroud radius. That is the source for shrouded system to make an improvement.

As the results analyzed above, this experimental work contributed to the confirmation of the shrouded system characteristics,the approximation of its flow field and its potential to the improvement from the shroud presence. For further optimizing the rotor configurations, the effects of rotor locations and switching speed, whose influences had been observed during the tests on the system overall performance, needs to be identified.

Chapter 6

Effects of Design Parameters on Rotor Configurations

For shrouded double rotor systems, the presence of another additional rotor and the shroud raise two important influential design variables: the axial locations of two rotors along the shroud (D_{abs}, D_{rel}), and the operational speeds. As the studies in last chapter demonstrates, the rotor's location can not greatly affect the system global behaviors. However, it is still necessary to be clear for further optimization of the rotor configurations. For rotational speed, as indicated, even if the system behavior is closed to being "mirrored" when the rotational speeds of two rotors are switched, still a slower first rotational speed can produce an improvement. Therefore for both variables, this chapter objects to explore their specific effects not only on the system global performance but also on the flow characteristics. Another rotor configuration $D_{abs} = 80$ mm and $D_{rel} = 40$ mm is thus introduced and compared to the best performed one. Due to the possibility to have tests on the middle plane between rotors, such rotor locations will also be used to explore the effect of speed switching.

6.1 Performance of SDR80-40

6.1.1 Overall performance

Through the development of two new diagrams: double N and mirrored diagrams, the overall performance of the shrouded system with two input rotational speeds can be presented in a more comprehensive way as introduced in Chap.5.2. Therefore for system with $D_{abs} = 80$ mm and $D_{rel} = 40$ mm (SDR80-40), its general performance and imperfect mirrored behavior can be explored as well according to Fig.6.1 and 6.2. Both figures actually show similar characteristics to SDR80-20: the velocity regime where the optimal performance appears is under the condition of the second or rear rotational speed higher than the first one; On the other hand, zero total torque can only be obtained as $N_1 > N_2$; Switching rotational speeds of the two rotors can generally provide a symmetric ("mirrored") performance while an improvement occurs when the first speed is kept lower. For the general performance distribution with same rotational speed regime, there is actually no significant difference when comparing to the 80-20 rotor configuration. This could be found for individual performances such as total thrust, power, torque and PL as well, seen in App.D.1.

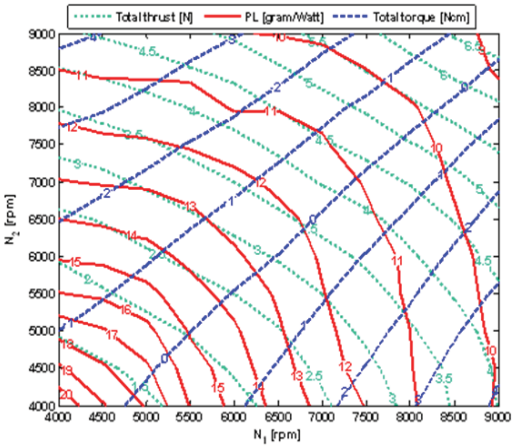

Figure 6.1: Performance with N_1 & N_2 for SDR80-40

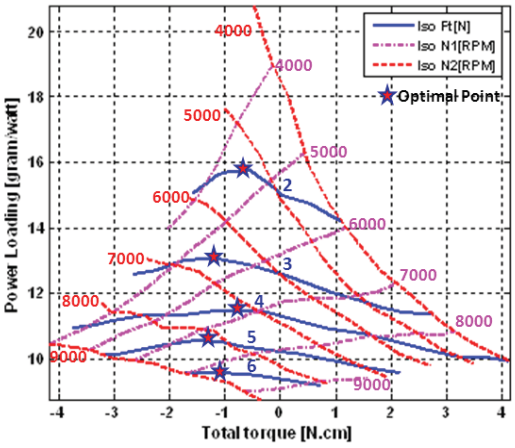

Figure 6.2: Performance with PL & Q_t for SDR80-40

6.1.2 Flow field

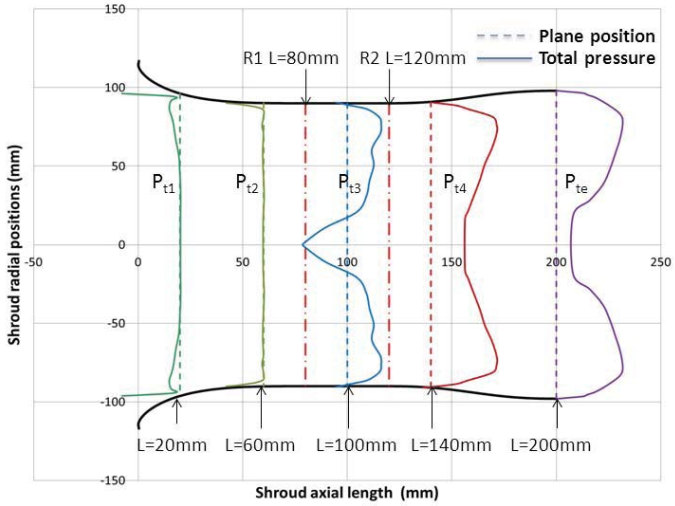

Figure 6.3: Total pressure distribution on 5 axial stations for SDR80-40

For the flow field exploration of the shrouded system in this work, SDR80-40 can be considered as a complementary explanation on it due to the middle plane between rotors being available for the tests. Fig.6.3 and 6.4 give a thorough insight for the total pressure and velocity distribution developed through the whole shroud passage. Five axial planes were chosen to be tested, those are the planes $L = 20, 60, 100, 140$ and 200 mm. The dotted line represents the tested axial station and the double rotor position. The corresponding solid line beside it is the total pressure or velocity profile on that axial station. Therefore the distance between the dotted and solid

line represents the magnitude of pressure. And the solid line located at the right of the dotted line, means the relative pressure or velocity magnitude is positive, but negative in a global context.

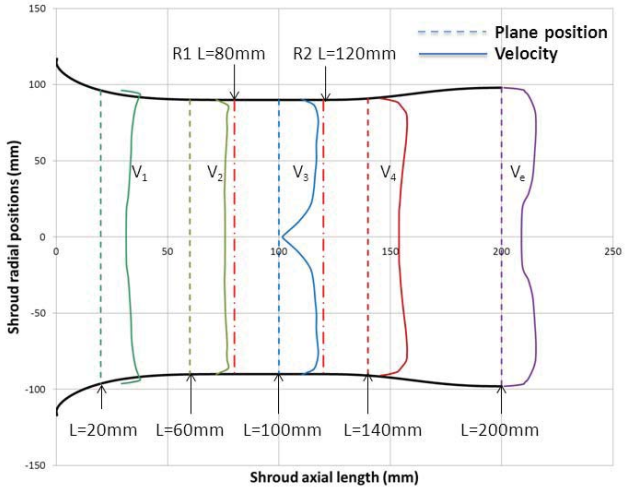

Figure 6.4: Velocity distribution on 5 axial stations for SDR80-40

In Fig.6.3, the pressure loss happens as well due to several reasons: the total pressure on the plane $L = 20$ and 60 mm and near the shroud wall is lower than zero due to boundary layer viscosity; the pressure is drastically reduced on following planes near the shroud wall. That is because additionally, it suffers from the tip vortices; a great loss near the shroud center on the middle plane between two rotors can be found. This is mainly caused by the rotor rotation which provoked a strong swirl at its root. Such loss is recovered on the plane $L = 140$ mm due to the front swirl compensation of the second rotor turning in the opposite direction.

Fig.6.4 presents the velocity development through the whole shroud passage. Globally, the velocity distribution on each plane is generally uniform except the positions where there is a strong effect of viscosity on the shroud wall, blade tip vortices and root swirl. As a consequence of total pressure loss, the velocity suffers a large decrease in the middle plane after the first rotor. According to the mass conservation law, small overall differences reasonably exist among different stations caused by the shroud profile which changes the cross surface areas.

The global aerodynamic characteristics shown in Fig.6.3 and 6.4 are almost coincident with the observation from SDR80-20. As for the location effect and switching speed effect, the detail will be made in following sections.

6.2 Effect of Rotor Location

6.2.1 Effects on global behaviors

For shrouded double rotor system, the problem of rotor locations is comprised of both absolute distance D_{abs} from the first rotor to the inlet and the relative distance D_{rel} between the two rotors, which can not be separated. This makes the analysis difficult. In order to obtain the preliminary impression on these two rotor locations effect on PL, the SSR and FDR were introduced initially.

Fig.6.5 and 6.6 show the effect of D_{abs} and D_{rel} on PL of SDR and FDR system respectively. Both indicate that the systems working in a lower rotational speed are affected significantly by the rotor locations. For SSR, the greatest benefit of PL happens at the rotor location D_{abs} equal to half of the rotor diameter. And the optimal inner rotor distance for FDR is 23% of rotor diameter. In a higher or middle level speed regime higher than 6000 rpm, rotor locations for both systems do not greatly affect the system global performance. This means the effects of rotor locations for SSR and FDR greatly depend on the rotational speed.

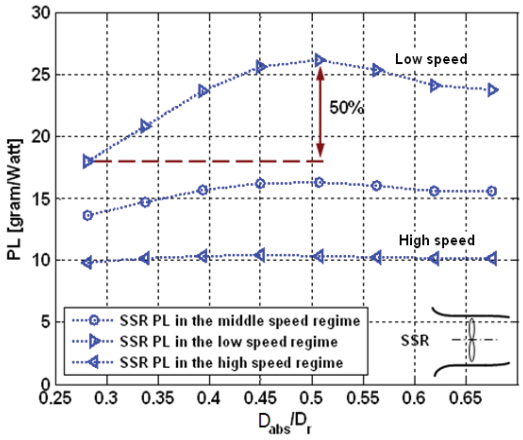

Figure 6.5: PL trend with locations of SSR

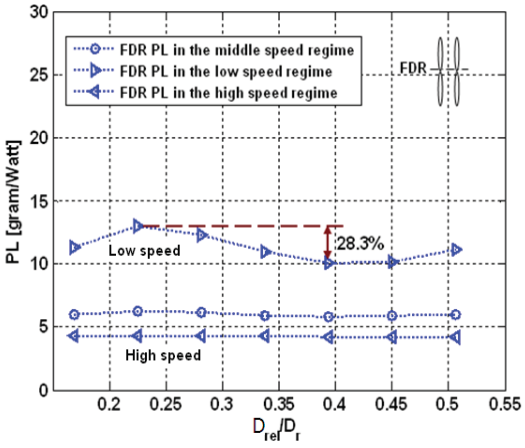

Figure 6.6: PL trend with locations of FDR

Therefore for the SDR systems, the effect of rotor locations is explored in all possible speed regime with the two same rotational speeds. However separating two rotor locations is still a problem. As presented in Fig.5.1 of Chap.5.1.1, the rotor locations actually affect the PL of SDR system negligibly. To specify their effects, two series of locations having $D_{rel} = 20$ and 40 mm under different D_{abs} were explored to reduce the experimental cost by limiting the location possibility. App.D.2 gives their comparison results: Both combinations of rotor locations ($D_{abs} = 80$, $D_{rel} = 20$ and $D_{abs} = 80$, $D_{rel} = 40$) situated in the shroud cylindric section perform better comparing to others. This is reasonable since a smaller gap between the shroud and rotor tip can improve the system.

Fig.6.7 shows the shroud contribution on different combinations of rotor locations. All the locations can provide more than half of the total thrust. However there is no clear effect trend by locations on the thrust contribution from the shroud, which really depends on the mass flow absorbed by the system and the friction generated by the shroud itself under a certain flow condition.

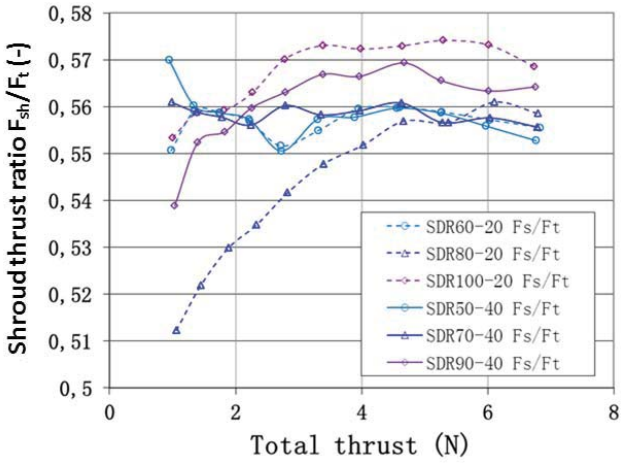

Figure 6.7: Shroud contribution on thrust of FDR with D_{rel} = 20 or 40 mm

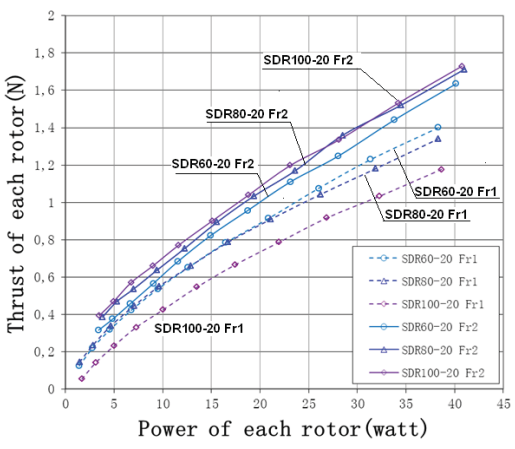

Figure 6.8: Rotor thrust of SDR with D_{rel} = 20 mm

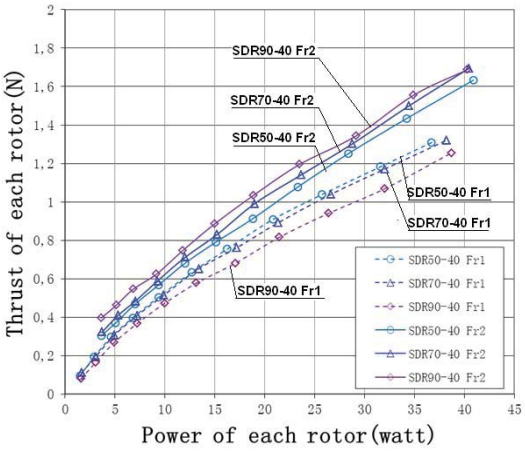

Figure 6.9: Rotor thrust of SDR with D_{rel} = 40 mm

As for their effects on rotor role, compared to shroud thrust contribution, Fig.6.8 and 6.9 show a relatively clear tendency of each rotor's thrust generation. All indicate that the second rotor plays a more dominant role on rotor thrust performance comparing to the first rotor. This has been revealed in Fig.5.18 of Chap.5.3.1. And it becomes more evidently when the first rotor is moved more far away from the inlet as D_{abs} becomes great for both series D_{rel} equal to 20 mm and 40 mm. It

should be reminded that the second rotor playing a more dominant role is contrary with FDR.

As the results' analysis of rotor location effects on each component of SDR, it should consider the effect factors on both shroud and rotors for two rotor locations chosen in order to improve the whole system performance.

6.2.2 Effects on the flow field

To explain the effect of rotor locations through aerodynamic characteristics, the best two locations 80-20 and 80-40 as analyzed above were applied at the speeds $N_1 = 6000$ rpm and $N_2 = 6000$ rpm.

First, the comparison on overall performance between these two location configurations is shown in Table.6.1. Even though 80-20 performs better or best as explained above, the comparison result reveals all the performance from location 80-20 only have a few grams more than the ones from 80-40. And the rotors perform better with the FoM improvement just about 0.01.

Table 6.1: Performance comparison between system with different rotor locations

SDR $D_{abs} - D_{rel}(mm)$	**80-20**	**80-40**
(N_1, N_2) (rpm)	(6000,6000)	(6000,6000)
F_{r_1} (N)	0.535	0.550
F_{r_2} (N)	0.760	0.752
F_{sh} (N)	1.530	1.513
PL (gram/watt)	13.6	13.1
$\dot{m}$ (Kg/s)	0.326	0.324
FoM (-)	0.67	0.66

Specifically, for the flow characteristics, Fig.6.10 presents the total pressure comparisons on the planes upstream of the front rotor, downstream of the rear rotor and at the exit between these two rotor locations. From Fig.6.10, the pressure at the root where r/R_{max} is close to zero on the middle planes for SDR80-40 reveals the system suffers from the wake greatly. The total pressure there is reduced until it becomes lower than -40 Pa. Compared to the pressure reduction of -10 Pascal at the blade tip, this indicates in the further that the loss from root wake seems more evident as the illustration in Chap.6.1.2. Through the comparison, for plane L=60 mm, two locations do not behave differently except at the tip, the pressure loss for SDR80-40 is more severe with total pressure reduction of -35.9 Pa. For plane L=140 mm, through the comparison at the root with the middle plane, the wake provoked by the root of the first rotating rotor seems to be limited and reduced by the second rotor which rotates in the opposite direction. However this is not so evident as analyzed in Chap.6.1.2 because the total pressure tested on plane L=140 mm is stopped at radial position approximately 15 mm from the center due to the obstruction of the support components. On the other hand, the difference caused by rotor locations on this plane is clear even if it is small. Globally the total pressure

line of SDR80-40 is wrapped within the one of SDR80-20. This implies the flow can be induced more energy by the rotors of system SDR80-20 which would have higher efficiency to convert the mechanical energy. Meanwhile, the higher induced power in some way means more mass flow for the incompressible air.

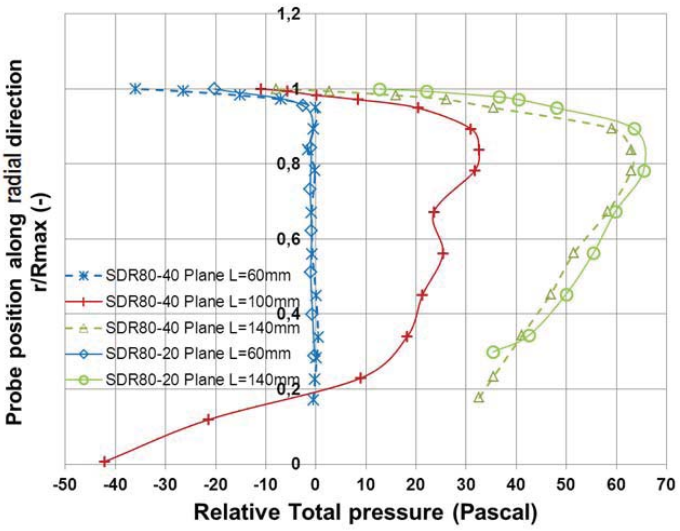

Figure 6.10: Comparisons on total pressure between rotor locations $D_{abs} = 80, D_{rel} = 20$ mm and $D_{abs} = 80, D_{rel} = 40$ mm

Fig.6.11 shows the comparison on the static pressure on the planes L=60, 140, 200 mm and the middle plane L=100 mm for SDR80-40. The trends of static pressures for planes L=60 mm and 140 mm seem no obvious difference as explained in Chap.5.3.3. And the pressure distributions on the plane in downstream wake for both locations are quite uniform. Meanwhile, two static pressure differences ΔP_1 and ΔP_2 are presented at one radial position among the plane in upstream front rotor, middle plane and the plane after the rear rotor for SDR80-40. It is observable that ΔP_2 is globally greater than ΔP_1. Although the thrust generated by each rotor comes from the static pressure itself, the greater pressure jump generated by the second rotor could still explain in some way that zero total torque does not appear for $N_1 = N_2$. This also predicts that the system would be unbalanced. For the system exit, SDR80-20 has the nozzle more adapted to the flow, the static pressure in the rear rotor wake is almost equal to ambient atmospheric. However with the second rotor moved backward, the flow is under-expanded and the effect of radial equilibrium is obtained.

As the discussion about the flow field on different planes of both locations, it could be predicted that the shroud of the system 80-20 would contribute greater static thrust compared to the other one. The detail on two locations in the whole speed regime can be seen in App.D.2. Fig.6.12 presents the wall pressure on the shroud for both locations at speeds $N_1 = N_2 = 6000$ rpm. As shown, the variation on the second rotor position does not change the distribution profile globally except

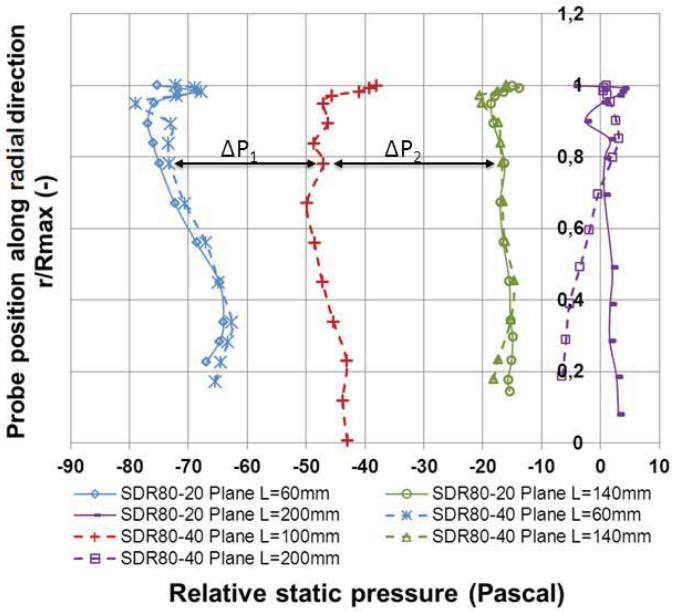

Figure 6.11: Comparisons on static pressure between rotor locations $D_{abs} = 80, D_{rel} = 20$ mm and $D_{abs} = 80, D_{rel} = 40$ mm

where close to the second rotor. However, the difference there does not generate at all the thrust. The places probably contributing shroud thrust are the inlet and the nozzle. The location 80-20 shows a slightly decreased pressure in the rear part of the inlet where curvature is negligible. Compared to it, the smaller pressure distributed on the whole nozzle affects more the final shroud contribution on the thrust as a negative effect due to the curvature seen in the subfigure. Generally,

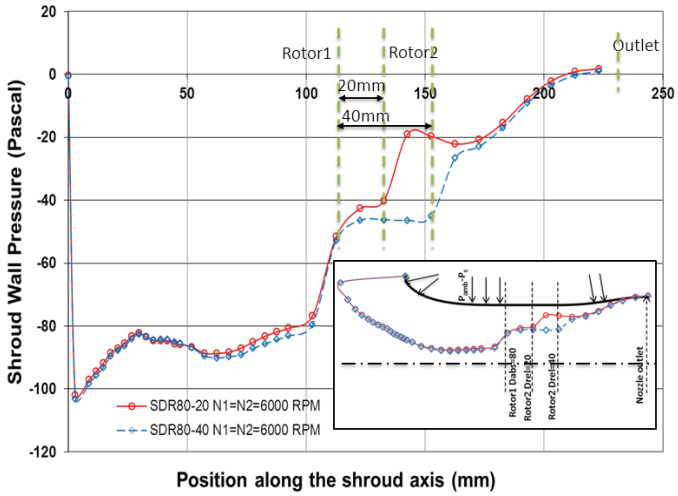

Figure 6.12: Comparisons on shroud wall pressure between rotor locations $D_{abs} = 80, D_{rel} = 20$ mm and $D_{abs} = 80, D_{rel} = 40$ mm

as the comparison shown on all the figures, although the location 80-20 shows a better performance for another location 80-40, their difference is slightly noticeable whether on global performance or on flow characteristics. As Nagashima revealed: the optimal hovering performance would be obtained when the wake boundary after the contraction behind the free upstream rotor is coincident with the one produced by the rear rotor [78]. For shrouded system, both wake boundaries from the two rotors are modified by the shroud presence and adapted to have similar scale as the shroud. This makes the rotor locations become less important than that in the free rotors. It can be therefore concluded that the effect of the rotor locations can be nearly ignored on the global performance compared to other factors, but keeping in mind that minimum IRD could be a priority choice for vehicle design.

6.3 Effect of Rotational Speed Combination

6.3.1 Propulsive behavior of each rotor

As introduction in Chap.4.2, the lowest rotational speed chosen to be tested for SDR is 4000 rpm due to the experimental stability and precision. However for the application of double rotor, another consideration for the operational speed is to ensure both rotors are propulsive for the system.

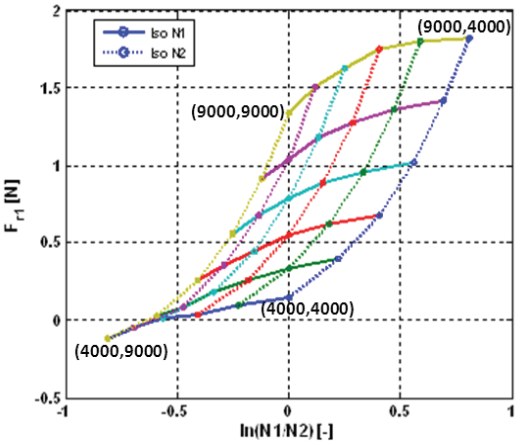

Figure 6.13: FDR80-40: Upper rotor force

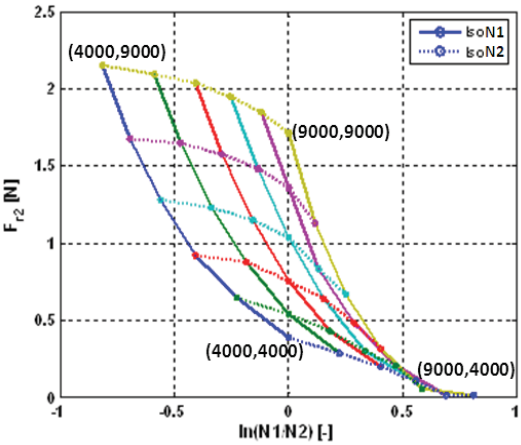

Figure 6.14: FDR80-40: Rear rotor force

Fig.6.13 and 6.14 show the thrust performance of each rotor for SDR80-40 under the speed regime from 4000 rpm to 9000 rpm. Fixing the first rotational speed at 4000 or 5000 rpm, a negative thrust is found in Fig.6.13 by the first rotor as $N_2 < 6000$ rpm. Meanwhile the second rotor always plays a positive role on thrust generation. Comparing the thrust performance at both highest speeds, the maximum thrust generated by each rotor appears all under the condition with the highest velocity of themselves but lowest from the other. Increasing another rotor's speed

always reduces the current one, such as the first rotor thrust decreasing with constant $N_1 = 4000$ rpm and N_2 from 4000 to 9000 rpm. All of these imply that the interaction between two rotors mutually deteriorates their performance, at least in terms of thrust production. The same phenomenons can be observed under different rotor locations such SDR80-20, which could be seen in App.D.3.

6.3.2 Flow analysis under switched speeds

Based on the analysis above, it indicated the first rotational speed should be kept above 5000 rpm to make sure the slower rotor is propulsive as well as the faster one. To specify the feasibility of exchanging the rotational speed, two combinations are chosen to explore the difference on flow characteristics: $N_1 = 6000$ rpm, $N_2 = 9000$ rpm (6000-9000) and $N_1 = 9000$ rpm, $N_2 = 6000$ rpm (9000-6000).

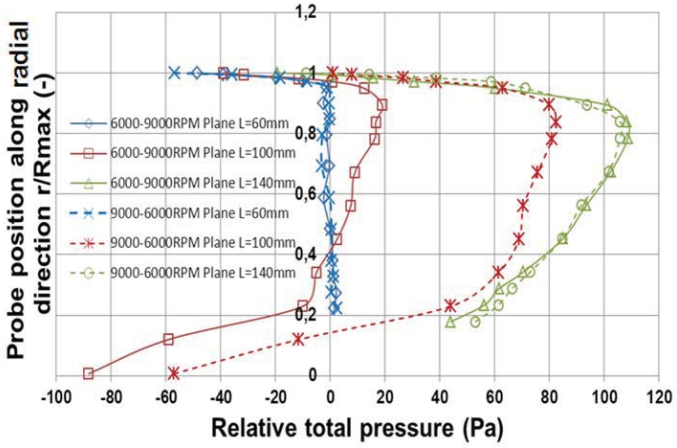

Figure 6.15: Total pressure distribution comparison on different axial planes

Fig.6.15 shows the comparison between these two speed combinations on the total pressure distribution at the planes $L = 60$, 100 and 140 mm. For both speed pairs, the pressure distribution in the plane $L = 60$ mm is almost the same. In the middle plane $L = 100$ mm, due to the faster first rotational speed 9000 rpm, its total pressure is naturally greater than the one 6000-9000. Both speed combinations show the pressure obviously suffers a great loss from both blade tip vortices and the root swirl. Evidently, the swirl effect behaves more important. After the second rotor, the wake provoked by the root of the first rotor is modified by the second one which rotates in the opposite direction. However this is not so obvious because the total pressure tested in the plane $L = 140$ mm is stopped at a radial position approximately 15 mm from the center due to the obstruction of the support components. For both speed combinations, total pressures seem to reach the same level. This reveals that switching speed does not effect the pressure energy transferring to the flow, at least in the region around the two rotors. For the static pressure distribution seen in Fig.6.16, on the plane $L = 60$ mm, the faster first speed can not produce as lower static pressure as 6000-9000 to aspirate more flow. At the middle

station $L = 100$ mm, for 6000-9000, because of the slower first speed, the flow is mainly dominanted by the second faster rotor. Since the two rotors are supported separately and no hub exists between them, the flow ejected by the first rotor forms a flow cone at the root with higher pressure. For 9000-6000, this effect is replaced or overpassed by the radial equilibrium due to the centrifugal effect leading tip pressure lower than the one at the root.

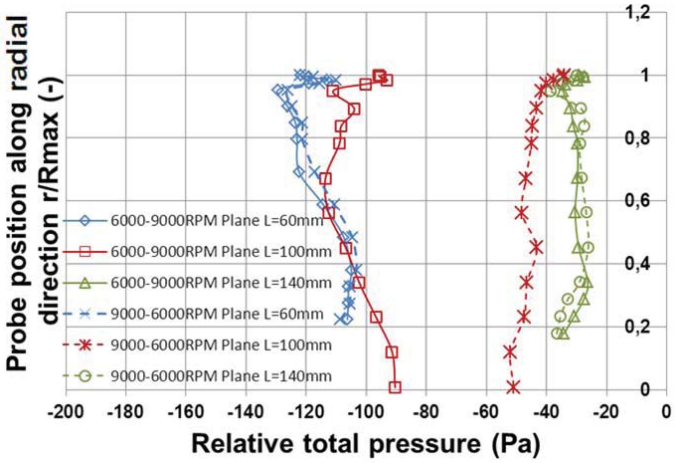

Figure 6.16: Static pressure distribution comparison on different axial planes

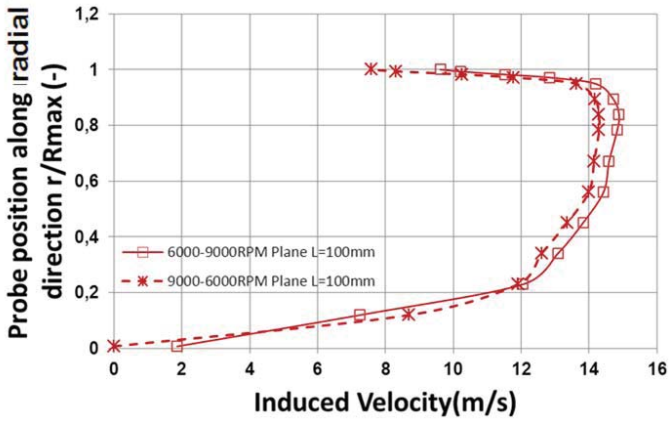

Figure 6.17: Velocity field comparison on middle plane between two rotors

According to Bernoulli equation, at planes $L = 60$ and 140 mm, the flow velocity for 6000-9000 is higher for 9000-6000 because of the lower static pressure, for the same total pressure. Particularly for the middle plane, because the greater difference makes it difficult to compare the two speed combinations, the velocity distribution based on the pressure measurements was calculated, seen in Fig.6.17. The velocity of the system 6000-9000 is almost constantly greater than the one with switched speed in the main region. This further proves slower first rotational speed is more

capable of aspirating and inducing more air flow. Compared to it, the massflow generated by the faster first rotor could make the slower rear one not to perform perfectly as the one in 6000-9000 or even run in the windmill state.

The increased mass flow makes the shroud contribution on the thrust performance different, as seen in Fig.6.18, which presents the static pressure distribution on the shroud for both conditions. At the entrance, the suction effect is increased (pressure decreased) with the slower first speed. That would directly make the shroud thrust increase. The magnitude of the pressure jump ΔP formed in the upstream and downstream by the current system does not present obvious difference with 9000-6000. However, this could not be considered equally to the one which forms the rotor thrust due to the uniform pressure distribution. On the nozzle, the exchanged speeds seems to have no effect on the shroud static pressure. Therefore globally the shroud of the 6000-9000 generates more thrust caused by larger mass flow, and by the depression effect.

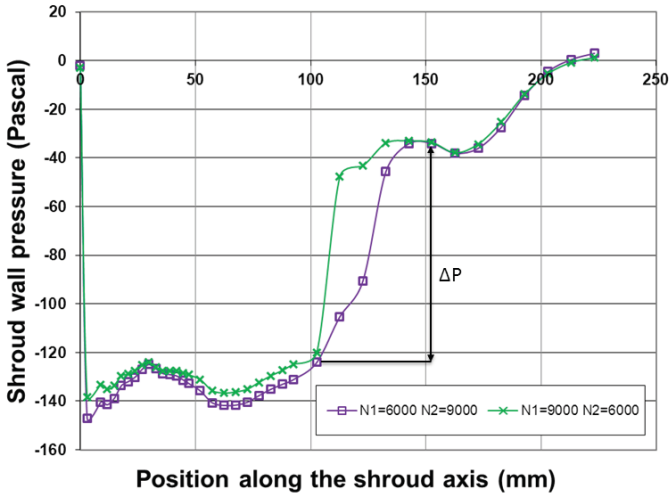

Figure 6.18: Shroud wall pressure from switching speeds

Table 6.2: Performance comparison between system with switched speeds

SDR 80-40 N_1&N_2	**6000& 9000**	**9000 & 6000**
F_{r_1} (N)	0.26	1.76
F_{r_2} (N)	2.04	0.31
F_{sh} (N)	2.79	2.62
PL (gram/watt)	10.03	9.80
$\dot{m}$ (Kg/s)	0.431	0.422
FoM (-)	0.63	0.59

The lower static pressure formed increases the rotors'ability to capture more mass flow. This is the basic reason for the improvement caused by the slower first rotor speed. Table.6.2 shows the details based on the performance averaged on

different planes. The mass flow aspirated by the system 6000-9000 and the corresponding shroud thrust is 0.1 Kg/s and 0.17 N more than the ones with exchanged speed. The two main performance metrics as FoM for rotors and PL for the whole system, are improved with the first slower speeds, even if the rotor power consumed ist higher than the one for 9000-6000.

6.4 Conclusions

To optimize the rotor configurations for shrouded system, the effects of rotor locations and rotational speed were explored. Two rotational speeds – $D_{abs} = 80$ mm, $D_{rel} = 20$ mm and $D_{abs} = 80$ mm, $D_{rel} = 40$ mm were explored on both global performance and flow field. To facilitate the measurements on the middle axial plane between two rotors, $D_{abs} = 80$ mm, $D_{rel} = 40$ mm was decided to be tests at the two rotational speeds pairs – the present one of $N_1 = 6000$ rpm, $N_2 = 9000$ rpm and their switched one. Two main conclusions were obtained:

- The analysis on the global performances and flow field generated by two rotor locations, reveals that the effect from the rotor locations is subtle. With the second rotor set toward backward, IRD/R_r = 0.4 (IRD=40 mm), the flow is under-expanded. The static pressure at exit is decreased and becomes non-uniform; The wall pressure distributed on the shroud is decreased at the after part of the entrance and also throughout the whole nozzle. The curvature of the nozzle makes negative thrust which is more evident than the decreased pressure happened on the entrance part with small curvature. All these slight differences make the rotor location: $D_{abs}/R_r = 0.9$, IRD/$R_r = 0.2$ (D_{abs}=80 mm, IRD=20 mm), perform better;

- The analysis on the global performances and flow field generated by two rotational speed pairs, indicate that the speed combination 6000-9000 is more capable of generating lower static pressure to aspirate more mass flow compared to its switched speeds 9000-6000. The increased mass flow makes the suction peak become stronger, which brings a relative better shroud behavior on the thrust contribution for the configuration with slower first rotor.

Part Ⅲ

3D Numerical Simulations and Comparisons between Experiments and Calculations

Plan of Part

Chapter 7

Methodology of 3D Simulation

Whether one dimensional theory or two dimensional simulation, they all use the actuator disc with pressure jump to replace the real rotor. This ignores the effects from the rotating motion and then can not simulate the wake and all secondary flows produced after rotors even if it might be reduced by the compensation from the second rotor turning at opposite direction. Moreover, for shrouded contra-rotating rotor, flow field is more complex than that of free rotor due to the interaction between shroud and rotors or between two rotors. For the shroud, the in-flow and the wake are refined by it. For double rotor, the tip vortex from upstream rotor impinges upon the downstream rotor. For rotor itself, it exists possibilities to have the vortex to vortex interactions. Therefore further in understanding more on the flow characteristics of the shrouded system, the methodologies for three dimensional numerical simulation were explored in this section: One method for simulating the rotating motion, mixing plane or sliding mesh, was firstly decided through the comparison; Considering the imposition of boundary conditions at the inlet and outlet, two computational fields were proposed and compared using a hybrid mesh built through ANSYS ICEMCFD 10.0 – structured mesh for rotating zones and unstructured mesh for air entrance and exit; For obtaining accurate revolution on vorticity and reducing the computational costs, a whole structured mesh was built and compared with the hybrid one via a commercial software Fluent 6.3. Finally the methodology for 3D simulation was decided.

7.1 Simulation Methods

7.1.1 Multiple reference frames

Generally, the equations of fluid flow is solved in a stationary or inertial reference frame. However, if problems involve rotating blades as in this work, solving it in a moving reference frame shows advantages. With such capability, Fluent allows to activate moving reference frames in selected cell zones. For complex geometries, multiple references could be used through breaking up problems into several zones, with well defined interfaces between the zones.

As for the best performed system in this work: shrouded contra-rotating rotor with the rotor locations at 80 mm from the inlet and 20 mm between two rotors, it involves two rotors rotating at the opposite direction. It needs two reference frames to define each rotating motion separated from the other zones which are mainly static, seen in Fig.7.1.

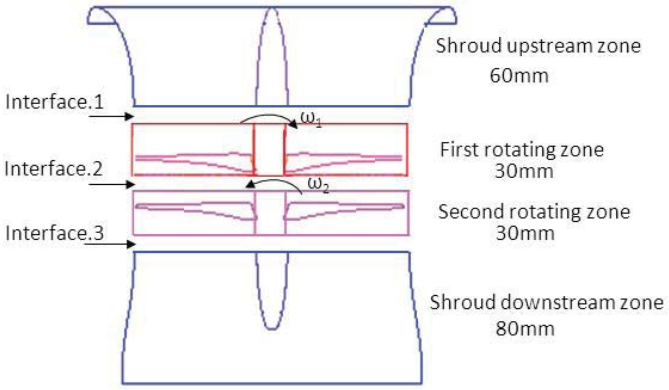

Figure 7.1: Scheme of zone separation and interfaces

Considering the different moving states in the system, Fig.7.1 shows the shrouded system itself is separated into four parts: the shroud upstream zone, the first clockwise rotating zone, the second counterclockwise rotating zone and the shroud downstream zone, with the different definitions of zone length. For the two rotating zones, they are defined to be 30 mm as long as each other. They are separated rightly in the middle of the two rotors. The first rotor zone composes of a short part of shroud inlet having 20 mm. The second rotor zone is then completely situated in shroud cylindric section. Even though some researches revealed the rotating domain size should be kept larger [79], that is obviously not feasible for the flow mainly in-duct. It should be noticed that here, the shroud upstream zone is not correspondent to the shroud geometric component: inlet, but a part of it. However, both upstream and downstream zones for the reference frames should be further adapted to the computational field according to the demand of the simulations.

Among different zones, special treatment should be made on the interfaces for the transformation of vector quantities, which depends on the velocity formulation being used, the detail can be found in Ref.[80]. In Fluent, it provides two typical ways to treat such interfaces: mixing plane and sliding mesh.

7.1.2 Mixing plane and sliding mesh approaches

Like the typical configuration of a single-stage axial flow turbomachine, its analysis often needs to identify the unsteady effects due to the flow interaction between the stator and the rotor (R/S). And the flow at the boundary between adjacent zones of R/S is surely not uniform, the sliding mesh could be a general approach for such case. Based on a final, time-periodic solutions, the data could be also time averaged during one period. Comparing that, probably the mixing plane for a steady solution sometimes would be more complicate if the flow is not radially uniform. For rotor-rotor (R/R) interaction in this work, the sliding mesh might be thus more suitable. However, both of these two methods will be tested at the beginning of the work. The details on their disadvantages and advantages are respectively introduced as

following:

For mixing plane method, flow-field data from adjacent zones are passed as boundary conditions that are circumferentially averaged on interfaces. Due to it the unsteadiness of flow such wake, separation and so on are removed. It is unable to resolve the interaction between two rotors as the influence of upstream rotor washing on the downstream one. However, it could reduce the computational cost to obtain approximations of the time-averaged results compared to the unsteady computations. It is often used to gain initial estimation of the flow;

For sliding mesh, it generally solves unsteady flow of time periodic. That is the flow solution repeats with a period related to the speeds of moving domains. Principally, the flux across the interface are computed on the cells from the intersection of the two interface zones, which is determined at each time step. As the most accurate method for simulating flows in multiple reference frames, meanwhile it has also the most computationally demanding.

Both mixing plane and sliding mesh, they do not need to have conformal meshes on the interfaces for different reference zones, even allows to apply different mesh types.

7.2 Computational Field, Mesh and Numerical Model

As illustrated above on the simulation methods for rotating body, the shrouded contra-rotating system itself is separated into four parts for different simulation reference frames. For specific computational fields, it needs to take into account of the actualities for the definitions of air inlet and downstream zones, which should be closer to the dynamic one as explored in Chap.3.5.3. Based on it, mesh and numerical model should be made.

7.2.1 Computational field

The computational field is composed of the air entrance, the rotor zone and the exit downstream zone. Both air entrance and downstream zone should be adapted to the reality and boundary conditions.

For air entrance, Several factors should be considered in its definition of computational field: firstly, corresponding to the reality, the boundary condition of the air inlet should be chosen as "Pressure inlet" which defines the upstream total pressure; secondly, the 2D simulations on the shroud inlet revealed that the geometrical leading edge radius has great difference with the dynamic one, which should be adapted for the system analysis; the experiments in Part.II also shown non uniform flow behaviors on the shroud geometrical inlet and leading edge. Therefore, to avoid the problems caused by the imposition of inlet boundary condition and make sure the flow passing through it has uniform features which could be close to the far flow field as much as possible, a kind of geometry similar half of sphere was introduced on the top of shroud inlet, seen in Fig.7.2. It shows that the computational field of air entrance includes sphere head geometry given a radius great enough which

is 2.5 times the rotor radius. It should be noticed that, in order to capture more information of the air flowing on the shroud inlet lip, the place where sphere cap is not rightly on the lip but a bit bending towards the external. Based on such definition of the inlet, flow angle is imposed too but it is assumed to have no effect since the velocity is very low at the inlet boundary.

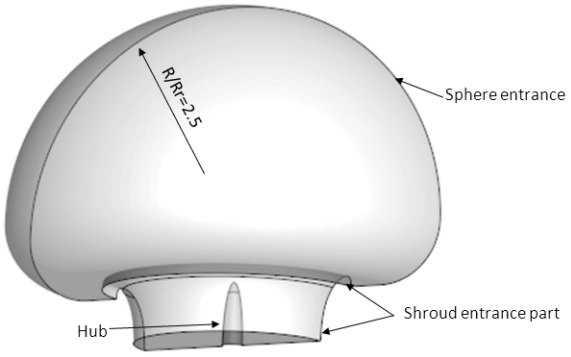

Figure 7.2: Computational field of air entrance

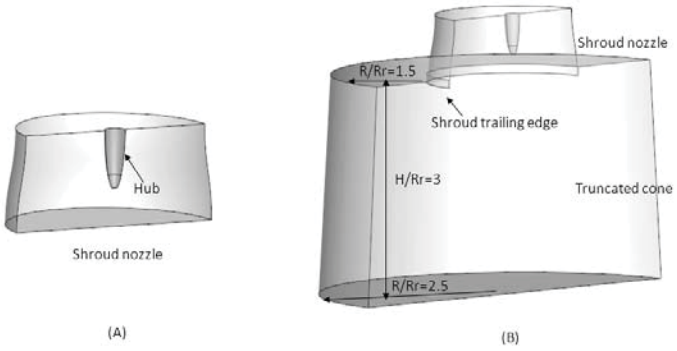

Figure 7.3: Computational fields without (A) and with (B) truncated zone

For the downstream zone, at its exit, the boundary condition "Pressure outlet" - static pressure condition, will be used. Such condition produces a difficulty to define the location where the exit is built. As explained above, since the pressure boundary is applied, the surface imposed by such a condition should have uniform flow features. This is quite difficult to find because the turbulence is considerable once the flow is exhausted after the nozzle exit, which demands a large space to calculate in the downstream shroud. Except the computation cost, this gives a difficulty as well to the simulation due to the mixing flow boundary between the exhaust flow and the ambient one, easily resulting in a reversed flow. The experiments in Part.II indicated that for the second rotor location at 20 mm after the first one, the static pressure on the exit could reach to the ambient one. This implies the "Pressure outlet" probably could be imposed directly on the shroud nozzle exit. And the computational field of the exit downstream domain could be firstly considered as shroud nozzle. However,

since the effect of such imposition on the upstream flow field are not sure, another computational field was defined as a truncated cone shape connecting to the shroud nozzle exit as larger as possible to allow the flow features on its outlet close to the demand of pressure boundary condition. These two corresponding computational zones for air expanding are presented in Fig.7.3.

As the explanation, the first definition of computational field on the exit downstream zone is the shroud nozzle naturally with the hub in the center. The second definition is adding a huge truncated cone followed to the shroud exit. This huge truncated cone has a top and bottom radii of 1.5 and 2.5 times the rotor radius, along with a height almost 3 times the rotor radius. As same as the sphere cap shape for air entrance, here in order to avoid the treatment on the boundary condition of shroud trailing edge, the truncated cone is extended few millimeters to its external. For both downstream fields, they will be verified firstly in the simulation in order to choose a better one for analysis the whole system.

For the computational field of two rotating zones, they are quite sure and fixed as same as the ones in the reference frame.

The whole computational field is finally comprised by the four separated domains: air entrance with half of sphere geometry head, two rotating zones and the air downstream domain of either shroud nozzle or additional together with the truncated cone shape. Therefore, two combinations of the computational fields were decided. As the system is axisymmetric, half of them are applied as a computational field in the final simulations.

7.2.2 Mesh

According to the geometry of computational fields, different mesh types were applied in different parts.

7.2.2.1 Air entrance and downstream exit domain

As shown in Fig.7.2, taking into account the geometry with sphere at the entrance, an unstructured mesh was chosen due to its simplicity for both air entrance and downstream domains in order to firstly verify the position imposing the "Pressure outlet". In ICEM, unstructured mesh does not need to build the block associating the geometry curves to its edges. This substantially simplify the mesh making procedures. The mesh on these two parts was made in ICEM as a whole, seen in Fig.7.4.

Fig.7.4 presents a tetrahedra unstructured mesh was mainly applied to generate the meshes on two computational field combinations of air entrance and downstream domains. For the boundary layer near shroud wall and hub, the prism mesh was used to treat the wall functions. The size of the first layer was placed at 0.03 mm and thus the same for double rotor. In total, 20 prism layers were created with the thickness geometrically increased.

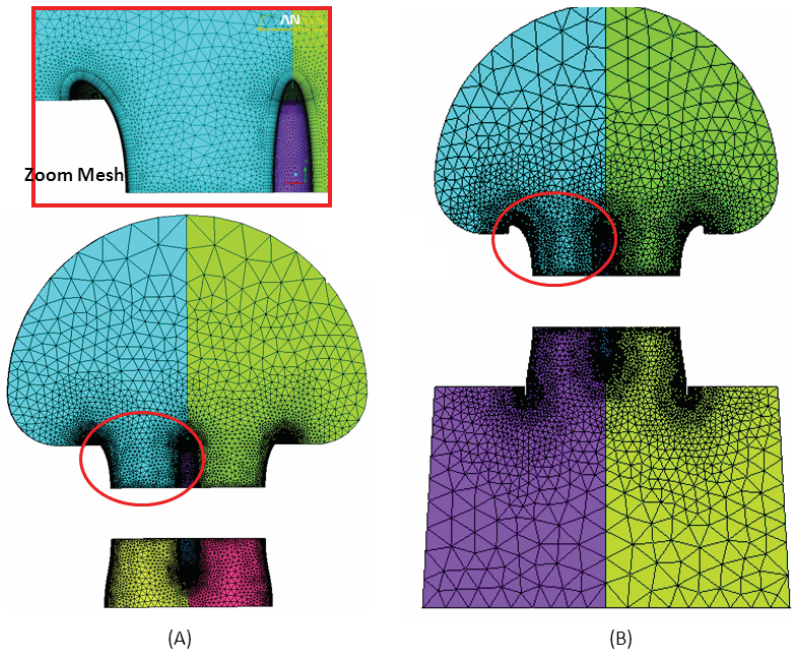

Figure 7.4: Unstructured mesh for air entrance and downstream domains without (A) and with (B) extended cone

7.2.2.2 Rotating zones

As the most important computational part of the systems, the rotating zones involves quite complicate flow physics as the wake generation, vortex interaction and so on, which affect the system performance. The treatment of the mesh in these two zones directly affects the simulation solution. Moreover, the geometry of rotor blade seems too complex to use unstructured mesh for controlling a better mesh arrangement. Hence a structured mesh of hexahedra type based on a well suited block topology is demanded.

One of main objectives for the mesh is minimizing the total size, which wins more importance for the double rotor. At the same time, the effects of boundary layer and turbulence have to be revealed, which requires a high density of the mesh near the wall and behind the blade in the region of the wake. Therefore, for the mesh refinement on the shroud wall and the hub, a utility of two "O-Grids" was decided due to the cylindric rotating computational field. This surely needs blocks to be well defined at the beginning.

Fig.7.5 (A) shows one O-grid block which was created around the hub and followed by another one near the shroud. The central block is radially divided into four parts for the blade and the collapse of the block edge around the blade tip, where would result in a mesh distortion once the hexahedra type is used, due to the sharp edges of the block adapted to both leading and trailing edges at the tip. Those tangential section at the tip restricts the blocks above and below it. Therefore the

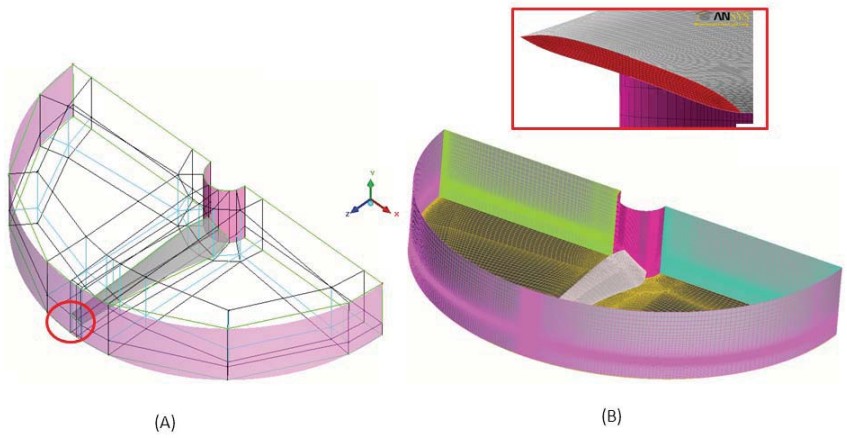

Figure 7.5: Block topology (A) and Structure mesh(B) of rotating zone

blocks around blade tip and between it and shroud are turned into Y-blocks, seen in the zooming subfigure.

Based on it, final mesh was made as shown in Fig.7.5 (B). Since the two rotational domains for the first rotor and second rotor are almost the same, so for the second rotating field, the mesh could be made exactly in the same way.

7.2.3 Numerical model

7.2.3.1 Boundary conditions

Based on the definition of the computational field, different conditions are decided to be given at its boundaries. As introduction on the two types of fields, the boundary conditions on the inlet and outlet have already been mentioned, where the "Pressure" inlet and outlet were given. These conditions are consistent to the reality. The detail on other boundaries could be seen in Fig.7.6.

For the first computational field definition, since the multiple reference frames have been decided to use, the surfaces connecting different domains are defined as interface condition. Three such boundaries are thus given. As the two rotors are defined as rotations relative to the air entrance and exit through constant rotational speeds given to the whole first and second rotating domains, the flow unsteady state could be considered to be periodically fluctuating. The symmetrical surfaces of each domains are then defined as periodic boundaries. For other solid parts as shroud, rotor and hub, they are all naturally thought as walls but with different definitions on movements: absolutely static state for shroud wall and hub, relative rotating motion relative to the adjacent cells for blades.

Except all the boundaries for first computational domain, the addition of truncated cone introduces another boundaries for the field: the surfaces on the top and side one. Here, because the flow turbulence might be evidently stemming from the wake and the mixing flow boundaries, under which a reversed flow is easily occurs on the exit. In order to avoiding the non-physical phenomena caused by the re-

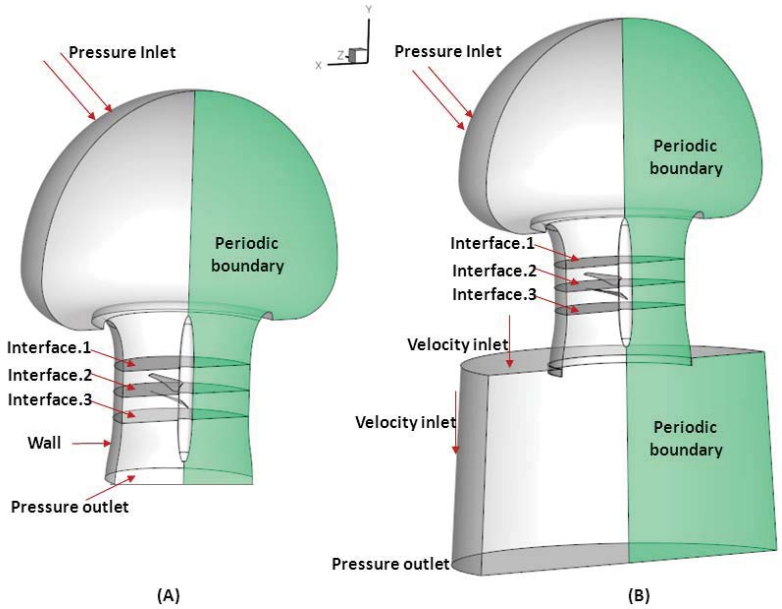

Figure 7.6: Boundary conditions of computational field without (A) and with downstream cone

versed flow, "velocity inlets" are then decided to give on these two surfaces. Also for minimizing the influence due to the velocity impositions, a minimum amount of velocity should be founded firstly to avoid the reverse flow.

7.2.3.2 Solvers

For choosing the numerical solvers, some basic characteristics of this shrouded system should be firstly identified, such as flow compression and turbulence, which are decided respectively by flow Mach number and Reynolds number.

Maximum velocity is expected at the tip of the blade due to the radius, where the local mach number could justify the air compression. As following equations, the Maximum mach number at the tip is about 0.25 which is surely maintained below the limit of $Ma = 0.3$ for compressible flow due to the maximum rotational speed. The air flow could be then assumed as completely incompressible. Therefore the "pressure-based" solver was chosen with an implicit numerical treatment.

$$\begin{aligned} &\text{radius of the blade tip:} && R_t = 0.089 \text{ m} \\ &\text{maximum rotational speed:} && N = 9000 \text{ rpm} \\ &\text{maximum velocity at the tip:} && V_t = \frac{N\, 2\pi\, R_t}{60} \approx 85 \text{ m/s} \\ &\text{Mach number:} && M_a = \frac{V_t}{a} \approx 0.25 \quad a = 343.24 \text{ m/s} \end{aligned} \tag{7.1}$$

According to the Reynolds number definition, for the shrouded system studied in this work, two Reynolds numbers for whole shroud system and special for the

blade were calculated in Eq.7.2. For the system, the characteristic velocity is given by the axial velocity, which is averagely around 10 m/s under a usual rotational speed for such system as shown in the experiments. The characteristic length is then considered as the shroud whole length 200 mm due to the should wall greatly inducing turbulent. For the blade, the classical Reynolds number on the airfoil at 75% blade length is considered, where the chord is around 9 mm and the velocity for 9000 rpm is approximate 62.8 m/s. As the equations, both Reynolds numbers for system and blade are far lower than 3000 which is the separation for turbulent and laminar flow. The flow is thus turbulent.

$$\begin{aligned}
&\text{Reynold number:} && Re = \frac{u\,d}{v} \\
&\text{Charateristic velocity:} && u_{sys} = 10 \text{ m/s} \qquad u_{bla} = 62.8 \text{ m/s} \\
&\text{Charateristic length:} && d_{sys} = 0.2 \text{ m} \qquad d_{bla} = 0.01 \text{ m} \\
&\text{Reynolds number:} && Re_{sys} \approx 85000 \qquad Re_{bla} \approx 40000 \gg 3000
\end{aligned} \tag{7.2}$$

Then for the simulation, Spalart-Allmaras turbulent model was chosen due to two reasons: using only one additional equation does not appear too costly; although relatively simple, it is known to have good results for boundary layers exposing adverse pressure gradient. As for the regions near the walls, two options are implemented in Fluent: if this mesh is sufficiently fine, that is to say, the centroid of the cell adjacent to the wall is located inside the viscous sublayer, the speed of the shear stress can be calculated directly. Otherwise, it is assumed that the centroid is located within the logarithmic layer and thus the logarithmic law is applied. The value determines the distinction between these two options is ${y_1}^+$. The viscous sublayer is characterized by values of ${y_1}^+$ of about ${y_1}^+ <1...5$. It follows a layer of overlap between $5<{y_1}^+<30$, after extending the logarithmic layer between $30<{y_1}^+<300$. The mesh must satisfy one of these requirements to avoid the buffer layer.

Since the simulation apply the multiple reference frames, the absolute velocity formulation was applied because of the relative huge air entrance and downstream exit zone having no rotating motion, and the shroud wall keeping fixed without relative movement. As the mesh cell number, calculations were redone with modified parameters for better calculation time and also convergence rate. "Coupled" method for pressure-velocity coupling was founded a significant decrement on these two demands. The Courant number is remained as 200 as default.

7.3 Calculations Based on Hybrid Mesh

Based on the two combinations of hybrid meshes, the preliminary calculations were conducted for several objectives: comparison between mixing plane and sliding mesh, choosing the downstream exit zones, and also validating the hybrid mesh.

7.3.1 Calculations with mixing plane method

For using mixing plane method, three pairs of mixing planes were made on the grid interfaces. However on the preliminary exploration of the mesh without downstream exit zone, the calculation results show a problem causing the date transferring through these mixing plane pairs at two same rotational speeds equal to 6000 rpm.

Table 7.1: Mixing Plane: Mass flow on different passages

Passages	Mass flow (Kg/s)
Inlet	0.2270
Upstream rotor passage	0.3504
Downstream rotor passage	0.3978
Outlet	0.4226

Table.7.1 presents the mass flow passing through different passages. There are great difference on the amount: the flow through the outlet is increased by 86% over the entrance. This difference is clearly non-physical and can not be neglected. This implies "mixing plane" is not practical and lose the precision for modeling the case which involves a great distortion of the flow.

7.3.2 Calculations with sliding mesh method

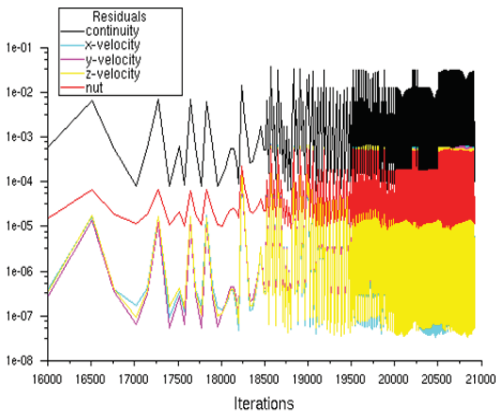

Figure 7.7: Residuals of calculations with extension exit

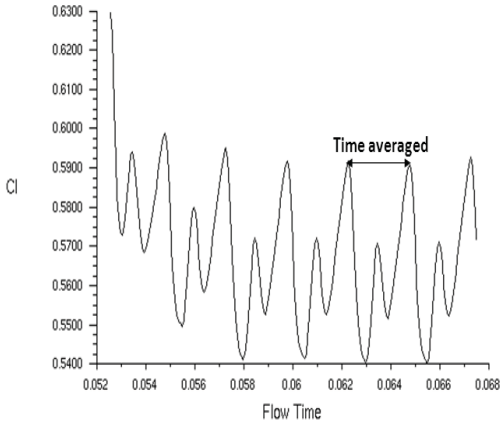

Figure 7.8: C_l of calculations with extension exit

The sliding mesh method realizes the gradual contra-rotation of two rotor mesh zones with instantaneous interpolation. For each position, the memorized solution is calculated according to an unsteady configuration. Therefore, the calculations are started with a relative large time step by which the system rotates 20°. This is used in the first five circles until the appearance of periodically stationary solution. A smaller time step which could allows the system rotates 2° is following used in order to obtain more precise solutions in two circles. Finally, the time averaged results on

pressure and velocity field are calculated at least during one periodic time. Through time step settings, both unstructured meshes with and without the exit downstream zone were calculated under the contrarotational speed pair $N_1 = N_2 = 6000$ rpm. Based on their final periodical revolutions independent on time, as the residuals and lift coefficient of rear blade seen in Fig.7.7 and 7.8, their comparison on the time averaged mass flow was made as Table.7.2.

Table 7.2: Sliding Mesh: Mass flow on different passages

Passages	**Mass flow (Kg/s)**	
	Without downstream zone	With downstream zone
Inlet	0.3307	0.3341
Nozzle Exit	0.3306	0.3341

Table.7.2 shows both meshes have effective solution of the mass conservations on the inlet and exit. The factor causes theis difference on mass flow is an ambient pressure rightly on the actual nozzle exit, which might influence the upstream flow condition. This effect still needs to be further identified.

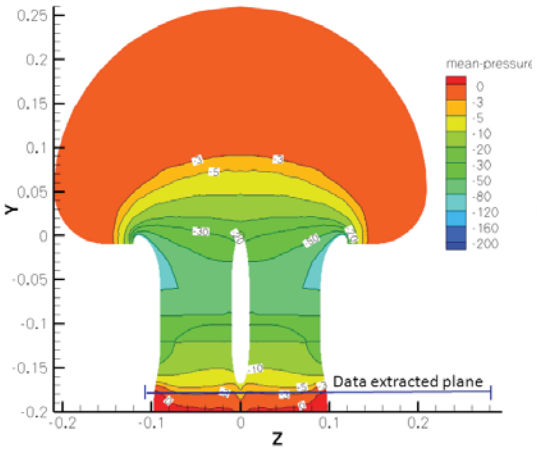

Figure 7.9: Mean static pressure for mesh without downstream zone

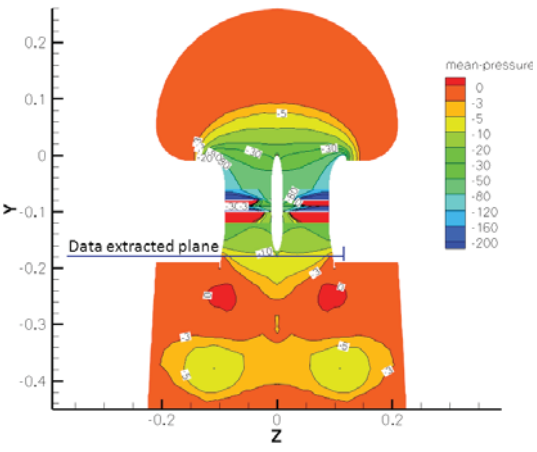

Figure 7.10: Mean static pressure for mesh with downstream zone

Comparing the mean static pressure distribution on iso surface $x = 0$, Fig.7.9 and 7.10 present that both computational fields have very similar features in the air entrance. However, the imposition of ambient pressure on the nozzle exit leads to a movement of the relative zero pressure up to the position parallel with the hub. On the contrary, the downstream computational field has a relative lower pressure distributed on the exit. Through extracting a specific lines 20 mm up from the nozzle exit, the comparison on the mean static pressure was made among the calculations of both computational fields and experiments, seen in Fig.7.11. It indicates that the pressure from the simulation with downstream computational field has quite

similar pressure distribution on most zones particularly close to the system center. Near the shroud wall, as explained in experimental study, between the pressure data tested respectively by the wall pressure transducers and static pressure probe, there is difference. That is because the modification from the probe to local flow decrease the precision of the experiment. Therefore comparing to the computation with the pressure boundary imposition directly at the actual shroud exit, globally the simulation with an extension of the downstream zone shows a similar trend of static pressure radial distribution at least. And their difference on the specific amount is basically came from the mass flow generation.

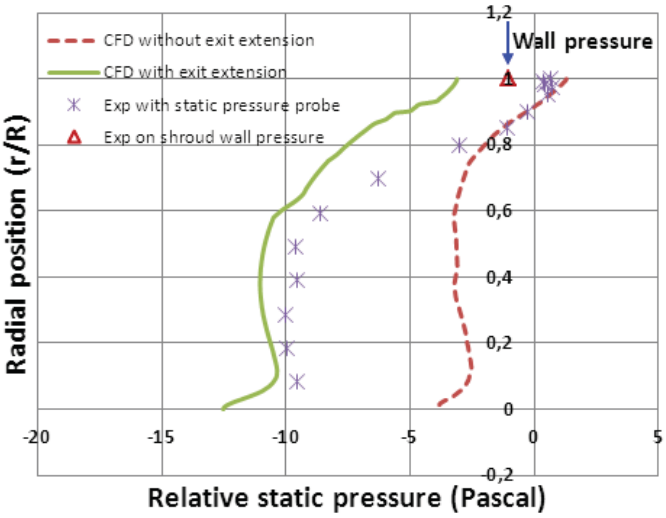

Figure 7.11: P_s among calculations on two meshes and experiments

However, for the distribution of vorticity magnitude which is typical quantity to evaluate the characteristics of flow velocity and flux, both Fig.7.12 and 7.13 show there is quite strong vorticity feature appearing in air entrance, particularly near the system axis before the hub head. On the contrary, a weak vorticity presents around hub head, where should exit an obvious velocity curl due to hub profile. All of those seems unlikely as the flow aspirated by the shrouded system should be uniform without a spin-driven motion before passing the two rotors. This is might caused by the unstructured mesh or inaccurancies in vorticity post post computation speically along the axis which Fluent can not accurately resolve.

As the explanation above, the computational field with air downstream zone after shroud nozzle exit is better for the ambient pressure imposition. Based on it, in views of the inaccuracy on the evolution of vorticity field, together taking the mesh quality and cell number as well as the computation costs into account, the unstructured mesh should be redefined or modified as a structured one.

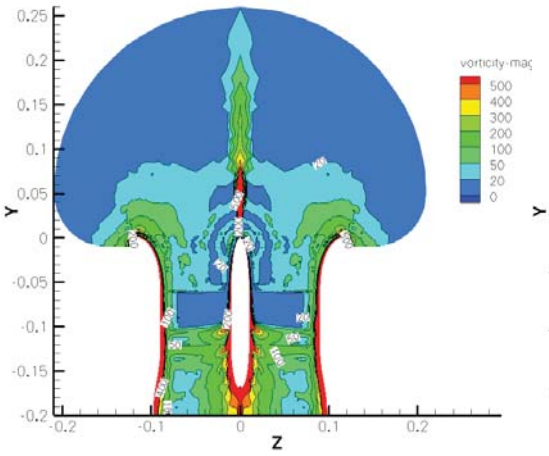

Figure 7.12: Vorticity for mesh without downstream zone

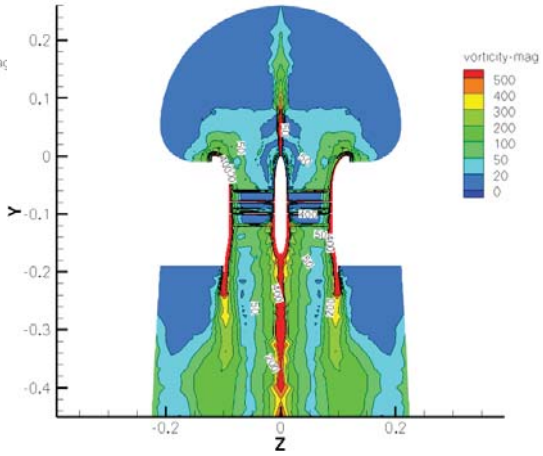

Figure 7.13: Vorticity for mesh with downstream zone

7.4 Structured Mesh Proposition and Calculation

7.4.1 Structured mesh

The advantage of structured mesh is to easily control the topology and refine the mesh at necessary positions, even though it brings more complex procedure on the block treatment. This has already seen in the mesh for two rotating zones. For the air entrance and downstream zones, it has been decided to built the structured mesh separately. The meshes for four different zones can be finally combined into a integration for whole system.

7.4.1.1 Air entrance and downstream zone

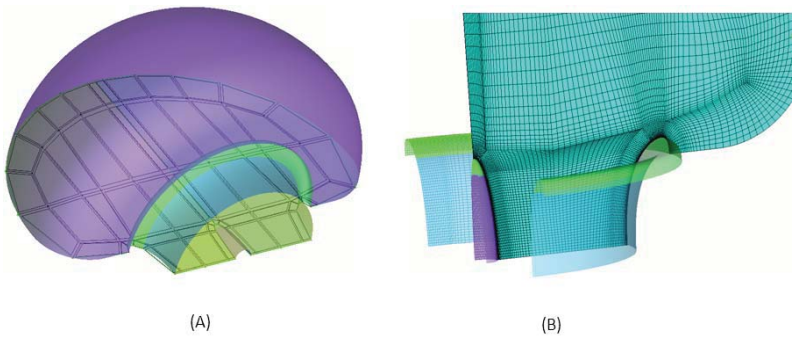

Figure 7.14: Block (A) and Mesh (B) of air entrance

Fig.7.14 shows the arrangement of the blocks and mesh for the air entrance. Obviously three main O-grids were made respectively for the sphere head, the hub and the shroud wall. The refinements of meshes on these three positions are then

controllable. The first mesh size from the the shroud and hub wall is defined as 0.03 mm that is proved to be sufficient for the utility of enhanced wall function with the Spalart-Allmaras turbulent model.

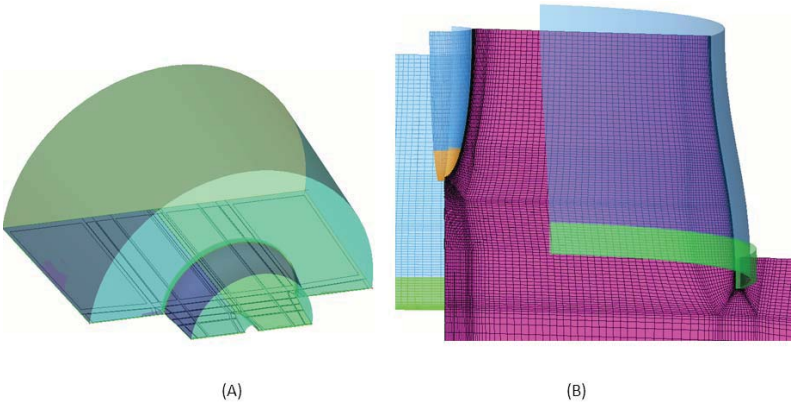

Figure 7.15: Block (A) and Mesh (B) of air downstream zone

Comparing to the air entrance, the treatment for the mesh of the exit downstream zone seems easier due to the regular shape of truncated cone. Fig.7.15 shows for the block topology two O-grids were made to refine the mesh on the solid walls of shroud and hub, as same as the air entrance. The refinement of mesh could be seen in Fig.7.15 (B). Both meshes for entrance and exit are quite similar.

7.4.1.2 Structured mesh for whole geometry

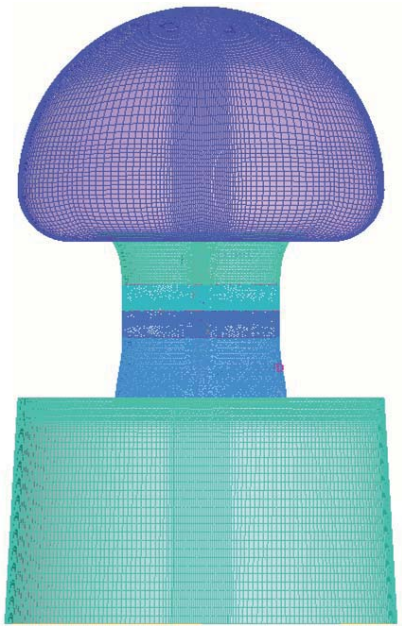

Figure 7.16: Overall view of whole structured mesh

The overall view of whole structured mesh can be seen in Fig.7.16. The field relative far from the shroud inlet and outlet having the meshes with relatively great size, greatly decreases the mesh number. Specifically for the meshes around or on the blade and hub, seen in Fig.7.17 and 7.18, the refinement were well made at the blade roots and adapted for different blade elements with different switched angles. It should be noticed that the meshes on the interfaces of different computational domains are not conformal, which is allowed by the method of sliding mesh as mentioned before. Those refinements greatly improve the mesh quality.

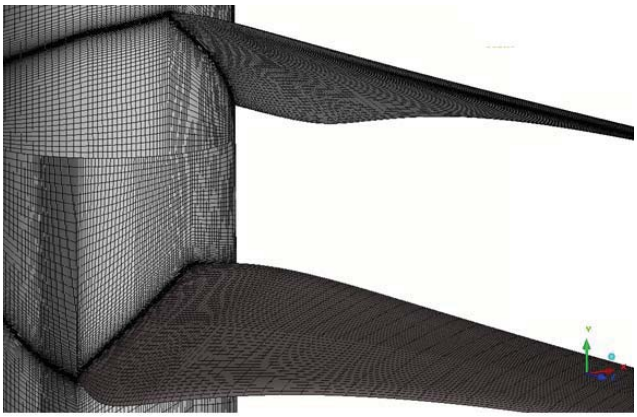

Figure 7.17: Mesh on the hub and blades

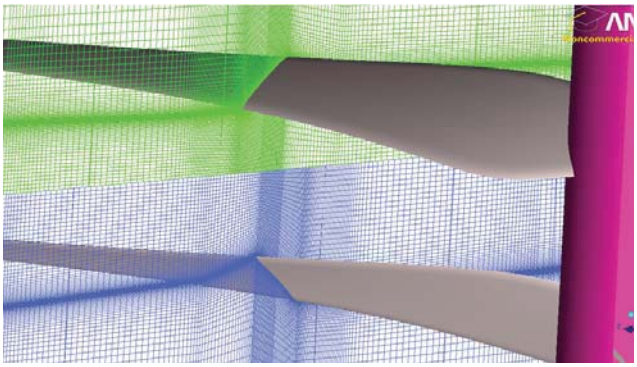

Figure 7.18: Mesh around blades

7.4.2 Comparison with unstructured mesh

Comparing to the unstructured mesh, the detail for improvements on mesh itself is summarized in Tab.7.3. The structured mesh decreases the cell number by about 1.65 million. This fastens the calculations at two same rotational speeds 6000 rpm, and saves time almost 48 hours. As for the mass flow obtained by different meshes, there is just few grams difference, which implies whether structured or unstructured mesh would not affect great on system global performance.

Table 7.3: Comparison between structured and unstructured meshes

Mesh	**Structured**	**Unstructured**
Mesh cell number	6050000	7700000
Determinant (min)	0.57	0.21
Equiangle Skewness (min)	0.22	0.15
Angle (min)	20.16	6.89
Quality (90% Mesh)	> 0.85	> 0.65
Performance	**Structured**	**Unstructured**
Computation time (h)	101.2	148.6
Rotational speeds (rpm)	6000-6000	6000-6000
Mass flow (kg/s)	0.3360	0.3341

Further in comparison on the vorticity as there is problem for unstructured mesh, Fig.7.19 indicates the huge field full of the strong vorticity shown in Fig.7.13 has been removed by the correct solution. Only small region around the hub head reasonably has relative intense vorticity. The vorticity is generated by the boundary layer and is convected in the wake. The most strongest is thus naturally occurred after two rotors, and following the hub end and nozzle exit.

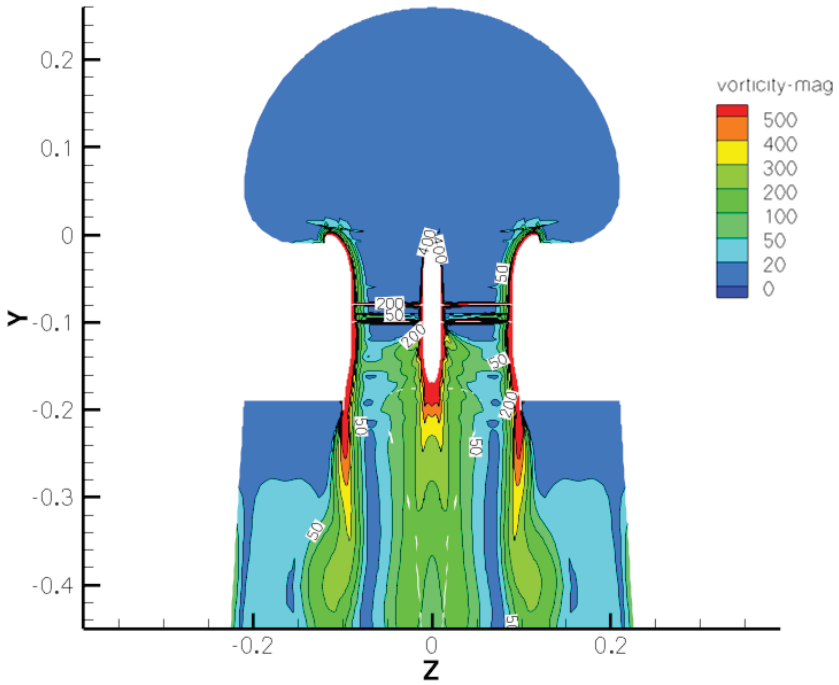

Figure 7.19: Vorticity for structured mesh

7.5 Conclusions

The methodology of 3D numerical simulation which introduces the real rotor profile and simulates the rotating motion was developed as an implemental tool for experiments. The method for treating the data transformation on interfaces between different zones, the definition of computational field, the boundary conditions and the mesh were decided through the calculations and comparisons. It could be summarized:

- The comparison on two methods for treating the data transformation on interfaces – mixing plane and sliding mesh reveals that for such system the mixing plane is not feasible to solve the physics reasonably. It results in a non-conservation of the mass flow at the different passages inside the shroud;
- The comparison on two definitions of computational field which all have an entrance of sphere cap but different exit with or without the downstream zone, indicates that a "pressure" boundary condition imposed rightly at the nozzle exit influences the upstream flow condition. It leads to an ambient pressure appearing advanced in the position parallel to the hub. Compared to that, a slightly difference from the computational field which has the downstream zone with the experiment can be supposed due to the difference of the mass flow;
- The comparison between unstructured mesh and structured mesh shows the latter gives a right solution on the distribution of the vorticity magnitude through Fluent. Furthermore, the structured mesh also saves the computation time while improving the mesh quality.

Therefore, the sliding mesh method, the computational field with downstream zone and a whole structured mesh were decided to be used in the further exploration of both steady and unsteady performance, based on a complete validation.

Chapter 8

Validation and Exploration of 3D Simulation

Based on the sliding mesh method, the computational field with half sphere air entrance and downstream domain of truncated cone shape, and the structured mesh for the whole propulsion system, this work aims to first validate the 3D simulation results with the experiments on steady characteristics including the global performance and flow field. Comparing with the extended momentum theory and 2D axisymmetric simulations, which replaced rotors as a pressure jump and did not consider the rotor profile influence, the 3D simulations introduced the actual rotors to explore the instantaneous features as a more efficient way. The unsteady characteristics were then analyzed through the 3D simulations, particularly on the flow pattern through the shroud passages, the blade spanwise and the tip. Due to the constraint of experiments, the effects of switched speeds and the rotor locations on the flow were complemented in 3D with numerical methods.

8.1 Validation and Observation of Steady Characteristics

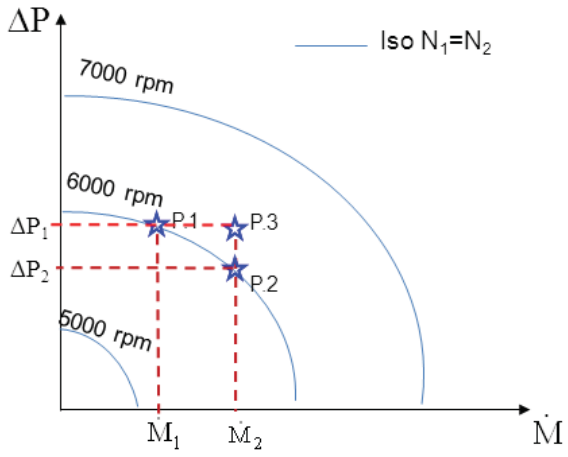

Figure 8.1: Pressure jump ΔP versus mass flow $\dot{m}$ for different iso speeds

For the rotor, the pressure jump ΔP formed on both sides of the rotors could stand for the rotors' function as a flow generator and quantify the rotor thrust

($F_R = \Delta P/A_R$). Meanwhile for shroud, its performance greatly depends on the mass flow $\dot{m}$. The system behaviors are thus basically steered by these two variables ΔP and $\dot{m}$. However, both of them have different relations with the rotational speeds, seen in Fig.8.1, which gives multiple possibilities to choose a reference for the validation and comparisons of the 3D simulations with the experiments. Fig.8.1 shows Points 1 and 2 have the same rotational speeds but generate different mass flow $\dot{m}_1$ and $\dot{m}_2$. Comparing P.1 with P.3, they are in different speed levels but with the same ability to generate mass flow. Similar comparisons among those three points on the relationship between speed and pressure jump can be derived. Therefore, for the general reference rotational speed chosen to be a comparison reference, this might produce differences on mass flow and pressure jump as well, since they are interdependent. Due to the difficulty to obtain an accurate location to define the pressure jump quantity, the mass flow can be considered as a reference for validations. Therefore, applying the references of the same rotational speeds (Ref.N) and mass flow (Ref.$\dot{m}$), the validation of 3D simulations will be conducted.

8.1.1 Global performance comparison based on $\dot{m}$ or N

Table 8.1: Comparison on global performance between CFD and Exp

Performance	Ref.N 3D CFD	Ref.$\dot{m}$ 3D CFD	Exp Exp	Ref.N Var (%)	Ref.$\dot{m}$ Var (%)
N_{r_1} (rpm)	6000	5790	6000	0	3.3
N_{r_2} (rpm)	6000	5790	6000	0	3.3
$\dot{m}$ (Kg/s)	0.3360	0.329	0.326	3.1	0.9
F_{r_1} (N)	0.641	0.558	0.535	15.5	4.3
F_{r_2} (N)	0.793	0.723	0.760	4.4	-4.8
F_{sh} (N)	1.790	1.600	1.530	16.9	4.5
F_t (N)	3.224	2.881	2.825	14.1	2.0
Q_{r_1} (N.m)	0.0168	0.0152	0.0148	13.4	2.7
Q_{r_2} (N.m)	0.0194	0.0179	0.0184	5.6	-2.7
P_t (watt)	22.730	20.140	21.215	7.2	-5.1
PL (g/watt)	14.6	14.5	13.6	7.5	6.6

Since the solutions are periodic, the global performance from the simulation was time averaged. Table.8.1 gives an overall view on the global performance comparisons between the 3D simulations (3D CFD) and experiments (Exp) based on the same inputs of two rotational speeds 6000 rpm and almost the same mass flow, which is approximately 0.326 kg/s, due to the difficulty of obtaining the corresponding speeds. Globally, the same mass flow input has a solution which is more consistent with that of experiments, as long as they have the same rotational speed input. For each system performance, the variation could be easily controlled lower than 5% except for PL. On the other hand, under the same speed input, the difference on mass flow is 3.1% with experiment, which brings a relatively large variation

on shroud thrust, F_{sh} of 16.9%. Meanwhile, the upper rotor generates 15.5% more thrust than in experiments. This might be caused by a possible blade distortion under a pressure loading in reality, which can not be considered in CFD. Those two great variations consequently lead to variations in torque, power and power loading.

When compared with the rotational speed, a better consistency with experiments based on the same mass flow indicates its importance on the system's global performance.

8.1.2 Flow field comparison based on $\dot{m}$ or N

Further in the validation on the flow field, Fig.8.2 indicates the simulation and experimental differences of shroud thrust between the simulations and experiments. Comparing with the test, the same mass flow input has closer distributions on shroud static wall pressure. The small difference on shroud thrust of 4.5% is mainly produced by slightly higher static pressure distributed at the locations where the leading edge starts to bend outward. Under the same speeds, the simulation obtains a global lower wall pressure on the shroud and consequently the shroud produces greater thrust with the increment of up to 16.9%.

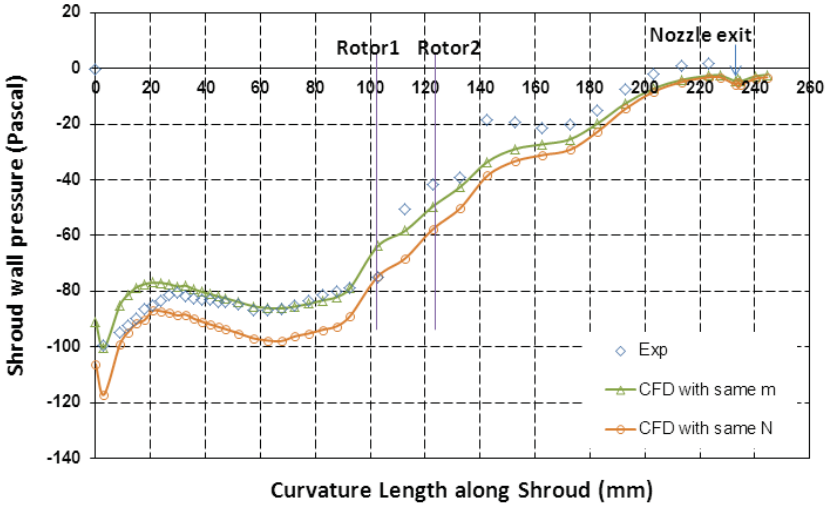

Figure 8.2: Comparison on P_{sh} among CFD and Exp based on the same $\dot{m}$ or N

For both solutions from simulations, it is obvious that the difference tends to be greater after the first rotor. It reaches maximum at the position 20 mm after the second rotor. Since the flow's unsteady features become significant during the rotor passage, and the experiment data was obtained according to a certain frequency, which it is not precisely time averaged, the existence of such difference seems to be logical. At 10 mm from the nozzle exit, the shroud wall pressure reaches the ambient pressure in the experiments but slightly over expanded in the simulations. To understand such difference, the flow structure near the shroud trailing edge should be explored deeper, as seen in Fig.8.3. At the shroud trailing edge, there are

vortices fields just under it due to the sharp corner. This makes the flow ejected from the shroud nozzle to be separated from that of the environment, and to be mixed at the downstream trailing edge. However, this might have not existed in the experiments due to the fabrication of a rounded edge.

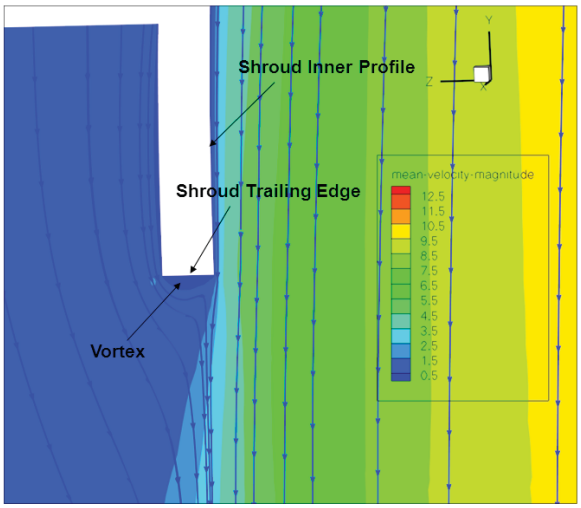

Figure 8.3: CFD: The flow streamline around the shroud trailing edge

Fig.8.4-8.7 and 8.8-8.11, respectively present the total and static pressures relative to the atmospher on several chosen axial planes of both calculations and tests.

Due to the difference of the rotational speeds, the current flow at 6000 rpm naturally provides a greater total pressure when compared to the rotational speed of 5790 rpm, as shown in Fig.8.4-8.7. Comparing with tests, on the main effective region, there is no great difference on the distribution of total pressure. And the same mass flow input seems more similar to that of tests particularly on the planes L=60 mm and nozzle exit, which is not obvious. It should be noticed that, the relative greater difference always appears at the positions near to the shroud wall where r/R_{max} is close to 1. The effect of the boundary layer is more significant in simulations. The reduction of total pressure near the wall lasts for a longer distance, which is more evident on planes before the rotors. This might be caused by the application of turbulent model Spalart-Allmaras and enhanced wall function, or maybe it is even because the actual boundary layer starts as laminar. On one hand, this model with one equation has relative lower precisions on solving the boundary layer. On the other hand, before passing the rotor passages, the flow has not been accelerated sufficiently and it behaves more like laminar, under which the flow is highly dominated by viscosity, the turbulent model probably a bit loses its feasibility.

From Fig.8.8-8.11, the simulation results perform relatively worse on the global consistence of the static pressure distribution tendencies specially for the axial planes after the rotors comparing with the total pressure. This might be caused by the complexity of the wake which makes the precision on solving the static pressure be-

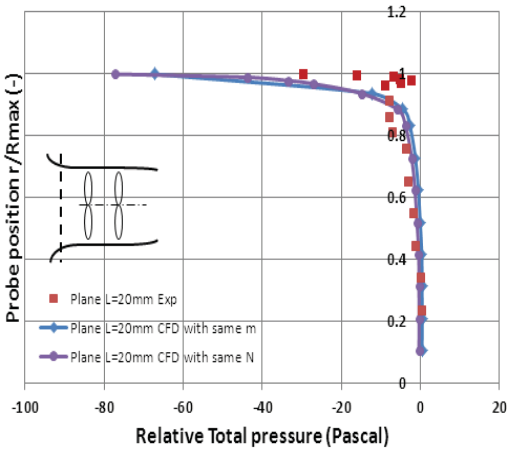

Figure 8.4: Total pressure comparison at Plane L=20 mm

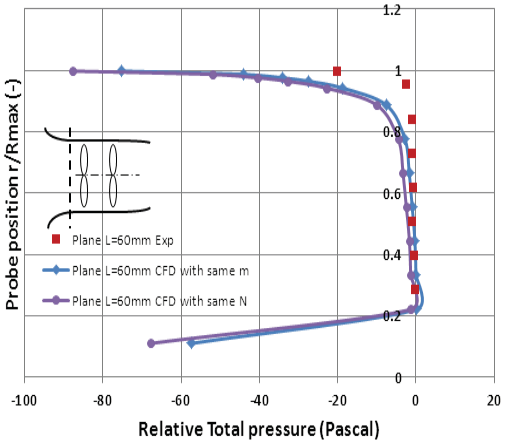

Figure 8.5: Total pressure comparison at Plane L=60 mm

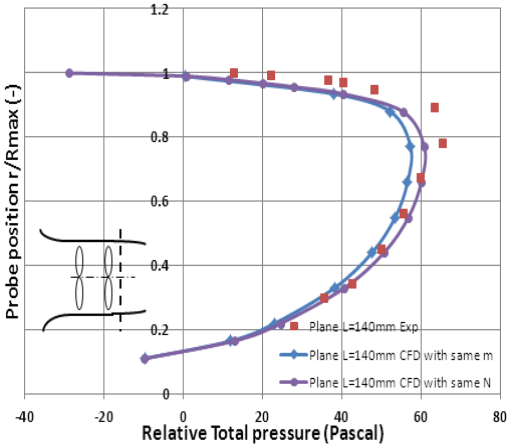

Figure 8.6: Total pressure comparison at Plane L=140 mm

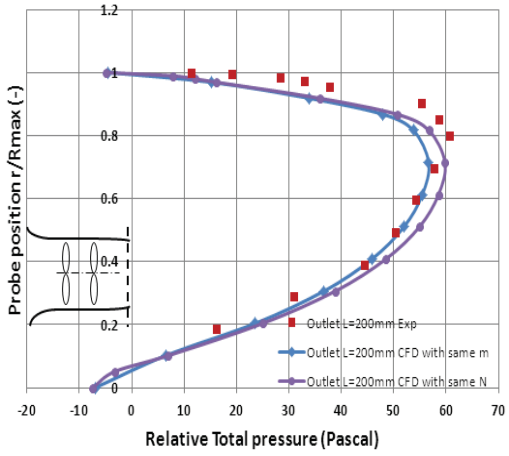

Figure 8.7: Total pressure comparison at Plane L=200 mm

comes relatively lower. For all four axial planes, again the same mass flow input has more similar solutions on the static pressure with the tests. It has quite consistent pressure on the main effective regions like total pressure. This could explain the smaller variations with tests on the global performance such as the rotor thrust in some way. However, at positions near the shroud wall, there is greater difference between simulations and the experimental data tested by the static pressure probe. This is caused by the fact that the probe makes the flow accelerate when it is quite close to the shroud wall. Such problem definitely does not exist in the static pressure tests by the shroud wall tubes connected to pressure transducers. Better agreement for simulations is thus obtained with the data tested by the shroud wall tubes which are more confident.

However, right at the nozzle outlet, both simulations have certain difference with the test on the static pressure distribution, seen in Fig.8.11. The pressure in

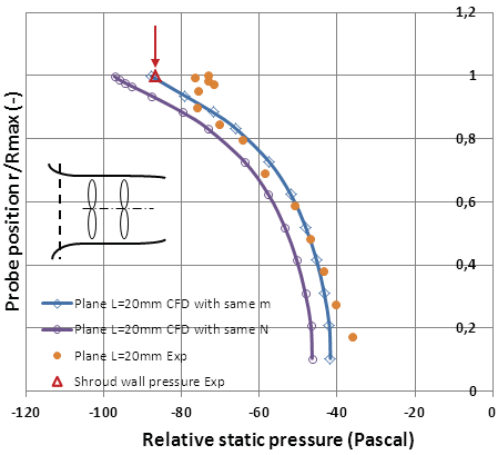

Figure 8.8: Static pressure comparison at Plane L=20 mm

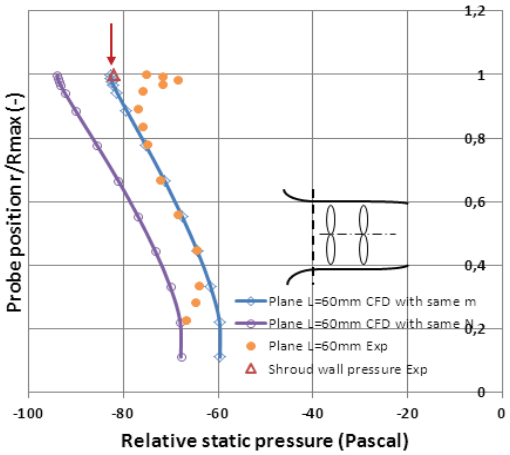

Figure 8.9: Static pressure comparison at Plane L=60 mm

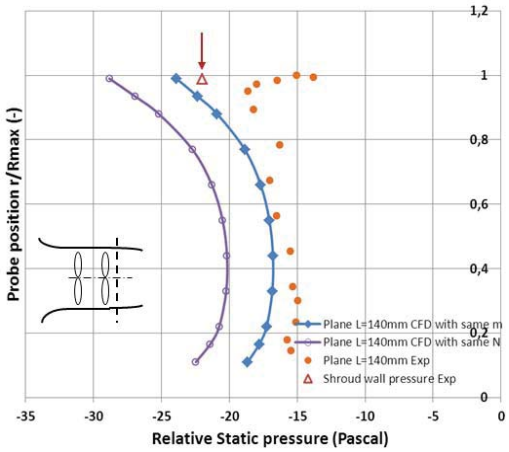

Figure 8.10: Static pressure comparison at Plane L=140 mm

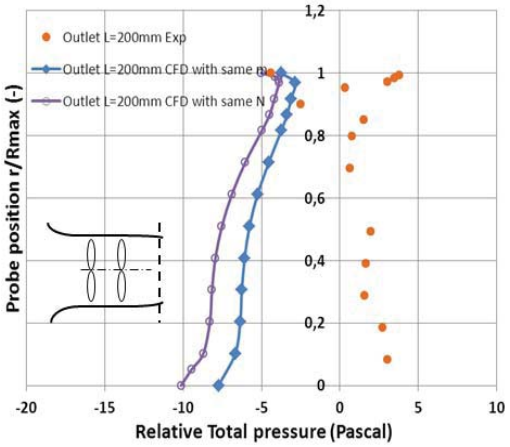

Figure 8.11: Static pressure comparison at Plane L=200 mm

simulations seems to be still affected by the centrifugal equilibrium. Its value is globally over the ambient pressure, and near the system axis it tends to become lower. This is because of the wake generated by the hub, seen in Fig.8.12. In the simulation, it is not possible to have the same geometry of the supporting structure for two rotors as in experiments. The hub is ended at the upstream shroud exit. This makes the wake have a certain size at the exit after its development. And this influences the effective exit surface used by the flow for its ejection or expansion. The velocity profile on this surface is thus changed. The reason why the static pressure at the outlet is different is that, such wake probably does not appear at the same location or have the same size as in experiments which have a supporting structure in the system center all along the shroud axis. However, as explained above, the precision of static pressure is quite sensitive and affected by the solution on the wake, such kind of difference could be acceptable due to its constraint influence.

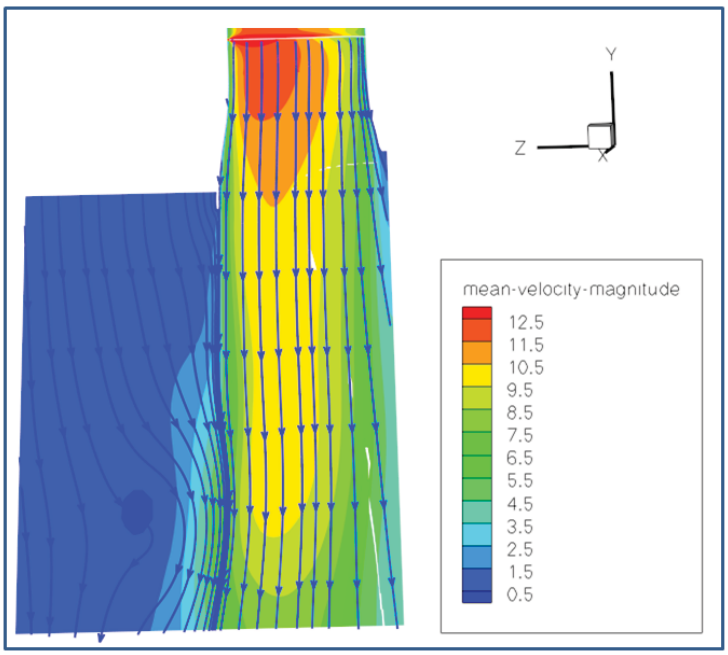

Figure 8.12: CFD: Flow in the downstream rotors

All the validation on global performance and flow field indicate the simulation is effective to model the propulsion system. It could be certainly applied to explore the potential steady and unsteady characteristics in order to understand more about the system.

8.1.3 Steady characteristics

Since the experimental data is limited to recognize the steady characteristics of the flow field through the whole shroud and double rotor passages due to the huge time cost, the detail on the time averaged flow field, specially for pressure and velocity, becomes feasible in simulation way. In this section, six isolated surfaces along the shroud axis which is Y in the simulation are located at the same positions as the ones chosen by tests: the inlet plane, planes which are 20, 60, 90, 140 mm from the inlet respectively, and the outlet. In the 3D simulation, the surface with Y equal to zero is the shroud inlet. The flow passing on these surfaces complements the understanding of the system.

Initially, the mean static pressure distributed on the six surfaces is presented in Fig.8.13 to Fig.8.18. Obviously, except the surface at Y=90 mm situated between the two rotors, the static pressure distributions on other stations have radially uniform feature.

At the inlet, seen in Fig.8.13, a wide region outside and around the shroud has pressure close to the ambient. This implies the definition of the computational inlet well corresponds the flow pattern. It should be noticed that here is a ring which has

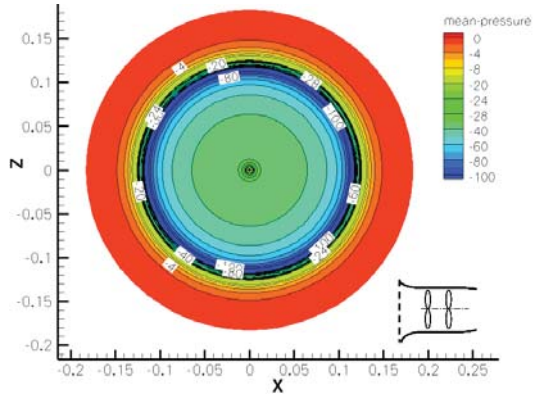

Figure 8.13: Inlet: Static pressure

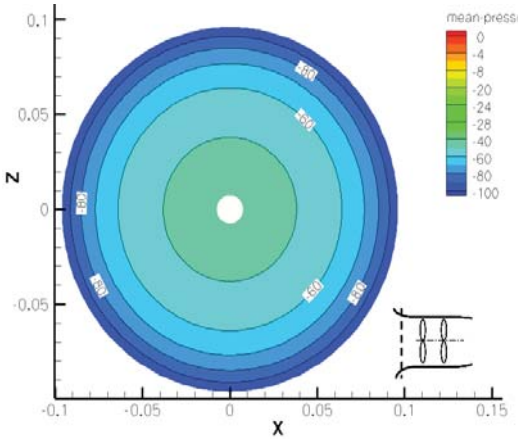

Figure 8.14: IsoY=20: Static pressure

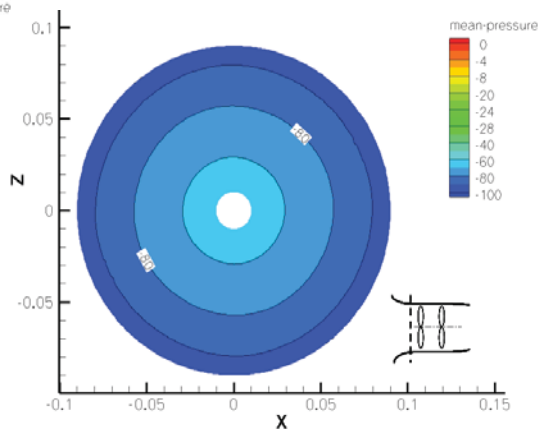

Figure 8.15: IsoY=60: Static pressure

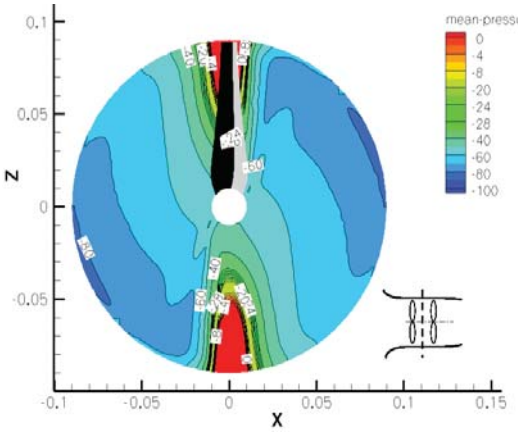

Figure 8.16: IsoY=90: Static pressure

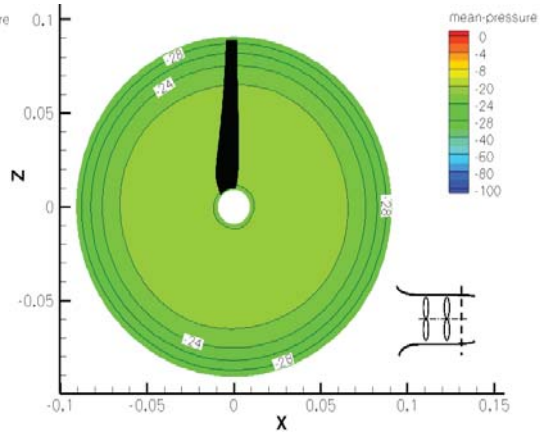

Figure 8.17: IsoY=140: Static pressure

the lowest static pressure at the inlet surface.

This lower pressure area lasts until right before the upstream rotor. From the surface Y=20 mm to 60 mm, the flow is depressed and accelerated by the narrowing shroud passage, which leads to a further decline in forms of pressure. On the surface at Y=90 mm which is between the two rotors, the pressure increases through the upper rotor and the circumferential distribution does not exit. The highest pressure near the blade tip is formed due to the low velocity. 40 mm after the second rotor, the pressure turns to be circumferentially distributed again until the outlet.

At the outlet seen in Fig.8.18, the pressure can not reach the ambient pressure and is a few pascals lower. The huge circumferential area outside the shroud that has a static pressure around -2 Pascal is due to the imposition of small velocity as the explanation of the definition on the expanding computational field.

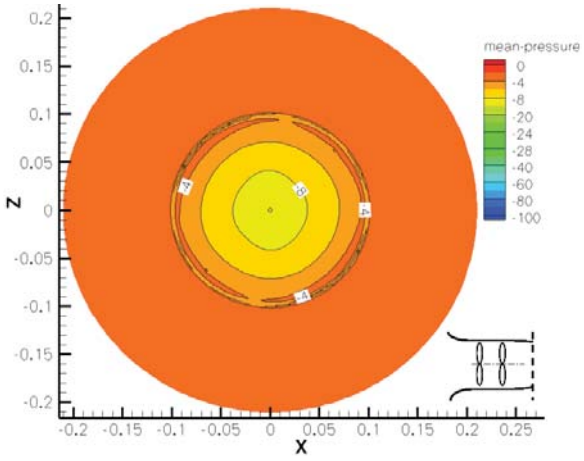

Figure 8.18: Outlet: Static pressure

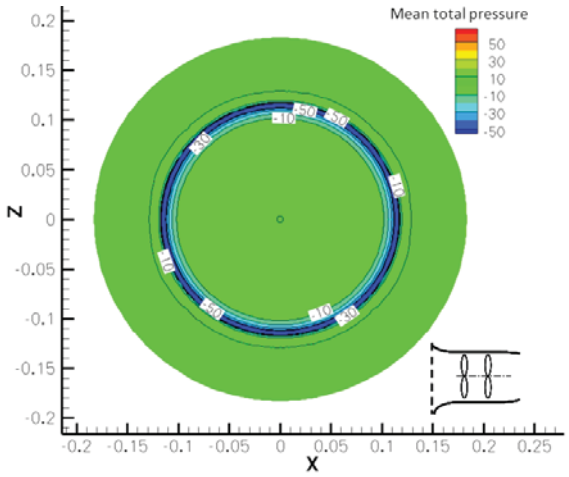

Figure 8.19: Inlet: Total pressure

For total pressure, seen in Figure from 8.19 to 8.24, its value is mainly kept close

at the inlet shown in Fig.8.19. Near the leading edge, there is a small ring with a total pressure lower than zero, because of the viscosity on the wall boundary layer. It results in a certain pressure loss.

Almost the same distribution is lasted to the surface Y equal to 20 and 40 mm where the flow is quite uniform, except the region of the shroud boundary layer. Before the first rotor at 80 mm from the inlet, the total pressure shows a loss due to the acceleration of the fluid by the curvature effect of the shroud and hub. The pressure loss becomes strongly pronounced near the shroud wall and hub after the first rotor's rotation. After the second rotor, the total pressure turns to be circumferentially distributed again and reaches the highest in the main region.

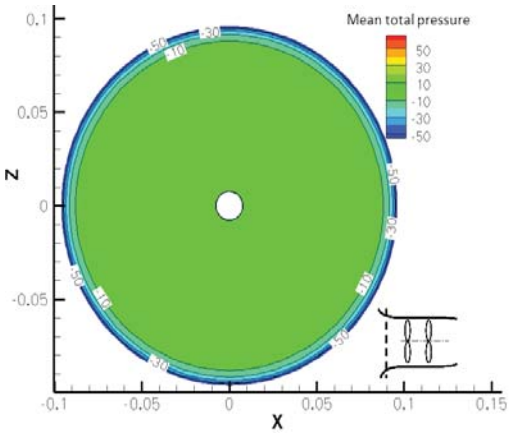

Figure 8.20: IsoY=20: Total pressure

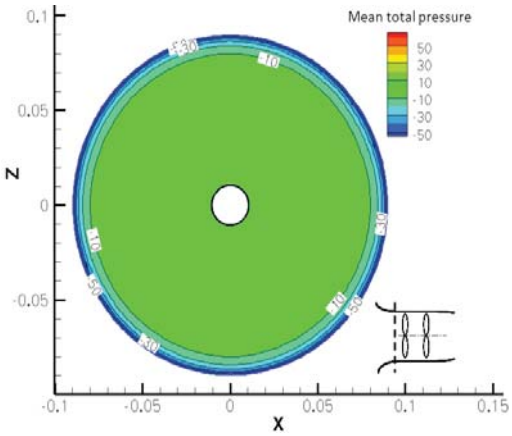

Figure 8.21: IsoY=60: Total pressure

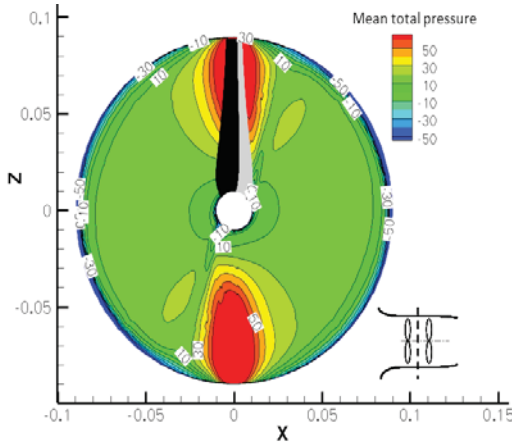

Figure 8.22: IsoY=90: Total pressure

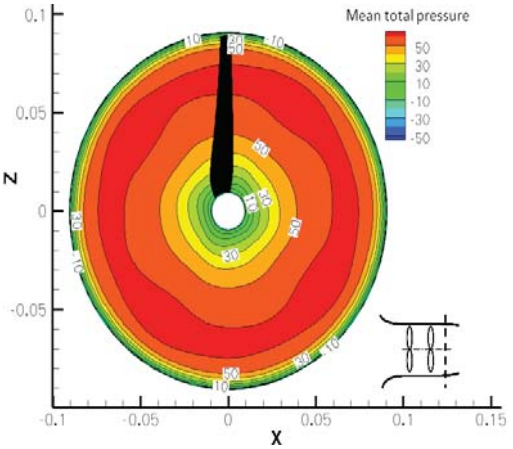

Figure 8.23: IsoY=140: Total pressure

The total pressure distribution at outlet is almost the same as the plane just after the second rotor. Also the huge field around the shroud nozzle exit keeps a total pressure close to that of the environment, seen in Fig.8.24.

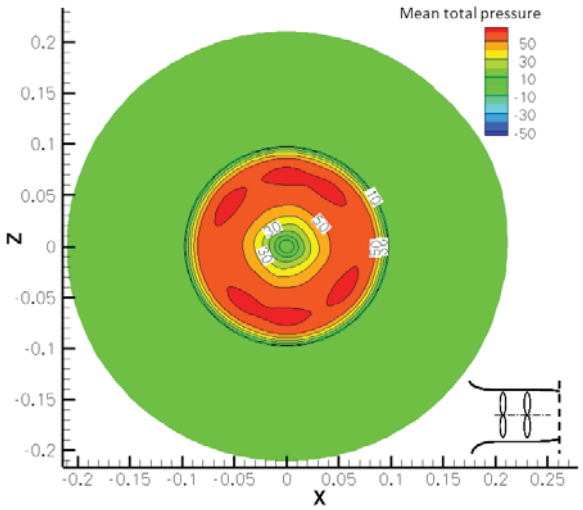

Figure 8.24: Outlet: Total pressure

Corresponding to the static and total pressure distribution whose difference is related to the velocity, the axial velocity can be observed from Fig.8.25 to Fig.8.29. The axial velocity distributed on these different planes has quite a constant value except at the inlet, seen in Fig.8.25. This relative lower axial velocity distribution around 7 m/s at the inlet comes from the greater surface area compared to the other stations.

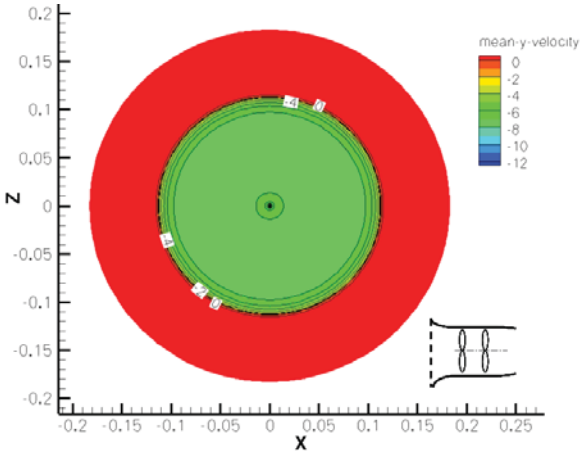

Figure 8.25: Inlet: Axial velocity

For the four stations inside the shroud, as the global trends of the pressure distribution, the axial velocity field has a circumferential distribution, except at the middle plane Y=90 mm, which greatly suffers from the rotating motions and their interactions. On this plane, the relative greater velocity appears on the circumference at the rotor span 0.3R to 0.9R. As a main component of the velocity, the axial one showed in these figures well confirms the observations in the pressure field,

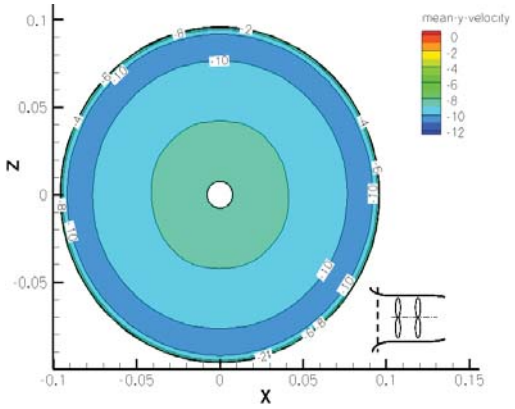

Figure 8.26: IsoY=20: Axial velocity

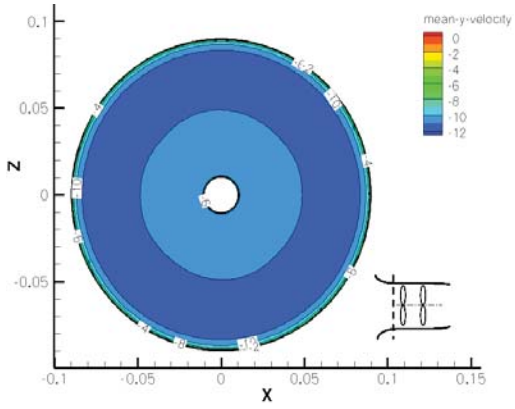

Figure 8.27: IsoY=60: Axial velocity

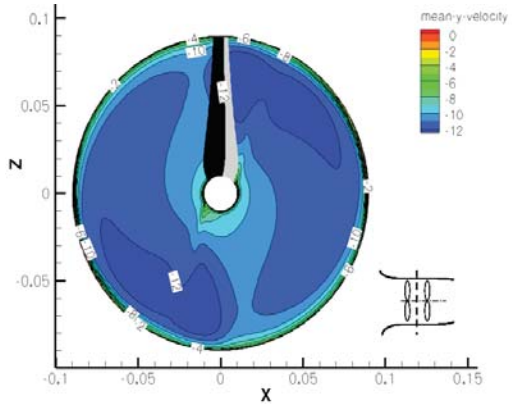

Figure 8.28: IsoY=90: Axial velocity

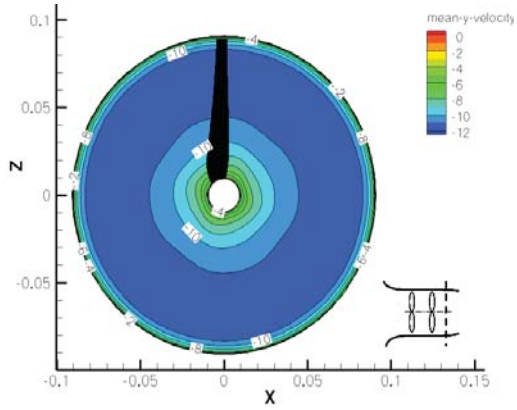

Figure 8.29: IsoY=140: Axial velocity

including the flow acceleration by narrowing shroud passage and the development of low axial velocity area on the shroud wall and hub.

Along the whole shroud passage, the flow development can be easily observed in Fig.8.30. The rotation aspirates the flow coming inside the shroud and accelerate it at the entrance. And it is unform in the main region but decreases on the shroud wall and hub. After the double rotor, the nozzle diffuser makes the flow slow down and the pressure distribution therefore increases. This might be compensated by the equivalent convergent flow which is generated by the thicken boundary layer of hub and shroud.

In conclusion, the time averaged flow field indicates a globally circumferential distribution of the quantities pressure and velocity in the upstream and downstream double rotor. It should remind that this can not be obtained in the unsteady flow field special in the flow after the rotors, where suffers from the wake.

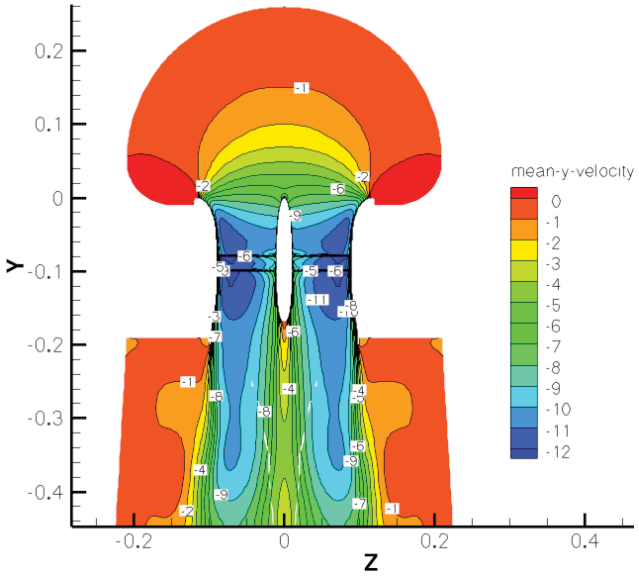

Figure 8.30: Iso X=0: Axial velocity

8.2 Unsteady Characteristics for $N_1 = N_2 = 6000$ rpm

8.2.1 Tangential velocity

The component of velocity – tangential velocity is a typical quantity to characterize the flow rotating motion. Again on the six selected iso-surfaces, the tangential velocity distribution is given in the Figures from 8.31 to 8.36. Globally, a circumferential distribution no longer exists in unsteady flow.

At the inlet seen in Fig.8.31, the tangential velocity is almost around zero, and can be considered to be uniform axial flow.

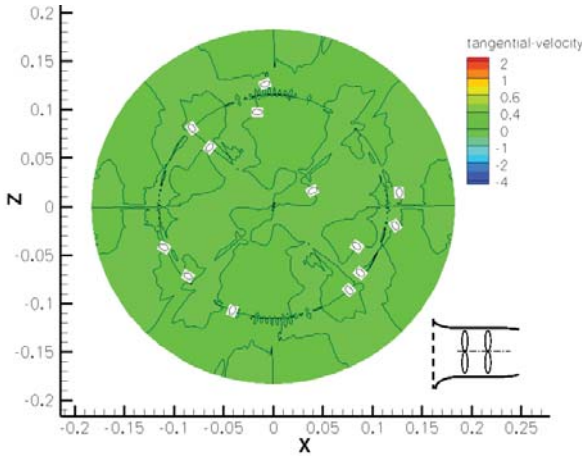

Figure 8.31: Inlet: V-Tangential

The uniform flow is lasted to the second station Y=20 mm. After it, with the

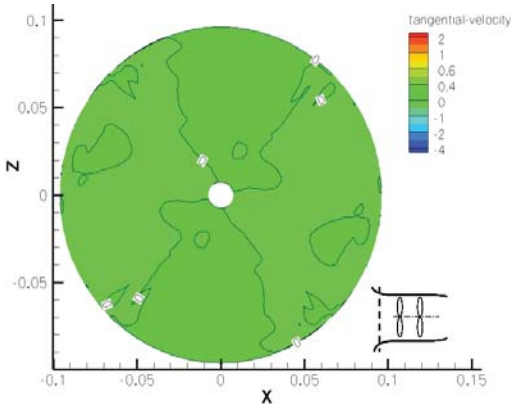

Figure 8.32: IsoY=20: V-Tangential

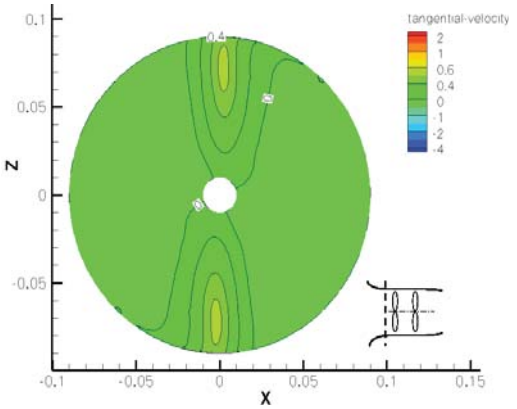

Figure 8.33: IsoY=60: V-Tangential

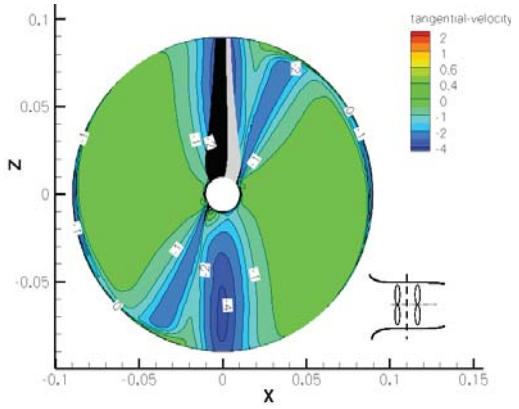

Figure 8.34: IsoY=90: V-Tangential

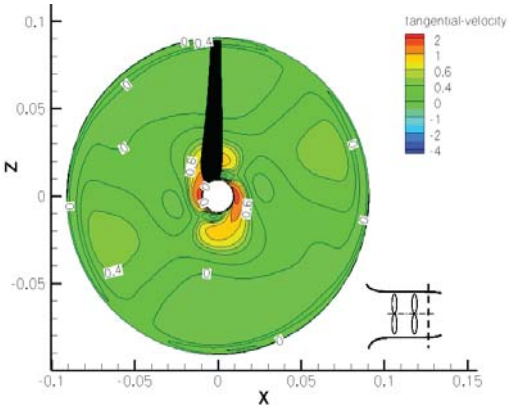

Figure 8.35: IsoY=140: V-Tangential

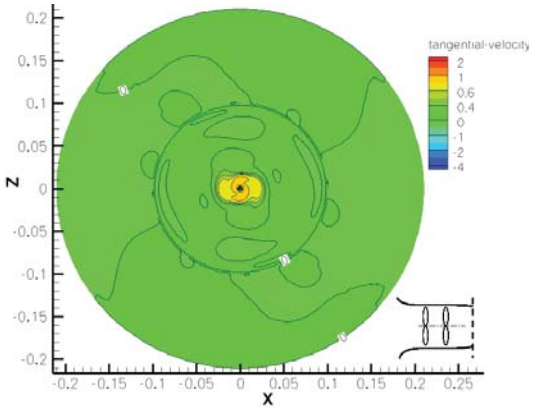

Figure 8.36: Outlet: V-Tangential

acceleration of the first rotor, the tangential velocity, specially near the blade, starts to become evident. Compared to other stations, a great tangential velocity is formed at the surface just after the first rotor and becomes quite evident. This is modified by the second rotor which rotates in the opposite direction, as seen in Fig.8.35. It should be noticed that another region close to the hub has strong tangential component of velocity. These imply a complicated flow pattern existing both at the blade tip and root.

At the outlet, the tangential velocity has decreased greatly to be half of the one on the surface Y=140 mm, seen in Fig.8.36. However, a greater tangential velocity still exists around the hub. This is to indicate again the effect at the outlet from the wake generated by the hub.

The tangential distribution on the iso-surface X=0 which crosses the double rotor confirms the phenomenon obtained from the analysis above. In addition, a strong tangential velocity is noted near the hub, where has a wake structure in a cut view.

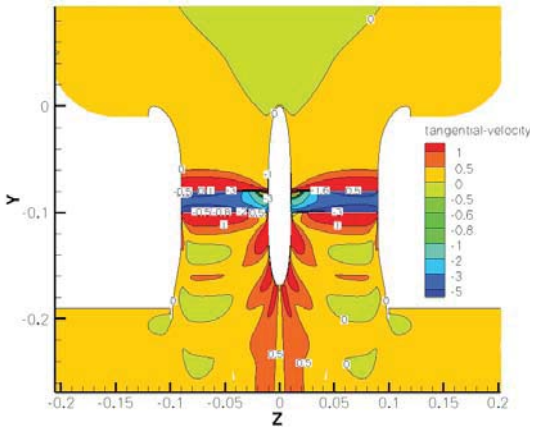

Figure 8.37: Iso X=0: Tangential velocity

8.2.2 Flow along blade span

To better understand the rotor performance, the contour of vorticity magnitude is presented at three spanwise stations $0.2R_r$, $0.75R_r$ and $0.96R_r$, seen in figures from 8.38 to 8.40. At each spanwise station, two views on the distribution of vorticity magnitude are given.

At the span of $0.2R_r$ which is quite close to the blade root, the view in the Z direction shows both rotors have a trailing vortex. From the view of the X direction. The flow of the trailing wake from the upper rotor is strongly engaged into the ones generated by the lower rotor. Specially for the lower rotor, the wake is extended with a downwash velocity. Another zone with a strong worticity appears just below its blade and tends to be extended to a long field in the downstream rotor.

Along the spanwise direction, at the position of $0.75R_r$, the trailing vortices from both rotors are separated into two main ones. Between rotors, there are several

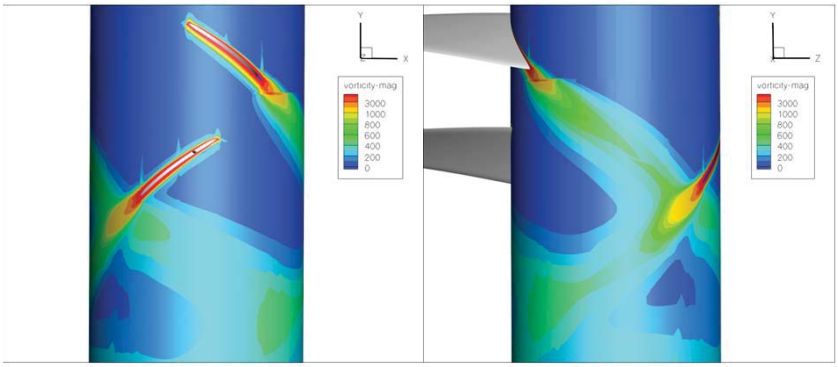

Figure 8.38: Vorticity of upper and lower rotor at span $0.2R_r$

zones that have a certain vorticity but quite tiny. From viewing the X direction, the impingement from the upper rotor's wake upon to lower one stops at this spanwise position. Comparing to the location $0.2R_r$, the flow passing through the lower rotor at $0.75R_r$ suffers less from the influence of the upper one.

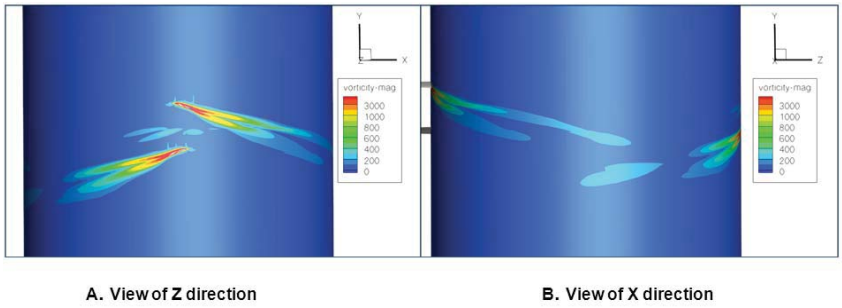

Figure 8.39: Vorticity of upper and lower rotor at span $0.75R_r$

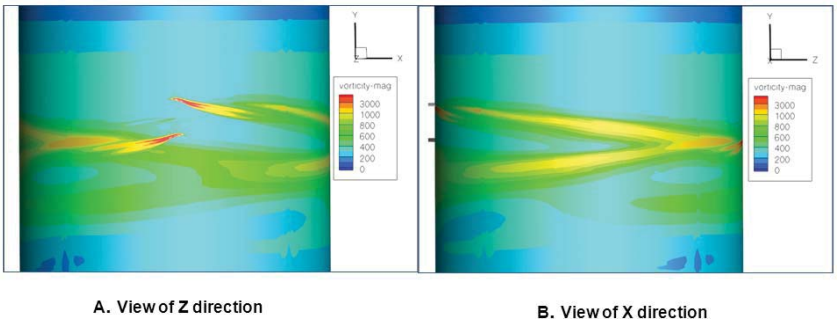

Figure 8.40: Vorticity of upper and lower rotor at span $0.96R_r$

At the span position of $0.96R_r$, a similar structure of trailing vortices as the one at the span $0.75R_r$ could be observed in the Z direction view. The wake flow impinging upon the lower one appears again. And the vorticity magnitude becomes

significant, due to the wake in the downstream shear region, and the effects from the shroud wall boundary layer. Overall, along the blade span, the flow separation does not occur at least for the positions above.

8.2.3 Flow at the blade tip

In the gap between the shroud and blade tip and also at the blade tip, a vortex is usually a significant phenomenon for hovering rotor. Due to the variation of velocity along the span, a pressure gradient is formed on the blade surface. Furthermore, the pressure on the suction surface differs from that on the pressure surface greatly so that tip flow generates. This vortex was indicated to be one of the critical sources resulting in an aerodynamic loss [81, 82]. Therefore it is obviously required to clear such vortex pattern, position and scale for the system in this work.

Fig.8.41 presents a constant pressure cone forming around the upper and lower rotor blade tips. Both pressure cones have low pressure value as the one at the suction surface. Such low pressure region can be explained a vortex appearance there.

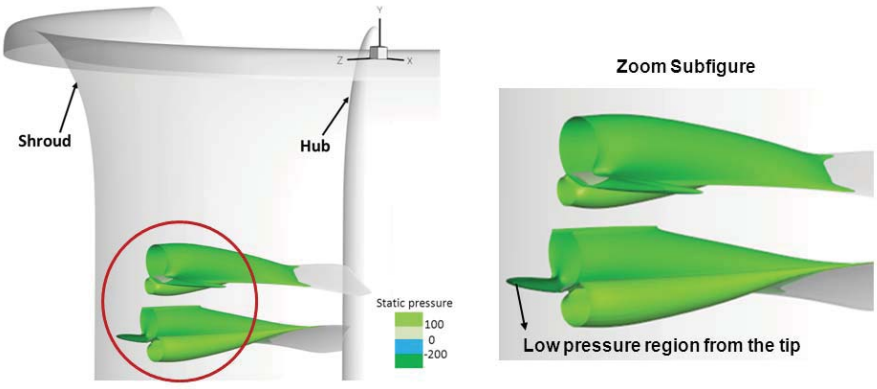

Figure 8.41: Iso pressure distribution around the blade tip

Corresponding to the phenomenon showed in the figure above, Fig.8.42 presents the streamlines around the blade tip. At the blade tip, it can be seen that both upper and lower rotor have the flow coming to the suction surface from the pressure surface. Two main tip vortices are therefore formed and expanded along with the rotations. A certain flow with downwash velocity from the tip vortex of the upper blade tip detaches the down blade suction surface and is directly engaged into its tip vortices.

Specifically for the vortex intensity, Fig.8.43 and Fig.8.44 indicate the helicity on several surfaces along the chord. Numerous vortical structures are illustrated in it: Globally, the tip vortex grows from the leading edge to the trailing edge; Due to flow separation developed along the chord direction, a complex tip vortex is produced in which a secondary vortex is generated on the suction surface. Meanwhile, with the vortex development along the chord, the secondary vortex is crashed into the

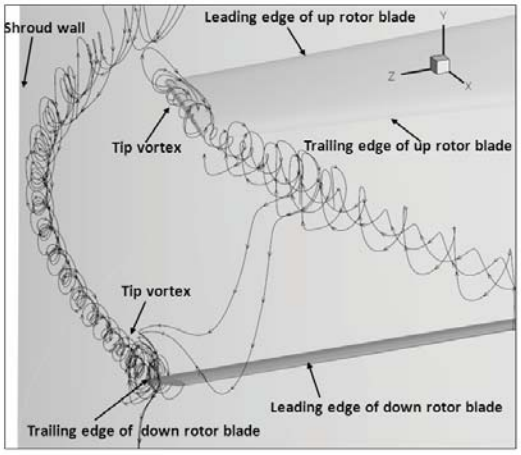

Figure 8.42: Streamlines at the upper and lower blade tips

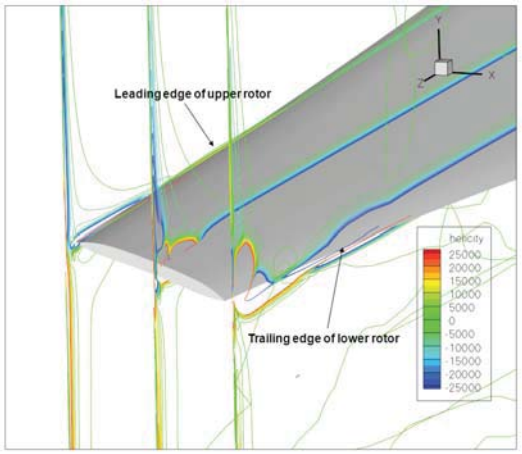

Figure 8.43: Axial vorticity at the upper blade tips

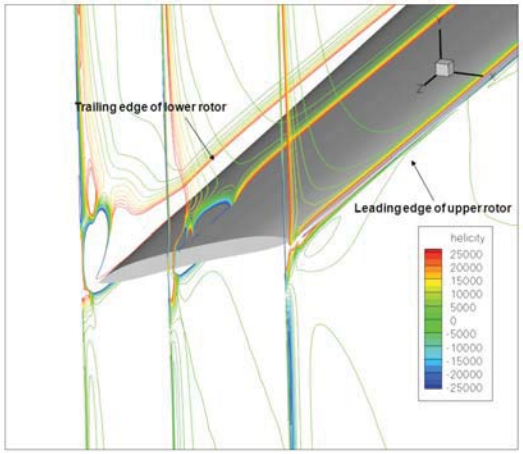

Figure 8.44: Axial vorticity at the lower blade tips

tip vortex more and more. Finally they are formed as the one with a relative large scale. Meanwhile another vortex structure develops at the trailing edge.

8.3 Parameter Effect Analysis through 3D Simulation

From the experimental analysis in Chap.6, the effects of rotor location variation and the switching of the two speeds were obtained first for the steady performance. Since there are limitations on the exploration of the unsteady characteristics with experiments, this section aims to use 3D simulation to solve it and further understand their effects based on the validation of the global performance.

8.3.1 Effect of rotor location

Another inner rotor distance of 40 mm was selected for the simulation processing as experimental analysis. Table.8.2 gives the validation results on the overall performance. It shows that, compared to the experimental tests, the mass flow in the simulation is a few grams greater. However, such kind of difference on the shroud and rotor behaviors could be acceptable and modified more precisely to have the same input mass flow.

Table 8.2: Comparison between computation and experiment

Performance	CFD SDR80-40	Exp SDR80-40	CFD SDR80-20	Exp SDR80-20
Mass flow (kg/s)	0.333	0.324	0.336	0.326
F_t (N)	3.209	2.815	3.224	2.825
F_s/F_t (-)	0.54	0.54	0.56	0.54
FoM (-)	0.68	0.66	0.68	0.67

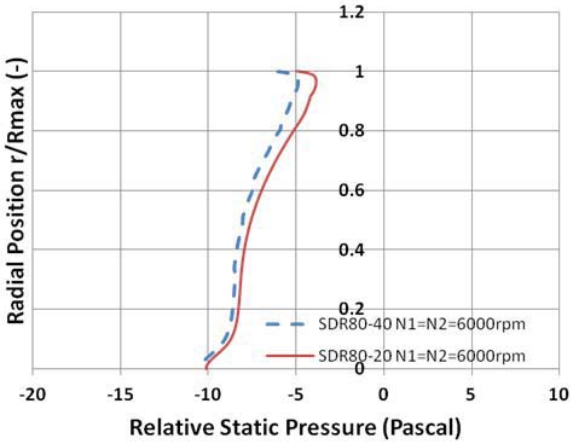

Figure 8.45: Relative static pressure at nozzle exit of SDR80-20 and SDR80-40

As for the two combinations of rotor locations 80-20 and 80-40, the better performance for shorter inner rotor distance is basically from the increased mass flow, which is mostly influenced by the flow condition in the shroud downstream. Fig.8.45 indicates the flow is under-expanded more at the outlet for the location 80-40, relative to 80-20. That is the reason why the relatively larger inner distance leads to a worse performance, even though the difference is barely noticeable.

For the unsteady characteristics, Fig.8.46 and 8.47 indicate the vorticity developed in the axial flow direction at the radial position 0.8R for the two rotor locations. For configuration SDR80-20, it is evident that the wake of the upper rotor blade is greatly engaged into the lower one developed at the beginning. Such interaction becomes weaker for SDR80-40. This is expected when changing inner rotor distance longer. However, it indicates for such shrouded contra-rotating system, the intensity of vortex and its development period between rotors balance the impact on the system's behavior.

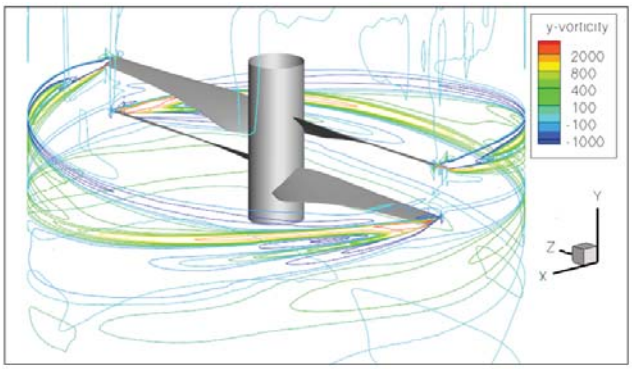

Figure 8.46: Y vorticity at radial surface 0.8R of SDR80-20

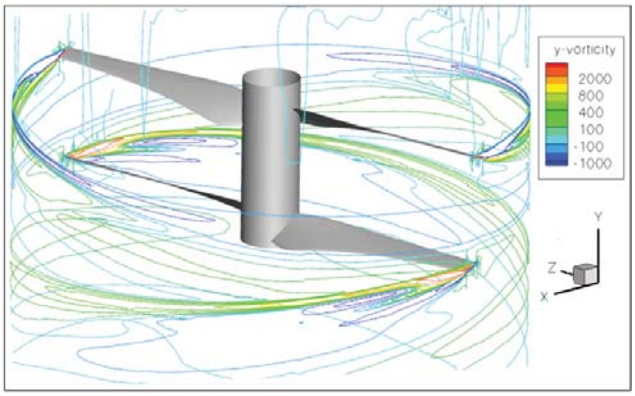

Figure 8.47: Y vorticity at radial surface 0.8R of SDR80-40

Specifically on the downstream shroud, an opposite physic phenomenon is observed in the distribution of vorticity magnitude in iso-surface X=0, shown in Fig.8.48. Actually, several main wake structures can be found in the downstream

shroud for two rotor configurations. They are situated around the hub, the shroud trailing edge and the downstream free flow respectively. Globally, the intensity of the wake for position 80-40 is coming out to be stronger when comparing it to 80-20. However, the wake scale is smaller. This is supposed due to the backward movement of the second rotor. However it needs to be further identified because of the smaller flow developing region presence at the same time. For the vortex at shroud trailing edge of both locations, its size is difficult to be defined by flow streamlines.

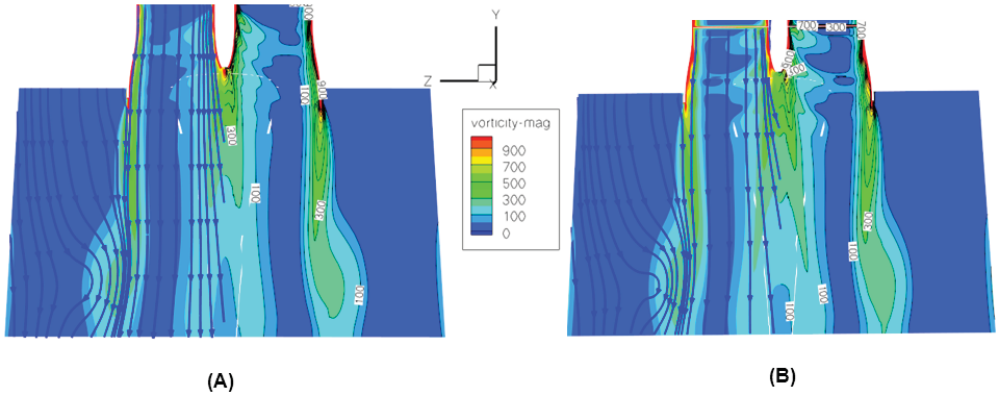

Figure 8.48: Vorticity at iso X=0 of SDR80-20 (A) and SDR80-40 (B)

8.3.2 Effect of switching speeds

Unfortunately, for the effect of switching two rotors' speeds, the comparisons between the simulation and the experiments show a opposite tendencies, seen in Table.8.3. Even though, there is not a great difference in the comparison of the same speed pair with the tests, the simulation has the benefits of a second slower rotational speed, which is contrary to the experimental results. The mass flow obtained by the calculations at the speed pair 9000-6000 is few grams greater than the one for 6000-9000. The greatest difference comes from the performance of the rotor with slower speed 6000 rpm, which presents a worse ability to transmit the mechanical energy to the fluid. Since the mass flow obtained by simulation is similar with the experiments, which means the rotors in the simulation have similar inflow conditions as in experiments, the basic source causing the difference is thus from the flow condition on the blade itself which results in different thrust or torque generation. The application of the turbulent model in simulations probably can not so precisely capture the flow deterioration such as the flow separation at blade leading edge. This ability might be further decreased when the rotor almost behaves like a windmill, under which the velocity angle is far from the perfect incident one.

Table 8.3: Comparison between computation and experiment

Performance	**CFD**	**CFD**	**Exp**	**Exp**
$N_1 - N_2$ (rpm)	6000-9000	9000-6000	6000-9000	9000-6000
Mass flow (kg/s)	0.426	0.432	0.431	0.422
F_t (N)	5.165	5.340	5.083	4.685
F_{R_1} (N)	0.33	1.84	0.26	1.76
F_{R_2} (N)	1.96	0.54	2.04	0.31
P_{R_1} (Watt)	7.36	39.23	9.23	39.62
P_{R_2} (Watt)	41.38	10.34	42.44	9.17
F_s/F_t (-)	0.56	0.55	0.55	0.56
FoM_{R_1} (-)	0.63	0.67	0.40	0.61
FoM_{R_2} (-)	0.67	0.74	0.68	0.47

8.4 Conclusions

Based on the numerical methodologies developed in the last chapter, the 3D computations were firstly validated by experiments. Following, they were used to more deeply explore the steady performances as well as the unsteady characteristics of the shrouded system. Since the different rotational speed could produce different mass flow which is a critical variable influencing the system performance, two references for validating the simulation were selected – rotational speed and mass flow. The main conclusions were as following:

- Whether the validations are conducted on global performances, shroud wall pressure or pressure field, the validation based on the same mass flow input provides a better consistence with the experiment results, except results on the exit. This is due to the geometrical difference on the rear part of the hub and the corner of shroud trailing edge between experiments and simulations. The 3D simulation globally works effectively;
- Through the validations, the explorations from simulations are:
  - For steady performance, 3D simulation reveals: the distributions on static pressure, total pressure and axial velocity at the selected six axial stations from shroud inlet to exit, have quite uniform features except the station between two rotors. They are globally changed almost only along the radial direction. Due to the first rotor rotation, the flow around blades loses such circumferential distribution. The uniform features appearing on the station just after the second rotor implies the rear rotor turning at opposite direction greatly compensates and thus reduces the wake;
  - For unsteady features, the flow along the blade span indicates a strong wake interaction between the upper and lower rotors at the locations of spanwise 0.2R and 0.96R. Particularly at the blade tip, two main structures of tip vortices were obtained by the streamlines. Due to the

flow separation developed along the chord direction, a complicated tip vortex is engaged by a secondary vortex which is generated on the suction surfaces for both rotors. In addition, a wake with a relativly large size appears in the downstream zone before the computational exit. All of these features dominate the flow unsteadiness;

- For further exploring the effects of the coaxial rotor configuration, the simulation revealed that, setting the second rotor backwards decreases the wake scale but increases its intensity in the downstream computational zone, which could compliment the experiment conclusion: better performance happens on the shorter inner rotor distance 20 mm compared to the 40 mm both along with the first rotor set 80 mm from the inlet. For the effect of switching speeds, simulations can not achieve the same phenomena, since the turbulent model can not so precisely solve the complex flow condition which is almost under the condition of windmill.

Chapter 9

Comparisons of 1D, 2D and 3D Calculations and Experiments

This chapter aims to compare all the calculations of theory extension, two dimension and three dimension (2D and 3D) with experiments on global performance, in order to check the availability of the theory extension, especially on choosing a suitable design regime of K_i, validate the design criteria proposed by 2D simulations on global performance, and obtain the difference among calculations. In view of the actuator disk applied in theoretical and 2D calculations, the comparisons and validations were then made through the same induced power and mass flow respectively.

9.1 Comparison Based on Induced Power

Generally, the system's performance is compared under the same input total power to the rotating rotors. However, since the actuator disc was used in the theory prediction and 2D simulations, under which the real rotor was assumed as a pressure jump to model the discontinuity of the pressure and velocity field, the comparison is no longer available to be made through such power but the one induced to the fluid, which is called induced power. The comparison results are presented in Fig.9.1-9.3.

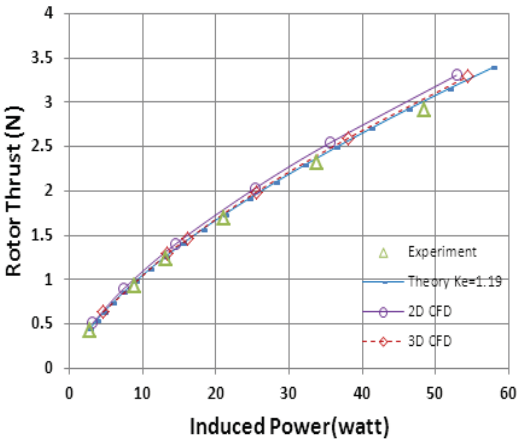

Figure 9.1: Rotor thrust comparisons

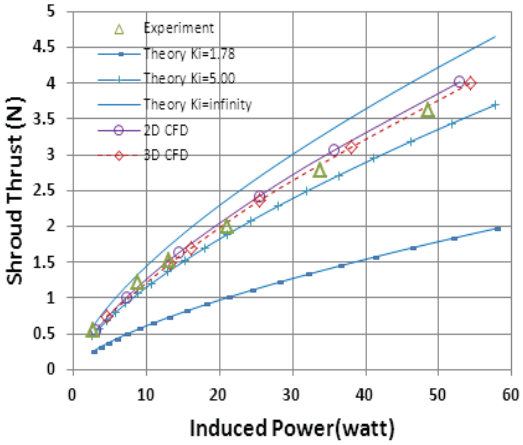

Figure 9.2: Shroud thrust comparisons

With the same power induced into the fluid, Fig.9.1 presents almost the same rotor thrust generation as the experimental one for all calculations in different di-

mensions. For 1D theory, in contract with the rotor thrust derivation in Chap.2, there is nothing decided by the shroud entrance as K_i does. However, for shroud thrust, as the main source of the thrust, the air entrance is critical due to the flow on its curvature. Fig.9.2 shows great difference between the theoretical one with the real geometric parameter $K_i = 1.79$ and experiments. On the other hand, the value of $K_i = 5$ performs similar. This difference becomes smaller as K_i increases until $K_i = \infty$. From Fig.9.2, it could be observed as well that both 2D and 3D simulations could obtain similar solutions on shroud thrust as the one from experiments. The minor difference on shroud thrust is decided by the mass flow, seen in Fig.9.3.

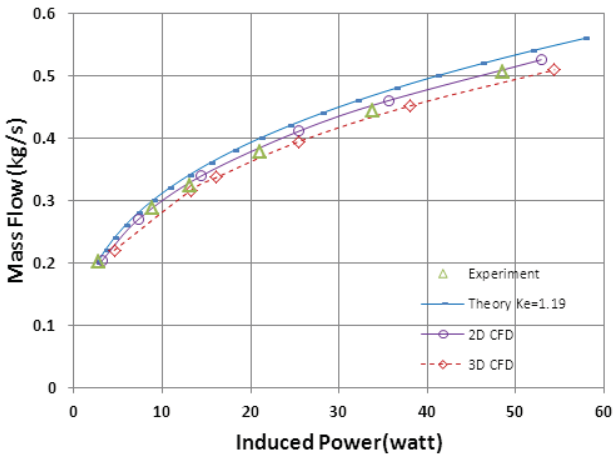

Figure 9.3: Mass flow comparisons

From Fig.9.3, compared to 3D and the actual experiment, 2D calculations keep a slight increase under the same induced power. This is in conflict with the phenomenon shown in Fig.9.1: a slightly greater rotor thrust corresponds to a greater pressure jump and consequently, to a reduced mass flow under the same induced power. This might be caused by the small velocity imposed in the far upstream shrouded system. For the theoretical one, the mass flow is completely decided by the nozzle exit parameter K_e. It has the same tendency in the experiments and also for the preliminary prediction it works well.

As for the global performance of power loading, to facilitate its comparison induced power was used, rather than mechanical power. Fig.9.4 indicates the 2D axisymmetrical simulation applied in this work to evaluate the shrouded system and propose the shroud design criteria is in perfect compliance with the experiments, particularly under the relative lower induced power. As shown for shroud thrust, the theoretically infinite K_i does not behave far from reality and the value $K_i = 5$ approaches more to the experiments. The value – $K_i = 1.79$, is not expected to work since this area is somewhat arbitrary and is subject to radial flow, which is assumed axial flow in the theory.

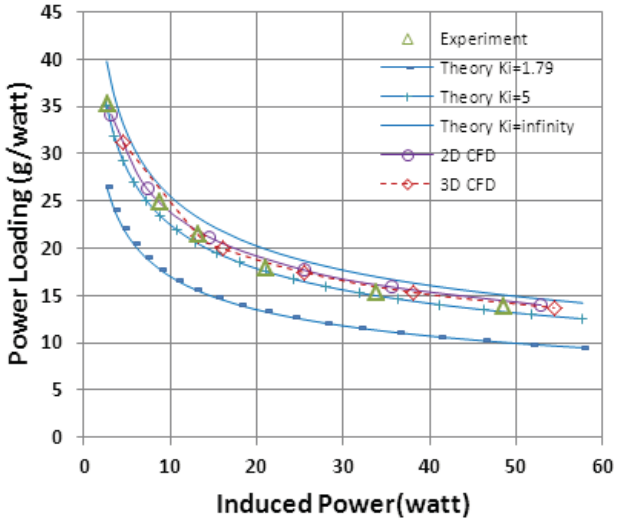

Figure 9.4: Power loading comparisons

9.2 Comparison Based on Mass Flow

As in the 3D simulation analysis of Chap.8, the mass flow aspirated by the shrouded system is a critical quantity for system's performance. And the comparison based on the same induced power actually does not only involve the mass flow, but the pressure jump. Therefore in order to further specify the mass flow effect, another comparison was made under the same mass flow, seen in Fig.9.5-9.6.

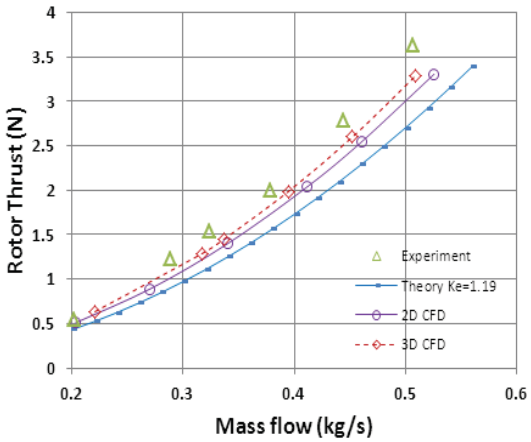

Figure 9.5: Rotor thrust comparisons

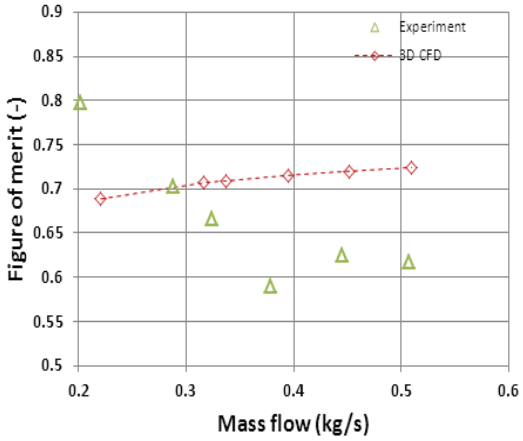

Figure 9.6: Figure of Merit comparisons

First of all, for the rotor component, the absolute quantity rotor thrust tested by the experiment as shown in Fig.9.5, is slightly higher than all calculations. And 3D simulations are closer to the test values, relative to the theory and the 2D

simulation. The correlation of rotor thrust with mass flow can be associated with a varying pressure jump for a fixed rotor radius. Meanwhile due to its main role of inducing power to the flow, the figure of merit for double rotor as introduced before is applied, seen in Fig.9.6. Here, results are only presented for the 3D simulation, since the actuator disk is applied in the theory and 2D calculations. It could be seen that, compared to tests, the 3D simulations have a low FoM for lower mass flows and higher FoM as it is increased. That is the tendency conflicting with the experiments. One main reason for it is that, the distortion becomes more noticeable for the higher pressure loadings caused by the increased mass flow. This is supposed to increase the blade tip gap when the blade distortion appears, which increases the tip vortex loss in experiments. However such phenomenon is not considered in 3D simulations.

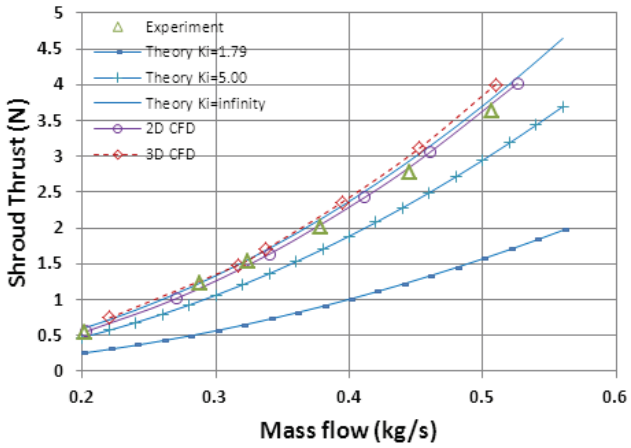

Figure 9.7: Shroud thrust comparisons

For the shroud component, basically through the shroud with fixed shape, the same mass flow should always provides almost the same thrust, seen in Fig.9.7. The calculations of 2D and 3D simulations are quite similar to the experimental one. The 2D and 3D computations' smaller thrust generation probably comes from the friction on the wall in the reality, which is more evident than in the simulations. For the theoretical solutions, the one with infinite K_i corresponds precisely to the tests. This is different with the analysis based on the same induced power shown in Fig.9.2. What the same is the value of $K_i = 5$ approaches to the tested shroud thrust.

The total thrust is comprised by the one from rotors and shroud, seen in Fig.9.8. Since the difference between calculations and experiments is mainly due to the shroud, which contributes great part of the total thrust as well, the comparison on total thrust does not seem greatly different with the one shown in Fig.9.7. As for the system global performance PL, the results displayed in Fig.9.9 are the same as the ones under the same induced power. Both 2D and 3D simulations offer a very precise evaluations on PL. However, for the theoretical analysis, in contrast with

the thrust performance, the value of $K_i = 5$ has a better solution relative to the infinite air entrance.

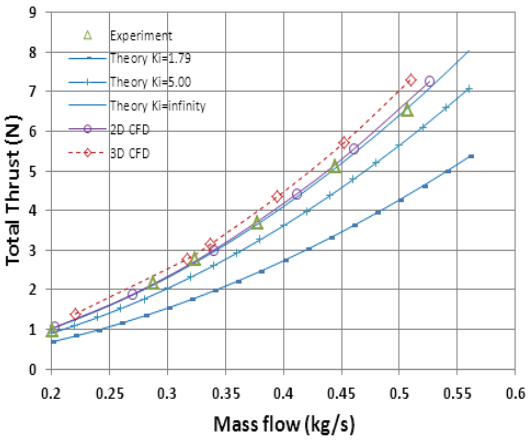

Figure 9.8: Total thrust comparisons

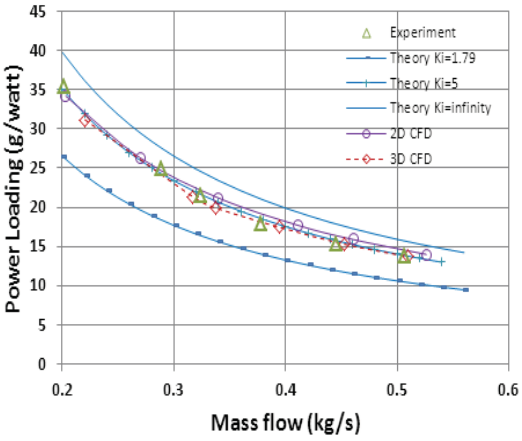

Figure 9.9: Power loading comparisons

Specifically for the theoretical results of shrouded system with a inlet definition of $K_i = 5$, Fig.9.10 presents the optimal design on a selection of nozzle parameter K_e. As analyzed in the theory extension, for such inlet, the optimal performance appears on the system with K_e approximating to 2.5, which is a bit deviated from the actual outlet ratio of $K_e = 1.79$. However, the outlet area ratio can not be so larger, accounting for flow viscocity, which could decrease the effective oultlet area.

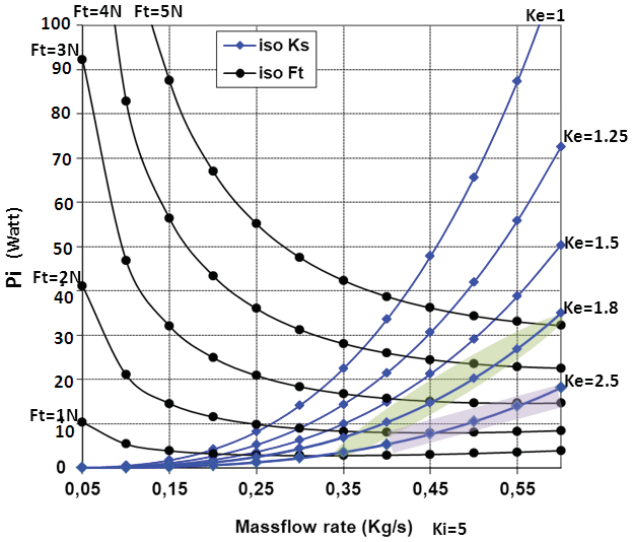

Figure 9.10: Theoretical optimal design of the shrouded system with $K_i = 5$

9.3 Conclusions

The conclusion obtained from the comparisons under both induced power and mass flow could identify: first, Froude theory with the entrance geometry definition of K_i equal to shroud inlet area divided by the rotor disc one, is not able to precisely predict the system's global performances, such as thrust and PL. For thrust of the shroud and the whole system, the infinite K_i seems more effective than the actual one, or may be a perfect upper limit. However, for PL, another value of $K_i = 5$ was found to provide a better calculation on it compared to the infinite entrance, along which Froude theory extension is practical for shroud nozzle design; The 2D simulations applied for shroud design through the evaluation on system behaviors as PL, is correspondent to that of the experiment and these perform effectively; For the 3D simulations, it works in a similar fashion when calculating the global performance as 2D, even if it involves the real rotor profile to replace the actuator disk used in 2D. This probably implies for system global performance, that the wake after the double rotor does not affect it considerably since its intensity is reduced by the second contrarotating rotor and modified by the shroud presence, as explained in the experiments and 3D simulations.

Chapter 10

Conclusion and Perspective

10.1 Conclusions

Since the shroud is a special component for the conventional rotary wing vehicles, the initial work is to predict the shroud effect through the basic momentum conservation equation. The double rotor is initially treated as a pressure jump, or an actuator disk, which was originally proposed for free rotors by Froude. In order to adapt Froude theory for the analysis of a shrouded system, it was extended by introducing two geometrical parameters which are the ratios of shroud inlet and outlet areas to actuator disk area.

Compared to the free rotor, whose wake has a natural contraction to half the rotor area, it has been shown that the nozzle has the dominant influence on controlling the inflow for a given power. The mass flow, increased by the nozzle with a greater outlet, improves the shroud thrust which is all came from the air entrance due to strong flow compression before the rotor disk. The shroud outlet with an area of half the actuator disk area, is the limit for the shroud contribution on the total thrust – negative or positive. Without any viscosity consideration and only imposing axial momentum to the system's sections, the theory extension reveals that a large outlet and inlet both bring an increase on the mass flow and in shroud thrust, respectively, for a given induced power. And this could be used to easily obtain an optimized design of the system with a finite inlet. And theoritically the outlet area for optimized performance is increased propotionally to half of the increased inlet area.

Since it is difficult for such theoretical model to take into account a shroud air entrance shape and to solve the effects of viscosity, a 2D axisymmetrical simulation was conducted with an actuator disk to solve the axial flow passing through the system which has the actual shroud profile. All possible geometric parameters which constrain the shroud profile were extracted and classified under each composition of the shroud - air entrance, cylindrical middle section and nozzle. Their effects were explored with independent varied parameters.

2D simulation results on the shroud nozzle effects proved that, the Froude theory extension reasonably predicts influences of the exit area except for flow separation due to viscosity. The optimized value of the exit radius is specified to be around 1.15 times the rotor radius. And whatever the nozzle length is, the optimal designed divergent angle is kept to be around 10.5°. For the air entrance effects, the leading edge radius is the only one which has significant effects on the performance. Its more important influence is the lower pressure region on the entrance inner surface, which

is constrained by the shroud maximum radius defined in the cylindrical section. Its optimized value is 1.3 times the rotor radius along with a maximum radius of approximately 1.44 times the rotor disk radius. For other parameters, within the non-separation region of the different cross-sections in the shroud with equivalent areas, the shroud nozzle and air entrance shape do not have any significant impact on the performance. According to those design criteria on the shroud profile in detail, one new shroud with an optimized design was proposed and fabricated for following determination of the underlying principles and limits of the operational range. Further system optimization through the approaches of both experiments and simulations was conducted.

By introducing the actual contrarotating coaxial rotor, a comprehensive experiment investigation was conducted to confirm the overall performance, approximating the flow field and optimizing the rotor configuration. Based on a new designed test bench, whose accuracy is validated by the consistency of the same variable tested in different ways and determined by the calibrations, measurements were made of thrust, torque, rotational speeds, wall pressure distribution on the shroud, and the pressure fields including total and static pressure on system axial stations. Several innovative diagrams such as double N and $In(N_1/N_2)$ diagrams, which adapt for dual rotor, allow to analyse the optimized performance for each corresponding speed regime.

Comparing to the previous one, the new shroud model increases the shroud thrust by 20% under a given usual power input and it contributes more than 50% of the total thrust. Comparing with the other three configurations which are the free single rotor (FSR), free double rotor (FDR) and shrouded single rotor (SSR), the configuration – shrouded double rotor (SDR) improves the power loading performance (PL) which evaluates the ability to generate thrust per unit power by up to 86% referred to FSR.

To further explore the benefits from the shroud as well as the system's characteristics, the shrouded and free double rotor systems were compared in detail. For global performance, an increase on mass flow around 65%, kept by the shroud presence, directly augments the total thrust by up to 80%. This increment basically comes from the shroud thrust due to its high thrust contribution. All these make the improvements on power loading by up to 80% and on Figure of Merit (FoM) constantly by 35%, which evaluates the ability to convert the mechanical energy into kinetic one by the rotors. For the rotor behavior, the important role of the first rotor on rotor thrust generation for FDR turns to be seconded when the system is shrouded. For the flow field, whatever the rotational speed is, the strongest suction peak (the lowest pressure) formed at the inlet where has the greatest curvature makes the potential to thrust contribution. Both shroud wall pressure and the static pressure tests have an equivalent ambient pressure at the exit. All those imply that the new designed shroud well adapts to the flow. The shroud presence effectively reduces the tip vortex loss and the contraction of the slipstream in the downstream wake, comparing to FDR, which has contraction just after the second rotor of a radius about 0.85 times the local shroud radius. This is the source for shrouded

systems to make an improvement.

To optimize the rotor configuration, the effects of rotor locations and rotational speed were explored. As shown in the double N and $In(N_1/N_2)$ diagrams, the tests on flow field further revealed: the rotor locations do not make great difference on global performance, setting the second rotor backward makes the pressure at the exit under-expanded; an optimized performance always occurs with the slower first rotational speed, which has greater ability to aspirate mass flow.

For shrouded contrarotating coaxial rotor, the flow field is complex due to the interactions between shroud and rotors or between two rotors, which influence the system behavior. Therefore though introducing the actual flow for exploring and understanding more on the flow characteristics of the shrouded system, a 3D numerical simulation which models the actual coaxial rotor in counter rotation was developed as a supplementary tool for experiments particularly for unsteady features. Due to the difficulty to build the same geometry as experimental facilities in the simulation, the small difference on the flow at the exit from the validation with the experiment based on the same mass comes from the different hub geometry, ending in the downstream shroud, which causes a wake and affects the numerical solution.

Based on the validation, a uniform radial distribution feature appears for all the steady performance along the shroud passages except the axial station between the two rotors, which is due to the first rotor's rotation. The uniform features appearing on the station just after the second rotor implies the rear rotor turning in the opposite compensates the wake. For unsteady performance, strong trailing wake interaction between upper and lower rotors presents at the blade near the root and the tip. The upper trailing wake is greatly engaged into the lower one; Due to the flow separation on the suction surfaces of both rotors, a complex tip vortex is engaged by a secondary vortex structure. These two vortices are mutually crashed and finally formed into the one with relative large scale; a wake with a relatively large scale appears in the downstream zone before the computational exit. All of these features dominate the flow unsteadiness.

To further explore the effects of the coaxial rotor configuration, the simulation revealed that, setting the second rotor backward decreases the wake scale but increases its intensity in the downstream computational zone, which could complement the experiment conclusion: better performance happens on the shorter inner rotor distance 20 mm, relative to the one for 40 mm, both along with the first rotor set 80 mm from the inlet. For the effect of switching speeds, simulations can not achieve the same phenomena as in reality.

Finally, all the calculations of theory extension, 2D and 3D simulations were compared with experiment results. The consistency between 2D, 3D simulations and the experiments further proves the optimally designed shroud model and unsteady features. For theory extension, the definition on shroud inlet should be adapted to the dynamic one, in order to capture the uniform flow feature. The ratio of 5, which already behaves similar to an infinite inlet, offers an acceptable consistence with experiments. It is practical to use that ratio for estimating the best performance

and the best nozzle outlet area.

10.2 Perspective

According to the observations from the theory extension, experimental and numerical analysis, here are several recommendations for future work:

For the whole system design, this work focused particularly on the shroud model optimization. For the optimized rotor profile, an existing pair of rotors was directly used on the whole of the system study. However, the phenomenon revealed by the experiments that the system optimized performance is not under the condition of zero total torque, which indicates there is still possibility for further improvement of the design of the rotor profile, in at least its pitch angle. Since for the application of MAVs, a better control and system balance are also important, the further optimization of rotor profile should be a task to follow this work. Meanwhile, the figure of merit could be improved for the coaxial rotor not only on the blade profiles, but also on its number, and provide the means to adapt the rotor torque according to the operational state requested by each local event of flight

For the theory development, its extension made in this work could well predict the system global performances with an infinite inlet and an actual shroud exit. However, a better definition of the inlet is still needed to be solved, in order to obtain a more precise evaluation of system behavior.

For the experiments done in this work, the global performances on thrust, torque, power and speeds could be obtained independently with a high accuracy, and the calibration each time before testing the shroud wall pressure increases the precision of the pressure transducers. For the main region, the probes used to test the total and static pressure on axial stations along the shroud passages work well. However, the precision would decrease once probes are closer to the shroud wall due to their modification of the local flow. Even though this problem basically comes from the way to test the flow rather than the probe precision itself, it is still needed to find other instruments which have less of an influence on the flow. The solution of this could be the probe with 5 holes to access the local radial component, or hotwire anemometry to take into account the unsteady component. Therefore, the tests using the hotwire should be made for further exploration of the flow field. The study using hot-wire could be a logical extension of the experimental study. It opens a complex area of study since it will not be possible to make a representation of the mean phase when there are two rotors rotating.

For the simulations done in this work, globally the methodologies developed for 3D computations show consistence with the experimental results. However, to solve the flow in the boundary layer of the shroud wall, specially before rotors, the simulation differ. That comes from the application of only one turbulent model through the whole system. For the flow before rotors, it is probably closer to laminar flow because it is being accelerated. Therefore, searching a way to apply the different turbulent models to different parts of the shrouded system might be interesting for

improving the solution on boundary layer by simulations.

Appendix A

Fundamental Froude Theory for Free Rotor System

This section provides the detailed derivation of the theoretical model used for predicting the performance of a or multiple free rotor(s). The aerodynamics of free rotor could give a preliminary prediction and comparable basics for the shrouded rotor(s) through the Froude model extension. For a more in-depth analysis and discussion of the aerodynamics of free rotor, Ref.[71] is recommended as a standard textbook.

A.1 Froude Model of Free Rotor

The simplest analysis method–Froude model that can be performed on a hovering rotor involves three well known conservation laws of mass, momentum and energy together with Bernoulli equation. It can be applied to the hovering rotor problem using the flow model showed in Fig.A.1. It is assumed that thrust loading is uniform over an infinity thin propeller disk which equals to infinity number of blades of an or multiple rotor system, and the flow is quasi-steady, irrotational, inviscid and incompressible perfect fluid.

Figure.A.1 displays an overview of the general configuration of the Froude model for a free rotor. Once the rotor is launched, the infinity air stream will be inhaled to the natural channel. And with the input of the power which keeps the rotor rotating, the pressure difference is formed at the two sides of the rotor, which gives the rotor vertical thrust to keep the position or attitude in the space.

According to those assumptions above, for one of the main aims of the Froude theory is to calculate the thrust, the Bernoulli equation is therefore used:

$$\frac{1}{2}v^2 + \frac{p}{\rho_\infty} = cte \tag{A.1}$$

Where v denotes the velocity, p_∞ the static pressure and ρ the density of the fluid that is air. Applying Bernoulli's equation to the different flow region, firstly from ∞ to 1, then from 2 to s, the following relations are obtained:

$$p_\infty + \frac{1}{2}\rho v_\infty^2 = p_1 + \frac{1}{2}\rho v_1^2 \tag{A.2}$$

$$p_2 + \frac{1}{2}\rho v_2^2 = p_s + \frac{1}{2}\rho v_s^2 \tag{A.3}$$

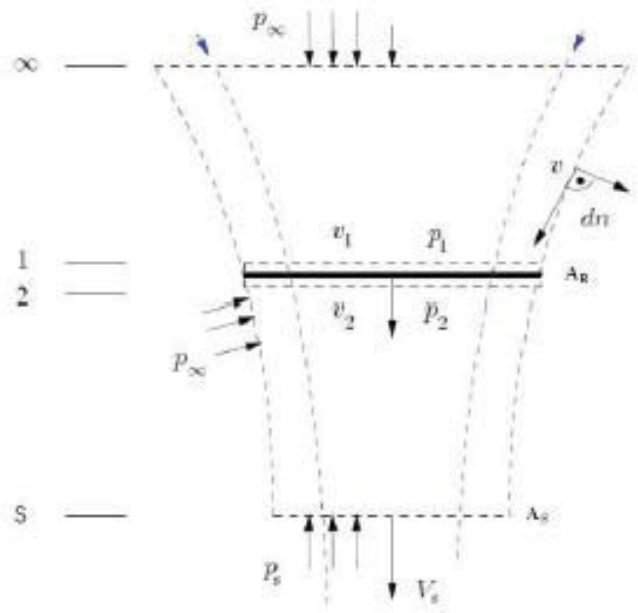

Figure A.1: The Froude model for a free rotor

As the real environment, taking $v_\infty = 0$ to simplify the math, and considering $p_s = p_\infty$ due to hypothesis 8 and $v_1 = v_2 = v_R$ due to hypothesis 7, combined the eq.A.2 and A.3, the static pressure jump $\triangle P$ at the rotor can be obtained:

$$\triangle P = p_2 - p_1 = \frac{1}{2}\rho v_s^2 \tag{A.4}$$

Using this static pressure difference, the thrust of the rotor is given as:

$$F_R = (p_2 - p_1)A_R = \frac{1}{2}\rho v_s^2 A_R \tag{A.5}$$

Besides the thrust, in order to get clear the relations between different variables such total pressure, static pressure and velocity, the momentum equations for invisible flow will be integral on the whole closed system that is began at inlet plane and ended at outlet plane.

$$\int_V \frac{\partial \rho v_i}{\partial t} dV + \int_S \rho v_i v_j \cdot n_j dS = -\int_S p n_i dS + \int_V \rho f_i dV + F_{K_i} \tag{A.6}$$

Where V denotes an appropriate control volume, S the surface of the control volume, f_i the volume force and F_{K_i} discrete force acting on designed points in the control volume. In addition to the hypotheses introduced above, the eq.A.6 can be adapted as following considerations:
1. No time dependencies: $\frac{\partial v_i}{\partial t} = 0$;
2. The integrated pressure over the entire stream tube becomes zero: $-\int_S p n_i dS =$

0;
3. No volume forces are considered, $f_i = 0$.
These simplifications result in:

$$\int_S \rho v_i v_j \cdot n_j dS = F_{K_i} \tag{A.7}$$

Applying this equation between points ∞ and 1, due to the fact that the vectors of the flow velocities are perpendicular to the rotor and outlet plane, the deformation of eq.A.7 is as following:

$$\rho v_R v_R A_R = -p_1 A_R \tag{A.8}$$

In the same way, between plane 2 and S, the following expression is obtained:

$$-\rho v_R v_R A_R + \rho v_S v_S A_S = p_2 A_R \tag{A.9}$$

Combined the eq.A.8 and A.9, the rotor thrust can be got.

$$F_R = \triangle P \cdot A_R = \rho v_R v_R A_R - \rho v_R v_R A_R + \rho v_S v_S A_S \tag{A.10}$$

Comparing the rotor thrust expression got by eq.A.1 and A.10, combined to the mass conservation law, it can lead to the following relations:

$$v_S = 2v_R \qquad A_S = \frac{A_R}{2} \tag{A.11}$$

The equations above means that the area of the slipstream at infinity is half the area of the rotor disk. From eq.A.10 and A.11, the expression for the induced velocity around the rotor as function of the thrust can be obtained.

$$v_R = \sqrt{\frac{F_R}{2\,\rho\,A_R}} = \sqrt{(\frac{F_R}{A_R})\frac{1}{2\,\rho}} \tag{A.12}$$

Where F_R/A_R is the disk loading, an important rotor operational parameter also denoted as DL. Through eq.A.13, the power required by a hovering rotor as a function of its thrust is given by:

$$P = F_R v_R = F_R \sqrt{\frac{F_R}{2\,\rho\,A_R}} = \frac{F_R^{3/2}}{\sqrt{2\rho A_R}} \tag{A.13}$$

The power calculated was assumed that the rotor was working in an ideal fluid with potential flow, it does not include any viscous loses. In fact since it is the theoretical minimum that the rotor will require for a given thrust, this is known as ideal power.

A.2 Main Merformance Prediction

As the explanation of Froude theory above, this model can be used to obtain a prediction of the variations in air pressure and velocity through the flow field of an or multiple rotor system. For hovering rotor, the total pressure upstream of the rotor is equal to ambient atmospheric pressure P_{atm}, while downstream of the rotor is equal to the sum of atmospheric pressure and disk loading DL. According to the mass conservation, $\rho A_i v_i = \rho A_R v_R$ and Bernoulli equations talked above, the pressure variation both at upstream and downstream of rotor are needed for the shape of the flow field boundary as a function of distance from the plane of the rotor disk. And generally the pressure variation relative to the atmospheric in the upstream of the rotor could be obtained by assuming the cross sectional area of the upstream flow varied 'linearly' from infinity to the area of the rotor disk. In the downstream rotor, for free system $A_e/A_R(= K_e) = \frac{1}{2}$, the geometry of the wake can be estimated by the Landgrebe wake model as Ref.[71].

Therefore, based on the analysis of Froude theory for free rotor, the behaviors of the pressure and the velocity along the longitudinal axis marked as Z of an airscrew are presented in Fig.A.2.

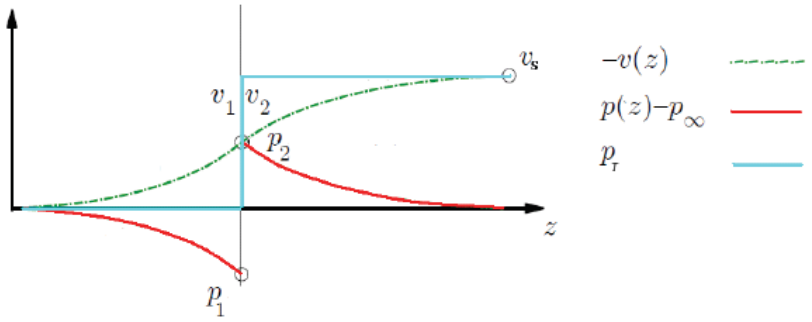

Figure A.2: The behaviors of free rotor according to Froude theory

Appendix B

2D Axisymmetrical Simulation Settings

This appendix provides a basic description of the theoretical background needed to understand the basis of CFD and the settings for two dimensional axisymmetrical simulations. A revision of the conservation laws for mass, momentum and energy was introduced firstly. Based on it, the chosen method to model turbulent–Reynolds Averaged Navier Stokes Equations, the discretization methods and some available solvers in Fluid 6.6 were then exposed.

B.1 Conservation Laws of Fluid Mechanics

In general, three laws from the basic equations of fluid mechanics:

- Continuity equation (mass conservation)
- Newton's second law (momentum conservation)
- Energy equation (energy conservation)

Continuity equation: This equation sets that the time rate change of mass in a closed, fixed control volume must equal the sum of the mass entering or leaving this volume through its boundaries and the "arised" and "disappeared" mass in the volume. It is given in differential form as:

$$\frac{\partial \rho}{\partial t} + \overrightarrow{\nabla} \cdot (\rho \vec{v}) = 0 \tag{B.1}$$

Momentum equation: This equation fixes that the time change rate of momentum in a closed, fixed control volume equals the sum of all the forces acting on the control volume (superficial forces on the boundaries and volumetric forces on the volume), the flow of momentum through the boundaries and the "arised" and "disappeared" momentum in the volume. Writing it in differential form:

$$\rho(\frac{\partial \vec{v}}{\partial \tau} + (\vec{v} \cdot \overrightarrow{\nabla})\vec{v}) = -\overrightarrow{\nabla} p + \overrightarrow{\nabla} \cdot \vec{\vec{\tau}} + \rho \vec{f_m} \tag{B.2}$$

$\vec{\vec{\tau}}$ denotes the tensor of viscous shear stress and represents the change of momentum due to the shear forces between all the single molecules in the control volume and f_m which denotes volumetric forces. To obtain closed solutions, this tensor must be expressed in function of the velocity and pressure. This equation remains

valid without restrictions. However, some assumptions are made in order to obtain a simpler formulation for the shear stress. The first is Newtonian fluid is assumed. It describes the proportionality relation of shear stresses to the velocity gradient acting perpendicularly. Two further assumptions are made: the fluid is assumed homogeneously and isotropically, which means that all fluid properties do not depend on orientation. Once these hypotheses have been introduced, the shear tensor leads to a correlation of the stress tensor with the flow field variables. And then the momentum equation can be solved through introducing this correlation. This is known as the Navier-Strokes equations and describe any kind of fluid flow.

Energy equation: This equation imposes that the time change rate of energy in a closed fixed control volume equals the sum of all the work done by forces from outside, the energy flow through all boundaries and the energy increase or decrease in the volume. In differential form, it is as follows:

$$\rho\frac{De}{Dt} = -\overrightarrow{\nabla}\cdot(p\vec{v}) + \vec{v}\cdot(\vec{\tau}\cdot\vec{v}) - \nabla\vec{q} + \rho\vec{f_m}\cdot\vec{v} \tag{B.3}$$

where e denotes the total energy: internal energy and kinetic energy.

For calculation of six variables of the flow field(density, pressure, temperature and velocity in three directions), only five equations showed above which momentum equation is in three directions are not enough. The state equation for a perfect gas is applied together for solving the physics.

B.2 Turbulence Modeling: RNGS

Compared to Direct Numerical Simulation on turbulent flow, for reducing the calculation resources, the Reynolds Averaged Navier-Stokes Equations (RANS) is frequently used. In this approach, the variables of the flow are composed of an averaged in time term ($\vec{\xi}$) plus small random fluctuations (ξ') which introduce the turbulent behavior. The variables are therefore expressed as:

$$u_i = \bar{u_i} + {u_i}', \qquad p = \bar{p} + p' \tag{B.4}$$

Consequently, the expression forms of continuity equation and momentum equation can be changed by introducing these two relations. And the new form of momentum equations is:

$$\rho\frac{\partial\bar{u_i}}{\partial t} + \rho\frac{\partial\bar{u_j}\bar{u_i}}{\partial x_j} = -\frac{\partial\bar{p}}{\partial x_i} + \mu\frac{\partial\tau_{ij}}{\partial x_j} - \rho\frac{\partial\overline{u_j'u_j'}}{\partial x_j} + \overline{\rho f_i} \tag{B.5}$$

It can be observed that additional terms representing turbulence appear. These terms ($\overline{u_j'u_j'}$) are known as Reynolds stresses. In order to close the equation, these terms must be modeled. Modeling these terms is the aim of the RANS turbulence models[]. Turbulence models based on turbulent viscosity introduce a viscosity coefficient characterized by a representative fluctuating speed v and a representative length of whirling structures l: v_t vl. The modeling of the Reynolds stresses is then done with the Boussinesq hypothesis:

$$-\overline{u'_j u'_j} = 2v_t S_{ij} - \frac{2}{3}k\delta_i j \tag{B.6}$$

where k denotes the turbulent kinetic energy and $\delta_i j$ denotes the Kronecker symbol. The turbulent viscosity coefficient must be then calculated. This can be done with zero, one or two additional equations depending on the turbulence model used such as Spalart-Allmaras, Standard $k-\varepsilon$, Shear Stress Transport $k-\omega$ models and so on. The application of each model are:

1. Spalart-Allmaras model: It is a "low cost" RANS model, as it uses only one equation. It was designed specifically for aerospace applications involving wall-bounded flows. It is suitable for mildly complex (quasi-2D) external and internal flows and boundary layer flows under pressure gradients. Moreover it results economical in time, as the use of only one equation results in lower calculation times;

2. Standard $k-\varepsilon$ turbulence model (SKE): It is a two equations turbulence model. One equation is used to calculate the turbulent kinetic energy k; the other is used to calculate the rate of dissipation ε. It is one of the most used models for flow simulations. It is a robust method, suitable for the calculation of free shear flows. However, it performs poorly for complex flows involving severe pressure gradients, separation and large streamline curvature. It is not appropriate for boundary layer problems. Some modified turbulence models exists, such as the renormalization group model (RNG) or the realizable model (RKE);

3. $k-\omega$ turbulence model: It is also a two equations turbulence model. These two equations are used to calculate the turbulent kinetic energy k and the specific dissipation rate ω. It was developed in parallel with $k-\omega$ models. They have a better performance in boundary layer flows involving pressure gradients. However, they are not appropriate for the calculation of external free flows;

4. Shear Stress Transport $k-\omega$ model (SST-KW): It is also a two equations turbulence model. It combines the advantages of both the $k-\omega$ and the $k-\varepsilon$ models. For the external flow, the $k-\varepsilon$ formulation is used. For the near wall flow, the $k-\omega$ formulation is used. For the transition to one formulation to the other, a function of variation of coefficients is used.

B.3 Discretization Methods

The most usual discretization method in commercial CFD software is the Finite Volume Method. Particularly, the solver Ansys Fluent, which will be used in this project, uses this kind of discretization method. In the Finite Volume Method, the differential coefficients are integrated over volume elements, which replace the complete calculation space. The resulting volume integrals over the volume are replaced by surface integrals applying Gauss theorem. The basic procedure for performing flow simulations using FVM consists in:

1. Dividing the complete calculation volume in mesh points.
2. Definition of the control volumes
3. Integrating equations over all control volumes

4. Expressing the development of the transport properties using polynomial approaches.

5. Solving the discretised equations system for the transport properties.

The first two steps summarizes in creating a correct mesh for the case to solve. Then, taking the transport equation for any of the transport properties (ϕ) integrated over the control volumes through Gauss theorem, which yields to an equation with surface integrals for the convection and the diffusion terms. The values of the transport properties at the interfaces of the control volume are obtained from the values at the center points by interpolation. For the calculation of these values different kind of polynomial approaches are used, which are applied to the values of adjacent mesh points of the surfaces. The classification of different polynomial approaches (linear, quadratic...) can be done by evaluating the discretization error. This error is analyzed by observing the evolution of the solution when the mesh point.s distance is reduced. It is defined as:

$$\frac{E_h}{E_{h/2}} = 2^n \tag{B.7}$$

where E_h denotes the error for a mesh points distance h, $E_{h/2}$ denotes the error for a mesh points distance $h/2$ and n denotes the order of the scheme. If reducing the distance to a half, reduces the error also to a half, the discretization scheme is of first order. If the error is reduced by a factor four, the discretization scheme is of second order. Therefore in this work, all the 2D simulation will apply the second order for discretization scheme for getting a better precision.

B.4 Solver Settings

Many solvers, that apply the described method above, solves almost any fluid dynamics problem. As it has been said, the solver used in this project is Fluent 6.3. Before launching any calculation using Fluent 6.3, some important parameters and settings must be defined. These settings depend on the kind of problem that will be solved, the available time and the precision needed, between others. A brief description on chosen of the more important settings will be described:

Solver: The solver used is the pressure-based segregated which requires less memory and adapts correctly to our problem. Green-Gauss Node Based gradient option is used to reduce false diffusion. Axisymmetric space is chosen;

Viscous model: Spalart-Allamaras is chosen due to it is great economy in calculation time with correct results for problems similar to the one being studied.

Interpolation method for momentum: In view of the calculation precision and time consumption, second order upwind is chosen. It has second order accurate. It is essential as the flow is not aligned with grid. This is useful for the mesh arrangement of the geometry in this work especially for the inlet lip.

Interpolation method for pressure: one method called PRESTO! is chosen. It is used for highly swirling flows, flows involving steep pressure gradients (porous media, fan model, etc.), or in strongly curved domains.

Pressure-velocity coupling: SIMPLEC is chosen because it allows a faster convergence on steady problems.

Appendix C

Experimental Setup Details

This appendix will focus on the introduction of the experimental instruments including the construction of three types sensors for testing thrust, torque and velocity, the motor which lanches two rotors, shroud model as well as the cosspondent pressure tested positions on it, and the calibration on different key quantities and so on.

C.1 Sensors

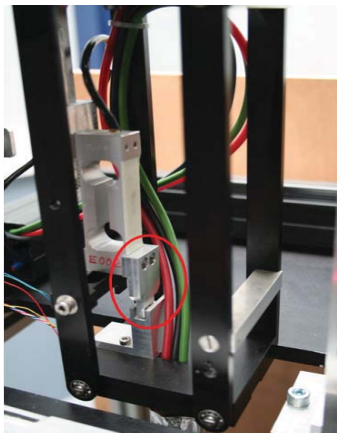

Figure C.1: Thrust sensor for rotor

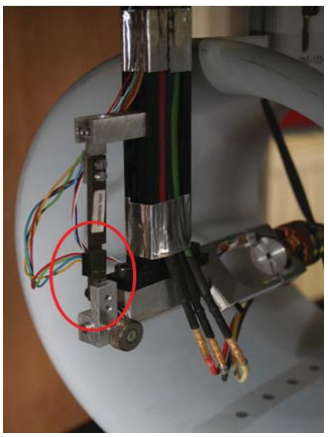

Figure C.2: Torque sensor for rotor

Figure C.3: Thrust sensor for shroud

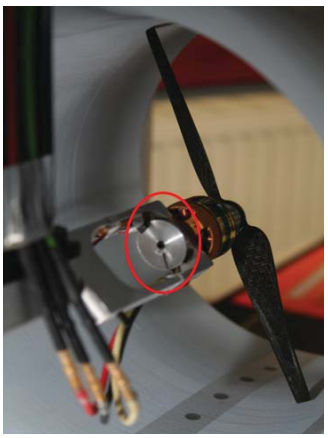

Figure C.4: Velocity sensor for rotor

C.2 Electric Motors

AXI2208/26 Electric Motor was Designed and Manufactured by Modelmotors Ltd. in the Czech Republic[83].

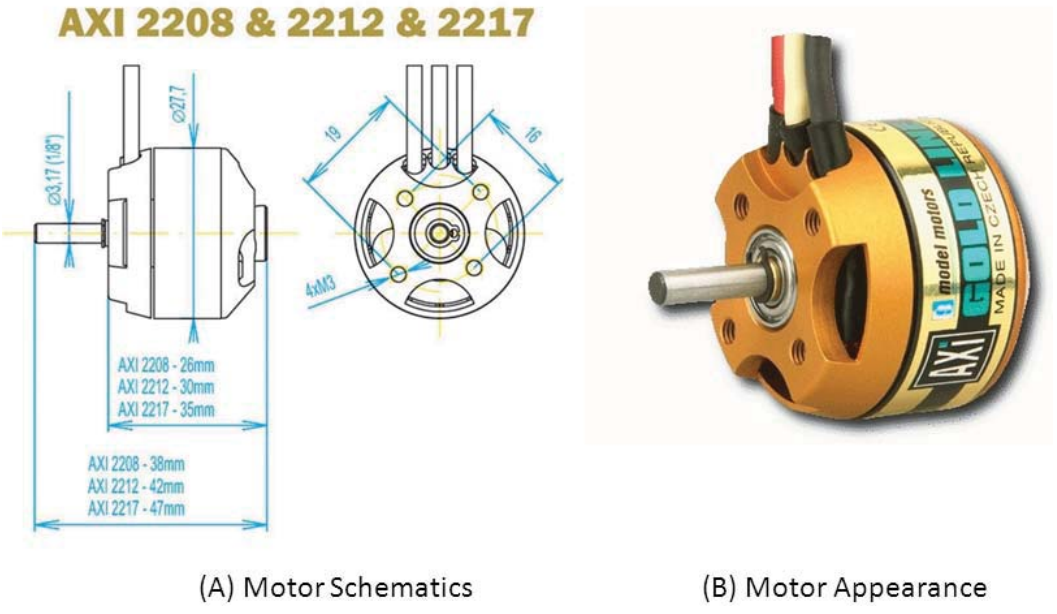

Figure C.5: Motor scheme (A) and appearance (B)

Table C.1: Parameters of motor

Parameter	**Value**
No. of Cells	6-8
Rpm/V	1420
Max. Efficiency	82%
Max. Efficiency Current	5-9A (>75%)
No. Load Current/10V	0.6A
Current Capacity	16 A/60s
Internal Resistance	155m0hm
Dimensions (Diameter x Length)	ϕ 27.7x26mm
Shaft Diameter	3.17mm
Weight With Cables	45g

C.3 Shroud Model and Pressure Tested Positions

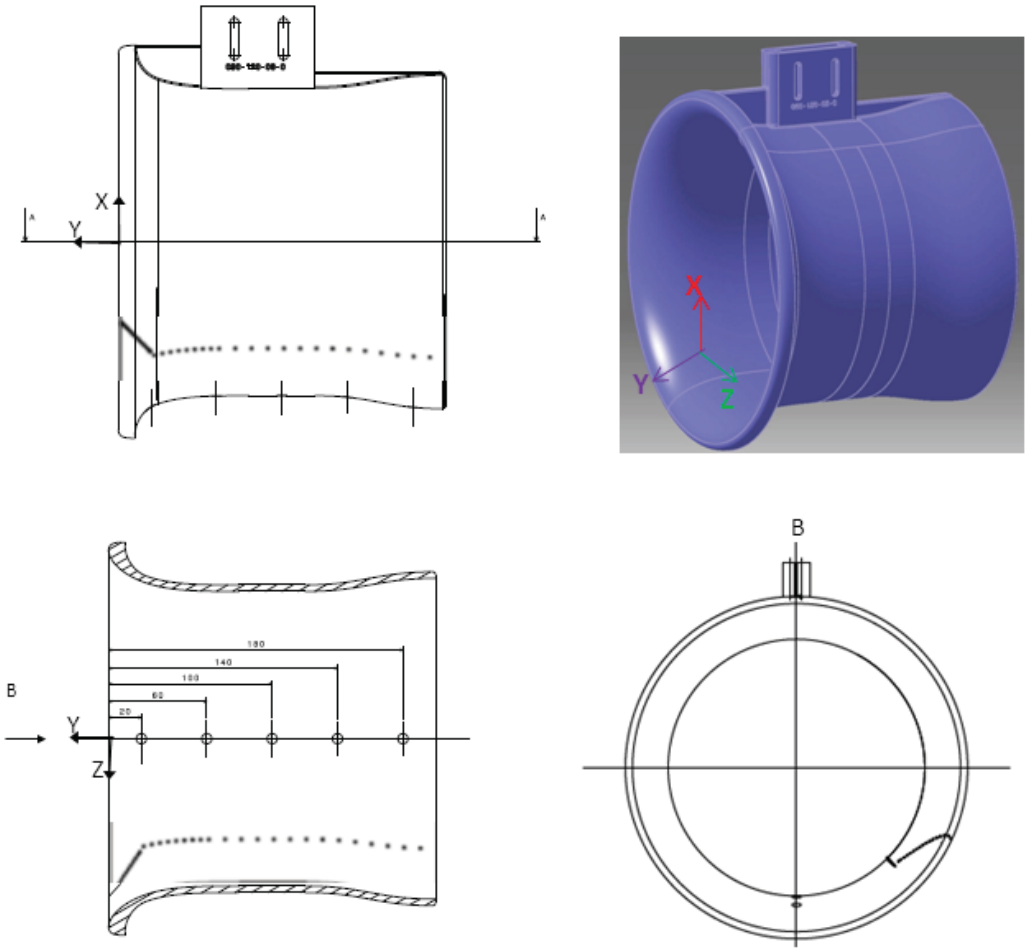

Figure C.6: Shroud and pressure tested positions

Table C.2: Installation positions of total pressue probe

Axial Position	x (mm)	y (mm)	z (mm)
No.0	-115.0	0	0
No.1	-96.2	-20	0
No.2	-90.2	-60	0
No.3	-90.0	-100	0
No.4	-90.9	-140	0
No.5	-97.1	-180	0
No.6	-98	-200	0

Table C.3: Installation positions of static pressue probe

Position	x (mm)	y (mm)	z (mm)
No.1	-47.7	-0.1	103.7
No.2	-47.9	-0.3	106.7
No.3	-48.3	-0.7	100.9
No.4	-49.2	-1.6	98.2
No.5	-50.4	-2.8	95.7
No.6	-51.6	-4.0	93.3
No.7	-53.0	-5.4	90.9
No.8	-54.3	-6.7	88.6
No.9	-55.7	-8.1	86.4
No.10	-57.2	-9.6	84.2
No.11	-58.6	-11.0	82.0
No.12	-60.1	-12.5	79.8
No.13	-61.5	-13.9	77.6
No.14	-63.0	-15.4	75.4
No.15	-64.4	-16.8	73.3
No.16	-65.6	-17.9	71.6
No.17	-68.0	-20.3	68.0
No.18	-67.8	-25.3	66.8
No.19	-65.8	-30.3	65.8
No.20	-65.1	-35.3	65.1
No.21	-64.6	-40.3	64.6
No.22	-64.2	-45.3	64.2
No.23	-64.0	-50.3	64.0
No.24	-63.8	-55.3	63.8
No.25	-63.7	-60.3	63.7
No.26	-63.7	-70.3	63.7
No.27	-63.6	-80.3	63.6
No.28	-63.6	-90.3	63.6
No.29	-63.6	-100.3	63.6
No.30	-63.6	-110.3	63.6
No.31	-63.6	-120.3	63.6
No.32	-63.8	-130.3	63.8
No.33	-64.3	-140.3	64.3
No.34	-65.3	-150.3	65.3
No.35	-66.5	-160.3	66.5
No.36	-67.7	-170.3	67.7
No.37	-68.7	-180.3	68.7
No.38	-69.1	-190.3	69.1

C.4 Test Bench Calibration

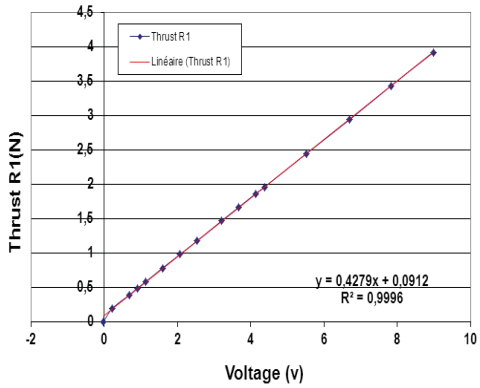

Figure C.7: Rotor.1 thrust sensor

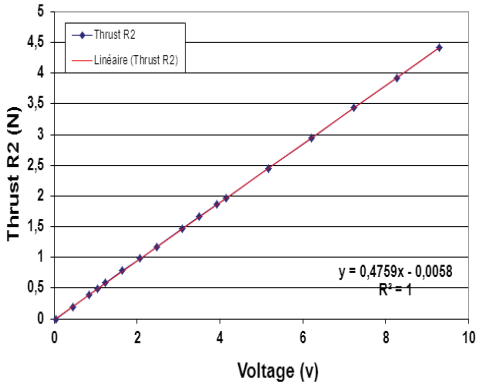

Figure C.8: Rotor.2 thrust sensor

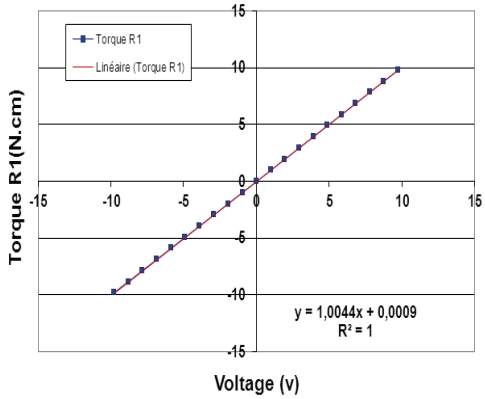

Figure C.9: Rotor.1 torque sensor

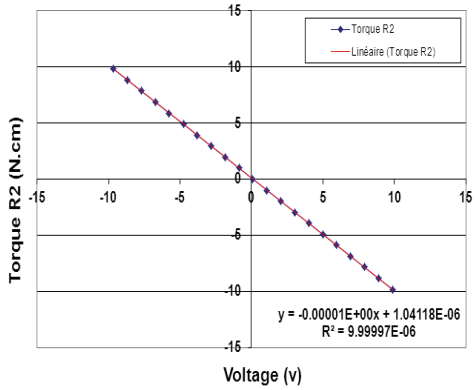

Figure C.10: Rotor.2 torque sensor

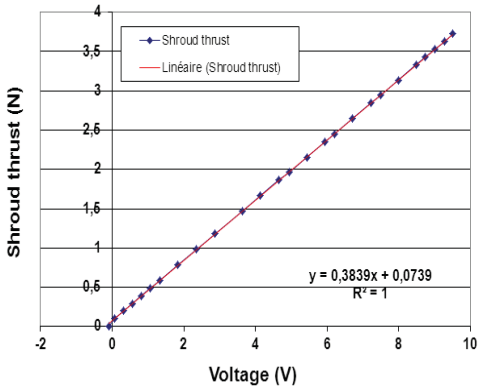

Figure C.11: Shroud thrust sensor

C.5 Main Performances Calculation

The expressions of main performances are summered in the following table:

Table C.4: The expression of main performances

Parameters	**FSR**	**FDR**	**SSR**	**SDR**
PL	$\frac{F_r}{Q\omega}$	$\frac{F_{r1}+F_{r2}}{Q_1\omega_1+Q_2\omega_2}$	$\frac{F_r+F_s}{Q\omega}$	$\frac{F_{r1}+F_{r2}+F_s}{Q_1\omega_1+Q_2\omega_2}$
FoM	$\frac{F_r\,V_i}{Q\omega}$	$\frac{(F_{r1}+F_{r2})\,V_i}{Q_1\omega_1+Q_2\omega_2}$	$\frac{F_r\,V_i}{Q\omega}$	$\frac{(F_{r1}+F_{r2})\,V_i}{Q_1\omega_1+Q_2\omega_2}$
V_i	$\frac{F_r}{2\,\rho\,A_r}$	$\frac{F_{r1}+F_{r2}}{2\,\rho\,A_r}$	$\frac{2\,K_s^2\,F_r}{\rho\,A_r}$	$\frac{2\,K_s^2\,(F_{r1}+F_{r2})}{\rho\,A_r}$
C_T	$\frac{F_r}{\rho\,A_r\,(\omega R)^2}$	?	$\frac{F_r+F_s}{\rho\,A_r\,(\omega R)^2}$	?
C_P	$\frac{Q\omega}{\rho\,A_r\,(\omega R)^3}$	?	$\frac{Q\omega}{\rho\,A_r\,(\omega R)^3}$	?
FoM(C_T,C_P)	$\frac{C_T^{\frac{3}{2}}}{\sqrt{2}C_P}$	?	$\frac{C_T^{\frac{3}{2}}}{2\sqrt{K_s}C_P}$	?

Appendix D

Experimental Complementary Results

D.1 Individual Performances of SDR80-40

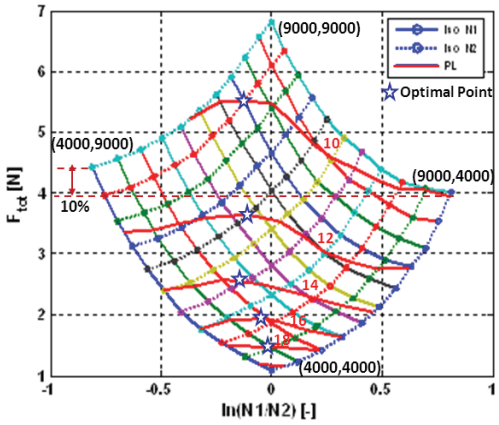

Figure D.1: F_t ver. InN_1/N_2

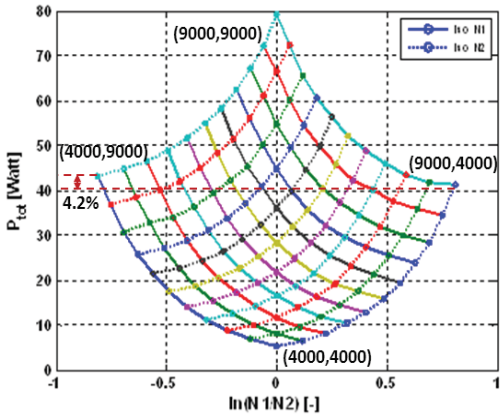

Figure D.2: P_t ver. InN_1/N_2

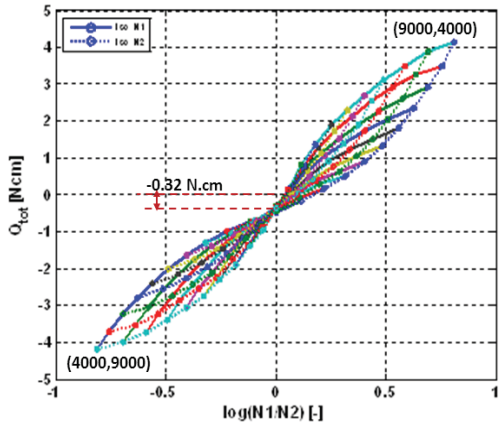

Figure D.3: Q_t ver. InN_1/N_2

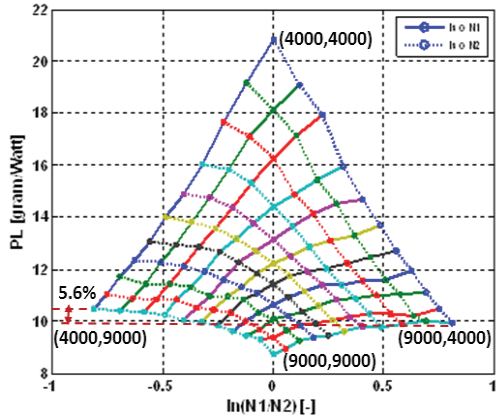

Figure D.4: PL ver. InN_1/N_2

D.2 Performances of SDR with $D_{rel} = 20$ or 40 mm

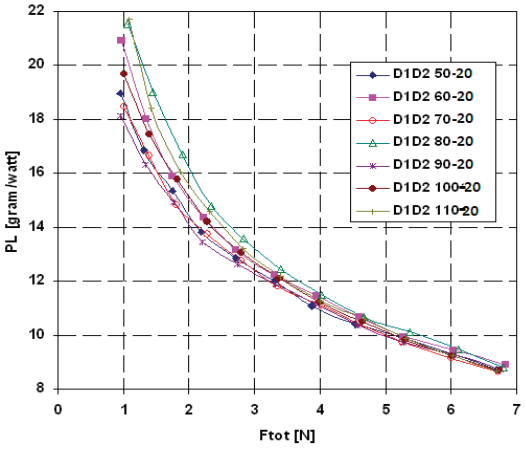

Figure D.5: PL ver. F_t with $D_{rel} = 20\ mm$

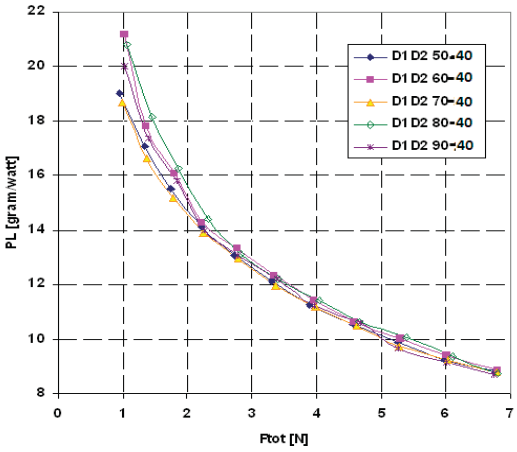

Figure D.6: PL ver. F_t with $D_{rel} = 40\ mm$

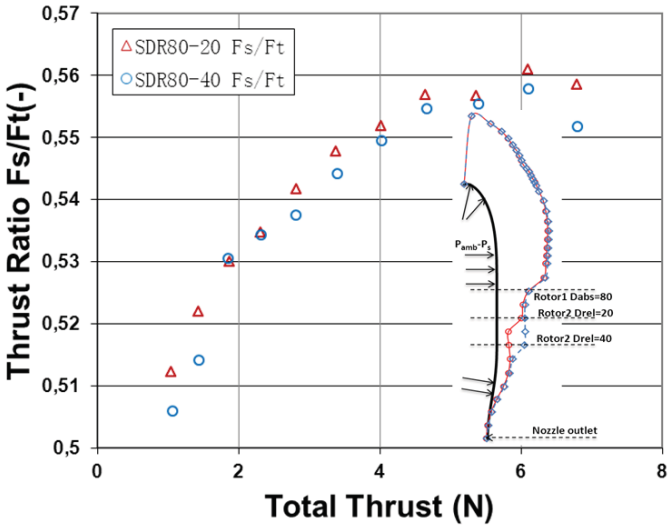

Figure D.7: Compsrison on shroud thrust between SDR 80-20 and 80-40

D.3 Rotor Thrust Performance of SDR80-20

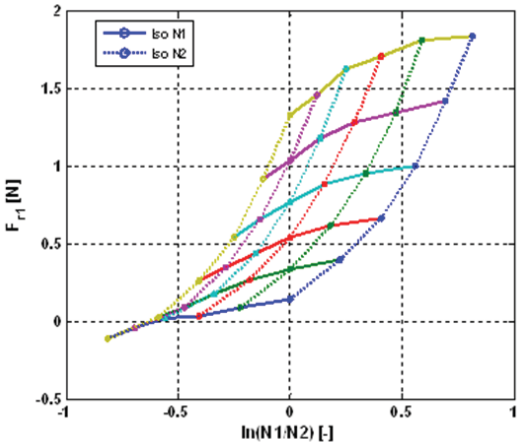

Figure D.8: SDR80-20: F_{r1} ver. $In(N_1/N_2)$

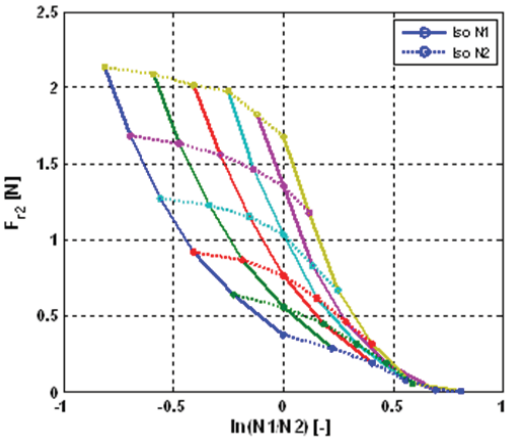

Figure D.9: SDR80-20: F_{r2} ver. $In(N_1/N_2)$

Bibliography

[1] Hundley, R. O., and Gritton, E. C.,"Future Technology-Driven Revolutions in Military Operations: Results of a Workshop," RAND National Defense Research Institute DB-110-ARPA, Santa Monica, CA, 1994 Defense Technical Information Center (DTIC) Accession Number ADA285478; (Cited on pages 1 and 191.)

[2] McMichael, J. M., and Francis, USA (FRet.), C.M.S., "Micro Air Vehicles Toward a New Dimension in Flight", U.S. Department of Defense Weapons Systems Technology Information Analysis Center Newsletter, Aug.7, 1997; (Cited on pages vii and 1.)

[3] Lowson, M. V., "Aerodynamics of Aerofoils at Low Reynolds Numbers," UAVs - 14th Unmanned Air Vehicle Systems International Conference, United Kingdom, April, 1999; (Cited on pages vii, 2 and 191.)

[4] Samuel, P., Sirohi, J., Rudd, L., Pines, D., and Perel, R., "Design and Analysis of a Micro Coaxial Rotorcraft," American Helicopter Society Vertical Lift Aircraft Design Conference, San Francisco, CA, Jan 19-21, 2000; (Cited on pages vii and 2.)

[5] Young, L., Aiken, E., Johnson, J., Andrews, J., R., D., and J., K., "New Concepts and Perspectives on Micro-Rotorcraft and Small Autonomous Rotary-Wing Vehicles", 20th AIAA Applied Aerodynamics Conference, St. Louis, MO, Jun 24-27, 2002; (Cited on pages vii and 2.)

[6] Bohorquez, F., and Pines, D., "Rotor and Airfoil Design for Efficient Rotary Wing Micro Air Vehicles", American Helicopter Society 61st Annual Forum Proceedings, Grapevine, TX, Jun 1-3, 2005; (Cited on pages vii and 2.)

[7] Leishman, J. G., "Principles of Helicopter Aerodynamics", 1st ed., Cambridge Aerospace Series. Cambridge University Press, New York, NY, 2000; (Cited on pages vii and 2.)

[8] Harrington, R. D., "Full-Scale-Tunnel Investigation of the Static-Thrust Performance of a Coaxial Helicopter Rotor", NACA TN-2318, Mar. 1951; (Cited on pages viii and 3.)

[9] Andrew, M. J., "Coaxial Rotor Aerodynamics in Hover", Vertica, vol. 5, 1981, pp. 163172; (Cited on pages viii and 3.)

[10] Thurston, S., and Amsler, R. C., "Review of Marine Propellers and Ducted Propeller Propulsive Devices", Journal of Aircraft, Vol. 3, No. 3, May-Jun 1966, pp. 255-261; (Cited on pages viii and 3.)

[11] Ham, N. D., and Moser, H. H., "Preliminary Investigation of a Ducted Fan in Lifting Flight", Journal of the American Helicopter Society, Vol. 3, No. 3, Jul 1958, pp. 17-29; (Cited on pages viii and 3.)

[12] Mouille, R., "The "Fenestron," Shrouded Tail Rotor of the SA.341 Gazelle," Journal of the American Helicopter Society, Vol. 15, No. 4, Oct 1970, pp. 31-37; (Cited on page 3.)

[13] Sacks, A. H., and Burnell, J. A., "Ducted Propellers - A Critical Review of the State of the Art," In Progress in Aeronautical Sciences, A. Ferri, D. Kuchemann, and L. H. G. Sterne, Eds., Vol. 3. Pergammon Press, The Macmillan Company, New York, NY, 1962, Ch. Part 2, pp. 85-135; (Cited on pages viii and 3.)

[14] Yaggy, P. F., and Goodson, K. W., "Aerodynamics of a Tilting Ducted Fan Configuration," NASA TN D-785, Ames Research Center, Moffett Field, CA and Langley Research Center, Langley, VA, Mar 1961; (Cited on pages viii and 3.)

[15] Stipa, L., "Experiments with Intubed Propellers," NACA TM 655, Jan 30, 1932 Translated from L'Aerotecnica (Rome), pp. 923-953, Aug 1931; (Cited on pages viii and 4.)

[16] Kruger, W., "On Wind Tunnel Tests and Computations Concerning the Problem of Shrouded Propellers," NACA TM 1202, Feb 1949 Translation of ZWB Forschungsbericht Nr. 1949; (Cited on pages viii and 4.)

[17] Platt, Jr., R. J., "Static Tests of a Shrouded and an Unshrouded Propeller", NACA RM L7H25, Langley Memorial Aeronautical Laboratory, Langley Field, VA, Feb., 1948; (Cited on page 4.)

[18] Donald M. Black, et al, "Shrouded propellers- A Comprehensive Performance Study", Division of Unites Aircraft Corporation; (Cited on page 5.)

[19] Taylor, R. T., "Experimental Investigation of the Effects of Some Shroud Design Variables on the Static Thrust Characteristics of a Small-Scale Shrouded Propeller Submerged in a Wing", NACA TN 4126, Langley Memorial Aeronautical Laboratory, Langley Field, VA, Jan 1958; (Cited on pages viii and 5.)

[20] Authors unknown, "An Investigation of the Shrouded Propeller Propulsive System on the Marvelette Aircraft", Mississippi State University, Aerophysics Department, August 1964; (Cited on pages viii, ix and 5.)

[21] Mort, K. W., "Summary of Large-Scale Tests of Ducted Fans", Conference on V/STOL and STOL Aircraft, Ames Research Center, Moffett Field, CA, Apr 1966, no. 8 in NASA-SP-116, NASA, pp. 97-113; (Cited on pages viii and 5.)

[22] Black, D. M., Wainauski, H. S., and Rohrbach, C., "Shrouded Propellers - A Comprehensive Performance Study", AIAA 5th Annual Meeting and Technology Display, Philadelphia, PA, Oct 21-24, 1968, no. AIAA-68-994, AIAA; (Cited on pages viii and 5.)

[23] Ruzicka, G., and Strawn, R., "Discrete Blade CFD Analysis of Ducted Tail Fan Flow", 42nd AIAA Aerospace Sciences Meeting and Exhibit, Jan. 2004; (Cited on page 5.)

[24] Séverac, E., Poncet, S., et al, "Large Eddy Simulation and Experimentation in an Enclosed Rotor-stator Flow", 18th Congrès Français de Mècanique, 2007; (Cited on pages ix and 5.)

[25] Thouault, N., Breitsamter, C., et al, "Numerical analysis of design parameters for a generic fan-in-wing configuration", Aerospace Science and Technology, 2009; (Cited on page 5.)

[26] Nouri, H., Ravelet, F., et al, "Experimental Investigations on the Design of a Ducted Counter-rotating Axial Flow Fans System", 46th Symposium of Applied Aerodynamics – Aerodynamics of Rotating Bodies, Mar. 2011; (Cited on page 5.)

[27] Vuillet, A., and Morelli, F., "New Aerodynamic Design of the Fenestron for Improved performance", 12th European Rotorcraft Forum, Garmisch-Partenkirchen, Germany, Sep. 1986; (Cited on pages ix and 5.)

[28] Cycon, J. P., "Decoding the Cypher UAV", Vertiflite, Vol. 36, No. 6, Nov/Dec 1990, pp. 56-58; (Cited on page 5.)

[29] Cycon, J. P., "Sikorsky Aircraft UAV Program", Vertiflite, Vol. 38, No. 3, May/Jun 1992, pp. 26-30; (Cited on page 5.)

[30] Thornberg, C. A., and Cycon, J. P., "Sikorsky Aircraft's Unmanned Aerial Vehicle, Cypher: System Description and Program Accomplishments", American Helicopter Society 51st Annual Forum Proceedings, FortWorth, TX, May 9-11, 1995, pp. 804-811; (Cited on page 5.)

[31] Walsh, D., and Cycon, J. P., "The Sikorsky Cypher(R) UAV: A Multi-Purpose Platform with Demonstrated Mission Flexibility", AHS International 54th Annual Forum Proceedings, Washington, D.C., May 20-22, 1998, pp. 1410- 1418; (Cited on page 5.)

[32] Cycon, J. P., Rosen, K. M., and Whyte, A. C., "Unmanned Flight Vehicle Including Counter Rotating Rotors Positioned Within a Toroidal Shroud and Operable to Provide All Required Vehicle Flight Controls", US Patent No. 5,152,478, Oct 6, 1992 Filed May 18, 1990; (Cited on page 5.)

[33] Gupta, N., and Plump, J., "Design of a VTOL Micro Air Vehicle that Incorporates Counter-Rotating, Reversible Thrust Propellers", AUVSI Unmanned Systems Conference, Baltimore, MD, Jul 31 - Aug 2, 2001; (Cited on page 5.)

[34] Dyer, K. G., "Aerodynamic Study of a Small, Ducted VTOL Aerial Vehicle", PhD thesis, Massachusetts Institute of Technology, Department of Aeronautics and Astronautics, Cambridge, MA, Jun 2002; (Cited on pages 5 and 22.)

[35] Plump, J. M., and Gupta, N. R., "Vertical Takeoff and Landing Aerial Vehicle", US Patent No. 6,691,949 B2, Feb 17, 2004 Application filed Jul 8, 2002; (Cited on page 5.)

[36] Sirohi, J., Tishchenko M., Chopra I., "Design and Testing of a Micro-Aerial Vehicle with a Single Rotor and Turning Vanes", Proceedings of the AHS 61th Annual Forum, Grapevine TX, 1-3 June 2005; (Cited on pages ix, 5, 6 and 191.)

[37] Pereira, J., and Chopra, I., "Effect of Shroud Design Variables on Hover Performance of a Shrouded Rotor for Micro Air Vehicle Applications", AHS International Specialists' Meeting on Unmanned Rotorcraft, Chandler, AZ, Jan. 2005; (Cited on page 6.)

[38] Pereira, J., et al, "Performance and Surface Pressure Measurements on A MAV-Scale Shrouded Rotor in translational flight", American helicopter Society International, May 1-3, 2007; (Cited on pages ix, 5, 6 and 191.)

[39] Timothy E. Lee, J. Gordon Leishman, and Omri Rand, "Design and Testing of a Ducted Coaxial Rotor System for Application to a Micro Aerial Vehicle", American helicopter Society International, May 10-13, 2010; (Cited on pages 6 and 191.)

[40] Preston Martin and Chee Tung, "Performance and Flowfield Measurements on a 10-inch Ducted Rotor VTOL UAV", AMERICAN HELICOPTER SOCIETY PAPER AHS 2004-0264; (Cited on pages ix and 6.)

[41] Coleman, C.P., "A Survey of Theoretical and Experimental Coaxial Rotor Aerodynamic Research", Proceedings of the 19th European Rotorcraft Forum, Cernobbio, Italy, Sept. 14-16, 1993; (Cited on page 7.)

[42] Leishman, J. G., and Ananthan, S., "Aerodynamic Optimization of A Coaxial Proprotor", American Helicopter Society International, May 9-11, 2006; (Cited on page 7.)

[43] Kuchemann, D., and Weber, J., "Concerning the Flow About Ring-Shaped Cowlings, Part II: Annular Bodies of Infinite Length with Circulation for Smooth Entrance", NACA TM 1326, Nov 1951 Translation of ZWB Forschungsbericht Nr. 1236/2, Nov 11, 1940; (Cited on page 7.)

[44] Kuchemann, D., "Concerning the Flow About Ring-Shaped Cowlings of Finite Thickness", NACA TM 1325, Jan 1952 Translation of ZWB Forschungsbericht Nr. 1235, Jun 13, 1940; (Cited on page 7.)

[45] Kuchemann, D., and Weber, J., "Aerodynamics of Propulsion", 1st ed., McGraw-Hill Publications in Aeronautical Science. McGraw-Hill Book Company, Inc., New York, NY, 1953, Ch. 6: The ducted propeller, pp. 125-139; (Cited on page 7.)

[46] Wright, G. P., Driscoll, J. T., and Nickerson, Jr., J. D., "Handling Qualities of the H-76 FANTAIL TM Demonstrator", American Helicopter Society 47th Annual Forum Proceedings, 1991, pp. 123-135; (Cited on page 7.)

[47] Hua, H., and Spyros, A. K., "Modeling of Contra-Rotating and Ducted Propellers via Coupling of a Vortex-Lattice with a Finite VolumeMethod", University of Texas at Austin, 49th AIAA Aerospace Sciences Meeting including the New Horizons Forum and Aerospace Exposition, 4-7 Jan.,2011, Orlando, Florida; (Cited on page 7.)

[48] Wright, G. P., Driscoll, J. T., and Nickerson, Jr., J. D., "Handling Qualities of the H-76 FANTAIL TM Demonstrator", American Helicopter Society 47th Annual Forum Proceedings, 1991, pp. 123-135; (Cited on page 7.)

[49] Quackenbush, T. R., Wachspress, D. A., Boschitsch, A. H., and Solomon, C. L., "Aeromechanical Analysis Tools for Design and Simulation of VTOL UAV Systems", American Helicopter Society 60th Annual Forum Proceedings, Baltimore, MD, Jun 7-10, 2004; (Cited on page 7.)

[50] Micheal, R. M., and Selden, B. S., "Theoretical Study of Ducted Fan Performance", Ames Research Center, NASA contract report, Jan. 1970; (Cited on pages ix and 7.)

[51] Joan, H., and Francesc, G., "Numerical Analysis of the Flow Between a Pair of Corotating Enclosed Disks", University of Arizona, Department of Aerospace and Mechanical Engineering, Tucson, Arizona, USA, CUG 1996 Spring Proceedings; (Cited on pages ix and 7.)

[52] Ahn, J., and Lee, K., "A Computational Method for the Performance Modeling and Design of a Ducted Fan System", AsiaSim 2004, LNAI 3398, pp. 113.121, 2005; (Cited on pages ix and 7.)

[53] Rajneesh, S., and Matthew, W. F., "Ducted Rotor Performance Predictions Using Momentum Theory and CFD", pubilication and date unknown; (Cited on pages ix and 7.)

[54] Rajneesh, S., and Surya, D., "Shape Optimization of a Ducted Rotor System for Aerodynamic Performance", US Army Research Laboratory, (Cited on pages ix and 7.)

[55] Kazutoyo, Y., FURUKAWA, M., INOUE, M., and FUNAZAKI, K., "Numerical Analysis of Tip Leakage Flow Field in a Transonic Axial Compressor Rotor", Department of Mechanical Engineering, Iwate University, Japan, Proceedings of the International Gas Turbine Congress 2003 Tokyo November 2-7, 2003; (Cited on page 7.)

[56] Andy, K., Osgar, J. O., and Paul, G., "Ducted Fan UAV Modeling and Simulation in Preliminary Design", AIAA Modeling and Simulation Technologies Conference and Exhibit 20 - 23 August 2007, Hilton Head, South Carolina; (Cited on page 8.)

[57] Marin, P.B., and Boxwell, D.A., "Design, Analysis, and Experiments on a 10-inch Ducted Rotor VTOL UAV", AHS International Specialist's Meeting on Unmanned Rotorcraft, Jan 18-20, 2005; (Cited on page 8.)

[58] Rebecca, L. S., and William E. M., "Aeroacoustic Investigation of Shrouded Counter-Rotating Propellers", AIAA, 1991; (Cited on page 8.)

[59] Bccky, S., "Manipulation of Upstream Rotor Leading Edge Vortex and Its Effects on Counter-rotating Propeller Noise", AIAA, 1992; (Cited on page 8.)

[60] Hurault, J., Kouidri, S., et al, "Measurement of wall pressure fluctuations for noise prediction in axial flow fans", J. Acoust. Soc. Am. 123, 3688, 2008; (Cited on page 8.)

[61] Weir, R. J., "Aerodynamic Design Considerations for a Free-Flying Ducted Propeller", AIAA Atmospheric Flight Mechanics Conference, Minneapolis, MN, Aug 1988, no. AIAA-88-4377, pp. 420-431; (Cited on page 8.)

[62] Fleming, J., Jones, T., Lusardi, J., Gelhausen, P., and Enns, D., "Improved Control of Ducted Fan UAVs in Crosswind Turbulence", AHS 4th Decennial Specialists' Conference on Aeromechanics, San Francisco, CA, Jan 21-23, 2004; (Cited on page 8.)

[63] Thipyopas, C., Barènes, R., and Moschetta, J.-M., "Aerodynamic Analysis of a Multi-Mission Short-Shrouded Coaxial UAV: part I - Hovering Flight," AIAA Applied Aerodynamics Conference, Honolulu, Hawaii, 18-21 Aug. 2008. (Cited on page 8.)

[64] Thipyopas, C., Barènes, R., and Moschetta, J.-M., "Aerodynamic Analysis of a Multi-Mission Short-Shrouded Coaxial UAV: part II - Translation Flight," AIAA Aerospace Science Meeting, Orlando, Florida, 4-7 Jan. 2010; (Cited on page 8.)

[65] Grondin, G., Thipyopas, C., and Moschetta, J.-M., "Aerodynamic Analysis of a Multi-Mission Short-Shrouded Coaxial UAV: Part III - CFD for Hovering Flight", AIAA Applied Aerodynamics Conference, Chicago, Illinois, 28 June - 1 July 2010; (Cited on page 8.)

[66] Rowland, B., "Design of Contra-rotating Coaxial Propellers", Diploma thesis, June. 2003; (Cited on page 9.)

[67] Sayers, B., "Experimental Study on Shrouded Contra-rotating rotor", Report, Dec., 2006; (Cited on page 9.)

[68] Quixada, D. M., "Study on Experimental and Theoretical approaches of Contra-rotating Shrouded Propellers", Diploma thesis, 2007; (Cited on page 9.)

[69] Henrion, S., "Performance Study of Shrouded Contra-rotating rotor", Report, Dec., 2008; (Cited on page 9.)

[70] Ritter, M. R., "CFD investigation of the ground effect and the propulsion system of BR2C micro drone", Diploma thesis, 2008; (Cited on page 9.)

[71] Leishman, J. G., Principles of Helicopter Aerodynamics, 1st ed., Cambridge Aerospace Series. Cambridge University Press, New York, NY, 2000; (Cited on pages 59, 159 and 162.)

[72] Kline, S. J. and McClintock, F. A., "Describing Uncertainties in Single-Sample Experiments." Mechanical Engineering, Vol.75, No.1, PP.3-8, 1953; (Cited on page 63.)

[73] Mar, D., Harold, Y., "Axisymmetric Analysis and Design of Ducted Rotors", Report, Dec. 2005; (Cited on pages xix and 59.)

[74] Betz, A., "Airscrews with minimum energy loss", Report, Kaiser Wilhelm Insititute for Flow Research, 1919; (Cited on pages xix and 59.)

[75] Glauert, H., "Elements of Airfoil and Airscrew Theory", Cambridge University Press, 1937; (Cited on pages xix and 59.)

[76] Benjamin, S., "Ètude Expérimentale de Doublet de Rotors Contrarotatifs", Laboratoire d'Aérodynamique et de Propulsion, ISAE, Dec. 2006; (Cited on page 72.)

[77] Deng, Y., Tao, R., Hu, J., "Experimental Investigation of the Aerodynamic Interaction Between Upper and Lower Rotors of a Coaxial Helicopter", Acta Aeronautica et Astronautica Sinica, Vol.24 No.1, Jan. 2003; (Cited on page 80.)

[78] Nagashima, T., Nakanish, K., "Optimum performance and wake geometry of coaxial rotor in hover [A]", Proceedings of the 7th European Rotorcraft and Powered Lift Forum, 1981; (Cited on page 97.)

[79] Zadravec, M., Basic, S., et al, "The Influence of Rotating Domain Size in A Rotating Frame of Reference Approach for Simulation of Rotating Impeller in A Mixing vessel", Journal of Engineering Science and Technology, Vol.2, No.2, 2007; (Cited on page 106.)

[80] Fluent Inc., "Fluent 6.3 Tutorial Guide", Sep. 2006; (Cited on page 106.)

[81] Yamada, K., Furukawa, M., et al, "Numerical Analysis of Tip Leakage Flow Field in a Transonic Axial Compressor Rotor", Proceedings of the International Gas Turbine Congress, Nov. 2-7, 2003; (Cited on page 139.)

[82] Phutthavong, P., Hassan, I., et al, "Unsteady Numerical Investigation of Blade Tip Leakage, Part 1: Time-Averaged Results", Journal of Thermophysics and Heat Transfer, Vol. 22, No. 3, 2008; (Cited on page 139.)

[83] Modelmotors ltd. www.modelmotors.cz. (Cited on page 170.)

List of Abbreviations

$\triangle P$ = Pressure jump on both sides of rotor $(P_1 - P_2)$, $Pascal$

$\dot{m}$ = Mass flow rate, kg/s^2

η_{motor} = Efficiency of the motor, $-$

FDR = Free double rotor, $-$

FoM = Figure of merit, $-$

FSR = Free single rotor, $-$

i = Number of the rotor, $-$

PL = Power Loading, $gram/Watt$

SDR = Shrouded double rotor, $-$

SSR = Shrouded single rotor, $-$

ω_i = Angular velocity of rotor i, rad/s

$\overline{D}_{abs}$ = The dimensionless of the absolute distance $(= D_{abs}/D_R)$,$-$

$\overline{D}_{rel}$ = The dimensionless of the relative distance $(= D_{rel}/D_R)$,$-$

ρ = Air density, kg/m^3

θ = Shroud nozzle divergent angle, $^\circ$

A_R = Actuator disk area with the rotor radius R, m^2

C_{le} = Leading edge curvature, $-$

C_P = Power coefficient, $-$

C_T = Thrust coefficient, $-$

D_{abs} = Absolute distance from the first rotor to the inlet, m

D_{rel} = Relative distance between two rotors, m

F_s = Standardized thrust, N

F_{ent} = Thrust generated by air entrance $(= F_{us})$, N

F_{noz} = Thrust generated by nozzle $(= F_{ds})$, N

F_{r_i} = Thrust of rotor i, N

F_R = Thrust generated by rotors, N

F_{sh} = Thrust generated by the shroud, N

F_T = Total thrust of whole system, N

K_e = Ratio of exit over rotor disk area, $-$

K_i = Ratio of inlet over rotor disk area, $-$

l_i = Shroud inlet length, mm

l_N = Shroud nozzle length, mm

N_s = Standardized rotational speed, rpm

N_i = Rotational speed of rotor i, rpm

P_1 = Pressure of upstream first rotor, $Pascal$

P_2 = Pressure of downstream second rotor, $Pascal$

P_s = Standardized pressure, $Pascal$

P_t = Total pressure, $Pascal$

P_{atm} = Far ambient static pressure, $Pascal$

P_e = Pressure at shroud exit, $Pascal$

P_i = Induced power, $Watt$

P_{stan} = Standard pressure, $Pascal$

P_{sta} = Static pressure, $Pascal$

PL_i = Power loading calculated with induced power, $N/Watt$

Q_s = Standardized torque, $N.m$

Q_{r_i} = Torque of rotor i, $N.m$

r_j = Radius of the ring j, m

R_e = Shroud exit radius, mm

R_i = Shroud inlet radius, mm

R_{le} = Leading edge radius ($= R_i$), mm

R_{max} = Shroud maximum radius ($= R_i$), mm

R_r = Shroud cylindrical radius, mm

V_∞ = Velocity in infinity far upstream, m/s

V_e = Induced velocity at shroud exit, m/s

V_0 = Velocity of vehicle, m/s

V_{in} = Induced velocity, m/s

V_R = Induced axial velocity through rotors, m/s

$W_{t_{mech}}$ = Total mechanical power, $Watt$

List of Figures

List of Tables

Analyse numérique et expérimentale
d'un doublet de rotors contrarotatifs caréné au point fixe

Cette étude se propose d'analyser le comportement du double rotor contra-rotatif caréné dans le cadre des échelles réduites des microdrones, pour exploiter le potentiel d'amélioration des performances stationnaires des rotors libres. La demande d'une performance propulsive de haut niveau, alors que les échelles sont très réduites constitue un véritable défi scientifique. De façon générale, par rapport au rotor libre, l'ajout de la carène permet de piloter la contraction de l'écoulement et offre un potentiel de poussée de carène. La tuyère par sa condition d'adaptation pilote le débit entrant à puissance donnée. L'augmentation du débit massique, par comparaison au système de rotor libre, amplifie la poussée à travers la dépression distribuée sur toute la surface de captation.
Pour comprendre les lois de fonctionnement d'un système propulsif caréné, il a d'abord été proposé un modèle théorique simplifié basé sur une extension de la théorie de Froude pour les rotors libres: le système rotor est assimilé à un disque actuateur, générateur de débit dans une conduite à section variable.
Une simulation Navier Stokes 2D axisymétrique a permis d'optimiser les paramètres de forme du carénage. Les simulations ont confirmé l'influence déterminante des sections d'entrée et de sortie, et relativisé l'impact des formes possibles, pourvu que les variations de sections limitent le décollement de la couche limite.
Après conception d'un banc d'essai utilisant un doublet de rotor coaxial placé dans cette carène optimisée, l'étude expérimentale complète et confirme les performances globales du système et qualifie l'écoulement méridien. Enfin, une simulation 3D instationnaire a été entreprise pour compléter l'analyse de l'écoulement autour des rotors.

Mots clés : Rotor coaxial, rotor contra-rotatif, rotor caréné, théorie de Froude, disque actuateur, carène, optimisation de performance, microdrone

Experimental and Numerical Analysis
of a Shrouded Contrarotating Coaxial Rotor in Hover

This study aims to analyze the behavior of shrouded, contrarotating coaxial rotor in the reduced MAVs' scale in order to exploit its potential to improve the free rotor steady performance. The high hover ability under low operational Reynolds number is therefore, a scientific challenge. Generally, comparing with free rotor, the addition of the shroud decreases the flow contraction and gives the potential to generate an extra thrust. A suitable nozzle can control the mass flow for a given power. The increased mass flow, comparing with free rotor, amplifies the thrust offered by the low pressure formed at the
air entrance.
To understand the principals of shrouded propulsion system, a simplified theory model was first proposed through the extension of Froude theory for free rotors: the double rotor is initially treated as an actuator disk, generating the flow at varied sections through the shroud passage.
A 2D simulation which accounts for an axial flow of viscous effects within the actual shroud profile, confirmed effects of all defined geometrical parameters. It further demonstrated that within the non-stalling region of the different crosssections, shroud shape and inlet shape do not have a significant impact on performance.
The experimental study, carried out with coaxial rotor, contributed to the confirmation of the overall performance and the approximation of the flow field through the shroud. Meanwhile, the 3D simulation, developed to better model the actual coaxial rotor in counter rotation, was validated to well solve the steady performance. It was applied to complement the analysis of the flow around the coaxial rotor.

Keywords: Coaxial rotor, contrarotating rotor, shrouded rotor, Froude theory, actuator disk, shroud, performance optimization, MAVs